SPIE.

HANDBOOK OF OPTICAL BIOMEDICAL DIAGNOSTICS

SECOND EDITION

Volume 1: Light–Tissue Interaction

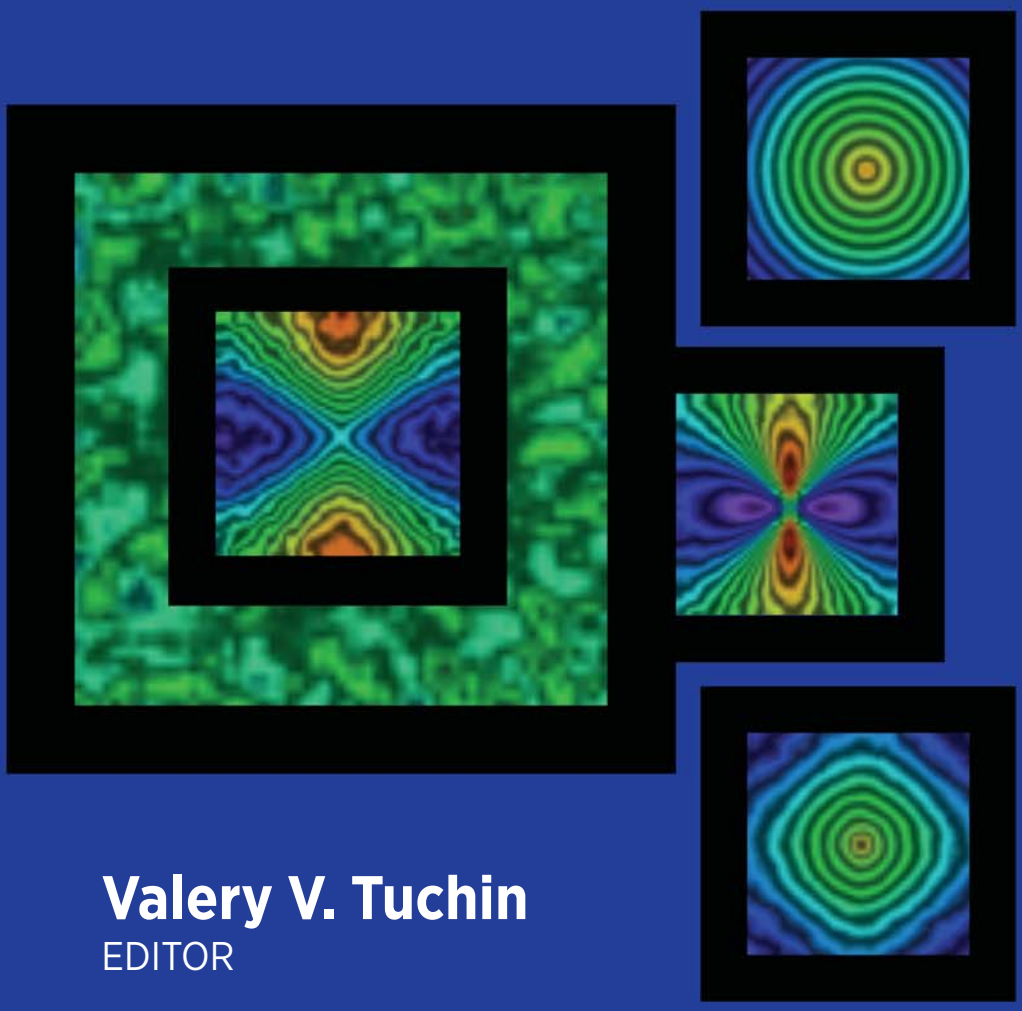

Valery V. Tuchin
EDITOR

Library of Congress Cataloging-in-Publication Data

Names: Tuchin, V. V. (Valerii Viktorovich), editor.
Title: Handbook of optical biomedical diagnostics / Valery V. Tuchin, editor.
Other titles: Optical biomedical diagnostics
Description: Second edition. | Bellingham, Washington : SPIE Press, [2016] | Includes bibliographical references and index.
Identifiers: LCCN 2015038341| ISBN 9781628419092 (v. 1 : alk. paper) | ISBN 9781628419139 (v. 2 : alk. paper)
Subjects: | MESH: Diagnostic Imaging—methods. | Microscopy, Confocal. | Spectrum Analysis.
Classification: LCC R857.O6 | NLM WN 180 | DDC 616.07/54—dc23
LC record available at http://lccn.loc.gov/2015038341

Published by
SPIE
P.O. Box 10
Bellingham, Washington 98227-0010 USA
Phone: +1 360.676.3290
Fax: +1 360.647.1445
Email: books@spie.org
Web: http://spie.org

Printed in the United States of America.
First printing.

SPIE.

Table of Contents

Chapter 1
Introduction to Light Scattering by Biological Objects

Nikolai G. Khlebtsov
Institute of Biochemistry and Physiology of Plants and Microorganisms, Russian Academy of Sciences, Saratov, Russia

Saratov National Research State University, Saratov, Russia

Irina L. Maksimova
Saratov National Research State University, Saratov, Russia

Igor Meglinski
University of Oulu, Oulu, Finland

Lihong V. Wang
Washington University in St. Louis, St. Louis, USA

Valery V. Tuchin
Saratov National Research State University, Saratov, Russia

National Research Tomsk State University, Tomsk, Russia

Institute of Precision Mechanics and Control, Russian Academy of Sciences, Saratov, Russia

1.1 Introduction

The practices of scattering and absorbing electromagnetic radiation enjoy wide use in various fields of science and technology that aim to study the structure and properties of inhomogeneous media. The theory and practice of light-scattering methods is now a fairly well-developed field, owing to the methods' profound importance for applications such as atmospheric and oceanic optics,[1–5] radio-wave propagation and radio communication,[6]

physical chemistry of solutions and colloids,[7] materials science and chemical technology,[8] biophysics, and laser biomedicine.[9,10] The theoretical models, experimental measurement procedures, and data interpretation methods have been developed by experts in various disciplines (from astrophysics to laser ophthalmology); therefore, there are certain traditions and terminological barriers that hinder effective interactions among various research groups. To illustrate, for experts in atmospheric optics and astrophysics, the ideology of radiation transfer theory (RTT)[2,3] is natural, and using language related to the apparatus of correlation functions and structural scattering factor is more habitual when interpreting data by small-angle x-ray scattering or neutron scattering.[7,8] Another example is the composite medium technology whose basic concepts are effective dielectric permeability and effective refractive index.[11] In colloid optics, the model of scattering via an isolated particle is most popular; this model is described either in terms of Maxwell's rigorous electromagnetic theory or on the basis of various approximations.[1,7,12]

Despite terminological and other differences, the basis of many methods using the scattering of neutrons, x-radiation, light, or radio waves proves to be sufficiently versatile. With respect to the scattering of electromagnetic waves of various frequencies, this versatility is probably explained by the common classical basis, Maxwell's electromagnetic theory, which is applied with physical models of scattering media. Even in the case of particle scattering due to potentials associated with this or another inhomogeneity of the medium,[13] the general theoretical interpretation of the scattering (e.g., in terms of T-matrix formalism) may be exactly the same as that in the case of electromagnetics.[14]

In view of the great diversity and structural complexity of biological systems,[9,10] the development of adequate optical models of the scattering and absorption of light is often the most complex step of a study. These models include virtually all sections of dispersion media optics: (1) simple single-scattering approximation; (2) incoherent multiple scattering, described by the radiation transfer equation (RTE); and (3) multiple-wave scattering in condensed systems of electrodynamically interacting scatterers and inhomogeneities. Quite plainly, such a broad range of problems rules out the possibility of a more or less detailed treatment of technical details. Therefore, the material presented in this chapter includes only certain elements of the theoretical apparatus used in the above-mentioned sections of scattering media optics; otherwise, it includes references to the relevant literature.

1.2 Extinction and Scattering of Light in Disperse Systems: Basic Theoretical Approaches

Three major directions can be distinguished in scattering media optics. The first is associated with the solution of diffraction problems for individual scatterers and with the determination of how absorption and scattering characteristics are

linked to the optical, geometrical, and structural parameters of particles.[12,15] Since the second half of the 1980s, a number of novel methods and algorithms have been developed that allow, in principle, quantitative results to be obtained for a very wide class of sizes, shapes, structures, and optical parameters of particles.[15] A brief survey of particle-scattering-theory methods is given in Section 1.3; more detailed information can be found in Ref. 16.

The importance of this domain of the scattering theory for applications to actual systems is determined by the following circumstances. First, for very rarefied and optically thin media, the scattering characteristics of an ensemble of particles (intensities, integral cross sections) are found by simple summation with no regard to the interference of scattered waves. What is known as single-scattering approximation consists therein. Of course, in some special cases, this approximation should be used with caution. For example, scattering in the forward direction is coherent at least when the time of the incident light coherence is greater than the time of its propagation in the scattering layer and is less than the characteristic time of particle configuration change. For small angles, therefore, it is the scattered fields, not intensities, that should be summed. However, for the typical sizes of the scattering sample, the domain of such angles turns out to be very small and may be neglected.[1,12] The single-scattering approximation may also be applied when scattered fields are summed with regard to geometrical phase shifts from different particles. However, the scattered fields themselves are calculated on the basis of excitation of the scatterer by the initial incident wave, i.e., with no regard to the radiation from other particles (see Section 1.7). Conditions necessary to apply the single-scattering approximation have been discussed by Mishchenko et al.[17]

Another important application of the theory of scattering by small particles is the calculation of the characteristics of the elementary scattering volume, which appears in the RTT.[2,6] Finally, the electromagnetic theory for an isolated particle determines the scattering operator, which is used in the multiple wave scattering theory (MWST)[18–20] and determines the particle's response to a specified exciting field. The RTT and MWST theories will be considered below.

The second trend of the light-scattering theory is associated with the RTE. The equation operates with photometric quantities and phenomenological characteristics of the medium such as scattering and absorption coefficients and the unit-volume-scattering indicatrix (also known as phase function or form factor).[2–4,6,21] In the RTT, multiple scattering is allowed, phenomenologically, on the basis of the energy conversation law and the ray intensity (or ray radiance) concept.[6] By now the RTE theory has been elaborated in detail (including formulas, tables,[22] and public-domain computer codes for the solution of various particular problems[23]).

The physical picture forming the basis of the RTT is based on the notion of mutual multiple reradiation of inhomogeneities. In essence, the subject of

the RTT is the kinetics of photon diffusion in an inhomogeneous medium. Inclusion of the Stokes polarization parameters in the RTT leads to the matrix formulation of the RTE;[3,21] however, the physical basis of the matrix RTT remains exactly the same as that in the scalar case. The elementary volume of the scattering medium plays the role of a quadratic detector that splits the field into incoherent beams (photons), and the scattering act itself is always interpreted in the energy sense, with averaging over time and volume.[24] The notions of photon diffusion in an inhomogeneous medium naturally lead to a statistical scheme of solving the RTE in the context of Monte Carlo (MC) ideology. This method calls for considerable computer resources, but it may be used for the realistic geometries of the experiment. This question is examined at greater length in Section 1.8. The microphysical basis of RTE and its derivation from Maxwell equations and statistical properties of scattering media was discussed by Mischchenko.[25]

The third, and the most rigorous, trend of the scattering theory is in essence the electrodynamics of statistically inhomogeneous media.[20,24] This approach considers multiple wave scattering by discrete or continuous inhomogeneities, the correlation statistics of scatterers, and the vector character of the electromagnetic field.[18–20] The basic physical principles of the theory of multiple wave scattering are the same for systems with continuous and discrete inhomogeneities, but details of the formalism are somewhat different. For definiteness, we will speak below of the case of discrete scatterers.

The theory of propagation and multiple scattering of radiation in a medium of interacting scatterers belong to a fairly complex class of many-particle electrodynamic problems. For their solution, special diagram methods have been developed that lead to the Dyson equation for Green's mean function or to the Bethe-Solpiter equation for Green's function correlation.[20] Because of difficulties of a purely mathematical nature, noticeable progress in this field, including the emergence of effective numerical algorithms, has only recently been made.[26–28]

Being fairly complex mathematically, the theory of multiple wave scattering is based on simple physical principles. First, it is assumed that the spatial configuration of all particles and its statistical properties are known. Second, it is assumed that the scattering operator of an isolated particle that describes the scattered field for a given exciting field is known. Since we are dealing with a system of electrodynamically interacting multipole oscillators, the exciting field is formed from the incident field, and the multiple scattered fields from all the other particles. Hence it is clear that the main difficulty of the theory is just to find the exciting field with regard to all possible orders of scattering from all the interacting particles. The different versions of the theory differ primarily in the methods of calculation of the exciting field with regard to the statistical properties of the ensemble

describing the spatial configuration and the optical properties of scatterers. Once the exciting fields have been found, further analysis consists in calculating the scattered fields of isolated particles and in adding these fields together with regard to phase shifts. Since we are dealing with random fields, one has to use the appropriate correlation analysis in order to calculate the observed photometric characteristics.

In the context of the rigorous MWST, the theory of coherent propagation of radiation in a medium with densely packed scatterers has been fairly well developed.[18,19,21] The basic result of this theory is the deduction of a *dispersion equation* for the effective wave number describing the coherent-field propagation in a medium and differing from the wave number of free space. This dispersion equation allows for the optical properties of scatterers and for the statistical properties of their spatial arrangement. As a rule, when deducing a dispersion equation, one makes certain simplifying assumptions. For example, quasi-crystalline approximation is used to break the infinite chain of multiple-scattering equations, and the Percus–Yevick approximation is used to describe pair correlations in particle positions.[29]

Significantly, there is a close relation between the theory of coherent light propagation in densely packed disperse systems and that in homogeneous molecular or crystalline media. The relationship between the refractive index n of such a medium, the concentration N, and the polarizability of molecules α is given by the well-known Lorentz–Lorenz formula[30]

$$\frac{n^2-1}{n^2+2}=\frac{4\pi}{3}N\alpha. \tag{1.1}$$

It is important for our consideration that this relation can be obtained as a result of derivation of the Ewald–Oseen extinction theorem.[30] In this derivation, the optical properties of a medium are treated on the basis of representation of the total optical field as a sum of the incident wave and all waves multiply scattered by molecules exited by an effective self-consisting field. Elimination of the incident wave and the arising of a new wave, propagating through the medium with velocity c/n, are due to the interference of the incident wave and self-consisting fields scattered by molecular dipoles in the forward direction. For other directions, the fields scattered from different, spatially fixed and physically small volumes $\delta V \ll \lambda^3$ would be totally suppressed because of the interference if no fluctuations were in the medium. However, the fluctuations violate coherence and are responsible for molecular scattering.

The problem with calculation of the effective propagation constant in a condensed medium is closely linked to the theory of effective optical constants.[11,31] The main object of this theory is to formulate a *mixing rule* where the actual dispersion medium could be replaced by a model homogeneous medium with effective optical constants. In the electrostatic

case, it is required that the calculated values of the effective dielectric permeability be as close as possible to the experimental measurements of this parameter for an inhomogeneous sample. In the optical case, the calculation of absorption and scattering for a homogeneous particle with an effective ε_{eff} should be as close as possible to the results of the numerical or natural experiments for an actual inhomogeneous particle.

A fundamental peculiarity of the MWST is that the optical properties of interacting particles differ from those characteristics that are obtained in solving the scattering problem for an isolated particle. In Section 1.4, we will see that the extinction cross sections of particles in a cluster do not coincide with the usual Mie calculation. Even in the simplest case of two absolutely identical contacting spheres, the scattering cross section of each particle will depend on the the separation between particles and the bisphere orientation with respect to the incident plane wave. This type of effect is commonly called the collective scattering effect or cooperative scattering effect.[20,24]

It should be emphasized that these cooperative effects may be of different nature and hence have different experimental manifestations. First, as indicated above, the exciting local field may differ substantially from the incident-wave field and even from the mean field in a dispersion medium because of the violent local fluctuations. In this case, each particle's optical response itself will differ substantially from the isolated-scatterer case. Even if the positions of the interacting particles are absolutely random and are in no way correlated, the optical properties of such a dispersion system will differ from the case of single scattering of noninteracting particles. Another cause for the emergence of cooperative effects in densely packed systems is associated with the constructive interference of individual scattered fields, which is due to the presence of a certain order in particle arrangement. The physical mechanisms of emergence of this order are connected with the competition from attraction (repulsion) forces and the entropy factor. The correlations in particle positions may be either short range or long range, depending on the nature of these forces. In the case of noncharged particles, only the short-range order is usually observed, which may be described using the solid-sphere model, the Lennard–Jones potential, and so on.[29]

In the general case, the cooperative effects of multiple scattering include both components, and their accurate calculation is, as noted above, a challenging task. However, for biological systems, the situation is simplified a bit because the optical properties of interacting particles usually do not differ widely from the properties of their environment. Therefore, even at multiple reradiation of particles the differences of the exciting field from the incident-wave field are not too notable. This means that the major influence on the optical characteristics of the medium is exerted not by the change in the local exciting fields, but by the scattered-fields interference, which is due to

correlations of the short-range positions. To a first approximation, the scattered fields themselves can be evaluated within the limits of a single approximation, i.e., assuming that the exciting field is equal to the incident-wave field. The development of that approach will be discussed below (Section 1.7).

A rigorous analysis of conditions for the applicability of this or that version of the light-scattering theory is a nontrivial problem,[20] in which one has to account for the coherence properties of the incident radiation; the size, concentration, and optical properties of particles; the characteristic time of stability of the medium microstructure (i.e., the characteristic times of the fluctuation relaxation); the geometrical parameters of the scattering sample; the photodetector characteristics; and so on.[24] For example, if the coherence time of the incident radiation is less than the time of the photon run between two consecutive scattering acts, then these scattering acts will be statistically independent. In this case—which is typical for neutron or x-ray scattering—either the RTT or the single-scattering approximation (near-transparent media) is applicable. Qualitatively, the possibility that each of the three approaches mentioned can be applied for describing radiation propagation and scattering in a dispersion medium is determined by five characteristic parameters: the wavelength λ; the size of particles (inhomogeneities) a; the mean distance between them (correlation radius) R; the geometrical thickness of the medium d; and the coherence length l_c. For concentrated dispersion media, $R \sim a$, so if the particle size is comparable to the wavelength, the scattering particles are not independent, and allowance should be made for multiple reradiation within the limits of the MWST. How the theory is formulated specifically depends on the ratio among the particle size, the wavelength, and the geometrical parameters of the scattering volume.

If the mean distance $R \gg a$, λ, l_c, (moderately concentrated and dilute media of arbitrary optical thickness), the RTT theory is applicable, and, again, its specific form will depend on the a/λ and R/d ratios (small-angle approximation, diffusion approximation, etc.[6]). From a physical standpoint, a necessary condition of RTT applicability is the smallness of the wavelength and particle size as compared with the characteristic length of the light-field extinction.[24] It should be noted, however, that sometimes the RTT is not applicable in principle. In particular, it is not applicable for describing the effect of enhanced back-scattering.[32,33]

In the case of dilute and optically thin dispersion media (when $R \gg a,\lambda$, and the optical thickness $\sigma_e d/R^3 \ll 1$, σ_e being the extinction cross section of the particle), the single-scattering approximation is applicable, in which photometric quantities, quadratic in the scattered field, are just an additive sum over the particles. It is important to keep in mind that the boundaries of applicability of single scattering differ substantially in the suspension-particle concentration (or in the optical thickness), depending on the type of effects

being measured. For instance, when measuring the scattering indicatrix, one sees that the contribution of multiple scattering is manifested at considerably lower concentrations than those in the case of measurement of the extinction of a collimated light beam. The physical causes for such different sensitivities of different effects are obvious. In the case of measurement of the indicatrix, the probability of multiple scattering in a specified direction increases with an increase in particle concentration. However, when measuring the extinction of a collimated beam, one sees that the probability of multiple noncoherent scattering does not affect the result (if only the receiver's aperture is small enough). Otherwise stated, the multiplicity of noncoherent scattering does not change the collimated transmission if the multiply scattered "photon" did not get into the photodetector.

The question under discussion is intimately linked to the important question of the boundaries of applicability of Bouguer's law under conditions of multiple scattering.[34–36] As is known, Bouguer's law (also known as the Beer–Lambert law) describes the exponential extinction of the incident-light intensity in a layer of thickness d

$$I(d) = I_0 \exp(-\bar{\tau} d) = I_0 \exp(-\tau), \tag{1.2}$$

where $\bar{\tau}$ and $\tau = \bar{\tau} d$ are the turbidity and the optical thickness of a sample, which in the single-scattering approximation are proportional to the extinction cross section σ_e and to the number particle concentration N,

$$\tau = \sigma_e N d. \tag{1.3}$$

Though the particle concentration and the geometrical thickness of the layer enter into relationship (1.3) in the same way, it is important to emphasize the fundamental difference between the optically dense, concentrated systems ($R \sim a,\lambda$) and the optically thick ($\tau \gg 1$), but dilute systems ($R \gg a,\lambda$).

In the first case, the scattering characteristics of the elementary volume of a suspension differ from the dilute-system parameters because of the electrodynamic particle interaction, and the relationship between the wave number in the medium and the particle concentration is nonlinear. More specifically, Eq. (1.3) is no longer valid. Physically, this can be seen from a simple qualitative example. Let an empty glass cuvette be filled up with a water aerosol that consists of submicron-sized droplets. As the droplet concentration (or the corresponding volume fraction f) increases, the imaginary part of the effective refractive index also increases from 0 to the values determined by[1]

$$n \approx 1 + 2\pi k^{-3} N S(0) \equiv 1 + N[2\pi k^{-3} \mathrm{Re} S(0) + i\sigma_e / 2\ k], \tag{1.4}$$

where $S(0)$ is the forward-scattering amplitude [we define it as the van de Hulst[1] amplitude $S(0)$ divided by the imaginary unit i]. As the scattering

becomes intensive enough, the coherent wave extinction gradually deviates from the linear law (1.4), then reaches a maximum and eventually, at the volume fraction $f \to 1$ (cuvette with water!), decreases to very small values corresponding to the transmittance of clear water.

A quantitative description of the above scenario is based on the theory of multiple scattering and coherent electromagnetic wave propagation in a densely packed disperse medium.[18,19,26] For example, in the Rayleigh limit, the concentration dependence $n(f)$ for spherical particles with radius $a \ll \lambda$ can be described by a generalization of the Mossotti–Clausius or Maxwell Garnett mixture formulas[18]

$$\varepsilon \equiv n^2 = 1 + \frac{3f\alpha_1}{1 - f\alpha_1}\left\{1 + i\frac{2}{3}x^3\alpha_1\frac{(1-f)^4}{(1-f\alpha_1)(1+2f)^2}\right\}, \tag{1.5}$$

$$\alpha_1 = \alpha/a^3 = \frac{\varepsilon_1 - 1}{\varepsilon_1 + 2}. \tag{1.6}$$

Here, $x = ka \ll 1$, ε_1 is the dielectric permittivity of spheres, the refractive index of the surrounding medium is supposed to be equal to 1, and the Percus–Yevick approximation was used to represent the pair distribution function. In the dilute case $f \ll 1$, Eq. (1.5) is equivalent to Eq. (1.4) with $S(0) \approx k^3\alpha(1 + i2x^3\alpha_1/3)$, whereas for the densely packed suspension with $f = (4\pi/3)Na^3 \to 1$, the extinction contribution due to light scattering vanishes and Eq. (1.5) reduces exactly to the Lorentz–Lorenz relation (1.1). Thus, for concentrated suspensions, the deviations from Bouguer's law are determined by the electrodynamic particle interaction and can be observed even at small geometrical thicknesses of the layer.

In the case of dilute, albeit optically dense, systems, the situation is entirely different. Here, the considerable optical thickness is ensured by the corresponding geometrical thickness of the scattering sample. The optical characteristics of the elementary volume are determined by the properties of isolated particles and are proportional to their concentration. The extinction of a direct (coherent) beam is determined by Bouguer's exponential law with optical thickness (1.3). As the geometrical path and the corresponding optical thickness increase, there occurs transformation of the primary coherent beam into multiply scattered noncoherent light. This transformation is described by the RTE, which includes Bouguer's extinction of the primary beam.[2,3,6] Thus, the difference from the single-scattering case is only that multiply scattered noncoherent light, as well as the attenuated incident light beam, also gets into the photodetector. This means that the effects of multiple light scattering during the measurement of collimated transmittance are physically manifested as effects of *small-angle scattering* or, more specifically, as effects of an increase in transmittance at the expense of single- and multiple-scattering

small-angle light flux. This situation is completely analogous to the well-known influence of small-angle scattering on the measurements of transmittance of dilute suspensions.[37,38] The ratio between the attenuated incident light and the small-angle flux depends not only on the layer thickness, but also on the optical scheme of photometry.[34,35,38] For example, if the primary beam is well collimated, and the detector's receiving aperture is small, the effects of small-angle distortions due to multiple scattering will be small up to a very large optical thickness.[34–36]

1.3 Theoretical Methods for Single-Particle Light-Scattering Calculations

1.3.1 Basic parameters for single-particle light scattering

Consider the scattering by a certain particle of a monochromatic [$\exp(-i\omega t)$] plane electromagnetic wave,

$$\mathbf{E}_0 = \mathbf{e}_0 \exp(i\mathbf{k}_0), |\mathbf{e}_0| = 1. \tag{1.7}$$

By virtue of linearity of Maxwell's equation, the scattered field $\mathbf{E}_s$ (in the direction $s = \mathbf{k}_s/k$) should be linearly related to the incident field via the *scattering affinor* $S(\mathbf{k}_s,\mathbf{k}_0)$[14,39]

$$\mathbf{E}_s = \frac{\exp(ikr)}{kr}\bar{S}(\mathbf{k}_s,\mathbf{k}_0)\mathbf{e}_0, \tag{1.8a}$$

the *vector amplitude of scattering*[14]

$$\mathbf{S}(\mathbf{k}_s,\mathbf{k}_0) = \bar{S}(\mathbf{k}_s,\mathbf{k}_0)\mathbf{e}_0, \tag{1.8b}$$

or the corresponding *amplitude scattering matrix*[15]

$$\begin{Bmatrix} E_{s1} \\ E_{s2} \end{Bmatrix} = \frac{\exp(ikr)}{kr}\begin{bmatrix} S_{11} & S_{12} \\ S_{21} & S_{22} \end{bmatrix}\begin{Bmatrix} e_{01} \\ e_{02} \end{Bmatrix}, \tag{1.9}$$

where the indices $1 = \parallel$ and $2 = \perp$ stand for the transverse components (i.e., $E_\parallel = E_\vartheta$, $E_\perp = E_\varphi$) relative to the planes containing the z-axis and the incidence direction $\mathbf{s}_0 = \mathbf{k}_0/k$ or the scattering direction $\mathbf{s} = \mathbf{k}_s/k$. As a rule, the incidence direction is chosen to be coincident with the z-axis,[1,12] so the transverse components of the fields are determined relative to the scattering plane ($\mathbf{s}$, $\mathbf{s}_0$). We note that different basis vectors for the transverse components of the field and different normalization in Eq. (1.9) are chosen by different authors.[1,12,15] As a consequence, the S_{ij} elements may differ.[15] It is important to emphasize that the amplitude scattering matrix relates the field components determined in *different* coordinate systems and, therefore, *is not a tensor.*

The amplitude scattering matrix gives a full description of the scattered field, but in actual experiments photocurrents are usually measured that are

proportional to quadratic field combinations. Therefore, to describe the monochromatic transverse wave one introduces four Stokes parameters, I, Q, U, V[1,12] or the corresponding column vectors $\hat{I}$. The linear relationship between the incident ($\hat{I}_0$) and scattered ($\hat{I}_s$) Stokes parameters is given by the *Mueller scattering matrix* (or simply the *scattering matrix*)[1,12]

$$\hat{I}_s = \frac{1}{k^2 r^2}\hat{F}\hat{I}_0. \tag{1.10}$$

The formulas expressing the 4×4 scattering matrix $\hat{F}$ in terms of the amplitude 2×2 matrix $\hat{S}$ can be found elsewhere.[1,12] The $\hat{F}$ matrix contains complete information about the scattering properties of the particle, but in practice one would measure only some scattered-light parameters, e.g., the scattering intensity $I_s(\theta)$ and the degree of linear polarization.

Particle scattering and absorption of light withdraws energy from the incident wave. This effect is consequently characterized by the extinction cross section σ_e having an area dimension. The product $I_0\sigma_e$ determines the total power of scattering and absorption. The scattering (σ_s) and absorption (σ_a) cross sections are determined in a similar way. According to the optical theorem,[1,12,14] the extinction cross section of linearly polarized light is proportional to the forward scattering amplitude

$$\sigma_e = \frac{4\pi}{k^2}\,\mathrm{Im}[e_0^* \bar{S}(\mathbf{k}_0,\mathbf{k}_0)\mathbf{e}_0], \tag{1.11}$$

where the asterisk denotes complex conjugation. In the more general case of the incident light with arbitrary polarization, the cross section σ_e is determined by way of the *extinction matrix*.[3,21] The scattering cross section is calculated by integration of the scattered intensity over all directions. For example, for the incident light with Stokes parameters (I_0, Q_0, U_0, V_0), we have

$$\sigma_s = \frac{1}{k^2 I_0}\int_{4\pi}[I_0 F_{11} + F_{12}Q_0 + F_{13}U_0 + F_{14}V_0]d\Omega(\mathbf{s}). \tag{1.12}$$

In the case of unpolarized light and spherically symmetrical scatterer, the relationship (1.12) is reduced to the usual integral of the indicatrix with respect to the scattering angle

$$\sigma_s = \frac{2\pi}{k^2}\int_0^\pi F_{11}(\theta)\,\sin\,\theta d\theta. \tag{1.13}$$

The asymmetry (anisotropy) parameter g is defined by equation

$$g = \langle\cos\,\theta\rangle = \frac{2\pi}{k^2\sigma_s}\int_0^\pi \cos\,\theta F_{11}(\theta)\sin\,\theta d\theta, \tag{1.14}$$

and its sign points to the preferential forward ($g > 0$), backward ($g < 0$), or symmetrical isotropic scattering ($g = 0$).

1.3.2 Exact analytical and numerical methods

The general statement of the single-particle scattering problem is rather simple and can be described as follows. A field $\mathbf{E}_0$ is incident on a scattering particle of volume V and excites the field $\mathbf{E}_i$ inside V. Outside V, an additional field, the diffraction field $\mathbf{E}_s$, is generated. It is required to calculate, on the basis of Maxwell's equations, the complete field $\mathbf{E}$, which equals $\mathbf{E}_i$ inside V, and $\mathbf{E}_0 + \mathbf{E}_s$ outside V, and that satisfies the boundary conditions at the particle surface as well as the radiation conditions at infinity. The general scheme being simple, a concrete solution to the problem depends essentially on the geometry of the scatterer and on the properties and structure of its substance. For example, the solution cannot be obtained in a general closed form even for a *spherical* particle with an anisotropic refractive index of a general type.[12] Therefore, in the theory of scattering by small particles various methods have been developed whose scope and effectiveness depend on the particular statement of a problem. From a current standpoint, an effective numerical algorithm realized on a personal computer is equivalent to an analytical solution, which as a rule also calls for nontrivial calculations. In this section, we will look briefly only at those methods that are most intensively used in biological applications. A more detailed discussion of the calculation methods can be found in a recent review.[16]

1.3.2.1 Separation of variables and T-matrix methods (SVM and TM)

The most important analytical solution is the theory of scattering by a homogeneous isotropic sphere, called the Mie theory[1,12] (the pioneering work on this problem is associated with a constellation of names[40–44]). To illustrate the basic results of the Mie theory, we give formulas for the extinction cross section, the scattering cross section, and the anisotropy parameter, following the designations[12]

$$\sigma_e = \frac{2\pi}{k^2} = \sum_{n=1}^{\infty}(2n+1)\mathrm{Re}(a_n + b_n), \tag{1.15}$$

$$\sigma_s = \frac{2\pi}{k^2}\sum_{n=1}^{\infty}(2n+1)(|a_n|^2 + |b_n|^2), \tag{1.16}$$

$$g = \frac{4\pi}{k^2\sigma_s}\left\{\sum_{n=1}^{\infty}\frac{2n+1}{n(n+1)}\mathrm{Re}\,(a_n b_n^*) + \sum_{n=1}^{\infty}\frac{n(n+2)}{n+1}\mathrm{Re}\,(a_n a_{n+1}^* + b_n b_{n+1}^*)\right\}, \tag{1.17}$$

where the coefficients a_n and b_n are called Mie coefficients.[12] The Mie theory is generalized for the case of concentrated spheres, particles with an

inhomogeneous profile of refractive index or with the optical activity of the substance, and also for the case of illumination by a focused laser beam. The relevant literature citations and effective computer codes can be found in Refs. 16 and 23.

For an infinite circular cylinder an exact solution at perpendicular incidence was first obtained by Rayleigh,[45] who addressed this problem once again in his last work written shortly before his death.[46] Though an infinite cylinder is not a three-dimensional (3-D) scatterer, this model is helpful in understanding light scattering and extinction by an anisotropic dispersion medium (see Section 1.7 below). References to literature that generalizes a simplest model can be found in Ref. 16. The Mie solution is also generalized to an arbitrary collection of spheres, but this subject concerns the problem of scattering by particle aggregates and will be treated separately in Section 1.4.

In Helmholtz's scalar equation, the variables are separated into 11 physically interesting coordinate systems.[47] But for a vector field containing *three* scalar functions, a complete separation of variables is possible only in six systems: (1) Cartesian, (2–4) three cylindrical, (5) conical, and (6) spherical. Therefore, Möglich's[48] formal solution for spheroidal coordinates was useless for all practical purposes until the method for separation of variables was adapted by Asano and Yamamoto[49] for numerical calculations via cutoff of infinite coupled (i.e., not fully separated) equations. Farafonov[50] improved the method described in Ref. 49 by using an ingenuous scheme of splitting fields into two types with an invariant angular part. By now, a large body of factual material has been assembled on the application of SVM in the calculation of scattering by spheroidal particles.[15,51]

The T-matrix method, which is well known in quantum theory,[13] was introduced into electromagnetic scattering by Waterman.[14] Contrary to the Green function method, the T-matrix relates not the fields themselves in a coordinate representation, but the expansion coefficients of the incident and scattered fields over some complete set of vector basis functions. For example, if one expands all fields in vector spherical harmonics (VSH) $\mathbf{Y}_{mnp}^{(\tau)}$ [13,47,52]

$$\mathbf{Y}_{mn1}^{(\tau)} = \mathbf{N}_{mn}^{(\tau)}(k\mathbf{r}), \mathbf{Y}_{mn2}^{(\tau)} = \mathbf{M}_{mn}^{(\tau)}(k\mathbf{r}), \tag{1.18}$$

of the first and third kind ($\tau = 1,3$), then the expansion coefficients for scattered (a_{mnp}) and incident (exciting, $p_{\mu\nu q}$) fields are related by

$$a_{mnp} = \sum_{\nu=1}^{\infty} \sum_{\mu=-\nu}^{\nu} \sum_{q=1}^{2} T_{mnp,\mu\nu q} p_{\mu\nu q}. \tag{1.19}$$

After being published in Ref. 53, the T-matrix method began to be used commonly in the scattering theory.[54–56] An important strong point of the method is the possibility that the problem on the orientational averaging of

the observed scattering characteristics may be solved analytically.[57,58] To illustrate, the extinction and scattering cross sections averaged over random particle orientations are expressed directly in terms of a T-matrix

$$\langle C_e \rangle = -\frac{2\pi}{k^2}\mathrm{Re}[\mathrm{Sp}(T)], \tag{1.20}$$

$$\langle C_s \rangle = \frac{2\pi}{k^2}\sum_{ab}|T_{ab}|^2, \tag{1.21}$$

where the symbol Sp in Eq. (1.20) stands for a spur over all T-matrix indices, and the symbol a or b in Eq. (1.21) signifies a combined multi-index (nmp).

1.3.2.2 Integral equation method

The integral equation method (IEM) occupies a special place in the range of theoretical methods, since it is a general approach in which, by using the affinor Green function[13]

$$G(\mathbf{r},\mathbf{r}') = (1 + k^{-2}\nabla\nabla)\frac{\exp[i\mathbf{k}(\mathbf{r}-\mathbf{r}')]}{4\pi|\mathbf{r}-\mathbf{r}'|}, \tag{1.22}$$

a boundary problem is reduced to an integral equation that includes the boundary condition and radiation condition at infinity[13,59,60]

$$\mathbf{E}(\mathbf{r}) = \mathbf{E}_0(\mathbf{r}) + k^2\int G(\mathbf{r},\mathbf{r}')[\varepsilon(\mathbf{r}') - \hat{1}]\mathbf{E}(\mathbf{r}')d^3\mathbf{r}'. \tag{1.23}$$

Therefore, the IEM is not merely a numerical approach, but also an efficient basis for the formulation of other methods [e.g., the method of moments,[61] the T-matrix method,[53,62] or the Rayleigh–Debye–Gans (RDG) method[6,13,59,63]]. In Eq. (1.23), the scattered field is expressed by way of an unknown distribution of *bulk* sources induced by an external field. In the electromagnetic theory, another approach is also used,[60,62] in which the scattered field is calculated by way of a *surface* source distribution.

The presence of singularity in Green's function (1.22) gives rise to a "self-term" that accounts for the difference between the average Maxwell field and the local (effective) Lorenz field.[59] The various formulations of IEM are in many ways different only in the methods for allowing for the self-term and in the methods for replacing the integral equation by its discrete counterpart.[64–67] The singular equation (1.23) can be represented, by the Fourier transform, as a nonsingular Fredholm integral equation (FIE) of the second kind,[68,69] which is solved numerically after the discrete-analogue substitution. It is interesting that the FIE kernel coincides with the second Born approximation for the integral equation obtained in Ref. 63. References to papers on the application of various IEM versions in problems of single-particle scattering are available for review.[16]

1.3.2.3 Discrete dipole approximation

In the theory of scattering by small particles, this method began to be employed intensively after the publication of a paper by Pursell and Pennypacker,[70] though undoubtedly its physical basis was known and applied elsewhere previously.[30] Yurkin et al. (see, e.g., Ref. 71, and references therein) developed an alternative discrete dipole approximation code (ADA version) with enhanced efficiency. A detailed consideration of discrete dipole approximation (DDA) or ADDA capabilities and limitations can be found in Ref. 71. The basic physical approximation is in substitution of the actual scatterer for an ensemble of discrete elements with volume V_i, polarizability α_i, and dipole moments $\mathbf{d}_i = \mathbf{d}(\mathbf{r}_i)$, $i = 1 - N$. All the other calculations, e.g., those of the dipole amplitudes, the scattered field, the integral cross sections, and the scattering matrix may be done absolutely rigorously. The equations for dipole moments are not hard to write from simple considerations based on the concept of an exciting field equal to the sum of the incident wave and the fields of other dipoles at a given point

$$\mathbf{d}_i(\mathbf{r}_i) = \alpha_i \left[\mathbf{E}_0(\mathbf{r}_i) + k^3 \sum_{j \neq i} G_{ij} \mathbf{d}_j(\mathbf{r}_j) \right]. \tag{1.24}$$

The tensor of dipolar scattering G_{ij} is determined by the known formulas[30]

$$G_{ij} = \exp(ikr_{ij})[G_1(kr_{ij}) + G_2(kr_{ij})\mathbf{R}_{ij} \cdot \mathbf{R}_{ij}], \tag{1.25}$$

$$G_n(z) = (-1)^n[-z^{-1} - (2n-1)(iz^{-2} - z^{-3})], \quad n = 1,2, \tag{1.26}$$

where $\mathbf{r}_{ij} = \mathbf{r}_i - \mathbf{r}_j$, $\mathbf{R}_{ij} = \mathbf{r}_{ij}/\mathbf{r}_{ij}$, and $\mathbf{a}\cdot\mathbf{b}$ is a dyadic. The solution of the system of linear equations (1.24) allows the calculation of all basic optical characteristics of an aggregate: the vector scattering-amplitude, $\mathbf{S}(\mathbf{k}_0, \mathbf{k}_s)$

$$\mathbf{S}(\mathbf{k}_0, \mathbf{k}_s) = k^3 \sum_i [\mathbf{d}_i - \mathbf{s}(\mathbf{s}\mathbf{d}_i)] \exp(-i\mathbf{k}_s\mathbf{r}_i), \tag{1.27}$$

and the integral cross sections of extinction C_e, absorption C_a, and scattering $C_s = C_e - C_a$

$$C_e = 4\pi k \mathrm{Im} \sum_i (\mathbf{e}_0\mathbf{d}_i) \exp(-i\mathbf{k}\mathbf{r}_i), \tag{1.28}$$

$$C_e = 4\pi k \sum_i \eta_i |\mathbf{d}_i|^2, \quad \eta_i = \frac{4\pi \mathrm{Im}(\varepsilon_i)}{V_i|\varepsilon_i - 1|^2}. \tag{1.29}$$

The important question about the choice of model polarization is left beyond the limits of the phenomenological scheme just described. It is well known[1] that the simplest choice based on the Mossotti–Clausius formula does not satisfy the optical theorem. Therefore, various approximations have been proposed in

the literature[64,70,72–75] that allow for the dipole-energy radiation losses and lead to complex polarizability even for the nonabsorbing dipole particle.

At first glance, it seems that the bulk IEM and DDA methods are based on different physical principles. Therefore, it is important to emphasize that the solution of Eq. (1.23) by the method of moments and the DDA solution actually lead to *identical* systems of linear equations for dipoles if equivalent assumptions have been made for polarizability in the DDA and for the self-term in the IEM.[66]

If a basis lattice has been specified and the algorithm of finding polarizability found, it remains only to fill the lattice nodes by the corresponding dipoles with regard to the inhomogeneity and shape of the scatterer. Essentially no limitations are placed on the geometry and, to a degree, on the properties of the material. This is the chief value of the method, particularly as applied to structurally complex biological objects.[76] The limitations of DDA are associated with the provision of convergence and accuracy of the results, which are impaired for optically rigid structures.

1.3.3 Approximate theories

With advances in computer facilities and new algorithms many approximate methods of the scattering theory lost their initial value. Despite this, they often give useful information for the qualitative understanding of the physics of phenomena and quantitative tendencies. In this section, we look briefly at only the basic physical principles of certain approximations. A closer look at the approximate theories and abundant references are available in Refs. 16, 77, and 78.

1.3.3.1 Rayleigh approximation

The basic ideas of all approximate methods are associated with definite regions of values of the most important diffraction parameters: the size parameter ka and the relative refractive index $m = n/n_0$. For example, if $ka \ll 1$ and $ka|m| \ll 1$, we are dealing with Rayleigh scattering, in which a particle scatters like an infinitesimal dipole $\mathbf{d} = \alpha \mathbf{e}_0$

$$\mathbf{E}_{sR} = k^3[\mathbf{d}_i - \mathbf{s}(\mathbf{s}\mathbf{d}_i)]\frac{\exp(ikr)}{kr}. \tag{1.30}$$

The dipole moment and the corresponding polarizability tensor are estimated from electrostatic equations.[1,12] The possibility of using an electrostatic approximation to calculate the dipole moment allows particles of virtually all shapes to be considered in the Rayleigh scattering theory.[79] The accuracy of the Rayleigh approximation has received in-depth treatment in Refs. 80 and 81.

Stevenson[82,83] generalized the Rayleigh theory by expanding the fields in powers of ka. This approximation was used to calculate the Mueller matrix of light scattering by random spheroids.[84] This chapter refers to other applications of the Stevenson approximation, as does Ref. 16.

1.3.3.2 Rayleigh–Debye–Gans approximation

In a large number of practically important cases, the relative refractive index of particles m is close to 1. In particular, for the overwhelming majority of biological structures, $m \sim 1$.[76] This condition is valid in an even greater number of cases for x-radiation or neutron scattering. Such particles are called "optically soft," and the corresponding approximation can be called an "approximation of optically soft particles."

The condition $|m - 1| \ll 1$ itself is not sufficient for the development of the theory, since the ratio between size and light wavelength and the phase-shift magnitude $\rho = 2ka(m - 1)$ are of major importance. The RDG approximation is applicable when two conditions are simultaneously fulfilled

$$|m - 1| \ll 1, \quad |\rho| \ll 1. \tag{1.31}$$

There are a number of names for the theory that is based on the assumptions in Eq. (1.31). The best-known name is the Rayleigh–Gans (RG) approximation.[1] We believe that the term RDG is best suited for the following reasons. The fundamental ideas of the method (including the derivation of successive approximations based on the integral relation for a scattered field) were formulated by Rayleigh in his 1881 paper,[45] and the formula for the sphere-scattering cross section was obtained by him in 1914.[85] In 1915, Debye[86] derived a general formula for the intensity of x-rays scattered by a randomly oriented particle ensemble. Later, Debye applied this approach to light scattering by polymer solutions,[87] which had a profound impact on the development of this trend.[7] In quantum mechanics, an analogue to Rayleigh iterations was developed by Born;[88] his name is rightly associated with this approximation. Thus, retaining the name of Gans in the name of the theory (RDG) makes sense only because the name RG approximation has received wide acceptance thanks to van de Hulst.[1]

The RDG approximation can be obtained by various means. For example, one may use general integral relation (1.23), assuming that the field inside the particle is the incident-wave field.[13] Another mean is based on the physical interpretation of scattering as a result of interference from the independent-dipole fields excited by an incident wave in particle volume V.[1,7] In either case, the scattered field is represented as

$$\mathbf{E}_s = \mathbf{E}_{sR} G(\mathbf{q}), \tag{1.32}$$

where $\mathbf{E}_{sR}$ is the Rayleigh scattered field (1.30), $\mathbf{q} = \mathbf{k}_s - \mathbf{k}_0$ is the scattering vector, and $G(\mathbf{q})$ is the interference function or the scattering form-factor

$$G(\mathbf{q}) = \frac{1}{V} \int \exp(-i\mathbf{q}\mathbf{r}) d^3\mathbf{r}. \tag{1.33}$$

Thus, in this approximation the polarization characteristics of scattered light do not differ from the Rayleigh case, and the angular ones differ only in the interference function. For particles of certain shapes the interference functions can be obtained as simple analytical expressions.[7] For example, for spherical particles with radius a and scattering angle θ

$$G(u) = \frac{3}{u} j_1(u), \quad u = qa = 2ka \sin\frac{\theta}{2}, \tag{1.34}$$

where $j_1(x)$ is the Bessel spherical function. Equation (1.34) is also valid for ellipsoids with semiaxes a, b, c, but in this case

$$u = \sqrt{(\mathbf{qa})^2 + (\mathbf{qb})^2 + (\mathbf{qc})^2}. \tag{1.35}$$

An important and simple generalization of RDG theory is that the dipole moment of a scatterer is calculated with regard to the possible *anisotropy of the substance*[7] or the *shape anisotropy*[84,89] of the particle. In this case, polarization effects arise that are absent in the standard version of the RDG.[1]

The usually measured quantity being the intensity of scattering from a randomly oriented particle ensemble, of practical interest is the averaged square of the interference function $<G^2(q)> = P(q)$, also called the scattering form factor.[7] In the theory of light scattering by substance-structure inhomogeneities, the analogous quantity is called the scattering structure factor.[8,90]

In the RDG approximation, the absorption cross section is proportional to volume and generally does not differ in form from the Rayleigh absorption cross section.[1] The scattering cross section should be found by integrating the intensity over all angles, since the optical theorem in the RDG approximation gives either absorption cross section or zero (nonabsorbing particles).

1.3.3.3 Anomalous diffraction and related approximations

Van de Hulst,[1] using Huygens and Babinet's principles, considered a problem on the scattering and extinction of light by a particle with size $a \gg \lambda$ and refractive index $m \sim 1$, i.e., under conditions of

$$|m - 1| \ll 1, \quad x \gg 1. \tag{1.36}$$

The formula obtained for the small-angle scattering amplitude by van de Hulst is a generalization of the Fraunhofer diffraction formula and allows the extinction cross section to be found by a simple integration

$$C_e = 2\mathrm{Re}\int [1 - \exp(-i\rho(z))]dS, \tag{1.37}$$

where $\rho(z) = 2ka(z)(m-1)$ is the phase shift of the ray propagating along the z axis, $a(z)$ is the ray pathlength inside the particle, and the integration is

performed over all rays that intersect the particle. It is not hard to see that in the anomalous-diffraction (AD) approximation, the scattering particle is treated as an ideal phase screen. In a similar way, the absorption cross section can be found as the sum of absorptions of all the rays

$$C_a = \int [1 - \exp(-2\mathrm{Im}\rho(z))] dS. \tag{1.38}$$

The applicability range of the AD theory for the scattering amplitude is restricted by small angles, but the cross-section formulas proved a very appropriate approximation for a wide range of particles. The general universal views of the dependence of the homogeneous-sphere scattering cross section on the parameter of the central-ray phase shift, $\rho = 2x(m - 1)$, is given by the well-known formula of Van de Hulst[1]

$$\sigma_s = \pi a^2 Q(\rho), \quad Q(\rho) = 2 - 4\frac{\sin\rho}{\rho} + 4\frac{1 - \cos\rho}{\rho^2}. \tag{1.39}$$

The AD approximation is easily applicable for nonspherical and inhomogeneous particles.[16] Specifically, for spheroids with the semiaxes (a,b,b) the formula for the effectiveness factor $Q(\rho)$ retains its view, but now the central-ray phase shift will depend on the symmetry-axis orientation a relative to light (direction cosine, $\cos\vartheta$)

$$\rho = 2kb(m - 1)/\sqrt{1 + (b^2/a^2 - 1)\cos^2\vartheta}. \tag{1.40}$$

The AD approximation is a version out of the wider family of high-energy approximations, including the Wentzel–Kramers–Brillouin (WKB) approximation, the eikonal approximation, etc.[13,16,91,92] The main disadvantage of all versions of high-energy approximations is that they ignore polarization effects. Meteen[93] offered an anisotropic modification of AD, in which phase shifts are allowed separately for ordinary and extraordinary waves. However, for isotropic nonspherical particles this theory reduces to a scalar version of AD.

For very large particles, the scattering can be considered as the result of interference of the rays that experienced multiple reflections and refractions in accordance with the laws of geometric optics (GO).[12,59] The diffraction at the edge of a particle, which gives a sharp peak in the small-angle region, may be accounted for separately as required. In the past few years, the GO method has been frequently applied in combination with MC simulations.[16] In the work,[94] a method called the physical optic approximation was suggested, in which the scattered field is expressed by way of the field at the particle surface according to the Huygens–Kirchhoff principle. To find the surface field, one has to use the laws of reflection and refraction. The accuracy

of the GO method for nonspherical particles was studied in a recent paper[95] on the basis of a comparison with the exact T-matrix results.

1.3.4 Other methods and approximations

Apart from the rigorous methods mentioned in Section 1.3.2, other algorithms and public domain codes[23,96] have also been described in the literature. Among such methods are the finite element method (FEM),[97] the finite difference time domain method (FDTDM),[98] and the point matching method (PM) (see the corresponding references in the overview[16]). The strong point of these methods is their applicability in principle to particles of arbitrary shapes and structures. FEM can be applied to solve the Helmholtz equation while FDTDM is used for Maxwell's equations immediately. Since in their nature these methods deal with local fields, a transition to the far scattered field is a special problem.[16]

Among other approximate methods are the perturbation method[99] and certain simple approximations. The perturbation method is based on expansion of an unknown solution to the problem of scattering in terms of a small parameter in the vicinity of an exact solution. Applied to nonspherical particles, this means that the solution is sought in the form of small deviations from the Mie solution, which are caused by the small deviations of the shape from the ideal sphere.[16,99] This approach is effective for a back-of-the-envelope analysis of light scattering by particles with stochastic surface properties[100] or with a weak anisotropy of the substance.[101,102]

To describe the scattering and absorption of light by nonspherical particles, Latimer[103,104] proposed hybrid approximations based on some combinations of RDG and AD theories for spheroids and the Mie theory for spheres. In a sense, such an approach is analogous to a more pragmatic strategy in which exact formulas or numerical data are approximated by simple analytical expressions.[105,106]

1.4 Extinction and Scattering by Aggregated and Compounded Structures

In this section, we discuss methods for calculating scattering and absorption characteristics for two types of structures: (1) large clusters formed as a result of small-particle aggregation and (2) composite structures, i.e., a "host" large matrix-particle with foreign "guest" inclusions. In either case, the cluster particles may be in direct contact with the immediate neighbors or be separated by interparticle distances in accordance with the statistical properties of the pair density–density correlation function. Such structures are physical models for many biological objects or processes. More specifically, immune precipitation,[107–109] sol-particle immunoassay (SPIA),[110,111] or cell agglutination[38,112,113] are well-known examples of the

formation of biological aggregates. Bacterial or eukaryotic cells are typical composite structures bounded by the cell wall and the membrane.[38,76] Methods for computing and applying light scattering in the study of aggregated and composite particles have been discussed in Refs. 114 to 116.

It should be emphasized that the cluster scattering theory can be applied to calculate light scattering by aggregated simple-in-structure biological particles or by individual complex particles. Depending on the size of cluster monomers, one can use the DDA approach (small monomers such as globular proteins, biospecific conjugates prepared from gold or silver nanoparticles,[111,113] etc.) or the more sophisticated superposition method (Section 1.4.2) if aggregates are formed from large cells like erythrocytes, leukocytes, or platelets. In spite of the fact that the present-day cluster scattering theory can consider these large aggregated cells only as homogeneous Mie spheres regardless of the complicated internal structure of actual cells, it is still very useful for describing the general futures of light scattering by the aggregated cells. In application of cluster scattering theory to complex nonspherical and nonhomogeneous biological cells or other individual structures by using DDA ideology, we can treat these complex light scattering targets as 3-D clusters built from small monomers of various sizes and optical properties.[76,115] This seems to be a powerful and versatile strategy to simulate light scattering by large, nonspherical, and nonhomogeneous individual biological particles.[117]

1.4.1 Approximate and discrete dipole approximation methods

In the case of optically soft particles, the interaction among monomers in an aggregate or a composite can be described within the limits of the approximate methods considered in the preceding sections. The simplest approximation is that of a homogeneous spherical particle with a certain effective refractive index, which is calculated using a certain mixing rule [Maxwell Garnett, Bruggeman, extended effective medium approximation (EEMA),[11] etc.]. If the size of an optically soft aggregate does not exceed the light wavelength, its scattering properties can be described within the limits of the RDG approximation, by summing the scattered fields from the monomers with regard to phase shifts. In a converse case, when the size of the aggregate is much greater than the wavelength, its extinction can be calculated by Eq. (1.37) of the AD approximation.[118]

The DDA method can be used in the optics of aggregates in two versions. If the size of monomers is much less than the light wavelength, the method is applied in its physical interpretation, when a monomer is considered as an infinitesimal point dipole and its dipole moment is calculated by electrostatics formulas.[116,119] In a more general case, the aggregated or composite structure is replaced by an ensemble of dummy dipoles on the basic lattice. In point of fact, this means that the monomers may be considered as a set of dipole

subdomains. Such a finer division increases the complexity of the calculations considerably.

1.4.2 Superposition method

A rigorous method for calculating the optical characteristics using an arbitrary configuration of N spherical particles[115] can be formulated simply enough, using the *generalized* Mie theory for an isolated spherical particle[120] and the superposition principle. The essence of the generalized Mie theory is: an arbitrary electromagnetic field $\mathbf{E}^i_{inc}$ incident on the i-th particle can be represented as an expansion in terms of VSH of the first order[115,120]

$$\mathbf{E}^i_{inc} = \sum_{n=1}^{\infty} \sum_{m=-n}^{n} \sum_{p=1}^{2} E_{mn} p^i_{mnp} \mathbf{Y}^{(1)}_{mnp}(k\mathbf{r}_i), \tag{1.41}$$

where the coefficients E_{mn} depend on the choice of normalization. For a plane wave, in which the incidence direction and polarization are specified by three Euler angles (α,β,γ) in the i-th coordinate system, expansion (1.41) with coefficients

$$\bar{p}^i_{mnp} = \exp(i\mathbf{kr}_i)\exp(-im\alpha)\frac{1}{n(n+1)}[\tau_{mnp}(\beta)\cos\gamma - i\tau_{mn3-p}(\beta)\sin\gamma] \tag{1.41a}$$

also holds. The functions $\tau_{mnp}(\beta)$ ($p = 1,2$) correspond to the well-known angular functions $\tau_{mn}(\cos\beta)$, $\pi_{mn}(\cos\beta)$.[115] The radial dependence of the first-kind VSH is given by spherical Bessel functions $j_n(kr_i)$ (or Ricatti–Bessel functions[115]). An expansion analogous to Eq. (1.41) but with other coefficients also holds for the *internal* field of each particle in an aggregate. To represent a *scattered* field, one has to use third-kind VSHs, based on spherical Hankel functions. Use of the boundary conditions on the sphere surface leads to the generalized Mie theory in the form of the following simple expressions for scattered-field coefficients:[120]

$$a^i_{mnp} = \bar{a}^i_{np} p^i_{mnp}, \quad p = 1,2, \tag{1.42}$$

where $\bar{a}^i_{n1} = a^i_n$, $\bar{a}^i_{n2} = b^i_n$ are the usual Mie coefficients for an isolated i-th sphere.[12] The fundamental physical result of Eq. (1.42) is that the scattering occurs without a coupling between electromagnetic modes. In the spirit of Fresnel's analogy,[115] the Mie coefficients $\bar{a}^i_{np}$ in Eq. (1.42) can be interpreted as the *reflection* coefficients for partial modes in the plane wave decomposition. In the same way, the Mie coefficients for the *internal* field can be interpreted as Fresnel coefficients of the *transmitted* partial waves.[115]

Equation (1.42) is a key one in the theory of scattering by sphere aggregates. To find the field scattered from each particle of the aggregate, all one has to do is to find the coefficients of expansion of the exciting field, which should then be multiplied by the usual Mie coefficients. The exciting field is found by the superposition principle

$$\mathbf{E}^i_{inc} = \mathbf{E}^i_0 + \sum_{j\neq i}^{N} \mathbf{E}^i_s(j). \tag{1.43}$$

For fields $\mathbf{E}^i_s(j)$ scattered by a j-th particle, the expansion (1.41) is also applicable. However, they cannot be used directly for finding the coefficients p^i_{mnp}, included in Eq. (1.42). The point is that these expansions will be written with respect to the coordinate systems not coincident with the center of the j-th particle, whereas Eq. (1.42) is written just in the i-th basis set. This problem is solved with the help of the addition (translation) theorem for VSH.[115] Performing this translation for the VSHs describing $N-1$ scattered fields, we can find the coefficients of expansion of the complete exciting field for the i-th particle. It is easy to see that the procedure described leads not to an explicit solution, but to a system of coupled linear equations for the coefficients p^i_{mnp}, which we will write

$$\sum_{j=1}^{N}\sum_{\nu=1}^{\infty}\sum_{\mu=-\nu}^{\nu}\sum_{p=1}^{2} H^{ij}_{mnp,\mu\nu q} p^j_{\mu\nu q} = \bar{p}^i_{mnp}. \tag{1.44}$$

The interaction matrix H in our formulation of the method is determined by the relationship

$$H^{ij}_{mnp,\mu\nu q} = \begin{Bmatrix} \delta_{ij}\delta_{m\mu}\delta_{n\nu} + (1-\delta_{ij})A^{ji}_{mn\mu\nu}\bar{a}^j_\nu & (1-\delta_{ij})B^{ji}_{mn\mu\nu}\bar{b}^j_\nu \\ (1-\delta_{ij})B^{ji}_{mn\mu\nu}\bar{a}^j_\nu & \delta_{ij}\delta_{m\mu}\delta_{n\nu} + (1-\delta_{ij})A^{ji}_{mn\mu\nu}\bar{b}^j_\nu \end{Bmatrix}, \tag{1.45}$$

where $A^{ji}_{mn\mu\nu}$ and $B^{ji}_{mn\mu\nu}$ are the coefficients of VSH translation, based on the spherical Hankel function of the first kind, $h^{(1)}_n(kr)$. If one multiplies Eq. (1.44) by the usual Mie coefficients a^i_{np} and uses relationship (1.42), then system (1.44) reduces to the known[115,120] system of equations directly for the scattered-field coefficients a^i_{mnp}.

From the structure of the interaction matrix it follows that an electrodynamic interaction leads to the excitement of partial modes, which might be absent in the incident radiation and the amplitude scattering matrix may become nondiagonal.

In practice, the infinite system (1.44) is cut off to a certain maximal order of the multipole expansion M that ensures the convergence of calculations of physical quantities. If Eq. (1.44) is solved and coefficients of multipole

expansion (1.42) are found, one can calculate all characteristics of the cluster scattering. For example, the extinction cross section is calculated by the equation

$$C_e = \frac{4\pi}{k^2}\sum_{i=1}^{N}\sum_{n=1}^{M}\sum_{m=-n}^{n}\sum_{p=1}^{2} c_{mn}\mathrm{Re}[a^i_{mnp}(\bar{p}^i_{mnp})^*], \tag{1.46}$$

where the coefficients c_{mn} depend on particular normalization of VSH and field expansions.

To calculate the amplitude scattering matrix, one has to translate the coefficients of individual-particle decompositions to the expansion coefficients a_{mnp} with respect to the common center of the cluster. The simplest way to do this is to employ the far-field approximation[121]

$$a_{mnp} = \sum_{j=1}^{N} a^j_{mnp}\exp(-ikr_j). \tag{1.47}$$

However, this scheme is ineffective for orientational averaging (see below).

In terms of the coefficients a_{mnp}, the amplitude-scattering matrix[1] $S_{ij}(\theta,\varphi)$ is calculated in a conventional way[115,122]

$$S_{11} = \sum_{m,n,p} s_{mn}\exp(im\varphi)\tau_{mnp}(\theta)a^0_{mnp}, \tag{1.48a}$$

$$S_{12} = \sum_{m,n,p} s_{mn}\exp(im\varphi)\tau_{mnp}(\theta)a^{90}_{mnp}, \tag{1.48b}$$

$$S_{21} = \sum_{m,n,p} is_{mn}\exp(im\varphi)\tau_{mn3-p}(\theta)a^0_{mnp}, \tag{1.48c}$$

$$S_{22} = \sum_{m,n,p} is_{mn}\exp(im\varphi)\tau_{mn3-p}(\theta)a^{90}_{mnp}, \tag{1.48d}$$

where the coefficients s_{mn} are determined by the normalization of VSHs and field decompositions, and the superscripts 0 and 90 are related to the transversal magnetic and electric modes of the incident light. We emphasize that matrix (1.48) is written in a coordinate system associated with the incident wave $k = z$; therefore, for the averaging over cluster orientations to be performed, one has to do repeated calculations for each cluster orientation. A more effective T-matrix approach is discussed in Section 1.4.3.

Let us consider the composite structures. In order to appreciate the essence of this method of solving the problem, it will suffice to consider the simplest structure in the form of a "host" sphere with a nonconcentric

spherical inclusion. We can interpret the process of scattering of such a structure in terms of the following Fresnel analogy.[115] An incident plane wave is projected onto the VSH basis, so that we have a set of incident partial modes. These modes induce in the host sphere transmitted and reflected partial waves with the reflection and transmission coefficients in accordance with the Mie theory. As has been said before, there is no mode coupling in this process. The inhomogeneity being nonconcentric with respect to the "host," each transmitted mode induces a multitude of reflection and transmission modes in the inhomogeneity. The amplitudes of the reflection and transmission are given by the Mie theory. The reflected modes of inclusion are incident *outgoing* modes with respect to the external sphere. If we reexpand these waves with respect to the "host" center, a problem arises that resembles the Mie theory but is for the outgoing waves crossing the inside spherical boundary between two media. This problem has a solution of the type (1.42). This process itself does not lead to mode coupling, but this coupling has occurred earlier, when we had to perform reexpansions of partial waves. A mathematical description of this physical picture is available in Ref. 115. If the expansion coefficients of the scattered field are found, the further calculations of the optical characteristics do not differ from the cluster case.

1.4.3 T-matrix formalism for cluster scattering

Usually, it is not just a calculation for an individual structure, but an averaged result over the statistical ensemble and orientations that is required. Formally such an averaging can be carried out by simple summation of the results calculated for various orientations and polarizations of the incident light, but this is a very ineffective way. The orientational averaging for clusters is more convenient to perform by using the T-matrix formalism,[122] as well as for nonspherical particles. Since all of the incident light properties are determined by expansion coefficients, and the T-matrix depends only on the properties of the scattering structure, intuition suggests that for an ensemble of structures with random orientations the observable physical quantities should somehow be expressed directly by way of the T-matrix. Thus, we can apply this approach to cluster structures as well; one needs only the recipe for calculating the cluster T-matrix. If we formally invert Eq. (1.44), we will get the T-matrix of an individual cluster particle[122]

$$a^i_{mnp} = \sum_j \sum_{\mu\nu q} T^{ij}_{mnp,\mu\nu q} p^j_{\mu\nu q}. \tag{1.49}$$

Using theorems of VSH addition, one can combine all of these single-particle T-matrices into a common cluster T-matrix[115,122]

$$T^0_{a,b} = \sum_{i,j} \sum_{c,d} J^{oi}_{ac} T^{ij}_{cd} J^{j0}_{db}, \tag{1.50}$$

where for simplicity we use the multi-indices a, b, c, and d to denote the order, degree, and mode (i.e., $a = mnp$, etc.). The matrices J_{ab}^{oi} describe the VSH translation to the common cluster center and are based on the spherical Bessel functions. The further calculations of the optical characteristics and their orientational averaging are performed according to the same scheme as that employed in the case of the usual nonspherical particles.[122]

1.4.4 Fractal aggregates

The structure of various biological aggregates may be described in terms of statistical (irregular) fractal clusters,[123] i.e., statistically self-similar objects with the fractal dimension $D_f < 3$ defined by power relations

$$g(r) \sim (r/R)^{D_f-3}, \quad N \sim (R/a)^{D_f}, \tag{1.51}$$

where $g(r)$ is the binary density-density correlation function, N is the aggregate particle number, R is the average size of aggregates (r.m.s. radius R, gyration radius R_g, etc.), and a is the size of monomers. From Eq. (1.51), one can see a main property of fractal aggregates: low average density and large density fluctuations within short-range distances. A direct consequence of such a property of binary density correlations of monomers inside a cluster is the already well-known[124] power law for the angular dependence of the static structure factor (normalized intensity) of light, x-ray, or neutron scattering $S(q) \sim (qR)^{-D_f}$.

The above-presented power laws for $g(r)$ and $S(q)$ are observed in the asymptotic sense only, when the scattering vector values of the probing irradiation satisfy the strong inequality $a \ll q^{-1} \ll R$.[125] In real experiments within the visible optical region the condition $qR \gg 1$ is usually not observed rigorously, since the average size of aggregates does not, as a rule, exceed 1 μm. In these cases, the character of the decrease in density correlations while approaching the cluster boundary becomes important. This decrease is described by using the so-called cutoff function $h(r/R)$, which is included in the complete correlation function $r^{D_f-3}h(r/R)$.[126,127] Several forms of $h(x)$, including the single exponential model $h(x) \sim \exp(-bx)$, were proposed in the literature (see the discussion and relevant citations in Ref. 127). Based on experimental data[127–130] and computer simulations,[126] the following approximation seems to be most appropriate for fractal aggregates:

$$h(x = r/R) \approx \exp(-bx^{\nu}), \quad \nu \approx D_f \approx 2, \tag{1.52}$$

where $b \sim 1$ for reaction-limited aggregates (RLCA),[123,124] and $b \sim 1/2$ for diffusion-limited aggregates (DLCA).[123,124]

In fractal cluster optics, the aggregates built from small metal nanoparticles are of special interest. Large density fluctuations and strong electrodynamic interaction of metal monomers result in specific linear[119] and

nonlinear[131] optical effects. The readers are referred to the relevant paper[119] and books.[116,131] Further, the monomers of an aggregate are assumed to be the optically soft particles. In this case, the optical properties of fractal aggregates can be understood in terms of the mean field theory (MFT).[132] It is assumed in MFT that all aggregate monomers have the same dipole moments directed along an average exciting field. The monomer interaction results only in renormalization of the average amplitude of dipole moments exciting by the average (mean) field. The scattered fields are calculated with taking into account the geometrical phase shifts. Therefore, the angular scattering characteristics in the RDG and MFT theories coincide.

Let us consider a monodisperse ensemble of fractal clusters each containing N small spherical particles of radius a. If N_0 is the number of primary particles per unit of suspension volume, then the scattering intensity of nonpolarized light by an ensemble of clusters may be written in the following form:[127]

$$I(q) = I_0 N_0 N |B|^2 \left[\frac{3}{16\pi}\sigma_{1s}(1+\cos^2\theta)\right] G^2(qa) S(q), \tag{1.53}$$

where σ_{1s} and $G(qa)$ are the integral scattering cross section and the scattering form factor of primary particles [Eq. (1.34)], respectively. The factor $|B|^2$ gives a mean field theory correction,[132] independent from the scattering angle θ, to the scattering structure factor that describes in the RDG approximation the effect of spatial correlations of primary particles in a cluster

$$S(q) = \frac{1}{N}\left[1 + (N-1)\int_0^\infty x^2 p(x)\frac{\sin qRx}{qRx}\,dx\right], \tag{1.54}$$

where $x = r/R$;

$$R^2 = 2R_g^2 = \sum_{ij} |\mathbf{r}_i - \mathbf{r}_j|^2 p(\mathbf{r}_{ij}) \tag{1.55}$$

is the r.m.s. radius of a cluster; and $p(\mathbf{r}_{ij})$ is the probability density for finding a randomly chosen pair of cluster particles separated by a vector $\mathbf{r}_{ij} = \mathbf{r}_i - \mathbf{r}_j$. Note that $p(\mathbf{r}_{ij})$ is closely related to the density–density correlation function $g(r)$.[126]

At small scattering angles, when $qR \ll 1$, the angular dependence of scattering is represented by the universal Guinier's expansion[124]

$$S(q) \approx 1 - (qR_g)^2/3, \tag{1.56}$$

while the asymptotic transition to the fractal regime $S(q) \sim (qR)^{-D_f}$ is determined by polydispersity and the form of the cut-off function.[125,126]

Detailed calculations of the scattering structure factor for various models of fractal clusters, as well as the relevant references can be found in Ref. 125.

The mean field theory factor[132] B is given by

$$B = \left[1 - \frac{3}{2}(N-1)\sin\delta\exp(i\delta)P(kR)\right]^{-1}, \tag{1.57}$$

$$P(\alpha) = \int_0^\infty x^2 p(x) P_1(kRx)dx, \tag{1.58}$$

$$P_1(z) = \frac{\exp(iz)}{z^2}\left[\sin z - \frac{z}{3}G(z) + \frac{1-iz}{z}\left(G(z) - \frac{\sin z}{z}\right)\right]q, \tag{1.59}$$

where δ is the phase shift of the p wave for a small spherical particle.[132] Analytical properties of function $P(kR)$ are discussed in Refs. 127 and 132.

Let us now consider the integral functions that describe the spectral dependence of light extinction for nonabsorbing systems. Turbidity of an ensemble of fractal clusters may be represented in the following form:[127]

$$\bar{\tau} = (N_0/N)\sigma_s = \tau_1 F_s(kR), \tag{1.60}$$

where $\tau_1 = N_0\sigma_{1s}$ is the turbidity of an ensemble of primary particles, and $F_s(kR)$ is the enhancement (coherence) factor equal to the scattering cross section of a cluster σ_s normalized on $\sigma_{1s}N$

$$F_s = \sigma_s/N\sigma_{1s}. \tag{1.61}$$

For absorbing monomers, one has to introduce the extinction cross section σ_e as well as the corresponding extinction F_e and absorption F_a factors. Then Eq. (1.60) can be rewritten as

$$\bar{\tau} = \frac{N_0}{M}\sigma_e = N_0\sigma_{1e}F_e = \tau_1 F_e, \tag{1.62}$$

$$F_e = \sigma_e/N\sigma_{1e} \equiv F_s\varpi + (1-\varpi)F_s, \quad F_a = \sigma_a/N\sigma_{1a}, \tag{1.63}$$

where $\varpi = \sigma_{1s}/\sigma_{1e}$ is the monomer albedo. In MFT, the total cluster absorption is simply equal to the sum of monomer absorptions, i.e.,

$$\sigma_a = N\sigma_{1a}, \quad F_a = 1. \tag{1.64}$$

One should remember that Eq. (1.64) holds only for weakly absorbing monomers, and it violates for metal[119] or soot[115] nanoparticles. Absorption of small clusters gives a main contribution to their total extinction; therefore, Eq. (1.64) can be used for the extinction coherence factor as well.

For small kR or for small $N \sim (R/a)^{D_f}$

$$F_s(kR) \approx N\left[1 - \frac{1}{3}(kR)^2\right], \tag{1.65}$$

so that the turbidity of an ensemble of clusters increases by the factor of N as compared to τ_1. To calculate the enhancement factor for arbitrary argument kR, the general relationship of the mean field theory can be used[127]

$$F_s(kR) = F_{1s}(kR)|B|^2, \tag{1.66}$$

where $F_{1s}(\alpha)$ is the enhancement factor in the single intracluster scattering approximation

$$F_{1s}(\alpha) = \frac{1}{N} + \frac{3}{2}\left(1 - \frac{1}{N}\right)\mathrm{Im}P(kR). \tag{1.67}$$

The behavior of the scattering enhancement factor at great N or kR values is given by the following asymptotic expression:[127]

$$F_s^{(1)} = A_1(D_f) + A(D_{f2})(kR)^{D_f-2}, \quad kR \gg 1, \tag{1.68}$$

where the constants A_1 and A_2 are determined by the cutoff correlation function (e.g., see explicit expressions in Refs. 126 and 127). The physical meaning of Eq. (1.68) is as follows: the turbidity of a cluster suspension does not depend on the cluster size R or cluster particle number N if $D_f < 2$, logarithmically depends on R if $D_f = 2$, and increases as $(kR)^{D_f-2}$ if $D_f > 2$. Note that asymptotic expression (1.67) is not applicable in the geometrical optics limit. Transition to this limit for fractal aggregates has been discussed in Ref. 133.

Aggregation of particles always leads to polydisperse systems of clusters. The evolution processes of cluster-mass distribution $f(N)$ have by now been well investigated theoretically, experimentally, and by computer simulation.[123,134] The most important result of these studies is the proof of the dynamic scaling, according to which the shape of the distribution curve is described by the universal function $\psi(N/N_n)$, which is not explicitly time dependent. The time evolution of cluster-mass distribution is described only by specific dependences of distribution moments $N_n(t)$ for DLCA and RLCA clusters.[123] Detailed consideration of polydispersity effects in fractal cluster optics can be found in Refs. 125 and 127.

1.5 Extinction and Scattering by Plasmon-Resonant Particles

1.5.1 Localized plasmon resonance of small metal spheres

Over the recent decade, gold (and other metallic) nanoparticles (NPs)[135] have attracted significant interest as a novel platform for various applications to nanobiotechnology and biomedicine[136–138] because of convenient surface bioconjugation with molecular probes[139] and remarkable plasmon-resonant optical properties.[140,141] Recently published examples include applications of NPs such as biosensorics,[142] genomics,[143] clinical chemistry,[144] immunoassays,[145] immune response enhancement,[146] detection and control of microorganisms,[147] optical imaging of biological cells (including cancer cell imaging with resonance scattering,[148] optical coherence tomography (OCT),[149] two-photon luminescence,[150] and photoacoustic[151] techniques), cancer cell photothermolysis,[152] and targeted delivery of drugs or genetic and immunological substances.[153,154] In particular, there is great interest in the development of nanoparticle-based vectors that decrease the toxicity of free drugs and ensure targeted delivery directly to tumor cells.[155–157] It should be emphasized that almost simultaneously with the beginning of the use of GNPs in biomedicine, acute questions were raised about the biodistribution and circulation of NPs in the bloodstream, their pharmacokinetics and elimination from the organism, and their possible toxicity to the organism as a whole or at the level of cyto- and genotoxicity.[158]

The absorption and scattering spectra of metal nanoparticles exhibit resonance UV–vis bands, which are absent in macroscopic samples. The nature of these bands is determined by the collective behavior of conduction electrons in the light wave field. In the electron gas of metals, collective plasma oscillations can be excited at frequency ω_p in the visible region.[12] An elementary quantum with energy $\hbar\omega_p$ is called a plasmon.[140] Because plasmons are the result of quantization of classical plasma oscillations, their properties can be derived from Maxwell's equations.

Collective fluctuations of the electron density on the boundary of a usual dielectric with the positive permittivity and a metal with the negative permittivity are called surface plasmons.[140] The excitation of surface plasmons by light is called a surface plasmon resonance (SPR) for planar structures with travelling waves and a localized surface plasmon resonance (LSPR) for metal nanoparticles.[159] These excitations are related to evanescent surface electromagnetic waves, which are not necessarily localized on the interface.

To describe the optical properties of plasmon-resonant nanostructures, one can use various computational approaches,[160] including the T-matrix method.[161] An elementary classical description of a plasmon resonance (PR) in a small metal sphere is as follows.[159] The electric field of an electromagnetic light wave displaces the cloud of free electrons and produces

uncompensated charges near a particle surface and corresponding returning forces. As mentioned above, the optical resonance related to these oscillations is called the LSPR. The term "surface" is used, first, because the returning force is caused by the polarization of the particle surface. Second, the radial component of the electric field inside the particle changes as r^{n-1}, so that it is stronger localized near the particle surface[12] (for $r \to a$) with increasing the mode order $n \gg 1$. In the general case, the eigenfrequency of such a "collective" oscillator does not coincide with the wave frequency and is determined by many factors, including the concentration and effective mass of conductive electrons, the shape, structure, and size of particles, interaction between particles, and the influence of the environment. However, for the elementary description, it is sufficient to use a combination of the usual dipole (Rayleigh) approximation and the Drude theory.[12] In this case, the absorption and scattering of light by a small particle are determined by its electrostatic polarizability α, which can be calculated by using the optical permittivity $\varepsilon(\omega)$ [or $\varepsilon(\lambda)$], where ω is the angular frequency and λ is the wavelength of light in vacuum. For a small sphere of volume V and radius a in a homogeneous dielectric medium with the permittivity ε_m, we have the following expressions for the extinction, absorption, and scattering cross sections:

$$C_{\text{ext}} = C_{\text{abs}} + C_{\text{sca}} = \frac{12\pi k}{a^3}\frac{\varepsilon_m \text{Im}(\varepsilon)}{|\varepsilon - \varepsilon_m|^2}|\alpha|^2 + \frac{8\pi}{3}k^4|\alpha|^2 \simeq 4\pi k \text{Im}(\alpha), \quad (1.69)$$

where $k = 2\pi\sqrt{\varepsilon_m}/\lambda$ is the wave number in the surrounding medium, and the polarizability α is given by[162]

$$\alpha = \frac{\alpha_0}{1 + \varphi(x)a^{-3}\alpha_0}, \qquad \alpha_0 = \frac{3V}{4\pi}\frac{\varepsilon - \varepsilon_m}{\varepsilon + 2\varepsilon_m} = a^3\frac{\varepsilon - \varepsilon_m}{\varepsilon + 2\varepsilon_m}. \quad (1.70)$$

Here, $x = ka$, the renormalization function $\varphi(x)$ is defined as[163] $\varphi(x) = 2 + 2(ix - 1)\exp(ix) \simeq -x^2 - i(2/3)x^3$, and Eq. (1.70) reproduces Meier and Wokaun's formula,[164] which has been generalized for spheroids by Moroz.[165]

Below, we will not distinguish the electrostatic polarizability from the renormalized polarizability, which accounts for radiative damping effects. In this approximation, the extinction of a small particle is determined by its absorption $C_{abs} = C_{ext} = 4\pi k \text{Im}(\alpha)$ and scattering contribution can be neglected.

As the particle size is decreased to the value comparable with the electron mean-free path ($a \sim l_e$), deviations of the phenomenological dielectric function $\varepsilon(\omega,a)$ of the particle from the bulk values $\varepsilon(\omega) = \varepsilon(\omega, a \gg l_e)$ can be expected. A general recipe for the inclusion of macroscopic tabulated data and size effects to the size-dependent dielectric function consists of the following.[140] Let $\varepsilon_b(\omega)$ be the macroscopic dielectric function, which can be

found in the literature from measurements with massive samples. Then the size-dependent dielectric function of a particle may be written as

$$\varepsilon(\omega,a) = \varepsilon_b(\omega) + \Delta\varepsilon(\omega,a), \tag{1.71}$$

where the correction term $\Delta\varepsilon(\omega,a)$ takes into account the contribution of size-dependent scattering of electrons to the Drude part of the dielectric function

$$\Delta\varepsilon(\omega,a) = \varepsilon_b^{\text{Drude}}(\omega) - \varepsilon_p^{\text{Drude}}(\omega,a) = \frac{\omega_p^2}{\omega(\omega + i\gamma_b)} - \frac{\omega_{p,a}^2}{\omega(\omega + i\gamma_p)}. \tag{1.72}$$

Here, $\gamma_b = \tau_b^{-1}$ is the volume decay constant; τ_b is the electron-free path time in a massive metal; $\omega_{p,a}$ is the plasma frequency for a particle of diameter a (we assume below that $\omega_{p,a} \simeq \omega_p$);

$$\gamma_p = \tau_p^{-1} = \gamma_b + \gamma_s = \gamma_b + A\frac{v_F}{L_{\text{eff}}} \tag{1.73}$$

is the size-dependent decay constant equal to the inverse electron mean transit time $\gamma_p = \tau_p^{-1}$ in a particle; L_{eff} is the effective electron mean-free path; γ_s is the size-dependent contribution to the decay constant; and A is a dimensionless parameter determined by the details of scattering of electrons by the particle surface. A particular value of the scattering constant A is determined by the particle size, shape, structure, etc. For details, readers are referred to papers by Coronado and Schatz[166] and Moroz.[167]

One can see from the expressions presented above that the polarizability and optical cross sections can have a strong resonance under the condition

$$\varepsilon(\omega_{\max} \equiv \omega_0) = \varepsilon(\lambda_{\max}) = -2\varepsilon_m. \tag{1.74}$$

The PR frequency can be estimated from the elementary Drude theory for the permittivity of a bulk metal

$$\varepsilon(\omega) = \varepsilon_{ib} - \frac{\omega_p^2}{\omega(\omega + i\gamma_b)}, \tag{1.75}$$

where ε_{ib} is the contribution of interband electronic transitions; ω_p is the frequency of volume plasma oscillations of free electrons; and γ_b is the volume decay constant related to the electron mean-free path l_b and the Fermi velocity v_F by the expression $\gamma_b = l_b/v_F$. By combining the above equations, one can obtain the following expressions for the resonance plasmon frequency and wavelength

$$\omega_{\max} \equiv \omega_0 = \frac{\omega_p}{\sqrt{\varepsilon_{ib} + 2\varepsilon_m}}, \quad \lambda_{\max} \equiv \lambda_0 = \lambda_p\sqrt{\varepsilon_{ib} + 2\varepsilon_m}. \tag{1.76}$$

Here, $\lambda_p = 2\pi c/\omega_p$ is the wavelength of volume oscillations of the metal electron plasma.

Equation (1.74) determines the very first ($n = 1$) dipole resonance of a spherical particle. Except this dipole resonance, higher multipoles and corresponding multipole (quadrupole, etc.) resonances can be also excited. For each multipole mode, the resonance condition exists, which is similar to Eq. (1.74) and corresponds to the resonance of the quadrupole, octupole, and so on, polarizability contributions. For spherical particles, these conditions correspond to the resonance relations for the partial Mie coefficients[12] $\omega_n = \omega_p(\varepsilon_{ib} + \varepsilon^m(n + 1)/n)^{-1/2}$, where n is the mode (resonance) number. To understand the physics of LSPRs, it is important to distinguish two possible scenarios of excitation of multipole resonances. The first case corresponds to small but nonspherical particles of irregular or uneven shape, when the distribution of induced surface charges is strongly inhomogeneous and does not correspond to the dipole distribution. This inhomogeneous distribution generates high multipoles even in the case when the system size is certainly much smaller than the wavelength of light. Prominent examples are cubic particles[168] or two contacting spheres.[169] As mentioned earlier, the field distribution near the contact point is so inhomogeneous that multipole expansions converge very slowly or diverge at all. The second scenario of high multipole excitation is realized with increasing the particle size, when the transition from the quasi-stationary to radiative regime is realized, and the contribution of higher spherical harmonics should be taken into account in the Mie series (or another multipole expansion). For example, while the extinction spectrum for a spherical silver particle with a 30-nm diameter is completely determined by the dipole contribution and has one resonance, the spectrum of a 60-nm sphere exhibits a distinct high-frequency quadrupole peak in addition to the low-frequency dipole peak.

1.5.2 Metal nanorods

Gold nanorods (NRs) possess unique optical properties because of their tunable VIS–NIR dipole plasmon resonances, as demonstrated in pioneering experiments[170] and simulations.[171] Owing to the shape- and size-controlled scattering and absorption properties, the gold NRs have found promising applications in biomedical applications, cancer diagnostics, photothermal destruction of cancer cells or murine macrophages *in vitro* (see also the citations in Ref. 172), and *in vivo* flow cytometry of circulating cells.[151] New potential biomedical applications of metal NRs can be expected because of their enhanced PR sensitivity to the dielectric environment[173] and their orientation with respect to polarized incident light,[174] including laser orientation alignment and trapping,[175] strong light scattering oscillations induced by Brownian rotation,[176] unusual depolarization of scattered light,[177] and anisotropic properties of NRs embedded in a solid matrix[178] or deposited on a substrate.[179,180] Recent advances in synthesis[181] and functionalization[182] of gold NRs will stimulate fast progress in biomedical technologies using

conjugates of gold NRs with biomolecules. For a comprehensive discussion of the chemistry, optics, and biomedical applications of metal NRs, the readers are referred to recent reviews.[162,174]

The optical properties of metal NRs can be understood in terms of an approximation of the particle shape by an prolate spheroid with semiaxes (a,b, b) and known analytic solution for the axial polarizability tensor

$$\alpha_{\parallel,\perp} \equiv \alpha_{a,b} = \frac{V}{4\pi} \frac{\varepsilon - \varepsilon_m}{\varepsilon_m + (\varepsilon - \varepsilon_m) L_{\parallel,\perp}}, \tag{1.77}$$

where the geometrical depolarization factors[12] satisfy the relation $L_{\parallel} + 2L_{\perp} = 1$, and $L = 1/3$ for spheres. Unlike spherical particles, expressions of type (1.76) now predict the appearance of two resonances corresponding to oscillations of electrons across and along the symmetry axis of a particle. In particular, the supersensitive tuning of the longitudinal resonance is explained by the modification of expression (1.76)

$$\lambda_{\max,\parallel} = \lambda_p (\varepsilon_{ib} + (1/L_{\parallel} - 1)\varepsilon_m)^{1/2}. \tag{1.78}$$

It follows from Eq. (1.78) that the dipole resonances of small gold or silver spheres ($5 \le 2a \le 30$ nm) in water are localized near 520 or 380 nm and do not depend on the particle size. By contrast, the longitudinal LPR of silver and gold nanorods can easily be tuned across the vis–NIR band by varying the aspect ratio, as $L_{\parallel}^{-1} \to \infty$ for needles and $L_{\parallel}^{-1} \to 0$ for thin disks, which predicts the strong red shift of the resonance with increasing the axial ratio of particles (when $L_{\parallel} \to 0$).

Figure 1.1 shows the extinction and scattering spectra of randomly oriented gold [Fig. 1.1(a) and (c)] and silver [Fig. 1.1(b) and (d)] NRs with the equivolume diameter $D = d_{ev} = 20$ nm and the aspect ratios $1 \le e = a/b \le 6$. The single-particle extinction and scattering properties are expressed in terms of the corresponding efficiency factors, i.e., the corresponding cross sections normalized to the geometrical cross section of an equivolume sphere. We see that the properties of particles depend very strongly on the metal nature. First, as the aspect ratio for gold rods is increased, the resonance extinction increases approximately by a factor of five, and the Q factor also increases. For silver, vice versa: the highest Q factor is observed for spheres, and the resonance extinction for rods is lower. Second, for the same volume and axial ratio, the extinction and scattering of light by silver rods are considerably more efficient. The resonance scattering factors for silver particles are approximately five times larger than those for gold particles. Third, the relative intensity of the transverse PR of silver particles with the aspect ratio above 2 is noticeably larger than that for gold particles, where this resonance can be simply neglected. Finally, principal differences are revealed for particles with the shape factor smaller than 2 [Fig. 1.1(c) and (d)].

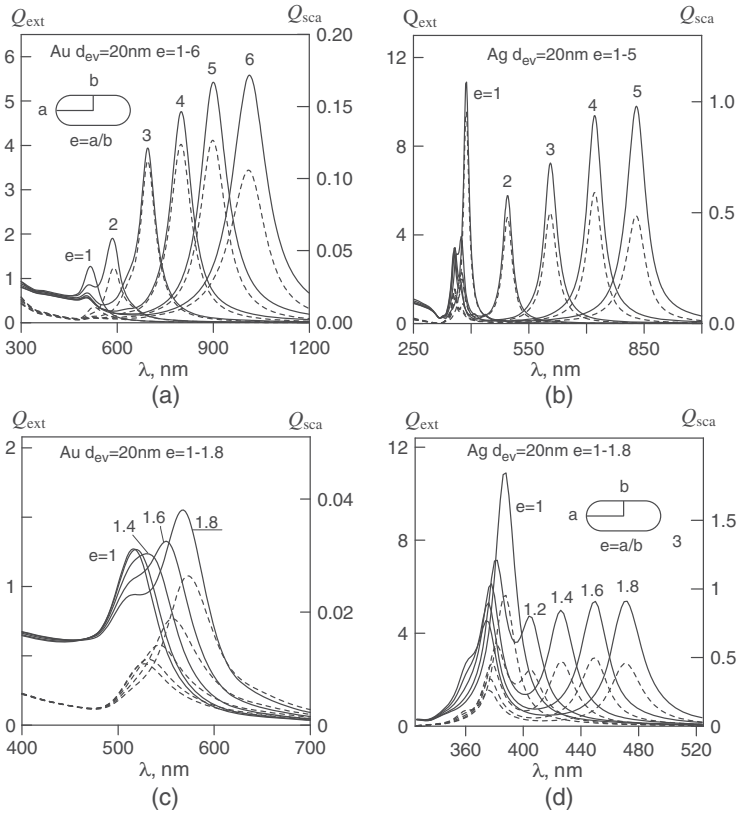

Figure 1.1 Extinction (solid curves) and scattering (dashed curves) spectra of randomly oriented (a) and (c) gold and (b) and (d) silver NRs (cylinders with semispherical ends). The equivolume diameter is 20 nm and the aspect ratio varies from 1 to 6. Panels (c) and (d) show the transformation of spectra at small deviations of the particle shape from spherical.

The resonance for gold particles shifts to the red and gradually splits into two bands with dominating absorption in the red region. The scattering band shifts to the red, and its intensity increases. For silver rods, the situation is different. The short-wavelength extinction resonance shifts to the blue, its intensity decreases, and it splits into two distinct bands. In this case, the intensity of the long-wavelength extinction band remains approximately constant; it is comparable with the short-wavelength band intensity and shifts to the red with increasing nonsphericity. The scattering and absorption spectra approximately reproduce these features.

1.5.3 Metal nanoshells

Gold nanoshells[183] are of great interest for biosensorics,[184] immunoassay, optical visualisation of biological objects, and laser photodestruction of cancer cells.[149] Note that the efficiency of nanoshells as photothermal labels

can be related not only to their heating but to the formation of explosive vapor bubbles.[185] The existing protocols of synthesis of gold nanoshells with a silica core[183] allow the preparation of particles of diameter 80–400 nm with a comparatively narrow size distribution. The resonance scattering of light by such particles exceeds by more than an order of magnitude scattering from usual colloidal gold particles of diameters 10–50 nm. Very strong scattering allows one to observe individual nanoshells in the dark-field microscope and opens up the way to the development of high-contrast labels for visualization of biologically specific interactions of conjugates (particles with attached probe macromolecules) with target molecules.

The optical properties of model nanoshells in the form of a bilayer sphere with a dielectric core can be calculated easily by using various programs of the Mie solution type. The PR wavelength is determined mainly by the ratio of the shell thickness to the core diameter and by the dielectric functions of the core, shell, and environment. Although numerical analysis can be performed quite easily, it is desirable to have a simple analytic method for quantitative estimates of the polarizability of nanoshells and their dipole optical properties. Such a method has been developed in Ref. 186 to calculate an equivalent average permittivity of a multilayered sphere. The main advantage of our approach is that now we can apply usual expressions for resonances of spherical particles to multilayer spheres with the equivalent average permittivity as well.

The resonance tuning of NRs and nanoshells is related to the shape and structure of the particles, respectively. The idea of a combination of these two particles in the form of an ellipsoidal nanoshell was proposed in Ref. 187. Such a structure was later called nanorice.[188] The principle of the dipole equivalence can easily be modified for such particles as well.[161]

Consider an initial particle with known polarizability—e.g., a dielectric spheroid with the symmetry semiaxes $a_1 \geq b_1$ and the dielectric permittivity ε_1 (Fig. 1.2).

It does not matter whether the initial particle is homogeneous or layered. The goal is to find the polarizability of the same particle, which is now covered by a metallic shell with the dielectric function ε_2. To this end, the initial particle is placed in an auxiliary homogeneous dielectric medium with the permittivity ε_2 and is surrounded by an imaginary confocal spheroid (a_2, b_2), where $a_2^2 = a_1^2 + s^2$, $b_2^2 = b_1^2 + s^2$, and s is the shell thickness. Then the imaginary particle is replaced by an equivalent homogeneous particle with an average permittivity ε_{av}, which gives an equivalent dipole moment. Therefore, the following equation holds:[161]

$$\frac{V_1}{L_1}\frac{\varepsilon_1 - \varepsilon_2}{\varepsilon_1 + \varphi_1\varepsilon_2} = \frac{V_2}{L_2}\frac{\varepsilon_{av} - \varepsilon_2}{\varepsilon_{av} + \varphi_2\varepsilon_2}, \quad \varphi_i = L_i^{-1} - 1, \quad i = 1,2, \tag{1.79}$$

where V_i are the volumes and L_i are the geometrical depolarization factors of inner ($i = 2$) and outer ($i = 2$) spheroids, respectively.

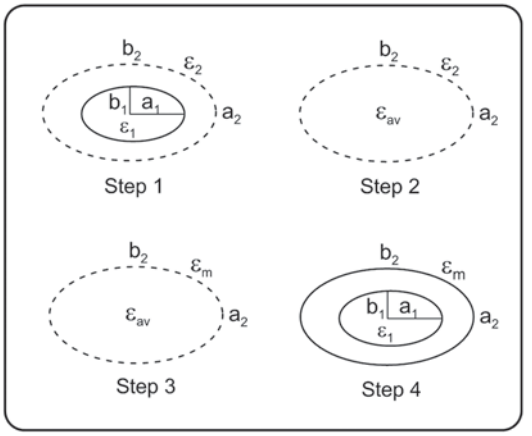

Figure 1.2 Scheme of the dipole equivalence method.[186] Step 1: The initial particle (ε_1, a_1, b_1) is embedded in an auxiliary medium with permittivity ε_2 and is surrounded by an imaginary confocal spheroid (a_2, b_2). Step 2: An equivalent particle (ε_{av}, a_2, b_2) is embedded in the auxiliary medium with permittivity ε_2. Step 3: The equivalent particle (ε_{av}, a_2, b_2) is embedded in the surrounding medium with permittivity ε_m. Step 4: The initial particle (ε_1, a_1, b_1) is covered by an outer layer (ε_2, a_2) and is embedded in the surrounding medium with permittivity ε_m. Steps 1 and 2 give identical dipoles in the auxiliary medium, whereas steps 3 and 4 give identical dipoles in the surrounding medium.

In fact, Eq. (1.79) defines the equivalent averaged permittivity, which gives identical dipoles in steps 1 and 2

$$\varepsilon_{av} = \varepsilon_2 \frac{1 + \varphi_2 f_{12}\alpha_{12}}{1 - f_{12}\alpha_{12}}, \quad \alpha_{12} = \frac{\varepsilon_1 - \varepsilon_2}{\varepsilon_1 + \varphi_1 \varepsilon_2}, \quad f_{12} = \frac{V_1 L_2}{V_2 L_1}. \tag{1.80}$$

In step 3, the equivalent particle of step 2 is placed in the surrounding medium with the dielectric permittivity ε_m. Finally, note that the dipole moment in step 3 equals that of step 4, thus giving the final analytical solution for the polarizability of the layered particle embedded in the surrounding medium

$$\alpha_{av}^{(2)} = \frac{V_2}{4\pi L_2} \frac{\varepsilon_{av} - \varepsilon_m}{\varepsilon_{av} + \varphi_2 \varepsilon_m}. \tag{1.81}$$

This solution has the same form as that for usual homogeneous spheroids. It is evident that the outlined procedure can be continued iteratively for an arbitrary number of confocal layers.

The LPR resonance condition $\mathrm{Re}(\varepsilon_{av}) \equiv \varepsilon'_{av} = -\varphi_2 \varepsilon_m$ can be recast as Eq. (1.74)

$$\varepsilon' \equiv \varepsilon'_2 = -2\varepsilon_m \varphi_{\pm}. \tag{1.82}$$

As the form of Eq. (1.82) is identical to that of Eq. (1.74), from Eq. (1.82), we immediately get the final solution for LPR wavelengths

$$\lambda_{\max} = \lambda_p [\varepsilon_{ib} + 2\varepsilon_m \varphi_{\pm}]^{1/2}. \tag{1.83}$$

In Eqs. (1.82) and (1.83), functions $\varphi_{\pm}$ are defined by the following expressions:

$$\varphi_{\pm} = \frac{p}{2} \pm \frac{1}{2}\left[p^2 - \varphi_2 \frac{\varepsilon_1}{\varepsilon_m} \frac{1 - f_{12}}{\varphi_1 - \varphi_2 f_{12}}\right]^{1/2} \tag{1.84}$$

$$p = \frac{1}{\varphi_1 - \varphi_2 f_{12}} \left(\frac{\varepsilon_1}{2\varepsilon_m}(1 + f_{12}\varphi_2) + \frac{\varphi_2}{2}(\varphi_1 + f_{12})\right). \tag{1.85}$$

The positive and negative signs in Eq. (1.83) correspond to the LPRs of the outer and inner boundary shells, respectively. For spherical gold nanoshells, the short-wavelength inner resonance cannot be resolved in absorption or scattering spectra, whereas for silver nanoshells it is clearly seen around 350 nm.[189]

It is instructive to show that the general solution [Eqs. (1.83) through (1.85)] recovers all limiting cases of interest: metal spheroids, nanoshells, and spheres. For homogeneous spheroids, we set $f_{12} = 0$, so Eqs. (1.80) and (1.84) reduce to $\varepsilon_{av} = \varepsilon_2 \equiv \varepsilon$, $\varphi_+ = \varphi_2/2 = (L_{\parallel,\perp}^{-1} - 1)/2$. This yields the usual electrostatic polarizability tensor (1.77).

For spherical nanoshells, we have to set $\varphi_{1,2} = 2$ and $f_{12} = V_1/V_2 = 1 - f_s$, where f_s is the volume fraction of the metal shell. Then Eqs. (1.84) and (1.85) reduce to the previously published results

$$\varphi_{\pm} = \frac{1}{2}\left[p_1 \pm (p_1^2 - (\varepsilon_1/\varepsilon_m))^{1/2}\right], \quad p_1 = \frac{\varepsilon_1}{\varepsilon_m}\left(\frac{3}{4f_s} - \frac{1}{2}\right) + \frac{3}{2f_s} - \frac{1}{2}. \tag{1.86}$$

For thin shells, we get asymptotic solutions $\varepsilon = -2\varepsilon_m p_1$ and $\varepsilon = -\varepsilon_1/2p_1$. The first solution can be recast as Eq. (7.10) in Ref. 140, but the second expression differs from Eq. (7.11) in Ref. 140, which seems to be erroneous. The corresponding resonance wavelengths of a thin nanoshell are as follows:[162]

$$\lambda_{\max} \equiv \lambda_+ = \lambda_p \left(\varepsilon_{ib} + \frac{3}{f_s}\left(\varepsilon_m + \frac{\varepsilon_1}{2}\right)\right)^{1/2}, \tag{1.87}$$

$$\lambda_{\min} \equiv \lambda_- = \lambda_p \left(\varepsilon_{ib} + \frac{2\varepsilon_1 \varepsilon_m f_s}{3(\varepsilon_1 + 2\varepsilon_m)}\right)^{1/2}. \tag{1.88}$$

Again, the maximal LPR wavelength can be tuned by varying the core/shell ratio $0 < f_s \leq 1$ ($f_s = 1$ for a homogeneous sphere and $f_s \to 0$ for a thin shell). In the limit $f_s \to 0$, the first resonance wavelength $\lambda_{\max} \to \infty$ and $\lambda_{\min} \to \lambda_p \varepsilon_{ib}^{1/2}$. By contrast, Eq. (7.11) in Ref. 140 reduces to $\lambda_{\min} \to \lambda_p(\varepsilon_{ib} + \varepsilon_1/2)^{1/2}$.

Finally, the properties of thick shells are close to those for homogeneous spheres. Indeed, by setting $f_s \to 1$ in Eqs. (1.87) and (1.88), we arrive at the following expressions:

$$\lambda_{\max} = \lambda_p(\varepsilon_{ib} + 2\varepsilon_m)^{1/2}, \quad \lambda_{\min} = \lambda_p\left(\varepsilon_{ib} + \frac{\varepsilon_1}{2}\right)^{1/2}. \tag{1.89}$$

One additional important note is in order here. The above equations determine the very first ($n = 1$) dipole resonances of particles. With an increase in the particle size, higher multipoles and corresponding multipole resonances can also be excited in larger particles. For example, in the case of spherical particles, these conditions correspond to the resonance relations for the partial Mie coefficients[161] $\lambda_n = \lambda_p(\varepsilon_{ib} + \varepsilon_m(n+1)/n)^{1/2}$, where n is the mode (resonance) number. With an increase in the sphere size, the multipole wavelength also increases.[190] The multipole modes in thin spherical nanoshells can be written as follows:[161]

$$\lambda_{n,\max} = \lambda_p[\varepsilon_{ib} + 2\varepsilon_m\varphi_n]^{1/2}, \qquad \varphi_n = \frac{1}{2}\left[p_n \pm (p_n^2 - (\varepsilon_1/\varepsilon_m))^{1/2}\right], \tag{1.90}$$

with the multipole parameter p_n being defined by the following expression:

$$p_n = \frac{q_n^2 + (\varepsilon_1/\varepsilon_m) + q_n(1 - f_s)[1 + (\varepsilon_1/\varepsilon_m)]}{2q_n f_s}, \quad q_n = \frac{n+1}{n}. \tag{1.91}$$

At the lowest dipolar order $n = 1$, Eq. (1.91) reduces to Eq. (1.86).

1.5.4 Coupled plasmon resonances: bisphere and linear chain examples

Along with the optics of individual PR particles, the collective behavior of the interacting PR particles is of great interest for nanobiotechnology.[191] The analysis of its features includes the study of various structures, beginning from one-dimensional chains with unusual optical properties.[192] Another example is the optics of two-dimensional (2-D) arrays,[193] in particular, clusters of spherical particles on a substrate and 2-D planar ensembles formed by usual gold or polymer-coated spheres.[172] The unusual properties of monolayers of silver nanoparticles in a polymer film[194] and on a glass substrate[195] have been recently discovered. A review of 3-D cluster optics can be found in Refs. 140, 162, 169, and 191.

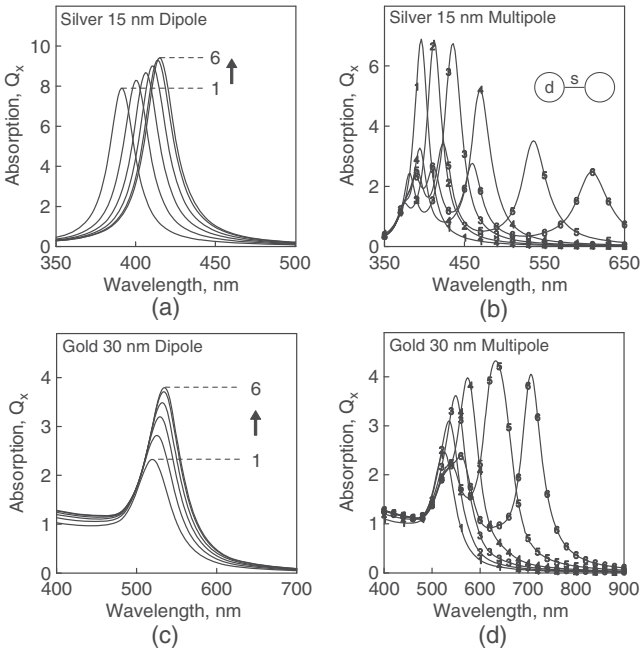

Figure 1.3 Absorption spectra at an incident light polarization parallel to the (a) and (b) silver and (c) and (d) gold bisphere axis ($x \equiv \|$). Calculations by the (a) and (b) dipole approximation and (c) and (d) GMM multipole codes for particle diameters $d = 15$ (silver) and 30 nm (gold) and the relative interparticle separations $s/d = 0.5$ (1), 0.2 (2), 0.1(3), 0.05 (4), 0.02 (5), and 0.01 (6).

In this chapter, we restrict our consideration of collective plasmons by only one instructive example: gold and silver bispheres of a diameter d separated by a variable distance s.

Figure 1.3 shows the absorption spectra calculated by the dipole and multipole approaches for two particle diameters $d = 15$ nm (silver) and 30 nm (gold) (for data for 60 nm, see Ref. 169). The numbers on the curves correspond to the relative interparticle separations s/d from 0.5 to 0.01. When the interparticle separation satisfies the condition $s/d \geq 0.5$, the absorption efficiencies approach the single-particle quantities so that the dipole and multipole calculations give identical results. However, the situation changes dramatically when the relative separation s/d is about several percent. The exact multipole approach predicts the well-known enormous theoretical[191] and experimental[196] red-shifting of spectra and their splitting[197] into two modes, whereas the dipole spectra show only a minor red shift.

In the case of silver bispheres [Fig. 1.3(a) and (b)], the resonance light scattering of 60-nm clusters exceeds the resonance absorption so that any comparison between the dipole and the multipole approaches becomes incorrect unless both scattering and absorption are taken into account for the total extinction. That is why we show only the calculated data for silver

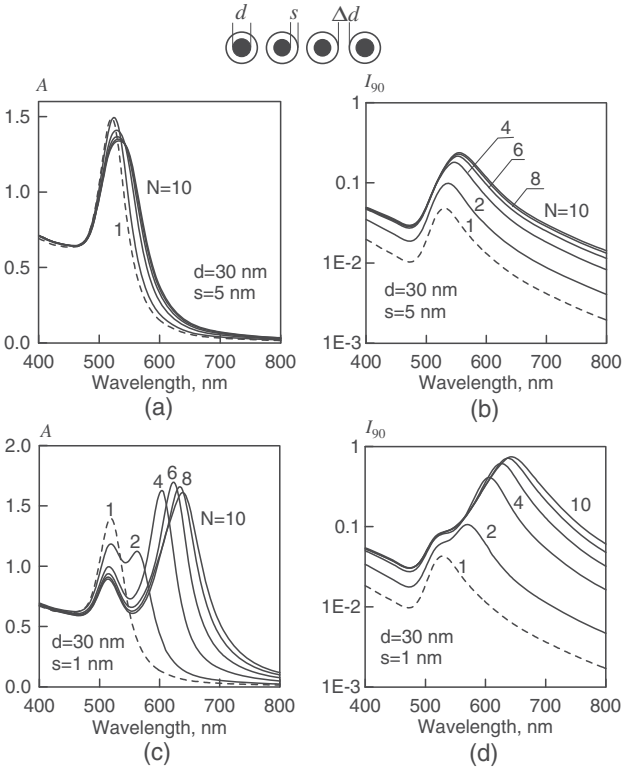

Figure 1.4 Extinction and scattering spectra of randomly oriented linear chains of two-layered gold (core)/dielectric shell particles with different particle number $N = 1$–10. Calculations for the core diameter $d = 30$ nm, (a) and (b) shell thickness $s = 5$ and (c) and (d) 1 nm, and separation distance $\Delta d = 0$.

nanospheres with $d \leq 60$ nm. At moderate separations ($s/d > 0.05$), the independent-particle spectrum splits into two modes; therefore, the data of Fig. 1.3(a) and (b) are in great part analogous to those of Fig. 1.3(c) and (d) and need no additional comment. However, at smaller separations $s/d < 0.05$, we observe the appearance of four plasmon resonances related to the quadrupole and the next high-order multipole excitations.

Strong binary coupling also is observed for linear chains of two-layer conjugates. Figure 1.4 shows the dependence of extinction $A(\lambda)$ and scattering $I_{90}(\lambda)$ spectra of randomly oriented linear chains built from two-layer particles with gold core and a dielectric shell. The number of particles is the variable parameter of curves. It is worth noting a principal difference between the spectra of densely packed [$s = 1$ nm, strong binary coupling, Fig. 1.4(c) and (d)] and rare chains [$s = 5$ nm, weak binary coupling, Fig. 1.4(a) and (b)].

The scattering intensity in Fig. 1.4(b) and Fig. 1.4(d) is expressed in the same scale and was calculated for the same gold concentration. In agreement with our previous observations,[191] the extinction spectra do not change

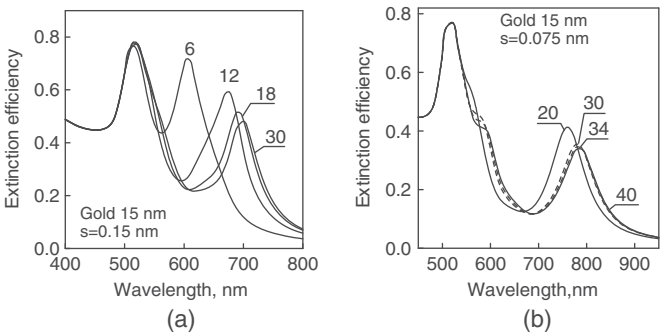

Figure 1.5 Extinction spectra of 15-nm randomly oriented gold bispheres in water, calculated by the exact T-matrix method. The sphere diameter is 15 nm, the separation distances between spheres are (a) 0.15 nm and (b) 0.075 nm, and the numbers near the curves designate the multipole orders that have been included in the single-particle field expansions of coupled equations.

essentially for small and rare aggregates [Fig. 1.4(a)], while the PR peak in the scattering spectra increases significantly due to constructive far-field interference. However, the peak position does not shift significantly.

For a thin dielectric shell, the transformation of extinction and scattering spectra are due to both the electrodynamic coupling and the far-field interference. Again, we observe a rapid saturation of particle-number effect. This can be interpreted as manifestation of an effective electrodynamic interaction between monomers, which belong to a finite conjugate group. Other examples of aggregated particles and their optical properties can be found in our works.[161,191]

The dependence of the extinction spectra on the total multipole order N_M is shown in Fig. 1.5. Remember once again that N_M means the maximal order of VSH in the coupled equations rather than the number of multipoles involved in the final calculations of optical characteristics. According to these computer experiments, one has to include extra-high single-particle multipole orders (up to 30–40) into coupled equations to calculate correctly the extinction spectra of 15-nm gold spheres separated by a 0.5–1% relative distance s/d. The extinction spectra were calculated by the exact T-matrix code for randomly oriented gold bispheres in water. It is evident from Fig. 1.4 that the convergence problems are related to calculations of the red-shifted resonance peak, which can be reproduced correctly if we retain the VSH with the order of about 30 in the case of 0.15 nm (1%) separation. For smaller separations [e.g., $s = 0.075$ nm, Fig. 1.5(b)], we note the appearance of a quadrupole resonance near 600 nm that can also be reproduced accurately only if we include multipoles of the 40th order into coupled equations.

The need to retain high multipoles for small spheres, which are themselves well within the dipole approximation, seems to be somewhat counterintuitive. It should be emphasized that the final calculations involve a rather small

number of multipoles (as a rule, less than 6). However, to find these small-order contributions correctly, one needs to include many more multipoles into coupled equations such as given by Eq. (1.44). The physical origin of this unusual electrodynamic coupling was first established by Mackowski[198] for small soot bispheres. He showed that the electric-field intensity can be highly inhomogeneous in the vicinity of minimal separation points between the spheres even if the external filed is homogeneous on the scale of bisphere size. Evidently, the same physics holds in our case, as the imaginary part of the dielectric permittivity is the main parameter that determines the spatial electric-field distribution near the contact bisphere point.

1.6 Tissue Structure and Relevant Optical Models

Biological tissues are optically inhomogeneous and thus scattering processes with light propagation play a substantial role. The scattered radiation contains information about sizes and shapes of tissue structural elements, their orientation, optical constants, and other parameters. To extract this information and interpret experimental results on light scattering, one needs to develop an appropriate optical model for a tissue and on its basis to solve the inverse problem of radiation propagation and scattering in the medium.

There is no rigorous theory describing light absorption and scattering by tissues and cell structures. However, important information on their optical properties may be obtained by studying the appropriate model objects. The complicated structure of tissues, high concentration of scattering particles, variability of their sizes, shapes, and optical constants makes the problem of constructing an adequate optical model quite cumbersome. It may be assumed that models, being the basis of the scattering equation, would be best matched to real objects. The main peculiarities of scattering effects are essentially controlled by simple factors. These factors for a single particle are[35] the size and shape of the particle, the internal structure of the particle, and the inherent inhomogeneity of the particle.

1.6.1 Continuous and discrete models of tissues

Two approaches may be considered for tissue modeling, namely, tissue's representation as a medium with the continuous random spatial distribution of optical parameters or as a discrete ensemble of scatterers. The choice of one or another approach is dictated both by the features of the tissue under study and, to a considerable extent, the kind of light scattering characteristics that are to be obtained in the result of the modeling. The microstructure of biological cells and tissues is complicated and difficult to be characterized quantitatively. The microstructure of a cell or tissue is revealed in light or electron micrographs as spatial density fluctuations that are the result of the

stain density variations of different structural components.[199] Most biological tissues are composed of structures with sizes that span a wide range. In the absence of a single dominant size, representation of a tissue as an ensemble of isolated and independent particles fails. Light scattering in these systems is possible to describe using the idea of a random continuum of index of refraction inhomogeneities with a varying spatial scale.[200] Similar problems have been investigated for light propagation through atmospheric turbulence[201] and for reflection by rough surfaces.[202]

The tissue representation as inhomogeneous medium with continuous spatial fluctuations of the index of refraction is, e.g., employed to examine the speckle structure of scattered radiation. The interest for the scale fluctuation properties of a speckle pattern appearing under the interaction of coherent radiation with the optically inhomogeneous objects is due to a possibility of extraction of information on the structure of scattering objects.[203]

Intriguing results for such a tissue model have been discussed by Schmitt et al.[200,204] In particular, the phase contrast microscopy was used to show the structure of the refractive index inhomogeneous in the tissues of mammals to be similar to the structure of frozen turbulence in a number of cases.[6] This result is of fundamental importance for understanding the peculiarities of radiation transfer in the tissue, and it may be a key for the solution of the inverse problem on tissue structure reconstruction. The above approach is usually exploited for tissues where there are no pronounced boundaries between elements and which are featured by significant heterogeneity. Figure 1.6 is the electronic micrograph of a rat liver represented as an example.[205]

The process of scattering at these structures may be described under certain conditions using the model of a phase screen.[206]

The second approach to tissue modeling is its representation as a system of discrete scattering particles. This chapter deals mainly with different aspects of radiation propagation in the tissues on the basis of the model of discrete scatterers. This model is to be advantageously used to describe the angular dependence of the polarization characteristics of the scattered radiation.[207]

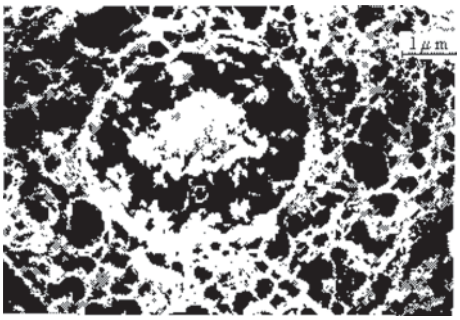

Figure 1.6 Electronic micrograph of a rat liver.[205]

Blood is an example of the most important biological disperse system that entirely corresponds to the model of discrete scatterers.

To properly choose a theoretical method and approximations for calculating the scattering characteristics of a particle system it is necessary to regard the main features of the tissue structure and namely, the shape and the size range of particles, their index of refraction and concentration. Consider some examples of discrete scatterer models for some tissue types.

1.6.2 Shape and sizes of particles in discrete tissue models

A biological medium is most often modeled by an ensemble of homogeneous spherical particles. This has a certain meaning since many cells, microorganisms and blood corpuscles are close in shape to spheres or ellipsoids. A system of noninteracting particles is the simplest version of this model. The solution of the problem of the diffraction of electromagnetic waves at a spherical particle is well known; this is the Mie solution.[12] The development of this model involves a consideration of the spherical particles structure,[15] namely, that of multilayered spheres and spheres with radial nonhomogeneity, anisotropy, and optical activity.

For tissues that have fiber structures, a system of long cylinders with different concentration is the most appropriate model. Muscular tissue, the cornea, and the sclera belong to these tissues formed essentially by collagen fibrils. The solution of the problem of diffraction at a single homogeneous or multilayered cylinder scatterer is also well known.[12]

The sizes of most biological cells and tissue structure elements are varied in a range from a few tens of nanometers to hundreds of micrometers.[9,208] Some examples are listed below. Bacteria usually have the size of a few micrometers.[208] The blood corpuscles (erythrocytes, leukocytes, and platelets) exhibit the following parameters. A normal erythrocyte in plasma has the shape of a concave–concave disc with a diameter varying from 7.1 to 9.2 μm, its thickness in its center 0.9–1.2 μm and 1.7–2.4 μm, respectively.[9] Leukocytes are formed like spheres of 8–22 μm diameter,[209] and platelets are thin discs with diameters from 2 to 4 μm. Most other human cells are in the range of 5–20 μm in diameter.[38]

The retinal nerve fiber layer comprises bundles of unmyelinated axons that run across the surface of the retina. The cylindrical organelles of the retinal nerve fiber layer (axonal membranes, microtubules, neurofilaments, and mitochondria[210]) as seen by electron microscopy were modeled as parallel cylindrical arrays in order to gain insight into their optical properties.[211] Axonal membranes, like all cell membranes, are thin (6–10 nm) phospholipid bilayers that form cylindrical shells enclosing the axonal cytoplasm. Axonal microtubules are long tubular polymers of the protein tubulin with an outer diameter of ≈25 nm, an inner diameter of ≈15 nm, and a length of 10–25 μm. Neurofilaments are stable protein polymers with a diameter of ≈10 nm.

Mitochondria are ellipsoidal organelles containing densely involved membranes of lipid and protein. They are 0.1–0.2 μm thick and 1–2 μm long. In the epidermal layer, the cells are large (average cross-sectional area ≈80 μm^2) and quite uniform in size.[200]

Hence, for most tissues the size parameter of the particle $x = 2\pi r/\lambda$ (where r is the particle radius, λ is the radiation wavelength) is varied in a range of $1 < x < 100$ in the visible region.

The size distribution of scattering particles in biological objects may be both essentially monodisperse as, e.g., in the optical eye tissues, and quite broad. There is no universal distribution function in dimension that would describe all tissues with equal adequacy. Gaussian, gamma, and power distributions are used as a function of particle size distribution in the optics of disperse systems.[9] It was particularly stated that scatterers in the epidermal layer of the skin exhibit a lognormal size distribution, whereas the spatial fluctuations in the index of refraction of dense fibrous tissues, such as the dermis, follow a power law.[200]

In cases where scattering at particles of complex shape is needed, different procedures are applied to calculate scattering at nonspherical particles, e.g., the method of T-matrices and others[15] (see above). The modeling of complexly shaped particles by spherical scatterers aggregates is possible. The light scattering peculiarities for a cell modeled by a spherical particle with inclusions are analyzed in Ref. 212. All of the above present a vast area of research; the specific nature of tissues is, however, not exhausted by these peculiarities.

1.6.3 Optical constants of tissues, heterogeneity, and optical softness

The measurement of the index of refraction for tissues and their components is one of the actual problems of tissue optics. Such studies have been performed for a comparatively long time,[213] but there is not adequate information in the literature even about an averaged index of refraction for different tissues.[9]

The matter surrounding the scatterers (intercellular liquid and cytoplasm), the so-called ground substance is composed mainly of water with salts and organic components solved in it. The ground matter index is usually taken as $n_0 = 1.35$–1.37. Scattering particles themselves (organelles, protein fibrils, membranes, protein globules) exhibit a higher density of proteins and lipids in comparison with the ground substance and thus a greater index of refraction $n_1 = 1.43$–1.47. This implies that structures with binary fluctuations of the index of refraction are the simplest model of tissue.

Absorption for most tissues in the visible region is insignificant except the absorption bands of blood hemoglobin and some other chromophores. The absorption bands of protein molecules are mainly in the near-UV region. Absorption in the IR region is essentially defined by water contained in tissues.

Many examples may be cited that confirm these regularities.[15] Brunsting and Mullaney[214] measured the indexes of refraction for cytoplasm and nucleous ovary cells of hamster and obtained the values $n_{\text{cytoplasm}} = 1.37$ and $n_{\text{nucleus}} = 1.39$. Schmitt and Kumar[215] obtained the indexes of refraction of 1.4–1.45 for the structural fibers of tissue and cell nuclei and that of 1.36 for the cell cytoplasm of different tissues. The nuclei and cell membrane of fibroblasts have an index of refraction of 1.48, the cytoplasm has an index of refraction of 1.38, and the averaged index of a cell is 1.42.[216] The index for *Bacillus subtilis* spores has a value of about 1.5, and its imaginary part is smaller than 0.01 in a wide spectral range.[217] The collagenous fibrils of cornea and sclera have a index of refraction of 1.47, and the refractive index of the ground matter is 1.35.[218]

The real part of the erythrocyte index with respect to plasma $m = 1.041 - 1.067$ ($\lambda = 600$ nm). Its imaginary part is varied within 10^{-2}–10^{-5} ($\lambda = 350$–1000 nm). The relative index for the human lymphocytes varies in the range of $1.01 < m < 1.08$.[219] The optical parameters of platelets have not been studied thoroughly; they are, however, referred to weakly absorbing soft particles (for the wavelengths bigger than 600 nm). Additional information on the refractive index of biological cells may be found in Ref. 220. A great deal of data on optical constants for various tissues is given in Ref. 9.

The above examples are evidence that tissue inhomogeneities have sizes comparable with visible or NIR wavelengths and a small relative index of refraction, hence they are to be considered as optically soft. This enables different approximation methods described in Sections 1.1–1.5 to be used for calculation.

1.6.4 Anisotropy of tissues

Many biological structures are optically anisotropic. A number of tissues contain single-axis birefringence structures.[221] For bone, muscular, and skin tissues, these are mineralized (hydroxylapatite crystals), myosinous and collagenous bundles, respectively. For the muscular tissue, the packing density of bundles in a multifractal is higher than that for the bone, and myosinous fibers in them show a smaller birefringence ($\delta n \approx 10^{-3}$). The predominant orientation of collagenous fibers in different regions of the cornea results in shape birefringence and dichroism.[222] The orientation structure of collagenous bundles of the skin dermis is extremely varied even for a small thickness of a microscopic section. Besides linear birefringence and dichroism, many biological objects show optical activity.

1.6.5 Volume fraction of the particles

An important parameter for the model of discrete particles that defines its optical properties is the packing density or, in other words, volume fraction of

the particles. This characteristic may be experimentally found using electron microscopy. This is one of the straightforward approaches based on measurement of the area occupied by an element of a particular size. The selected region is viewed as a slice through a 3-D surface that is divided into subcubes for counting the number of elements with the same size. The volume fraction occupied by the elements is proportional to the number of subcubes counted. Employing this procedure and the electron microscopy data one would calculate volume fraction f_i occupied by the particles with size d_i. Unfortunately, systematic errors may take place that may lead to different values of the volume fraction evaluated for varying thicknesses of the section. The Holmes effect to Delesse's theorem has been used to eliminate these errors.[223] Estimations for a volume fraction occupied by scattering particles may also be calculated by comparing the weights of a native tissue and dry rest with the known density of separate tissue components.

As a rule, the volume fraction occupied by the scattering particles in such tissues as muscle, cornea, sclera, and eye lens covers from 20% to 40%. Conventionally the whole blood contains approximately 5×10^6 erythrocytes in 1 mm^3. Erythrocytes make up to 40% of the blood volume. The volume fraction f of erythrocytes in the blood is called the hematocrit H. For normal blood, $H = 0.4$. The remaining 60% of the blood volume is the plasma–an essentially transparent water solution of salts. The concentration of other scatterers would amount from percent fractions to a few dozens of percents.

1.6.6 Effects of spatial ordering

A substantial role in tissues is played by the spatial organization of particles forming them. As said above, with very small packing densities, we deal with incoherent single or multiple scattering at independent particles. If the volume fraction occupied by the particles is 0.1 or more, coherent concentration effects appear. The concentration of scattering particles is sufficiently high for most tissues, therefore spacing between individual scatterers is comparable with their sizes. If the particle-size distribution is close to the monodisperse one, then such dense packing entails a spatial degree of order on the arrangement of the particle. The effects of spatial ordering should be taken into account when constructing the adequate optical model of such tissues.

Spatial ordering is of utmost importance for optical eye tissues, nevertheless, aspects considered below are more or less inherent in all tissues, particularly in the skin or muscles. The spatial degree of order of densely packed systems of scattering particles ensures a high transmission of cornea and eye lens that is responsible for our seeing the surrounding world. The cornea would scatter to 90% of light incident and we would see essentially nothing if all its fibers were arranged randomly and scattered light independently. The real situation is, however, different.

The effect of multiple scattering does much to light propagation in dense disperse systems. The propagation of light in densely packed disperse biostructures shows a number of intriguing peculiarities that enable the optical eye tissues to be considered as natural photon crystals. Like artificial photon crystals presenting structures with periodical variations of the index of refraction with characteristic scales on the order of light wavelength, statistically ordered biostructures demonstrate high transmission spectral regions and a band of frequencies for which the propagation of electromagnetic waves is forbidden. Bandgaps are due to the effects of light scattering at a system of ordered particles. The positions and depth of these suppression bands highly depends on the size, refractive index, and spatial arrangement of scattering particles.

The importance of the spatial degree of order is conveniently illustrated by comparing the optical properties of the cornea with that of sclera (Fig. 1.7). Now let's consider the structure of cornea and sclera in more detail.[9,224–231]

The cornea is the frontal section of the eye's fibrous capsule, its diameter is ≈ 10 mm. The sclera is a turbid opaque tissue covering nearly 80% of the eye and serving as a protective membrane providing for, along with the cornea, counteraction against internal and external forces and thereby keeping the shape of the eye.

Both tissues are composed of collagenous fibrils immersed in a mucopolysaccharide ground substance. The collagenous fibrils have a shape

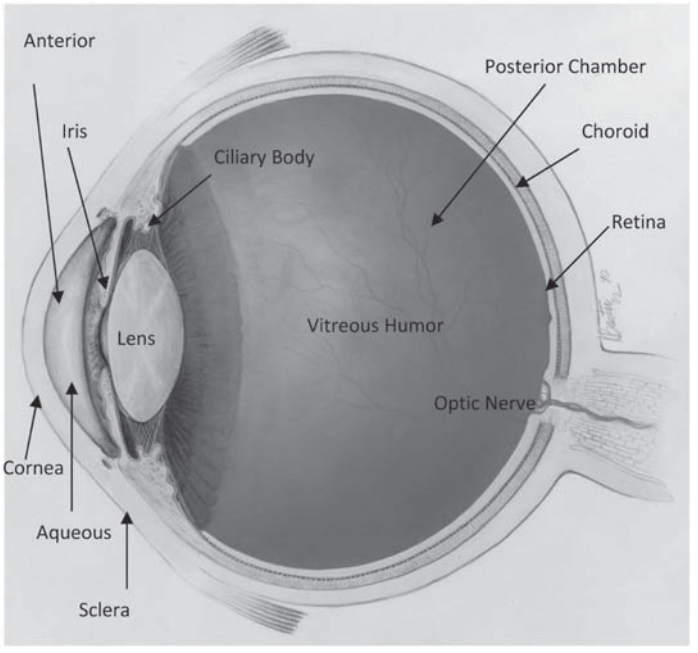

Figure 1.7 The human eye. The cornea is the transparent tissue of the anterior surface of the eye. The sclera is the white of the eye, and it is opaque.[9] National Eye Institute, NIH (Figure NEA04). See color plates.

close to that of a cylinder. They are packed in bundles like lamellae. All fibers are aligned within every lamella nearly in parallel with each other, the lamella plane and tissue surface. The indexes of refraction for the fibers and the ground substance surrounding them differ markedly from others and amount to 1.470 and 1.345, respectively.

The cornea fibril diameters varied from 20 to 31 nm for different species of animals, but their variations are less than 10% for each concrete species of animals or men, i.e., the fibrils are quite uniform in diameter (Fig. 1.8). The spacing between the fibril axes is 50–60 nm.

The collagenous fibril diameters of the sclera are widely spread from 25 to 230 nm. Spacing between the centers of adjacent fibrils in the bundle is about 100–300 nm (Fig. 1.8).[9,224,230] As has been mentioned, the collagenous fibrils are packed in bundles and lie in them nearly parallel with each other, but not so regularly as in the cornea. Furthermore, groups of fibrils in a certain bundle are separated from each other by comparatively large regions that are randomly distributed in space.

While both tissues are composed of similar molecular components, they have different microstructures and thus very different physiological functions. The sclera of the eye is opaque to light, scattering at almost all wavelengths of visible light, thus appearing white. The cornea is transparent, allowing for more than 90% of the incident light to be transmitted. The collagen fibrils in the cornea have a much more uniform size and spacing than those of the sclera,[225] resulting in a greater degree of spatial order (hexagonal quasi-crystal) in the organization of fibrils in the cornea as compared with the sclera (Fig. 1.8).[226,227]

It is believed that the spatial order and small size and spacing of the collagen fibrils are responsible for the transparency of the cornea, while the

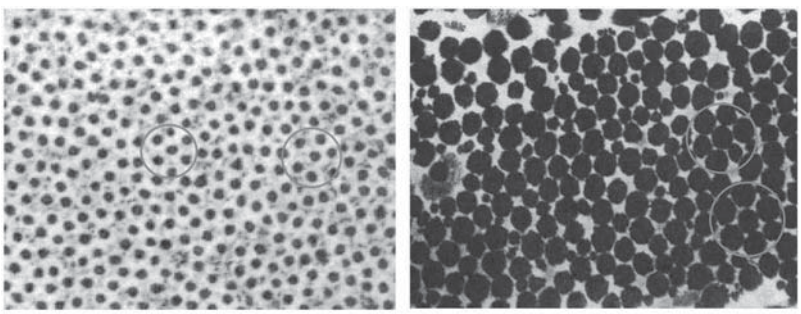

Figure 1.8 The high-magnification electron micrographs of the human (a) cornea ($\times$32,000) and (b) sclera ($\times$18,000) showing a cross section of the collagen fibrils [dark circular areas embedded in a mucopolysaccharide ground substance (bright areas)]: for (a) cornea collagen fibrils have a uniform diameter and are arranged in the same direction within the lamellae and form a hexagonal quasi-crystal; (b) scleral collagen fibrils, which display various diameters, and thus more randomly packed; however, they can be locally quasi ordered.[9,230]

lack of spatial order and large size and spacing of the fibrils are responsible for the opacity of the sclera.

The transmittance of a densely packed disperse system can be calculated using the radial distribution function $g(r)$, which statistically describes the spatial arrangement of particles in this system. The function of the radial distribution of scattering centers $g(r)$ may be calculated for some tissues on evidence derived from electron microscopy.

The technique of experimental $g(r)$ determination involves the counting of the number of particles, placed at a specified spacing from an arbitrarily chosen initial particle, followed by its statistical averaging over the whole ensemble. In a 2-D case, the particle number ΔN at the spacing from r to $r + \Delta r$ is related to function $g(r)$ by the following equation:

$$\Delta N = 2\pi\rho g(r) r \Delta r, \tag{1.92}$$

where ρ is the mean number of particles for a unit area.

The radial distribution function $g(r)$ was first found for the cornea by Farrell et al.[228] using experimental data. Figure 1.9(a) depicts the typical result for one of the cornea regions, as obtained by determining the ratio of local to mean density of centers as a function of radii taken about 700 fibril centers. The results of similar studies for the eye sclera[229] are illustrated in Fig. 1.9(b); the data are calculated for several regions of sclera using electron micrographs from Ref. 230, averaging about 100 fibril centers.

Function $g(r)$ for the sclera was obtained on the basis of the spatial distribution of fibril centers neglecting discrepancy in their diameters. A noisy

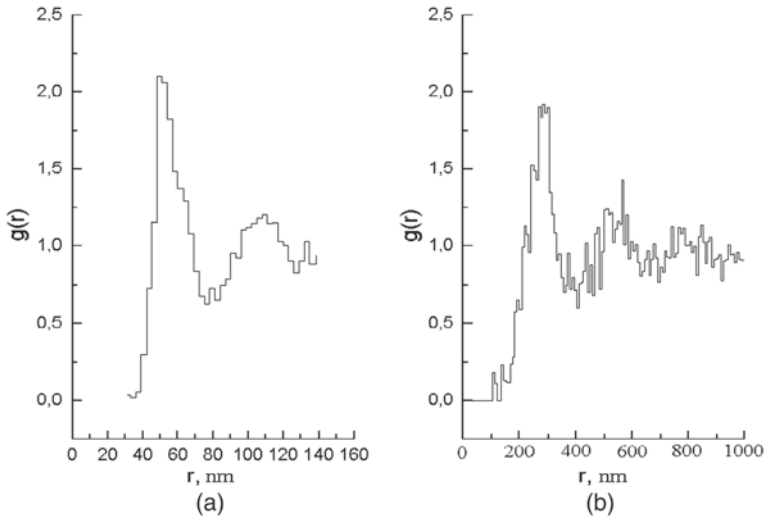

Figure 1.9 Histogram representation of the radial distribution functions $g(r)$, as obtained using the electron microscopy for (a) the rabbit cornea[228] and (b) the human sclera[229].

curve is elucidated by a small volume of statistical averaging. In spite of assumptions made earlier about a noncorrelated distribution of the sclera fibers in space,[231] the results obtained using electron microscopy attest to the presence of near-order degree in the sclera; albeit this degree of order is less pronounced as that in the cornea. The low value of interference interaction contribution is due to both a smaller degree of order in the arrangement of the sclera fibers and a strong discrepancy in the scattering amplitude at different-sized fibers within the band inherent in the sclera.

Similar results of a comparative examination of the cornea and the sclera were obtained using the method of spatial frequency analysis in Refs. 226 and 231. A linear log–log plot of the Fourier spectrum is an indication of the power-law relationship between the amplitude and the frequency of Fourier components. The 2-D Fourier spectrum is a plot of squared amplitude of the Fourier components as a function of spatial frequency. In an isotropic medium, the spatial frequency of the Fourier components is represented by the reciprocal radial distance from the center of Fourier spectrum in μm^{-1}.

The spatial density fluctuations representing the microstructure can be resolved into Fourier components.[226,231] The Fourier components of any micrograph provide a complete basis for a detailed, quantitative, and unique description of the microstructure.

The microstructural information obtained by the 2-D Fourier analysis is related to transparency and opacity of the cornea and the sclera, respectively. The distributions of the Fourier components can be determined from the profiles of the Fourier spectra (Fig. 1.10). The abscissa represents the spatial frequency of the Fourier components in units of nm^{-1}. The ordinate represents the normalized amplitude of the Fourier components in the upper-left quadrant of 2-D Fourier spectra. The vertical dashed lines represent the reference 200-nm dimension. The peaks in the profiles are due to rings in the 2-D Fourier spectra. Profile peaks represent Fourier components with higher

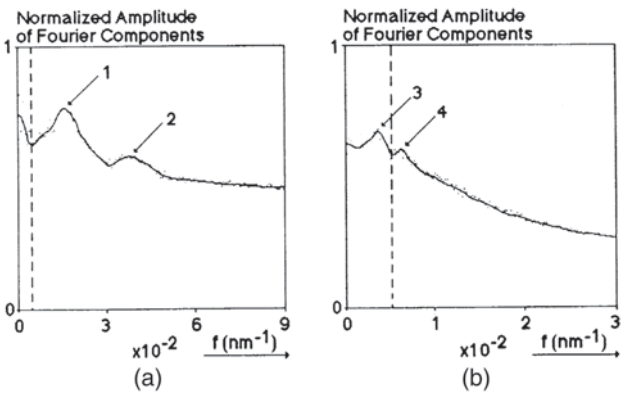

Figure 1.10 Profiles of the 2D Fourier spectra of (a) the cornea and (b) the sclera.[226]

amplitude relative to the background. These Fourier components represent the predominant spatial density fluctuations: the collagen fibril center-to-center spacing. While peaks 1 and 3 represent the fundamental Fourier components, peaks 2 and 4 represent the first harmonics. The curves in the profiles are drawn by averaging the two nearest neighbors of the pixel. The profiles showed that the major Fourier components of the cornea caused by the fibril center-to-center spacing were smaller than 200 nm. The major Fourier components of the sclera were larger than 200 nm. Also, the microstructure of the cornea revealed greater spatial order than the sclera.

The eye lens is also an example of the tissue for which the spatial degree of order is of crucial importance. Like a lens, it focuses light to form an image at the retina because of its high index of refraction and transparency. The eye lens exhibits a certain viscosity and is capable of altering its radius of curvature under the action of accommodation muscles and thus its focal length. It is gel, i.e., a cross-linked polymer plus low molecular liquid system where the polymer forms a spatial cross-linked sewn structure.[8] A similar structure is inherent in traditional marmalades and gelatin.

Brewster was the first to demonstrate regularly repeating structures in the lens tissue that is presently known as the lens fibers. The lens transparency is limited by two physical phenomena, namely, the absorption and scattering of visible light. The first phenomenon is negligible in a normal lens because the lens components contain a small number of chromophores. Light scattering proceeds at the protein conglomerates of the lens. The lens protein amounts to about 90% of its dry weight and its concentration is about 0.2 to 0.4 g/mL, i.e., it is the greatest one for tissues. The lens proteins are specific for the given tissue; they are called crystallines. This is due to the fact that in the nineteenth century they considered the lens as a crystal similar to ice. However, only the near-order degree exists in the lens and it appears to be sufficient for ensuring transparency.

The idea of the near-order degree in the organization of the lens proteins that provides for its transparency was first proposed by Benedek.[213] The main role among the ocular lens proteins is played by water-solved α crystallins whose shape is close to the spherical one with a diameter of about 17 nm. The studies of lens transparency, along with their major value, are of importance in connection with a wide propagation of such phenomenon as turbidity; the cataract. The structural bases of the cataract have remained an object of intense research for many years.[213,232,233]

The method of x-ray small-angular scattering was used to examine the tissues of the ocular lens for the bull and the frog.[234] It was shown that different structural states of crystallins may exist in the lens. A small-angular diffraction maximum is inherent in the region for Bragg distances $D = 15$–20 nm for one of the states that is explained by the near order of macromolecular complexes of crystallins (α-crystallin). No maxima were observed for other states.

The 2-D Fourier analysis has an immediate application in the study of the microstructure of the ocular lens.[235] The Fourier method can be applied to the study of microstructural change as a function of differentiation, aging, or pathogenesis in the cytoplasm or extracellular matrix.

1.6.7 Fractal properties of tissues

Almost all material, excluding monocrystals, are disordered in one or another sense. Fractal geometry[236] regards an accident quantitatively and thus it enables one to describe such random systems as polymers, colloidal aggregates, and porous materials. The qualitative feature of fractal objects is the invariance of their main geometric peculiarities, such as the magnification variation in the microscope with varying scale (see Section 1.4). The fractal properties of scattering systems strongly affect their light scattering.[124] The same mass of particles may induce small scattering in a dense cluster and significantly greater scattering in the fractal one. The fractal structure is most clearly pronounced with scattering in the case of multiple scattering.[116] The peculiarities of multiple scattering at the fractals are caused by a slowly falling correlation of the particle density. The fractal effects at the multiple scattering are observed even for fractal clusters whose sizes are shorter than the wavelength.

Since the spatial distributions of the constituents of many types of tissues appear to satisfy the conditions of statistical self-similarity,[227,237] fractal analysis may potentially provide a much simpler foundation for the analysis of tissue. Statistical self-similarity implies that the object is composed of building blocks with inherent statistical regularities that can be described by power law. The correlations of a variety of tissues in the refractive indices exhibit characteristics of a random fractal with a Hurst coefficient between 0.3 and 0.5.[200]

The tissue structure can be represented as a multifractal composed of various fractal formation types.[221,237] For the bone tissue the main fractal elements are trabeculae (formations with flatly lying mineralized fibers), and osteons (regions with the spiral-like orientation of fibers raised at an angle of 30–60 deg).[221] The above fractal types form an architectonic multifractal network. The geometric dimensions of biofractals are sufficiently great (100–1000 μm). In many cases, the fractal geometry yields a key to understanding the scattering peculiarities of these objects.

Quantitative models of the micro-optical properties of biological tissues have potential applications in several areas of biomedical optics.

1.7 Light Scattering by Densely Packed Correlated Particles

Certain regularities exist in densely packed media with characteristic dimensions on the order of the wavelength between the phases of waves scattered by adjacent particles and it is necessary to sum the amplitudes of scattered waves under the calculation of light scattered by the system with

regard to phase relations. The interference interaction may result both in a varied total amount of scattered energy and an altered angular dependence of scattered light as compared with similar quantities for a system of noninteracting particles. The alteration of angular dependences can be particularly noticeable for biosystems since particle sizes are comparable with the light wavelength. In concentrated optically thick disperse systems a substantial role may also be played by the effects of multiple scattering.

The softness of the biotissue scattering particle makes it possible to restrict oneself with the single-scattering approximation in a number of cases. To correctly exploit this approximation, we need the optical thickness of the object under study to be small enough, i.e., $\tau < 0.1$.[1] For strongly scattering structures this means a necessity to restrict oneself with thin histological sections.

The theory of light scattering by densely packed correlated particles is principal for such tissues as eye lens, cornea, and sclera. This theory explains the transparency of the cornea and normal eye lens as well as their turbidity by pathology and opacity of the sclera. It was noted in Section 1.6. Besides, the theory of light scattering by densely packed correlated particles should also be important for investigations of subepithelial tissues, whole blood, and other bio-objects, which have been explored in other chapters in this book.

The characteristic relations between the scatterer sizes in tissues and the wavelength of visible light are close to similar relations between the liquid molecules and the x-ray radiation. Moreover, the near-order degree of order in the arrangement of bioparticles resembles that of the molecule degree of order in the liquid. Thus, the description of light propagation in tissues relies, to a significant extent, on the methods for describing the x-ray radiation diffraction in the liquid.[238] The light scattering in the correlated disperse systems operates with the statistical characteristics of these systems. The function of radial distribution $g(r)$ is just such a statistical characteristic of the spatial arrangement of scatterers.

1.7.1 Pair distribution function $g(r)$

Consider N spherical particles in a finite volume. To statistically describe their spatial arrangement a pair distribution function $g(r)$ may be employed.[239] The pair distribution function $g_{ij}(r)$ is proportional to the conditional probability of finding a particle of type j at the distance r from the origin given that there is a particle of type i at the origin (Fig. 1.11). For noninterpenetrable spheres, the interparticle forces are zero except for the fact that two particles cannot interpenetrate each other.

The arrangement of particles in a densely packed system is not entirely random. The near-order degree of order is observed in their arrangement; they are more ordered the greater the density of scattering centers and the narrower their distribution in size; and $g(r) = 0$ near the origin of coordinates in the

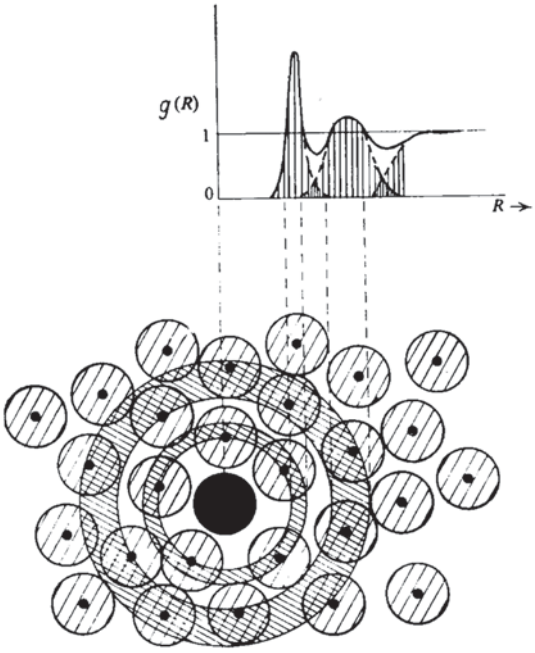

Figure 1.11 Diagram of radial distribution function $g(r)$ that is proportional to the probability of particle detection at a certain distance r from an arbitrarily fixed particle.[239]

region with a radius on the order of effective particle diameter that points to the interimpenetrability of a particle. Function $g(r)$ has a few maxima whose positions correspond to distances from the chosen particle to its first, second, etc. neighbors. Nonzero values of minima are indicative of a particle's migration between various coordination spheres. It is obvious that correlation between the pairs of particles should be degraded with growing r, hence $\lim_{r\to\infty} g(r) = 1$. Function $g(r)$ is the relation of the local density in the given sample, i.e., it is a probability to reveal a scatterer at the specified distance from the center chosen.

The medium composed of N scatterers considered here is analogous to an ensemble of mixture of L types of particles in the study of statistical mechanics, by considering the dynamics and positions of the particles with regard to the interparticle forces. Studies have been made in obtaining the pair distribution functions using various approximate theories. One of the important results is based on the Percus–Yevick (PY) approximation. As applied to a model of hard spheres distributed in a 3-D space, there exists the analytical solution of this equation. To find the function of radial distribution, the MC method is also used.

The solution of the Ornstein–Zernice equation for the case of single species has been solved by Wertheim.[240] For the case of two species, the solution can be found in the paper by Lebowitz.[241] For the case of general L species, the solution is obtained by Baxter based on a generalized

Wiener–Hopf technique.[21,242] The polydispersity of the real system is approximated by an L-step distribution function.

For monodisperse systems containing spherical particles with diameter d, $g(r)$ would be presented in the approximation of solid spheres, as follows:[243]

$$g(r) = 1 + \frac{1}{4\pi f}\int_0^\infty \frac{H_3^2(z)}{1 - H_3(z)}\frac{\sin zx}{zx} z^2 dz, \quad \text{for } x > 1, \tag{1.93}$$

where $x = r/d$,

$$H_3(z) = 24f \cdot \int_0^1 c_3(x)\frac{\sin zx}{zx} x^2 dx, \quad c_3(x) = -\alpha - \beta x - \delta x^3, \tag{1.94}$$

$$\alpha = \frac{(1+2f)^2}{(1-f)^4}, \quad \beta = -6f\frac{(1+\frac{1}{2}f)^2}{(1-f)^4}, \quad \delta = \frac{1}{2}f \cdot \frac{(1+2f)^2}{(1-f)^4}, \tag{1.95}$$

where f is the volume fraction occupied by particles.

1.7.2 Light scattering by a system of particles in the single-scattering approximation

Let us consider the light scattering by a system of N spherical particles. In general, the field affecting a particle in this system differs from the field of incident wave E_{inc} in that it also contains the total field of adjacent scatterers. Within the single-scattering approximation (Born's approximation), the field affecting the particle does not essentially differ from that of the initial wave. Regarding double scattering as a field affecting the particle, one needs to take the sum of the initial field and the single-scattered field, and so on.[20] In as much as biological particles are optically soft, the use of the single-scattering approximation often yields satisfactory results for the systems of these particles.

The field scattered by a particle with the center defined by radius-vector r_j differs from that scattered by a particle, which is placed at the origin of coordinates by a phase multiplier characterizing the phase shift of waves. This phase difference is $\frac{2\pi}{\lambda}(\mathbf{s}_0 - \mathbf{s})\mathbf{r}_j$, where $\mathbf{s}_0$ and $\mathbf{s}$ are the unit vectors of the directions of incident and scattered waves. The difference of these vectors is called the scattering vector $\mathbf{q}$, and

$$\mathbf{q} = \frac{2\pi}{\lambda}(\mathbf{s}_0 - \mathbf{s}). \tag{1.96}$$

Taking into account that the wave vector module is invariable with elastic scattering, the value of the scattering vector is found as follows:

$$q = 2\frac{2\pi}{\lambda}\sin(\theta/2), \tag{1.97}$$

where θ is the angle between directions $\mathbf{s}_0$ and $\mathbf{s}$, i.e., it is the scattering angle. The amplitude of a wave scattered by the system of N particles will be

$$E_s = \sum_{j=1}^{N} E_{sj} = \sum_{j=1}^{N} E_{0j} e^{i\mathbf{q}\mathbf{r}_j}, \tag{1.98}$$

where E_{0j} is the amplitude of scattering by an isolated particle. The intensity of single scattering for the given spatial realization of the N particle arrangement is

$$I = |E_s|^2 = \sum_{j=1}^{N} E_{oj} \sum_{i=1}^{N} E_{0i}^{*} e^{i\mathbf{q}(\mathbf{r}_j - \mathbf{r}_i)}. \tag{1.99}$$

For real systems, the mean scattering intensity by an ensemble of particles is measured due to thermal particle motion, finite measuring time, and finite area of a photodetector, as

$$<I> = <\sum_{j=1}^{N} \sum_{i=1}^{N} E_{oj} E_{0i}^{*} e^{i\mathbf{q}(\mathbf{r}_j - \mathbf{r}_i)}> . \tag{1.100}$$

The French brackets show the averaging over all possible arrangement configurations for the particles of the system. This equation presents a sum of two contributions for a noncoherent scattered intensity. One of them defines the light distribution on the assumption that there is no interference of light scattered at various particles. Another term regards the interference effect on the light field structure and depends on the degree of order in the arrangement of particles that is characterized by the radial distribution function $g(r)$. For an isotropic system of identical particles, we may write

$$<I> = N|E_0|^2 S_3(\theta), \tag{1.101}$$

$$S_3(\theta) = \left\{ 1 + 4\pi\rho \int_0^R [g(r) - 1] r^2 \frac{\sin qr}{qr} dr \right\}, \tag{1.102}$$

where $q = \frac{4\pi}{\lambda} \sin\frac{\theta}{2}$. Quantity $S_3(\theta)$ is the so-called structure factor. This structure factor describes the variation of the angular scattering intensity distribution which appears with a higher particle concentration. Within the approximation of hard spheres the structure factor is represented in the form

$$S_3(\theta) = 1/[1 - H_3(q)], \tag{1.103}$$

where $H_3(q)$ is defined by Eq. (1.94).

With small concentrations, we may make use of the approximation of excluded volume where $g(r) = 0$ with r being shorter than the particle diameter and having a unit value over long distances. In this approximation,

the structure factor for a system of spherical particles takes the form that was first found by Dirac:

$$S_3(\theta) = 1 - f\Phi(qa), \tag{1.104}$$

where a is the particle radius, and $\Phi(qa)$ is the function defined by

$$\Phi(qa) = \frac{3(\sin qa - qa\cos qa)}{(qa)^3}. \tag{1.105}$$

Quantities a and λ can be on the same order for tissues, thus the first maximum of this function would be observed at angles achieving tens of degrees. Function $\Phi(qa)$ modulates the angular dependence of scattering intensity by diminishing its values at small angles and generating a diffusion ring at angles θ corresponding to the function $\Phi(qa)$ maximum.

Within a very small concentration of inhomogeneities, the structure factor is nearly a unit and the intensity of scattering by a disperse medium is essentially a sum of the contributions of independent inhomogeneities.

The structure factor changes slightly as a function of scattering angle for particles whose dimensions are much smaller than the wavelength, and the interference interaction in the systems of soft particles reveals itself mainly in a uniform decrease of scattering intensity in all directions (Fig. 1.12). For systems of large particles, the structure factor differs noticeably from a unit only in the region of small scattering angles where it is of an oscillating nature. The interference interaction of scatterers in one angular band reduces the scattering intensity and in the other band, the scattering intensity is raised as compared with that for a system of the equivalent number of independent particles (Fig. 1.13).

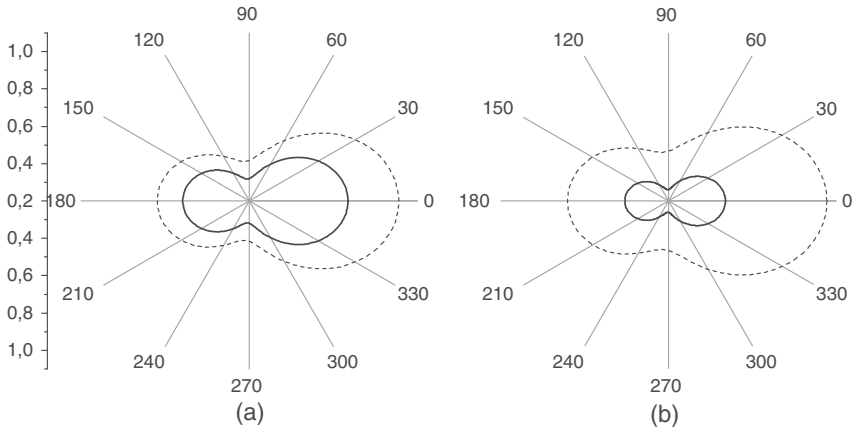

Figure 1.12 Angular scattering intensity dependences for a system of small interacting spherical particles of 50 nm in radius; $m = 1.105$, $\lambda = 633$ nm, and the volume fractions $f = 0.04$ (a) and $f = 0.1$ (b). The dotted lines indicate independent particles.

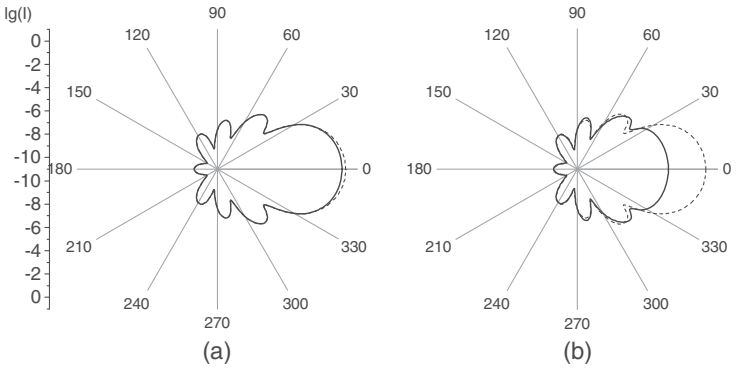

Figure 1.13 Angular scattering intensity dependences for a system of large interacting spherical particles of 500 nm in radius; $m = 1.105$, $\lambda = 633$ nm, and the volume fractions (a) $f = 0.04$ and (b) $f = 0.4$. The dotted lines indicate particles.

For the case where light is incident normally to the axes of infinitely long identically aligned cylinders with radius a, the structure factor is defined within the approximation of single scattering, as follows:

$$S_2(\theta) = \left\{1 + 8f \int_0^R [g(r) - 1] J_0\left(\frac{2\pi a}{\lambda} r \sin\theta\right) dr\right\}. \tag{1.106}$$

As the light is incident perpendicular to the cylinder axis, the scattered light propagates only in the direction perpendicular to the axis.

1.7.3 Angular characteristics for polarized light scattering

The angular dependence of the light scattering intensity of the systems of spherical and cylinder particles within the single-scattering approximation is described by Eqs. (1.101), (1.102), and (1.106). The structure factor altering the angular dependence of scattered light is defined by the statistical characteristics of the spatial particle arrangement, and it is independent of the state of light polarization. The angular dependences of all scattering matrix elements of identical particles are multiplied by the same quantity as the result of interference interaction within the single-scattering approximation. Consequently, the light scattering matrix (LSM) for this system coincides with that of an isolated particle under the commonly used normalization for the magnitude of its first element.

Unlike monodisperse systems, the normalization of matrix elements by M_{11} does not eliminate the influence of the structure factor on the angular dependences of matrix elements for differently sized densely packed particle systems.[244] As a practical matter, of particular interest are binary systems formed by a great number of small particles and a small number of coarse particles. This problem arises with the diagnostics of initial stages of protein coagulation, in particular, with the early diagnostics of the ocular lens turbidity.[244]

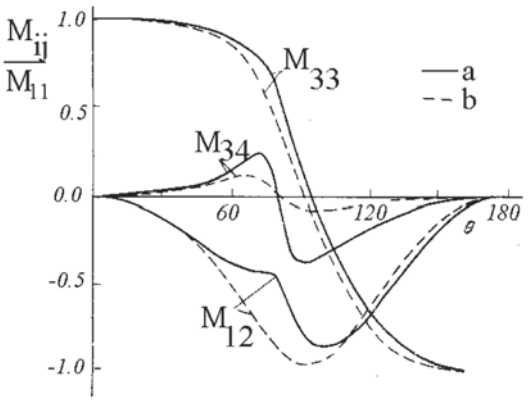

Figure 1.14 The calculated normalized LSM angular dependences of binary mixture of small and large spherical particles ($d_1 = 60$ nm, $d_2 = 500$ nm; $f_1 = 0.3$, $f_2 = 0.02$; $m = 1.107$; and $\lambda = 633$ nm): (a) interacting and (b) independent particles.

Figure 1.14 depicts the calculated results for the LSM of a mixture of spherical particles of diameters $d_1 = 60$ nm and $d_2 = 500$ nm for the volume fractions (spatial volume to total scattering system volume ratio) $f_1 = 0.3$ and $f_2 = 0.02$. For comparison, the LSM angular dependences of the same binary mixture—shown in Fig. 1.14 by a dashed line—have been calculated neglecting cooperative effects (within the assumption of an entirely arbitrary arrangement of scattering particles). The relative index of refraction $m = 1.07$, and the light wavelength is 633 nm.

It is seen from Fig. 1.14 that the normalized LSM of a dense binary mixture is substantially altered due to the interference interaction. The high concentration of small particles is responsible for the degree of order in their arrangement followed by a lower intensity of scattering in all directions except the direction of straightforwardly propagating light. As a consequence, the results of the solution of the inverse problem for the experimental LSM of dense particle mixture that were obtained at neglecting the cooperative effects should yield an overestimated value for the relative fraction of large particles. The LSM variations due to the cooperative effects are of a more complicated nature for a binary system whose two components are sized on the order of the wavelength of incident light and they could not be interpreted so uniquely, as in the preceding case. Numerical estimates for binary systems of different compositions show[244] the considered effects to be of the most crucial importance for the LSM in the visible region for the mixtures of particles with $d_1 < 200$ nm and $d_2 > 250$ nm.

1.7.4 Spectral characteristics of scattering systems

The scattering strongly deforms the spectral biotissue characteristics since the extinction of transmitted light is defined not only by the absorption coefficient as a function of the wavelength, but also by a light fraction taken from the

beam because of the scattering. The latter process complexly depends on the wavelength, structure, and size of particles.

The spectrum of collimated transmission of a disperse layer is interpreted as a spectral dependence of a weaker coherent component of light. Finding the coherent component of light, scattered at a system of inhomogeneities correlated in the space, is a complicated physical task exhibiting all of the difficulties inherent in the problem of light propagation through a system of many bodies.[243] Assuming that the intensity of the coherent light component is reduced with a longer distance by the exponent law due to scattering and absorption, the transmission of a disperse layer of thickness x would be described using the Bouguer–Beer–Lambert law

$$T = \exp(-\rho\sigma_e x), \tag{1.107}$$

where ρ is the particle density, and σ_e is the extinction cross section for a single particle of the layer. For low particle concentrations, it is equivalent to the extinction cross section of an independent particle. For greater f values, the quantity σ_e is determined not only by the properties of a single inhomogeneity but also by their volume concentration. Within the assumption that the absorption cross section is independent of the packing density, σ_e may be calculated as a sum of the absorption cross section of the independent particle and the scattering cross section obtained by taking into account correlation of the scatterers.

With the knowledge of the angular scattering intensity distribution of the system of particles, one would calculate the scattering cross section for a single particle in the system. Having integrated the scattering intensity over all directions in the space, the total amount of energy scattered by the system can be found. The scattering cross section for the system of spherical particles is obtained similar to Eq. (1.13), however, the intensity must be calculated by using the structure factor.

The scattering cross section for the system of cylinder particles, illuminated by a plane wave incident in the direction normal to the cylinder axis, is defined by numerically integrating over all possible scattering directions in a plane perpendicular to the cylinder axis

$$\sigma_s \propto \int_0^{2\pi} I(\theta)d\theta. \tag{1.108}$$

Dividing σ_s by the particle number N, one may find the scattering cross section for a single particle of the system. The result obtained may differ substantially from the scattering cross section of an independent particle.

Even the scattering cross-section for an independent particle sized on the order of a wavelength has a very strong nonmonotonous dependence on the wavelength. Effects associated with dense packing also have a substantial

dependence on the wavelength. As a result, the transmission spectra for a system of identical particles can differ highly depending on the packing density and the degree of order. A clear example of such a dependence is presented by the transmission spectra of the cornea in the norm and with its turbidity caused by a disrupted spatial degree of order and by appearing regions denuded of fibrils, the so-called lakes.[245]

The extinction of a collimated incident beam due to complex angular/wavelength dependence of the scattered light in the dense systems, even for nonabsorbing ones, would result in substantial differences in the transmittance in different spectral regions. The values of the real and imaginary part of the indices of refraction depend weakly on the wavelength far from the absorption bands and may be assumed to be constant at calculations. In systems of small nonabsorbing particles, the interference interaction causes the shift of the short-wavelength transmission spectrum boundary to a smaller wavelength and a slightly greater steepness of the spectrum (Fig. 1.15). If a scattering system is formed by particles whose sizes are comparable with the wavelength, then the spectrum of this system would be nonmonotonous even with no absorption.

For particle systems with absorption, in the vicinity of the absorption bands, the real and imaginary parts of the complex index of refraction of the particles demonstrate pronounced spectral dependences. Figure 1.16 illustrates the transmission spectra calculated for two systems of differently sized particles with the refractive index described by the Lorentz contour.[12] The scattering deforms the symmetric contour of the absorption line and the spectrum appears different for systems of differently sized particles with varying packing density.

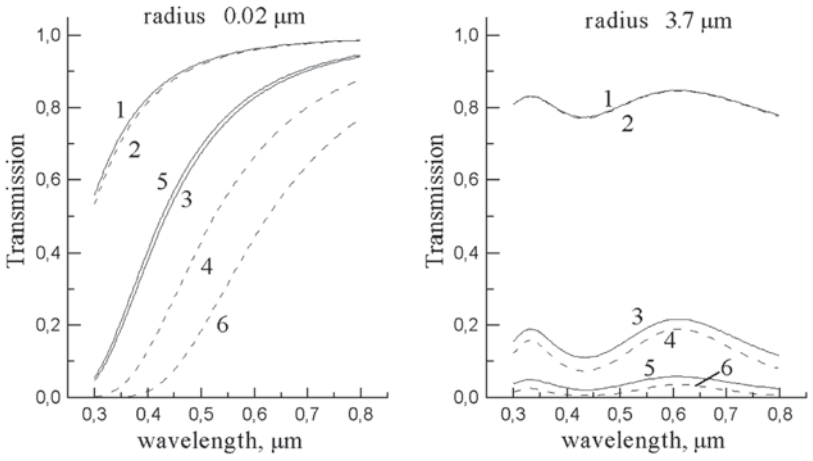

Figure 1.15 Calculated transmission spectra for the systems of nonabsorbing interacting particles (solid lines) and at approximation of noninteracting particles (dashed lines); $m = 1.1$, $f = 0.01$ (1, 2), $f = 0.1$ (3, 4), and $f = 0.2$ (5,6).

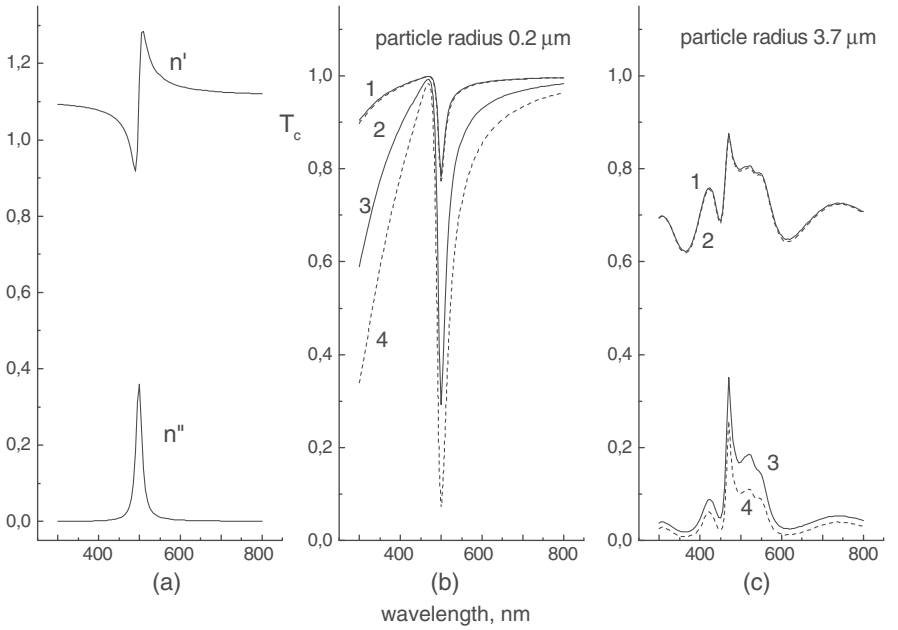

Figure 1.16 Spectral dependence of real and imaginary part of the relative complex index of refraction for (a) particles with the Lorentz contour center at $\lambda = 500$ nm; transmission spectra for the slab of thickness (b) $L = 3$ mm and (c) 0.1 mm of the disperse systems of particles (solid lines); independent particles (dotted lines); $f = 0.01$ (1,2) and $f = 0.1$ (3,4).

For example, the transmission spectrum for whole blood differs substantially from that for the hemolyzed blood because in whole blood, hemoglobin is localized in erythrocytes, which are strong light scatterers.[6] Therefore, it is much easy to estimate blood saturation with oxygen by using the absorption spectra for the hemolyzed blood.[246] A detailed review of spectral characteristics for various tissues and blood is given in Ref. 9.

For the densely packed system of large optically soft particles within the approximation of hard spheres and at neglecting of mutual particle reradiation, the following equation was obtained for the transmission of a layer with thickness L that accounts for coherent effects:[247]

$$T_c = \left[1 - \frac{2b}{(1+b)} \cdot \frac{\sigma_e}{\pi \cdot a^2} + \frac{b^2}{(1+b)^2} \cdot \frac{2\lambda}{\pi \cdot a^3} \sigma_s I_1(0)\right]^{L/2a}, \qquad (1.109)$$

where $b = 1.5f \times \exp(1.5f)$, and $I_1(0)$ is the intensity of forward scattering at a single particle of diameter $2a$. This formula is transformed into the Bouguer–Beer–Lambert law for the scattering systems of noninteracting particles under the rarefaction of the scattering layer.

Not only coherent weakened light but also a portion of noncoherently scattered light is usually recorded in real experiments because of the finite

angular aperture of the receiving unit. For this reason, a transmittance called the instrumental transparency found experimentally is somewhat different from the coherent transmission T_c.

For the first time, the approximation regarding the near-order degree of order has been used to describe the propagation of light in a tissue in Refs. 224, 228, and 245, with calculating the transmission spectra of the cornea. The near order in the arrangement of scattering particles and the related interference interaction of scattered light are the cause of the high transparency of the human eye optical tissues in their normal state.[248,249]

The spectral characteristics vary most strongly with high packing densities, as the volume fraction occupied by particles exceeds 50%. For these dense systems, the considered approximation of single scattering is incorrect and it is necessary to account for the effects of the reradiation of particles.

Unlike the transmission spectra, the spectral dependences of the intensity of light scattered in different directions are poorly studied. This is related, on the one hand, to experimental difficulties due to the need for standard spectral devices to be rearranged. On the other hand, a comparison of different experimental results is difficult because the form of the scattering spectrum depends substantially on the geometry of the system under study. Nevertheless, the scattering spectra are of great interest. The authors of Ref. 250 measured the absorption and scattering spectra of the chest muscle of a chicken in the visible range. The scattering spectra visually define the observed tissue color, and they can be employed for express estimating of tissue condition.

One traditional method for eye ocular lens diagnostics assumes the observation of varying color characteristics for light scattered at an angle. The qualitative analysis of composition alteration for the scattering particles of the eye lens with age by measuring the scattering spectra[251] is given in Ref. 252. The analysis of spectral scattering characteristics lies in the basis of the method for measuring the skin erythema.[253] Reference 254 describes some applications of the "scattering spectral method" along with viscosimetry and sedimentation data to the study of *Yersinia pestis* capsular protein.

1.7.5 Consideration of multiple-scattering effects in a system of densely packed particles

In real disperse systems containing a great number of particles, multiple scattering takes place. The spatial correlation of single inhomogeneities results in a necessity to consider the interference of multiple scattered waves.[20,247] In a case when effects of particle reradiation in the densely packed disperse system are not negligible, the distinction of an effective field in a medium from the incident wave field is induced. Under this condition, the approach based on the statistical theory of multiple wave scattering seems to be most

promising for describing the collective interaction between an ensemble of particles and electromagnetic radiation.[20,247]

The rigorous theory of multiple wave scattering is constructed on the basis of fundamental differential equations for the fields combined with a statistical approach.[20] The resulting field in any point of the space is displayed as the sum of the incident wave fields and all possible multiple scattered waves with regard to their phases. The total field $E(r)$ at the point r is the sum of the incident field and scattered fields from all particles [Eq. (1.43)]

Twersky has derived a closed system of integral equations describing the processes of multiple scattering.[255] A rigorous solution in a general form has not been found yet for this problem. For its solution, various approximations whose efficiency is determined for every particular case should be exploited. One of the most efficient approximations to describe tissue optics is a so-called quasi-crystalline approximation proposed for densely packed systems.[256]

Averaging in Eq. (1.43) over different configurations of the system yields an infinite set of equations. The quasi-crystalline approximation corresponds to the condition when this set is limited to the second step. The obtained closed system of equations for the effective field is reduced to a system of linear equations by expanding in terms of vector spherical or cylindrical harmonics. The explicit form of coefficients is quite cumbersome for the obtained system.[21,257] Coefficients involve the radial distribution function, taking into account correlation of the particle arrangement, and the coefficients of Mie row expansion for a single particle. The equality to zero for the determinant of the system of linear equations yields the dispersion relation for the effective propagation constant k_{eff} in this medium.[258] For the systems of particles whose sizes are small compared to the wavelength, the expression for k_{eff} has the view[21]

$$k_{\text{eff}}^2 = k^2 + \frac{3fy}{D}k^2\left[1 + i\frac{2}{3}\frac{k^2a^2y}{D}S(\theta = 0)\right], \tag{1.110}$$

where

$$y = \frac{n_1^2 - n_0^2}{n_1^2 + 2n_0^2}, \quad D = 1 - fy, \quad S(\theta = 0) = \frac{1}{1 - H_3},$$
$$H_3 = -24f\left(\frac{\alpha}{3} + \frac{\beta}{4} + \frac{\delta}{6}\right),$$

f is the volume fraction of particles with the refractive index n_1 embedded into ground medium with $n = n_0$, and α, β, and δ are defined from the approximation of the hard spheres [Eq. (1.95)]. The calculated effective index of refraction $n_{\text{eff}} = n'_{\text{eff}} + in''_{\text{eff}}$ is complex, even if particles and ground medium surrounding them exhibit no intrinsic absorption. The imaginary part of the effective index of refraction n''_{eff} describes the energy loss of the incident

plane wave due to scattering in all directions. The transmittance of the scattering layer with thickness x is defined as

$$T = \exp\left(-\frac{4\pi}{\lambda} n''_{\text{eff}} x\right), \tag{1.111}$$

where $(4\pi/\lambda)n''_{\text{eff}}$ is the extinction coefficient, and n''_{eff} decreases with a higher wavelength and nonmonotonously depends on the particle concentration. For small particle concentration, the transmittance of the layer decreases with particle concentration increase (increase of their volume fraction f); however, due to particle pair correlation starting from $f \approx 0.1$, a so-called clearing effect takes place. The real part of the effective index of refraction in this approximation is essentially independent of the wavelength and alters monotonously with growing particle concentration to approach the refractive index of the particle material. The near order appearing in the scatterers' arrangement with their greater concentration not only provides for conditions for the manifestation of the secondary scattered wave interference,[259] it also affects the character of propagation of noncoherent multiple scattered light. This may be accompanied by the so-called concentration effects of darkening and clearing.[259]

The optical softness of tissues enables calculations to employ an expansion by scattering multiplicities with restricting to low orders. In Ref. 260, an expression for the effective index of refraction of the eye cornea modeled by the system of cylinder scatterers was obtained in the framework of expansion by scattering multiplicities. The effects of polarization anisotropy were analyzed with respect to the double scattering contributions.

The problem of scattering and absorption of electromagnetic radiation by the composite medium is so complicated that the exact solution of Maxwell's equations under the appropriate boundary conditions is unpractical.[6] For this reason, it seems to be attractive to have a way to determine some averaged optical properties of heterogeneous materials that would enable us to treat the heterogeneous material in the same way that we consider homogeneous media. Based on the theory of multiple wave scattering, various expressions were derived for the effective parameters of a disperse medium.[18,261]

Using a definite set of assumptions concerning the shapes of inclusions and the topology of a mixture, one can obtain the appropriate analytical expression for an effective dielectric constant as a function of volume fraction f and dielectric constants ε_1 and ε_0 of individual components (see Section 1.2) or corresponding indices of refraction, $n_1 = \sqrt{\varepsilon_1}$ and $n_0 = \sqrt{\varepsilon_0}$. The simple mixing rules often used in various applications include volume averages of the dielectric constants or indices of refraction[11]

$$n_{\text{eff}} = f n_1 + (1 - f) n_0. \tag{1.112}$$

Using the theory of multiple scattering, Twersky[262] succeeded in deriving the approximate expressions for absorption μ_a and scattering μ_s coefficients with describing the light scattering in the blood. The blood hematocrit H is related to the erythrocytes concentration ρ and to the volume of one erythrocyte V_e by the following ratio:[6]

$$\rho = H/V_e. \tag{1.113}$$

Thus, the absorption coefficient μ_a is

$$\mu_a = (H/V_e)\sigma_a. \tag{1.114}$$

For sufficiently small values of H ($H < 0.2$), the scattering coefficient is given by a similar equation

$$\mu_s = (H/V_e)\sigma_s. \tag{1.115}$$

For $H > 0.5$, the particles become densely packed, and the medium is almost homogeneous. In this case, the blood may be considered as a homogeneous medium containing hemoglobin in which scattering particles are included from plasma surrounding red blood cells (RBCs). Within the limits of $H \to 1$, "plasma particles" disappear, and the scattering coefficient should tend to zero. This results in the following approximate equation for μ_s:

$$\mu_s = \frac{H(1-H)}{V_e}\sigma_s, \tag{1.116}$$

where coefficient $(1-H)$ regards the scattering termination with $H \to 1$. Dense packing ($H = 1$) is unattainable, and the packing influence should not be described by the simple function $(1-H)$. For example, if the particles are the hard spheres, H may not exceed 0.64. Then we should take[262]

$$\mu_s = (H/V)\sigma_s F(H), \tag{1.117}$$

where function $F(H)$ must monotonously decrease from a unit with $H = 0$ to zero with a certain limit value of H. Reference 263 presents the following dependence of scattering coefficient μ_s on the hematocrit H for thin blood layers

$$\mu_s \approx H(1-H)(1.4-H). \tag{1.118}$$

1.7.6 Birefringence of a system of anisotropic particles

Besides the crystal birefringence caused by the anisotropic properties of molecules they contain, there also exists a so-called birefringence of the form.[30] The latter phenomenon may be observed in an ordered system of particles made from an optically isotropic material whose sizes are great compared to those of molecules but are small with respect to the wavelength.

The difference of refractive indices for two orthogonal states of linear polarization of an incident plane wave at light propagation in a system of thin dielectric plates is described by[30]

$$n_e^2 - n_o^2 = -\frac{f(1-f)(n_1 - n_m)}{(1-f)n_m^2 + f \cdot n_1^2}, \tag{1.119}$$

where f is the volume fraction of plates, and n_1 and n_m are the refractive indices of plates and the surrounding medium, respectively. This implies that this system behaves like a negative single-axis crystal with its optical axis being normal to the plate surface. Wiener[30] succeeded in obtaining the following expression for a system of thin cylinder rods with $f \ll 1$

$$n_e^2 - n_o^2 = \frac{f(1-f)(n_1^2 - n_m^2)^2}{(1+f)n_m^2 + (1-f)n_1^2}, \tag{1.120}$$

where f is the volume fraction of rods, and n_1 and n_m are the refractive indices of rods and the surrounding medium, respectively. This difference is always positive and, thus, the system formed by thin cylinders constitutes a positive single-axis crystal. This means that the rod system behaves like the positive single-axis crystal with its optical axis being in parallel with the rod axes. Equation (1.120) is consistent with the results obtained by Rayleigh[264] for a system of parallel cylinders, even if f is not very small compared with a unit, provided that the difference between the refractive indices n_1 and n_m is small (optically soft particles).

The author of Ref. 265 has derived a more general expression that describes the birefringence within the limit of thin cylinders for an arbitrary value of f:

$$n_e - n_o = \frac{f(1-f)(n_1 - n_m)^2}{(1-f)n_m + f n_1}. \tag{1.121}$$

This equation corresponds to the Wiener equation (1.120) with $|n_1 - n_2| \ll 1$.

The form birefringence is used in biological microscopy. The sign of the observed difference points to the particle shape being close to that of the rod or the plate and, if n_1 and n_m are known, one can assess the volume fraction of the particles. To distinguish between the form birefringence and the birefringence of the particle material, one is able to change the refractive index of the base material. The form birefringence vanishes at $n_1 = n_m$. Linear dichroism, i.e., different wave attenuation for two orthogonal polarizations, is defined by the difference between the imaginary parts of effective indices of refraction of particles and surrounding medium. Depending on the relation between the size and the optical constants of the scatterers, this difference could be positive or negative.

1.8 Application of Radiative Transfer Theory to Tissue Optics

The classical radiative transfer theory (RTT) is found on energy consideration and serves as a basis for photometry. The initial development of the RTT is usually associated with the names of Bouguer and Lambert. Photometry operates with energy characteristics that describe the light detection capabilities by using quadratic detectors. The classical phenomenological theory of light transfer makes use of the pictorial concept of ray optics supplemented by a statistical assumption of fields being entirely mutually incoherent for rays propagating in different directions. This assumption allows one to summarize the average intensities of rays coming from the different directions ignoring the phase relations. This formulation is widely used in atmosphere optics,[266] the optics of photographic layers, and tissue optics.

In the classical theory of light transfer that considers the wave field as an ensemble of incoherent rays, the main notion is the radiation intensity (or brightness) $I(r,s)$ defining the mean energy flow dP through an area da which is concentrated in a solid angle $d\Omega$ near direction s in the frequency interval $(\nu,\nu + d\nu)$,

$$dP = I(r,s)\cos\theta da d\Omega d\nu. \tag{1.122}$$

This theory is valid for an ensemble of scatterers located far from one another and has been successfully used to work out some practical aspects of tissue optics. The governing differential equation of this theory is called the Boltzmann equation used in the kinetic theory of gases and in the theory of neutron transfer.[267] The main stationary equation of the RTT for monochromatic light has the form[6,9]

$$\frac{\partial I(\bar{r},\bar{s})}{\partial \bar{s}} = -\mu_t I(\bar{r},\bar{s}) + \frac{\mu_s}{4\pi}\int_{4\pi} I(\bar{r},\bar{s}')p(\bar{s},\bar{s}')d\Omega', \tag{1.123}$$

where $I(\bar{r},\bar{s})$ is the radiation intensity at point $\bar{r}$ in direction s, (W m^{-2}sr^{-1}); $p(\bar{s},\bar{s}')$ is the scattering phase function; and $d\Omega'$ is the unit solid angle in direction s'. It is assumed that there are no radiation sources inside the medium. Equation (1.123) with the appropriate initial and boundary conditions defines the behavior of the radiation intensity. Equation (1.123) refers to the energy balance in an infinitely small medium volume: the rate of variation for the radiation intensity along the beam is found by scattering in the given direction s from all other directions s' (integral term) and by attenuation due to scattering and absorption [term $-\mu_t I(r,s)$].

The phase function $p(\bar{s},\bar{s}')$ describes the scattering properties of the medium and is in fact the probability density function for scattering in the direction s' of a photon traveling in the direction s; in other words, it characterizes an elementary scattering act. If scattering is symmetric relative

to the direction of an incident wave, then the phase function depends only on the angle θ between directions s and s'.

The scattering indicatrix $p(\bar{s},\bar{s}')$ may be specified either as a table obtained by measuring or calculating, or as an analytical expression.

A portion of the radiation intensity that decreases due to scattering and absorption while passing through volume V containing scattering particles is called the attenuated incident intensity and satisfies the following equation:

$$\frac{\partial I_{ri}(\bar{r},\bar{s})}{\partial \bar{s}} = -\mu_t I_{ri}(\bar{r},\bar{s})\,. \tag{1.124}$$

Another portion, appearing in the medium due to scattering, is called the diffusion intensity. Since the total intensity

$$I(\bar{r},\bar{s}) = I_{ri}(\bar{r},\bar{s}) + I_d(\bar{r},\bar{s}) \tag{1.125}$$

satisfies Eq. (1.123), the diffusion intensity can be found from the equation

$$\frac{\partial I_d(\bar{r},\bar{s})}{\partial \bar{s}} = -\mu_t I_d(\bar{r},\bar{s}) + \frac{\mu_s}{4\pi}\int_{4\pi} I_d(\bar{r},\bar{s}')p(\bar{s},\bar{s}')d\Omega' + \varepsilon_{ri}(\bar{r},\bar{s}), \tag{1.126}$$

where $\varepsilon_{ri}(\vec{r},\vec{s})$ is the equivalent source function given rise by the attenuated incident intensity.[6] Equation (1.124) is the differential form of the Beer–Lambert–Bouguer law for the scattering medium with absorption. This means that the Beer–Lambert–Bouguer law is valid for any optical thickness for the attenuated incident intensity within the framework of the transfer theory. Deviations from this law, e.g., caused by dense particle packing and manifested as optical clearing or darkening at concentration change, are ignored by the RTT.

As the vector nature of the electromagnetic field is accounted for the radiation intensity should be replaced by an intensity matrix that describes not only the intensity, but also the polarization properties of radiation with μ_t and μ_s being matrix quantities as well. The order in which matrices are incorporated into the equations should be taken into account. The scalar equation (1.123) is exploited in optics to describe light radiation in cases where the polarization effects may be neglected.

The integro-differential equation (1.123) is too complex to be employed for the analysis of light propagation in scattering media directly. There are two approaches to the problem under study. With one of them, one proceeds to obtain a general solution with unknown coefficients, and then to find these coefficients by means of the appropriate boundary conditions. Another approach is in passing from the differential equations with specified boundary conditions to integral equations for the certain unknown functions. For simple geometries, the approach based on the integro-differential equation is widely

used. For complex geometries, it is often more convenient to proceed with the integral equations and to obtain their approximate solutions.

The exact solutions of the radiative transfer equation (RTE) (1.123) and of the integral equation for the beam intensity were obtained only for a small number of particular cases. Planar parallel geometry and isotropic scattering are the examples for which the solutions have been found and are written in the form acceptable for calculations. In practice, one would be forced to apply to approximate solutions in most cases.

We do not aim to describe all or most methods to solve the RTE; this is referred to the literature.[6,9,20,266,267] Instead, we will consider a few approximations that are often used in tissue optics and have a clear physical meaning.

1.8.1 Approximation methods for solution of the radiation transfer equation

1.8.1.1 The first-order approximation

For weak scattering, as the scattering medium is rarefied and the scattering volume is small, iteration may be used to solve the RTE. In the first approximation, the iterative solution yields the result known as the first-order approximation of the RTT.[6] In this approximation, it is assumed that the total intensity incident on the particles is approximately equal to the attenuated incident intensity that is known. Thus, the solution within the first-order approximation is[6]

$$I(\bar{r},\bar{s}) = I_{ri}(\bar{r},\bar{s}) + I_d(\bar{r},\bar{s}), \tag{1.127}$$

$$I_d(\bar{r},\bar{s}) = \int_0^s \exp[-(\tau-\tau_1)] \cdot \left[\frac{\mu_s}{4\pi} \int_{4\pi} I_{ri}(\bar{r}_1,\bar{s}')p(\bar{s},\bar{s}')d\Omega'\right] d\bar{s}', \tag{1.128}$$

where I_{ri} is the attenuated incident intensity, I_d is the diffuse intensity, and $\tau = \int_0^s \rho\sigma_e ds$, $\tau_1 = \int_0^{s_1} \rho\sigma_e ds$ are the optical pathlengths.

The so-called first-order solution is realized for optically thin and weakly scattering media ($\tau < 1$ and single-scattering albedo $\Lambda = \sigma_s/\sigma_e < 0.5$) when the intensity of the transmitting (coherent) wave is described by Bouguer's law [Eq. (1.2)]. Given a narrow beam (e.g., a laser), this approximation may be applied to optically denser tissues ($\tau > 1$, $\Lambda < 0.9$).

1.8.1.2 Diffusion approximation

With a longer optical path, the directional diagram of scattered light is broadened and at last it becomes almost isotropic: the scattered light "forgets" the direction of initial wave propagation in the depth regime. To describe this almost isotropic radiation, a diffusion approximation would be used that would appear to be significantly simpler than the original integro-differential

equation, since it is reduced to the solution of differential equations. Because of this, the diffusion approximation is widely used as an effective approach to account for multiple scattering.

As one derives the diffusion equation, one should pass from the RTE to an infinite system of equations for the coefficients of expansion of beam intensity I into a series over spherical harmonics. The reduction of this system results in the so-called P_L approximation, the simplest of which is a system of equations for four functions that are equivalent to the diffusion approximation. There exist also other means to derive the diffusion equations for the diffusion coefficient. All distinctions disappear, however, with passing to the limit of weak absorption, as it is valid for many tissues. This is easy to understand from the physics of the diffusion approximation.[20] Actually, the description of scattering as a certain diffusion process only becomes adequate if the scattering effects dominate upon the absorption ones. Also, the diffusion approximation does not allow one to describe boundary effects manifesting themselves near the boundaries where the radiation "has not yet forgotten" the boundary and initial conditions.

The diffusion theory provides a good approximation in the case of small scattering anisotropy factor $g \leq 0.1$ and large albedo $\Lambda \to 1$. For many tissues, $g \approx 0.6$ to 0.9 and can be as large as 0.990–0.999 for blood.[9,218] This significantly restricts the applicability of the diffusion approximation. It is argued that this approximation can be used at $g < 0.9$ when the optical thickness τ of an object is of the order 10–20. However, the diffusion approximation is inapplicable for an input beam near the object's surface where single- or low-step scattering prevails.

The first-order approximation is valid only when the volume density, equal to the relation between a volume occupied by the particle and the entire volume of the medium, is substantially less than 1%. If the volume density is much greater than 1%, the diffusion approximation provides for good results. For volume density on the order of 1%, neither the near-order approximation nor the diffusion approximation can be valid, and we need to solve the RTE.

1.8.1.3 Small-angular approximation

The incident wave may be represented as a narrow collimated beam in many cases of laser diagnostics of tissues. Examples are the determination of bacteria concentration in liquids using a laser beam,[268] and detection of blood oxygen saturation by means of an optical fiber catheter.[246]

For the case of large scattering particles whose diameters are comparable or greater than the wavelength, the scattering intensity in a narrow sector of angles in the forward scattering direction is high. This enables the description of collimated beams to be simplified significantly by using a small-angular approximation, which is applicable for short propagation routes where the beam remains sufficiently strongly collimated. The RTE in the small-angular

approximation allows for an exact solution, however, the solution looks quite cumbersome and not friendly for numerical calculations. A simpler approximation corresponds to the consideration of the scattered light diffusion in angular variables.

1.8.1.4 Flux theory

The radiation intensity I itself is not often of interest but instead its integrals yielding the energy characteristics of the radiation field is used. If illumination is diffuse and the medium is sufficiently turbid providing the light diffusion scattering, experimental results are well described by the two-flux Kubelka–Munk theory.[9] This theory relies on a model of two light fluxes propagating in the forward and backward directions. The extension of two-flux Kubelka–Munk theory to a four-flux theory makes it possible to describe a collimated beam incidence onto the medium. The four-flux model[6,269] is actually two diffuse fluxes traveling to meet each other (Kubelka–Munk model) and two collimated laser beams, the incident beam and the beam reflected from the rear boundary of the sample.

A seven-flux model is the simplest 3-D representation of scattered radiation and an incident laser beam in a semi-infinite medium.[270] Of course, the simplicity and the possibility of expeditious calculations of the radiation dose or rapid determination of tissue optical parameters (solution of the inverse scattering problem) are achieved at the expense of accuracy.

There exist various numerical procedures to solve the RTE. A more exact solution of the RTE is possible using the discrete ordinates method (multiflux theory) in which Eq. (1.123) is converted into a matrix differential equation for illumination along many discrete directions (angles).[6] The solution approximates an exact one as the number of angles increases. Many computer programs are available to solve the RTE under different conditions.[23]

1.8.1.5 Vector radiative transfer equation

As it was already shown, the majority of tissues are turbid media showing a strong scattering and much less absorption (up to two orders of magnitude fewer than scattering in the red and NIR). Moreover, in their natural state (nonsliced), tissues are rather thick. Therefore, multiple scattering is a specific feature of a wide class of tissues.[9,271–275]

Polarization effects at light propagation through various multiple-scattering media, including tissues, are fully described by the vector RTE (VRTE).[9,268,276–291] The RTT originated as a phenomenological approach based on considering the transport of energy through a medium filled with a large number of particles and ensuring energy conservation. This medium, composed of discrete, sparsely, and randomly distributed particles, is treated as continuous and locally homogeneous. In the framework of the RTT, the scattering and absorption of the small volume element follow from the

Maxwell equations and are given by the incoherent sums of the respective characteristics of the constituent particles; the result of scattering is not the transformation of a plane incident wave into a spherical scattered wave but, rather, the transformation of the specific intensity vector (Stokes) of the incident light into the specific intensity vector of the scattered light.[56]

For macroscopically isotropic and symmetric plane-parallel scattering media, the VRTE can be substantially simplified as[56]

$$\frac{d\mathbf{S}(\bar{\mathrm{r}},\vartheta,\varphi)}{d\tau(\bar{r})} = -\mathbf{S}(\bar{\mathrm{r}},\vartheta,\varphi) + \frac{\Lambda(\bar{\mathrm{r}})}{4\pi}\int_{-1}^{+1} d(\cos\vartheta')\int_{0}^{2\pi} d\varphi'\bar{\mathbf{Z}}(\bar{\mathrm{r}},\vartheta,\vartheta',\varphi-\varphi')\mathbf{S}(\bar{\mathrm{r}},\vartheta',\varphi'), \tag{1.129}$$

where $\mathbf{S}$ is the Stokes vector; $\bar{\mathrm{r}}$ is the position vector; ϑ and φ are the angles characterizing the incident direction and the polar (zenith) and azimuth angles, respectively;

$$d\tau(\bar{\mathrm{r}}) = \rho(\bar{\mathrm{r}})\langle\sigma_e(\bar{\mathrm{r}})\rangle ds \tag{1.130}$$

is the optical pathlength element; ρ is the local particle number density; $<\sigma_e>$ is the local ensemble-averaged extinction coefficient; *ds* is the pathlength element measured along the unit vector of the direction of light propagation; Λ is the single-scattering albedo; ϑ' and φ' are the angles characterizing scattering direction, the polar (zenith) and the azimuth angles, respectively; $\bar{\mathbf{Z}}$ is the normalized phase matrix

$$\bar{\mathbf{Z}}(\bar{\mathrm{r}},\vartheta,\vartheta',\varphi-\varphi') = \mathbf{R}(\Phi)\mathbf{M}(\theta)\mathbf{R}(\Psi), \tag{1.131}$$

where $\mathbf{M}(\theta)$ is the single-scattering Mueller matrix; θ is the scattering angle; and $\mathbf{R}(\phi)$ is the Stokes rotation matrix for an angle ϕ:

$$\mathbf{R}(\phi) = \begin{bmatrix} 1 & 0 & 0 & 0 \\ 0 & \cos 2\phi & -\sin 2\phi & 0 \\ 0 & \sin 2\phi & \cos 2\phi & 0 \\ 0 & 0 & 0 & 1 \end{bmatrix}. \tag{1.132}$$

This phase matrix links the Stokes vectors of the incident and scattered beams, specified relative to their respective meridional planes. To compute the Stokes vector of the scattered beam with respect to its meridional plane, one must calculate the Stokes vector of the incident beam with respect to the scattering plane, multiply it by the scattering matrix (to obtain the Stokes vector of the scattered beam with respect to the scattering plane), and then compute the Stokes vector of the scattered beam with respect to its meridional plane. Such a procedure involves two rotations of the reference plane: $\Phi = -\phi$; $\Psi = \pi - \phi$ and $\Phi = \pi + \phi$; and $\Psi = \phi$. The scattering angle θ and the

angles Φ and Ψ are expressed via the polar and the azimuth incident (ϑ, φ) and scattering angles (ϑ', φ').[9,56]

1.8.2 Monte Carlo simulation

1.8.2.1 Introduction

The MC method, being widely used for the numerical solution of the RTT equation[9,290–296] in different fields (astrophysics, atmosphere and ocean optics, etc.) appears to be especially promising for the solution of direct and inverse radiation transfer problems for media with arbitrary configurations and boundary conditions, in particular for the purposes of the medical polarization optical tomography and spectroscopy.[9,269,273,286–289,293–301] The method is based on the numerical simulation of photon transport in scattering media. Random migrations of photons inside a sample can be traced from their input until absorption or output occur.

The straightforward simulation using the MC method has the following advantages: (1) one can employ any scattering matrix, (2) there are no obstacles for the use of strongly forward-directed phase functions or experimental single-scattering matrices, (3) the polarization calculation takes only a twofold increase in computation time over that needed for the evaluation of intensity, (4) any reasonable number of detectors can be accounted for without noticeable increase of the computation time, (5) there are no difficulties in determining the radiation parameters inside the medium, and (6) it is possible to model media with complex geometry where radiance depends not only on the optical depth but also on the transverse coordinates.

The liability of the obtained results to statistical variations on the order of a few percent at an acceptable computation time is the main disadvantage of the MC technique. For a twofold increase of the accuracy, one needs a fourfold increase in the computation time. The MC method is also impractical for great optical depths ($\tau > 100$).

1.8.2.2 Simulation algorithm

A few MC codes for modeling of polarized light propagation through a scattering layer are available in the literature (see, e.g., Refs. 9, 281, and 286–301). To illustrate the MC simulation technique, the algorithm described in Ref. 300 and applied to model the angular dependencies of the scattering matrix elements is discussed. Let a flux of photons within an infinitely narrow beam be incident exactly upon the center of the spherical volume filled up by the scattering particles.[300] The path of a single photon migration in the medium is accounted for in a process of computer simulation. The photons are considered in this case as ballistic particles. Different events possible in the course of the photon migration are estimated by the appropriate probability distributions. In the model under study, the photons would either be

elastically scattered or absorbed under their collisions with the medium particles. A certain outcome of every event is found by a set of uniformly distributed random numbers. The probability of scattering in the given direction is determined in accordance with scattering by a single particle. One is able to specify the cross section of scattering and values of the scattering matrix elements for every photon interaction with a scatterer.

When an incident photon enters a scattering layer, it is allowed to travel a free pathlength, l. The l value depends on the particle concentration ρ, and extinction cross section σ_e. The free pathlength l is a random quantity that takes any positive values with the probability density $p(l)$:

$$p(l) = \rho\sigma_e e^{-\rho\sigma_e l}. \tag{1.133}$$

The particular realization of the free pathlength l is dictated by the value of a random number ξ that is uniformly distributed over the interval [0, 1]:

$$\int_0^l p(l)dl = \xi. \tag{1.134}$$

Substituting Eq. (1.133) into Eq. (1.134) yields the value l of the certain realization in the form

$$l = -\frac{1}{\rho\sigma_e}\ln\xi. \tag{1.135}$$

If the distance l is larger than the thickness of the scattering system, then this photon is detected as transmitted without any scattering. If, having passed the distance l, the photon remains within the scattering volume, then the possible events of photon–particle interaction (scattering or absorption) are randomly selected.

Within the spherical system of coordinates, the probability density of photon scattering along the direction specified by the angle of scattering θ between the directions of the incident and scattered photons and by the angle ϕ between the previous and new scattering planes is given as

$$p(\theta,\phi) = \frac{I_s(\theta,\phi)\sin\theta}{\int_0^{2\pi}\int_0^{\pi} I_s(\theta,\phi)\sin\theta d\theta d\phi}, \tag{1.136}$$

where $I_s(\theta, \phi)$ is the intensity of the light scattered in the direction (θ, ϕ) with respect to the previous direction of the photon, defined by angles ϑ and φ. For spherical particles, this intensity is given by the Mie formulas with allowance for the state of polarization (SOP) of each photon. An integral $I_s(\theta, \phi)$ over all scattering directions determines the scattering cross-section

$$\sigma_s = \int_0^{2\pi}\int_0^{\pi} I_s(\theta,\phi)\sin\theta d\theta d\phi. \tag{1.137}$$

The probability density of photon scattering along the specified direction, $p(\theta, \phi)$, depends on the Mueller matrix of the scattering particle $\mathbf{M}(\theta, \phi)$ (a single-scattering matrix) and the Stokes vector $\mathbf{S}$ associated with the photon. The single-scattering Mueller matrix $\mathbf{M}(\theta, \phi)$ links the Stokes vectors of the incident $[\mathbf{S}_i(0, 0)]$ and scattered $[\mathbf{S}_s(\theta, \phi)]$ light. For spherical scatterers, the elements of this matrix may be factorized

$$\mathbf{M}(\theta,\phi) = \mathbf{M}(\theta)\mathbf{R}(\phi). \tag{1.138}$$

The elements of the single-scattering matrix $\mathbf{M}(\theta)$ of spherical particles matrix are given by the Mie formulas,[1,12] which are functions of the scattering angle θ and diffraction parameter $x = 2\pi a/\lambda$, where a is the radius of the spherical particle and λ is the wavelength in the medium.

The matrix $\mathbf{R}(\phi)$ describes the transformation of the Stokes vector under rotation of the plane of scattering through the angle ϕ, which is defined by Eq. (1.132). Thus, the intensity of the light scattered by spherical particles is determined by the expression

$$I_s(\theta,\phi) = [M_{11}(\theta)I_i + (Q_i \cos 2\phi + U_i \sin 2\phi)M_{12}(\theta)], \tag{1.139}$$

where Q_i and U_i are the components of the Stokes vector of the incident light. As it follows from this equation, the probability $p(\theta, \phi)$ [Eq. (1.136)], unlike the scattering matrix [Eq. (1.138)], cannot be factorized; it appears to be parametrized by the Stokes vector associated with the scattered photon. In this case, one should use a rejection method to evaluate $p(\theta, \phi)$.

The following method of generating pairs of random numbers with the probability density $p(\theta, \phi)$ may be used.[300] In the 3-D space, the function $p(\theta, \phi)$ specifies some surface. The values (θ, ϕ) corresponding to the distribution $p(\theta, \phi)$ are chosen using the following steps: (1) a random direction (θ_ξ, ϕ_ξ) with a uniform spatial distribution is selected, the values of the random quantities θ_ξ, and ϕ_ξ distributed over the intervals $(0, \pi)$ and $(0, 2\pi)$, respectively, are found from the equations

$$\cos\theta_\xi = 2\xi - 1, \quad \phi_\xi = 2\pi\xi, \tag{1.140}$$

where ξ is a random number uniformly distributed over the interval (0,1); (2) the surface specified by the function $p(\theta, \phi)$ is surrounded by a sphere of radius $\mathbf{R}$, equal to the maximum value of the function $p(\theta, \phi)$, and a random quantity $r_\xi = \xi\mathbf{R}$ is generated; (3) the direction (θ_ξ, ϕ_ξ) is accepted as the random direction of the photon scattering at this stage, provided the condition $r_\xi \le p(\theta_\xi, \phi_\xi)$ to be satisfied. In the opposite case, steps 1 and 2 are repeated again.

The migration of the photon in the scattering medium can be described by a sequence of transformations for the related coordinate system. Each scattering event is accompanied by a variation of the Stokes vector associated

with the photon. The new Stokes vector $\mathbf{S}_{n+1}$ is a product of the preceding Stokes vector, transformed to the new scattering plane, and the Mueller matrix $\mathbf{M}_k(\theta)$ of the scattering particle

$$\mathbf{S}_{n+1} = \mathbf{M}_k(\theta)\mathbf{R}_n(\phi)\mathbf{S}_n, \tag{1.141}$$

where the matrix $\mathbf{R}_n(\phi)$ [see Eq. (1.132)] describes rotation of the Stokes vector around the axis specifying the direction of propagation of the photon before the interaction.

For the chosen scattering direction, the Stokes vector is recalculated using Eq. (1.141) and expressions for elements of the single-scattering Mueller matrix for a homogeneous sphere made of an optically inactive material.[12] The value thus obtained is renormalized so that the intensity remains equal to unity. Thus, the Stokes vector associated with the photon contains information only about the variation of the SOP of the scattered photon. Real intensity is determined by the number of detected photons in the chosen direction within the detector aperture.

The above procedure is repeated as long as the photon appears to be outside the scattering volume. In this case, if the photon propagation direction intersects the surface of the detector, the photon is detected. Upon detection, the Stokes vector is rotated from the current plane of the last scattering to the scattering plane of the laboratory coordinate system. The values obtained are accumulated in the appropriate cells of the detector whose number is defined by the photon migration direction. Furthermore, with registering, the photon is classified in accordance with the scattering multiplicity and the length of a total path. For every nonabsorbed photon, the direction and the coordinates of a point at which it escapes the scattering volume, as well as the number of scattering acts it has experienced, were also recorded. The spatial distribution of radiation scattered by the scattering volume can be obtained with regard to polarization by analyzing the above data for a sufficiently great number of photons.

To find the full LSM of an object, one has to detect the light scattering for four linearly independent states of polarization of the incident light $\mathbf{S}_{1i}$, $\mathbf{S}_{2i}$, $\mathbf{S}_{3i}$, and $\mathbf{S}_{4i}$. This allows one to construct the following system of linear equations:

$$\mathbf{CM}' = \mathbf{S}', \tag{1.142}$$

where $\mathbf{M}'$ is the column matrix composed of be found matrix elements of the LSM of the object, and $\mathbf{S}'$ is the 16-element vector containing the Stokes vector elements recorded upon light scattering for the four independent states of the incident light polarization. The transformation matrix $\mathbf{C}$ is determined by the choice of the initial set of the Stokes vectors of the incident light. Having solved this system of equations for the set of Stokes vectors:

$\mathbf{S}_{1i} = (1,1,0,0)$, $\mathbf{S}_{2i} = (1,-1,0,0)$, $\mathbf{S}_{3i} = (1,0,1,0)$, and $\mathbf{S}_{4i} = (1,0,0,1)$, one finds the desired LSM of the object, $\mathbf{M}' = \mathbf{M}$

$$\mathbf{M} = \frac{1}{2}\begin{bmatrix} I_1 + I_2 & I_1 - I_2 & 2I_3 - (I_1 + I_2) & 2I_4 - (I_1 + I_2) \\ Q_1 + Q_2 & Q_1 - Q_2 & 2Q_3 - (Q_1 + Q_2) & 2Q_4 - (Q_1 + Q_2) \\ U_1 + U_2 & U_1 - U_2 & 2U_3 - (U_1 + U_2) & 2U_4 - (U_1 + U_2) \\ V_1 + V_2 & V_1 - V_2 & 2V_3 - (V_1 + V_2) & 2V_4 - (V_1 + V_2) \end{bmatrix}, \tag{1.143}$$

where the elements of the Stokes vectors of the scattered light obtained in each of these four cases are denoted as $\mathbf{S}_n = (I_n, Q_n, U_n, V_n)$, $(n = 1, 2, 3, 4)$. As a result, one may calculate the angular dependencies for all elements of LSM with allowance for the contributions of multiple scattering.

1.8.2.3 Calculation of LSM for a multiple-scattering system

The simulation was performed for the systems of spherical particles with relative index of refraction, $m = 1.2$, which are uniformly distributed within a spherical volume at volume fraction $f = 0.01$.[300] In the calculations, the illuminating beam was assumed to be infinitely narrow and incident exactly upon the center of the scattering volume in the zero angle direction, and the scattered radiation is detected at different scattering angles in the far zone by a detector with the full angular aperture of 1 deg in the scattering plane and 5 deg in a plane that is perpendicular to the scattering one.

The calculated angular distributions of the total scattering intensity for different scattering systems of spherical particles with a small radius, $a = 50$ nm, or large radius, $a = 300$ nm, are presented in Fig. 1.17. The average multiplicity of scattering of the detected radiation increases with increasing dimensions of the scattering system. For systems of small particles at illumination in the visible range (633 nm), approximation of the Rayleigh scattering is applicable. For rather small dimensions of the scattering volume of 1 mm of diameter, the contribution of single scattering is predominant. This follows from the intensity angular dependence, which is rather isotropic, Fig. 1.17(a). As the dimensions of the scattering system increase, the fraction of contributions of the higher multiplicity scattering grows as well. For a 20-mm-diameter system, the detected light contains noticeable contributions of scattering of the 10th to the 20th multiplicity. With a further increase of the system dimensions, most of the incident light is scattered in the backward direction and the scattering intensity in the forward half-plane vanishes. For this reason, beginning from a certain value, the dimensions of the scattering system hardly affect the shape of the diagram of the scattering multiplicity distribution.

Systems composed of particles with a size of the order of the wavelength [Fig. 1.17(b)] also show an increase in the contributions of higher-order

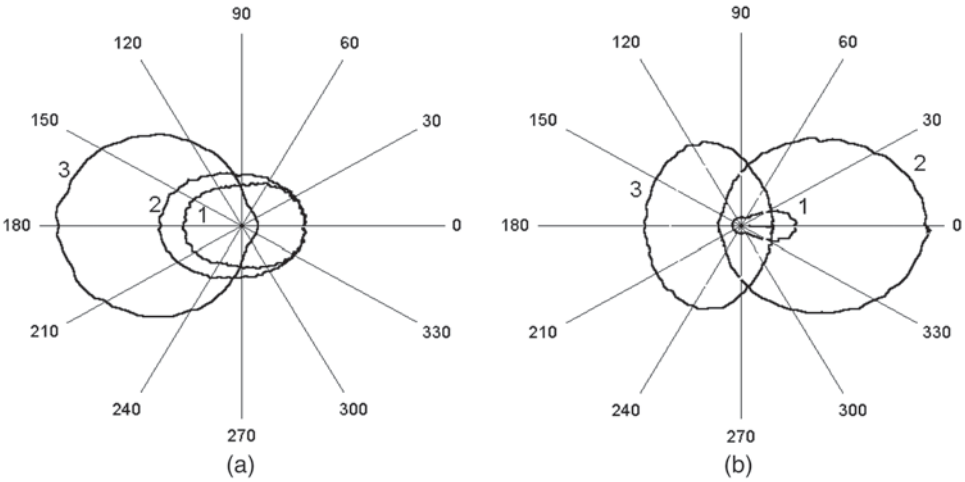

Figure 1.17 Angular distributions of the total scattering intensity for the multiple-scattering systems of spherical particles having relative refractive index $m = 1.2$ and uniformly distributed within a spherical volume at volume fraction $f = 0.01$: (a) particles with small radius, $a = 50$ nm, diameter of the system is equal to (1) 1, (2) 2, and (3) 20 mm; and (b) particles with large radius, $a = 300$ nm, diameter of the system is equal to (1) 0.002, (2) 0.2, and (3) 2 mm; the infinitely narrow unpolarized light beam is incident exactly upon the center of the scattering volume in the zero angle direction; the wavelength is 633 nm (see Refs. 9 and 300).

scattering with increasing dimensions of the scattering system. The system transforms from the forward- to backward-directed scattering mode at rather small thickness, 2 mm in diameter.

As is seen, the intensity of unpolarized light at the higher scattering multiplicity weakly depends on the scattering angle and carries almost no information about the size of the scattering particles. Note that systems of small particles at triple scattering may already be considered as nearly isotropic, while angular distributions for the large particles, strongly elongated in the forward direction at single scattering, remain anisotropic for sufficiently high scattering multiplicity [four to six scattering events for the system with a 0.2 mm diameter, Fig. 1.17(b)].

The view of the LSM elements' angular dependences under the conditions of multiple scattering differs substantially from that for the LSM of a single–scattering system. It is seen from Figs. 1.18 and 1.19 that the multiple scattering flattens the angular dependences of the LSM elements. The solid line shows the result of calculation of a normalized LSM for an isolated spherical particle with the similar radius and relative index of refraction. All elements of the LSM are normalized to the M_{11} element (total scattering intensity) along the given direction, and the element M_{11} is presented in the plot as normalized to unity in the forward direction; its actual intensity distributions are presented in Fig. 1.17.

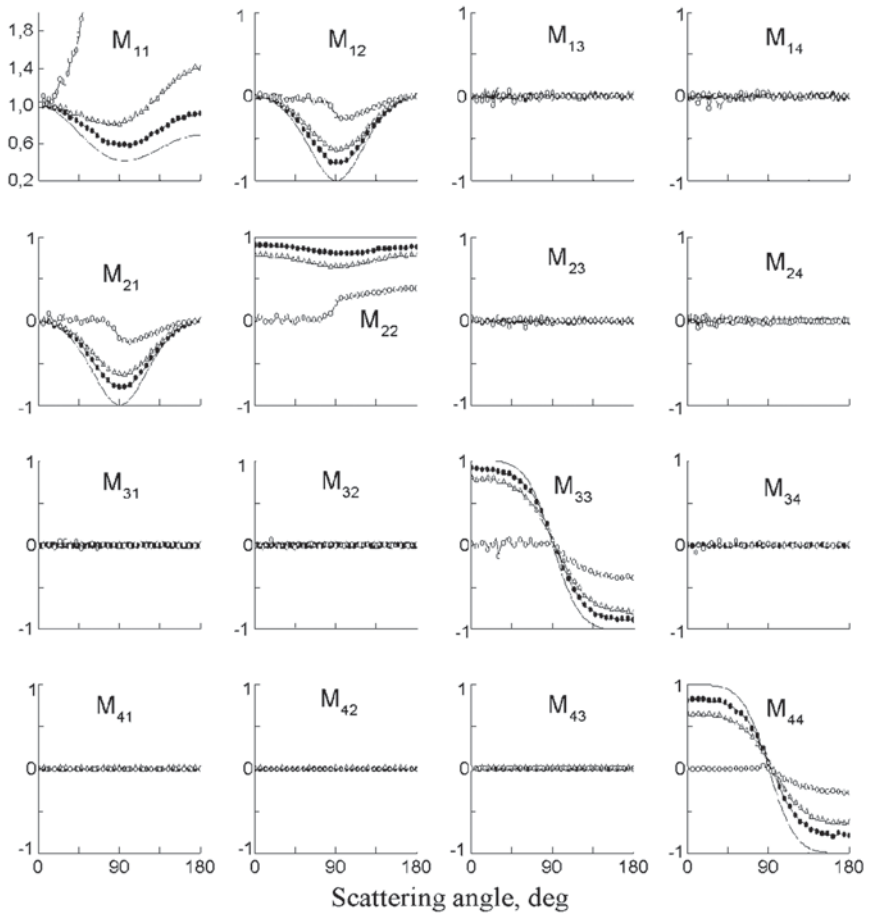

Figure 1.18 The MC simulation: the angular distributions of the LSM elements for the multiple-scattering systems of small spherical particles ($a = 50$ nm, $m = 1.2$) uniformly distributed within a spherical volume ($f = 0.01$); diameter of the system is equal to 1 mm (–•–), 2 mm (–△–), and 20 mm (–○–); the solid line shows the results of calculations in the approximation of single scattering; the infinitely narrow unpolarized light beam is incident exactly upon the center of the scattering volume in the zero angle direction; the wavelength is 633 nm (see Refs. 9 and 300).

Since the single-scattering angular distribution for particles with sizes substantially exceeding the Rayleigh limit is strongly asymmetric, the scattering intensity at large angles is very low. For this reason, one must trace the trajectories of a great number of photons to obtain good accuracy in this angular range. Therefore, to demonstrate the fine structure of the angular dependence of the matrix elements, one needs to use in the simulation at least 10^7–10^8 photons.

For the scattering by particle suspensions in a spherical volume of small diameter, almost all the detected photons are singly scattered. An increase in

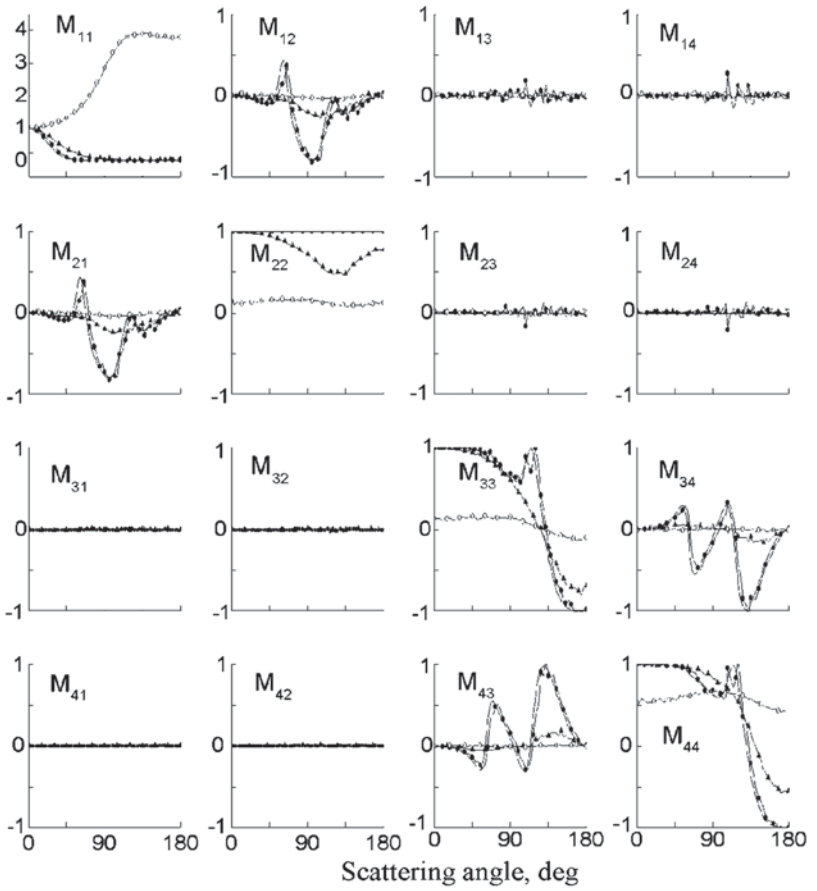

Figure 1.19 The MC simulation: the angular distributions of the LSM elements for the multiple-scattering systems of large spherical particles ($a = 300$ nm, $m = 1.2$) uniformly distributed within a spherical volume ($f = 0.01$); diameter of the system is equal to 0.002 mm (–•–), 0.2 mm (–△–), and 2 mm (–○–); the solid line shows the results of calculations in the approximation of single scattering; the infinitely narrow unpolarized light beam is incident exactly upon the center of the scattering volume in the zero angle direction; the wavelength is 633 nm (see Refs. 9 and 300).

the optical thickness considerably enhances the contribution of multiple scattering. The angular dependences of the LSM elements have a form close to the single-scattering LSM, provided that the optical thickness of the scattering system τ does not exceed unity for the systems of large particles considered ten or above for systems of small particles.

The multiple-scattering intensity (the element M_{11}) for a volume of large diameter decreases with increasing scattering angle slower than the single-scattering intensity. As the object diameter further increases, the backward scattering becomes predominant (see Figs. 1.17–1.19). In the systems of small particles (see Fig. 1.18), the growth of the multiple-scattering contributions is

accompanied by a gradual decrease in magnitude of all of the elements except for M_{11}, i.e., the form of the LSM approaches that of the ideal depolarizer. In particular, the magnitudes of the elements M_{12} and M_{21} decrease in nearly the same way; the elements M_{33} and M_{44} also decrease in magnitude, but M_{44} decrease faster. As a result, multiple scattering gives rise to a difference in the detected values of the elements M_{33} and M_{44}, even for the systems of spherical particles. The values of the element M_{22} become smaller than unity, this decrease being more substantial in the range of scattering angles close to 90 deg. Thus, the manifestation of the effect of multiple scattering in monodisperse systems of spherical particles, which is revealed in the appearance of nonzero values of the differences $|M_{33}–M_{44}|$ and $|1–M_{22}|$, is similar to the manifestation of the effect of nonsphericity of the scatterers observed under conditions of single scattering.[207]

For large particle systems, the multiple scattering also decreases the magnitudes and smooths out the angular dependences of the normalized elements of the LSM (see Fig. 1.19). The corresponding angular dependences, as compared to the LSM of small particles, show the following specific features: the minimum value of the element M_{22} is reached not at 90 deg, but rather at large scattering angles; the fine structures of the angular dependences for all elements are smeared even in the presence of a small fraction of the multiply scattered light; and, finally, a very important result that the element M_{44}, unlike other elements, in the limit of high scattering multiplicity, tends to 0.5 rather than to zero for all scattering angles. Such a form of the LSM means that the radiation scattered by the large particles holds the preferential circular polarization at higher scattering multiplicities. This result may serve as a confirmation of preferential survival of different types of polarization under conditions of multiple scattering for different sizes of scattering particles or tissue structures.[276,279,302]

The process of multiple scattering of the photons during their migration is considered as a series of successive rotations of their coordinate systems, determined by the scattering planes and directions. Since these rotations are random, the detected photons will be randomly polarized and, hence, the detected light will be partially depolarized. The depolarization will increase with the increasing multiplicity of scattering. For the moderate optical thicknesses (object diameter of 0.2 mm, $f = 0.01$), the depolarizing ability is strongly different for different directions. The scattered light may be almost completely polarized in the region of small scattering angles and completely depolarized at large angles ($\theta = 120$ deg) and be partly polarized in the backward direction. The angular range of the strongest depolarization corresponds to the angle at which the element M_{22} acquires minimum values (see Fig. 1.19).

The simulated dependences allow one to estimate the limits of applicability of the single-scattering approximation when interpreting the

results of experimental studies of disperse scattering systems. It follows from these simulations that modifications of the LSM of monodisperse systems of spherical particles due to the effects of multiple scattering have much in common with modification of the LSM of singly scattering systems upon deviation of the shape of the particles from spherical. This fact imposes serious limitations on the application of the measured LSM of tissues for the inverse problem solving to determine particle nonsphericity. The appropriate criteria to distinguish the effects of multiple scattering and particle nonsphericity have to be developed.

It is important to note that the comparison of MC simulation accounting for all orders of multiple scattering with the analytical double-scattering model had indicated no essential change in the back-scattering polarization patterns.[303] This is due to the fact that the main contribution comes from near-double-scattering trajectories in which light suffers two wide-angle scatterings and many near-forward scatterings among multiple-scattering trajectories. The contributions of such multiple but near-double scattering trajectories are obviously well approximated by the contributions of the corresponding double-scattering trajectories.

The above MC technique of photon trajectory modeling is well suited to the simulation of multiple-scattering effects in a system of randomly arranged particles. Furthermore, this scheme allows for an approximate approach to describe the interference effects caused by space particle ordering. To this end, one should include the interference of scattered fields into calculations of the single-scattering Mueller matrix and integral cross sections for a particle. In other words, at the first stage one accounts for the interference effects for simulation of the *single-scattering* properties, and then uses these properties in the MC simulation of *multiple scattering*. Such an approach is admissible if the size of a region of the local particle ordering is substantially smaller than the mean free photon pathlength.

In general, for polarized light propagated in a strongly scattering medium, the multiple scattering decreases the magnitudes and smooths out the angular dependences of the normalized LSM elements, characterizing polarized light interaction with the medium. For media composed of large particles, specified by a high degree of single-scattering anisotropy or considerable photon transport length, the scattered radiation holds the preferential circular polarization at higher scattering multiplicities. This theoretical result serves as a confirmation of preferential survival of different types of polarization under conditions of multiple scattering for different sizes of scattering particles or tissue structures.

Given the known character of the Stokes vector transformation for each scattering act, the SOP following multiple light scattering in a highly scattering medium can be found using various approximations of the multiple-scattering theory or the MC method. For small particles, the effects

of multiple scattering are apparent as the broken symmetry relationship between LSM elements $M_{12}(\theta) \neq M_{21}(\theta)$, $M_{33}(\theta) \neq M_{44}(\theta)$, and a significant reduction of linear polarization of the light scattered at angles close to $\pi/2$.[304]

1.8.2.4 Degree of linear and circular polarization of light interacting with tissues

For a system of small spatially uncorrelated particles, the degree of linear ($i = L$) and circular ($i = C$) polarization in the far region of the initially polarized (linearly or circularly) light transmitted through a layer of thickness d is defined by the relation[279]

$$P_i \cong \frac{2d}{l_s} \sinh(l_s/\xi_i) \cdot \exp(-d/\xi_i), \tag{1.144}$$

where $l_s = 1/\mu_s$ is the scattering length, and

$$\xi_i = (\zeta_i \cdot l_s/3)^{0.5} \tag{1.145}$$

is the characteristic depolarization length for a layer of scatterers $d \gg \xi_i$, $\zeta_L = l_s/[\ln(10/7)]$, $\zeta_C = l_s/(\ln 2)$.

As can be seen from Eq. (1.144), the characteristic depolarization length for linearly polarized light in tissues that can be represented as ensembles of Rayleigh particles is approximately 1.4 times greater than the corresponding depolarization length for circularly polarized light. One can employ Eq. (1.144) to assess the depolarization of light propagating through an ensemble of large-scale spherical particles whose sizes are comparable with the wavelength of incident light (Mie scattering). For this purpose, one should replace l_s by the transport length $l_{tr} \cong 1/\mu_s'$ and take into account the dependence on the size of scatterers in ζ_L and ζ_C. With the growth in the size of scatterers, the ratio ζ_L/ζ_C changes. It decreases from $\sim$1.4 down to 0.5 as $2\pi a/\lambda$ increases from 0 up to $\sim$4; it remains virtually constant at the level of 0.5 when $2\pi a/\lambda$ grows from $\sim$4 to 15.

MC numerical simulations and model experiments in aqueous latex suspensions with particles of various diameters demonstrate that there are three regimes of the dependence of the ratio of the degree of linear polarization to the circular polarization for transmitted light, P_L/P_C, on d/l_{tr}.[279] In the Rayleigh range, P_L/P_C grows linearly with the increase of d/l_{tr}. In the intermediate range, this ratio remains constant. In the range of Mie scattering, this quantity decreases linearly. Such behavior of this quantity is associated with the transition of the system under study from isotropic scattering to anisotropic. Qualitatively, the physical mechanism behind the change in the depolarization is associated with the fact that a considerable probability of backward scattering in each event of light–medium interaction (isotropic scattering) does not distort linear polarization, whereas backward

scattering for circular polarization is equivalent to the reversal of polarization direction (similar to reflection from a mirror), i.e., it is equivalent to depolarization. For the same reason, in the case of a strongly elongated scattering phase function, the degree of circular polarization in an individual scattering event (anisotropic scattering) for light propagating in a layer should remain nonzero for lengths greater than the degree of linear polarization.

These arguments also follow from the above MC simulation of polarized light interaction with multiple-scattering systems[300] and experimental works.[302,305] For example, at high-scattering multiplicities the radiation scattered by the large particles holds the preferential circular polarization (LSM element M_{44} is far from zero for all scattering angles) (see Fig. 1.19). At multiple scattering, the LSM for a monodisperse system of randomly distributed spherical particles is modified to be approximately identical to the single-scattering LSM of the system containing nonspherical particles, or optically active spheres.

Thus, different tissues or the same tissues in various pathological or functional states should display different responses to a probe with linearly and circularly polarized light. This effect can be employed in both optical medical tomography and for determining optical and spectroscopic parameters of tissues. As follows from Eq. (1.144), the depolarization length in tissues should be close to the mean transport pathlength l_{tr} of a photon, because this length characterizes the distance within which the direction of light propagation and consequently, the polarization plane of linearly polarized light, become totally random after many sequential scattering events.

Since the length l_{tr} is determined by the parameter g characterizing the anisotropy of scattering, the depolarization length should also substantially depend on this parameter. Indeed, the experimental data of Ref. 306 demonstrate that the depolarization length l_p of linearly polarized light, which is defined as the length within which the ratio $I_{\|}/I_{\perp}$ decreases down to 2, displays such a dependence. The ratio mentioned above varied from 300 to 1, depending on the thickness of the sample and the type of tissue. These measurements were performed within a narrow solid angle ($\sim 10^{-4}$ sr) in the direction of the incident laser beam. The values of l_p differed considerably for the white matter of brain and tissue from the cerebral cortex: 0.19 and 1.0 mm for $\lambda = 476$–514 nm and 0.23 and 1.3 mm for $\lambda = 633$ nm, respectively. Human skin dermis (bloodless) has a depolarization length of 0.43 mm ($\lambda = 476$–514 nm) and 0.46 mm ($\lambda = 633$ nm). The depolarization length at $\lambda = 476$–514 nm decreases in response to a pathological change in the tissue of aorta wall: 0.54 mm for a normal tissue, 0.39 mm for the stage of tissue calcification, and 0.33 mm for the stage of necrotic ulcer. Whole blood with a low hematocrit is characterized by a considerable depolarization length (about 4 mm) at $\lambda = 633$ nm, which is indicative of the dependence on the parameter g, whose value for blood exceeds the values of

this parameter for tissues of many other types and can be estimated as 0.966–0.997[9,307] (see Chapter 2).

In contrast to depolarization, the attenuation of collimated light is determined by the total attenuation coefficient μ_t. For many tissues, μ_t is much greater than μ_s'. Therefore, in certain situations, it is impossible to detect pure ballistic photons (photons that do not experience scattering), but the forward scattered photons retain their initial polarization and can be used for imaging.[308,309] This is illustrated by Fig. 1.20, which presents the experimental data for the decay of the degree of linear polarization P_L obtained for various tissues and blood as a function of light transmission.[302]

The authors of Ref. 310 experimentally demonstrated that laser radiation retains linear polarization on the level of $P_L \leq 0.1$ within $2.5l_{tr}$. Specifically, for skin irradiated in the red and NIR ranges, we have $\mu_a \cong 0.4\ \text{cm}^{-1}$, $\mu_s' \cong 20\ \text{cm}^{-1}$, and $l_{tr} \cong 0.48$ mm. Consequently, light propagating in skin can retain linear polarization within a length of about 1.2 mm. Such an optical path in a tissue corresponds to a time delay on the order of 5.3 ps, which provides an opportunity to produce polarization images of macro-inhomogeneities in a tissue with a spatial resolution equivalent to the spatial resolution that can be achieved by the selecting of photons using more sophisticated time-resolved techniques. In addition to the selection of diffuse-scattered photons, polarization imaging makes it possible to eliminate specular reflection from the surface of a tissue, which allows one to use this technique to image microvessels in facile skin and detect birefringence and optical activity in superficial tissue layers.[311–316]

Polarization imaging is an innovative technology in biophotonics.[9,294,308–326] The most prospective approaches for polarization tissue imaging, in particular, linear polarization degree mapping, 2-D backscattering Mueller matrix measurements, polarization-sensitive OCT, and

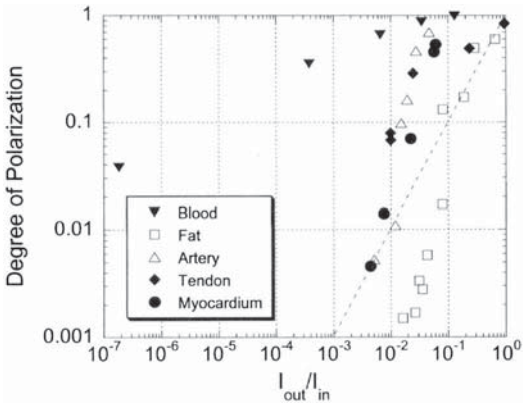

Figure 1.20 Degree of linear polarization in different tissues as a function of the sample optical transmittance, $I_{out}/I_{in} \equiv T$, on 633 nm. Each point is an average of three measurements.[302] The error bars representing standard deviation of measurements are smaller than the used symbols.

full-field polarization-speckle technique will be discussed in this and the following chapters.

The registration of 2-D polarization patterns for the backscattering of a polarized incident narrow laser beam is the basis for the polarization imaging technique. The major informative images can be received using the back-scattering Mueller matrix approach. To determine each of the 16 experimental matrix elements, a total of 16 images should be taken at various combinations of input and output polarization states.

In weakly absorbing media showing a small-angular multiple scattering, the degree of linear polarization for a Henyey–Greenstein phase function is described by[325]

$$P_L = -[(\mu_s' z)^4/2\theta^2] \cdot \left[\sqrt{1 + (\theta/\mu_s' z)^2} - 1\right]^2 \cdot [1 + (\theta/\mu_s' z)^2]. \qquad (1.146)$$

This means that in a very small angle range ($\theta \ll \mu_s' z$) the degree of polarization does not depend on the depth (z)

$$P_L = -\theta^2/8. \qquad (1.147)$$

At the wings of the scattering angle dependence ($\theta \gg \mu_s' z$), it tends to

$$P_L = -\theta^2/2, \qquad (1.148)$$

which equals the degree of polarization of singly scattered light.

1.8.2.5 Simulation of two-dimensional reflection and transmission LSM

Rakovic et al.[327] present the MC-based simulations of the diffusely back-scattering intensity patterns that arise from illuminating a turbid medium with a polarized laser beam. It is rigorously shown that, because of the axial symmetry of the system, only seven elements of the effective back-scattering Mueller matrix are independent. Other studies have demonstrated that information on the properties of turbid medium can be obtained by analyzing the SOP of diffusely back-scattering polarized laser light. Applications of this technique that have been investigated include the measurements of the average particle size, the scattering coefficients and the anisotropy factor of particle suspensions,[268] and the study of biological material.[328] Hielscher et al.[268] generalized the concept of an effective Mueller matrix and measured the 2-D Mueller matrix of back-scattering light. Rakovic et al.[327] extended this work to include a theoretical, computational, and experimental verification of the use of the incoherent scattering theory to explain the patterns seen in polarized light back-scattering from the suspensions of polystyrene spheres (Fig. 1.21). Yao et al. measured depth-resolved Mueller-matrix images using polarization-sensitive optical coherence tomography.[329,330]

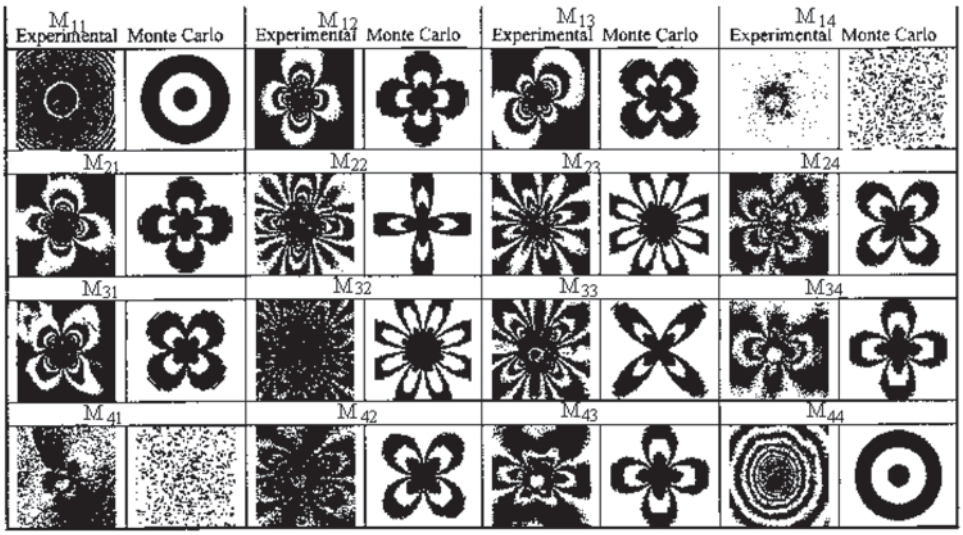

Figure 1.21 Experimental and MC counted back-scattering Mueller matrix.[327] The phantom was comprised of a 0.05-wt% suspension of polystyrene spheres (of diameter 2.02 μm) in deionized water. The approximate size of each image was 1.6 by 1.6 cm. The light wavelength was 633 nm. The smaller values correspond to contours located further from the center of each plot.

Figure 1.22 shows the reflection and the transmission Mueller matrices of a turbid medium with parameters characteristic to tissues.[294] The patterns of the reflection Mueller matrix are identical to those reported in Refs. 288 and 327 (see Fig. 1.21). The symmetries in the patterns can be explained by the symmetries in the single-scattering Mueller matrix and the turbid medium.[327] The transmission Mueller matrix has different patterns from the reflection Mueller matrix. One of the noticeable differences appears in elements M_{31} and M_{13}, which are antisymmetric in the reflection Mueller matrix but symmetric in the transmission Mueller matrix. This difference is caused by the mirror effect in the reflection process of the scattered light.

1.8.2.6 Simulation of the spectra of transmission, reflection, and scattering

The collimated transmission is understood as a detection of a relative fraction of photons running out of the scattering layer close to the forward direction that exhibit a slight lateral shift corresponding to their entrapment by the specified receiving aperture.

If light is incident onto a layer of parallel cylinder particles normal to the cylinder axes, the scattered light propagates in a plane perpendicular to these axes. Consequently, this problem has to be considered as a 2-D one. When calculating the collimated transmission or the integral characteristics of light scattering, the results calculated for linearly polarized light that is normally incident to the surface of a system of layers that are randomly

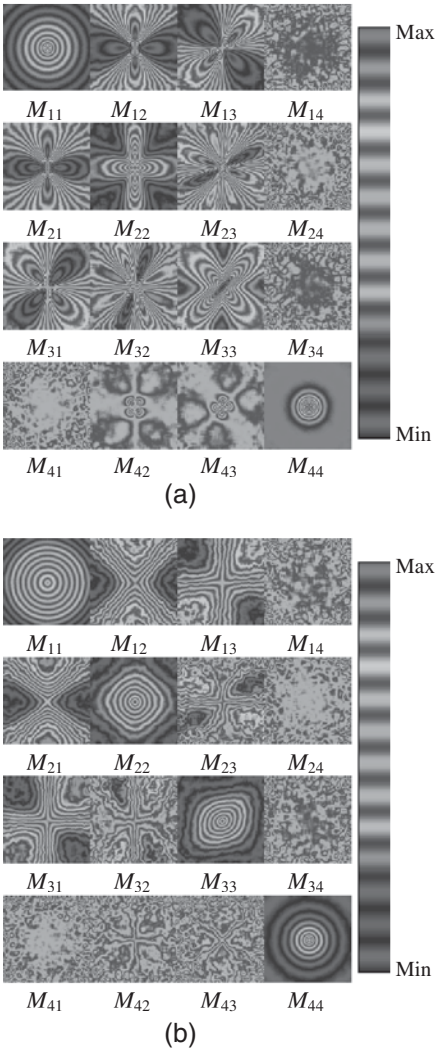

Figure 1.22 (a) Reflection and (b) transmission Mueller matrices of a slab of turbid medium with a scattering coefficient of 4 cm^{-1} and a scatterer radius of 0.102 μm.[294] The calculated Mueller-matrix elements are normalized to the M_{11} element to compensate for the radial decay of intensity. Each of the images is displayed with its own color map to enhance the image contrast. The size of each image is 4×4 cm^2. (See color plates.)

aligned around the direction of light propagation are equivalent to those obtained for light incident onto a system of uniformly oriented layers. It is, therefore, possible to restrict oneself by considering the 2-D problem if the effects of rescattering between different layers are negligible, which substantially simplifies the problem. It is, however, unfair for the angular dependence of scattering.

The simulation shows that dependence of transmission on the layer thickness is described by two exponential terms. This allows for study of the transition from predominantly single scattering to the diffusion regime of scattering as thickness increases. The MC method also makes it possible to study the kinetics of light scattering as the relative index of refraction in a disperse medium is varied. The above effects have been investigated in detail with the example of the eye sclera optical clearing (see Section 1.10 about the sclera optical clearing and temporal spectra). The MC method is also useful for simulating the spectral characteristics of scattering in different directions.[331]

1.9 Nephelometry and Polarization Methods for Diagnostics of Bioobjects

This section deals with the study of methods for the diagnostics of the parameters of biological particles and tissues with regard to the angular and polarization characteristics of elastically scattered light. These methods are simple to realize and they easily undergo computer control. Moreover, the study of the angular dependence of the scattered light intensity for measuring the size or density of particles suspended in a fluid (the so-called nephelometry) has a long history and is widely used in very different areas of biology and medicine.[332] As for the analysis of polarization effects, it is made use of very rarely with light scattering, although this analysis yields more extensive information on a scattering object. The polarization of light scattered by biological cells can reveal properties not evident from measurements of the total scattered intensity alone. Therefore, we consider in detail the problems of laser polarization nephelometry, the methods for the computer-controlled measurement of angular dependencies of the LSM elements, and potentials for diagnostics.

The most complete information on elastic light scattering by an object is contained in the LSM (see Section 1.3). The LSM elements and their dependencies on the scattering angle contain information on the structure and properties of the object under study. The solution of the appropriate inverse problems can provide the size distribution function of scattering particles, their index of refraction, shape and orientation. The rigorous solution is, however, possible only for a small class of objects. Most biological objects have a quite complex structure, hence even the solution of a straightforward problem is a quite difficult task. Along with this, in a number of cases a qualitative estimation of the object's properties would be sufficient, requiring no exact solution of the inverse problem. The general view of experimental scattering matrix and symmetry relations for its elements allow us to compare the object under study with a certain class of scattering systems. The evaluation of the state of the object under study by using the

experimental LSM can be done with the help of the relations between the matrix elements. These relations can also be a criterion for estimation of the correctness of experimental results.

1.9.1 Relations between the LSM elements: depolarization criterion

The nature and mathematical expressions of relations between 16 LSM elements were considered in Refs. 333 through 335. It has been shown that there are nine equalities relating the matrix elements for a nondepolarizing system that is usually understood as a system whose Mueller matrix is obtained by coherently summing the amplitude matrices of single elements of the system.

It has been established[336,337] that for depolarizing systems six of the above mentioned equalities are transformed into the following inequalities:

$$\begin{aligned}
&(M_{11}+M_{22})^2-(M_{12}+M_{21})^2 \geq (M_{33}+M_{44})^2+(M_{43}-M_{34})^2\\
&(M_{11}-M_{22})^2-(M_{12}-M_{21})^2 \geq (M_{33}-M_{44})^2+(M_{43}+M_{34})^2\\
&(M_{11}+M_{21})^2-(M_{12}+M_{22})^2 \geq (M_{13}+M_{23})^2+(M_{14}+M_{24})^2\\
&(M_{11}-M_{21})^2-(M_{12}-M_{22})^2 \geq (M_{13}-M_{23})^2+(M_{14}-M_{24})^2\\
&(M_{11}+M_{12})^2-(M_{21}+M_{22})^2 \geq (M_{31}+M_{32})^2+(M_{41}+M_{42})^2\\
&(M_{11}-M_{12})^2-(M_{21}-M_{22})^2 \geq (M_{31}-M_{32})^2+(M_{41}-M_{42})^2. \qquad (1.149)
\end{aligned}$$

Another important characteristic for the scattering matrices is the number $\mathrm{Tr}(M)$

$$\mathrm{Tr}(M)=\sum_{i,j=1}^{4} M_{ij}^2, \qquad (1.150)$$

where M is the scattering matrix normalized to the first element.

It was shown that the equality $\mathrm{Tr}(M)=4$ is a necessary and sufficient condition for this matrix M to describe a nondepolarizing object.[338] For depolarizing objects,$\mathrm{Tr}(M)$ takes values from 1 to 4. These inequalities enable one to clearly classify various objects and in some cases to verify the experimental results. The application of the above relations to the analysis of the LSM of different biological objects has been described.[339] The symmetry relations for the LSM of an ensemble of particles are considered.[340] A collection of particles of random orientation has a scattering matrix of the form

$$M(\theta)=\begin{pmatrix} m_{11}(\theta) & m_{12}(\theta) & m_{13}(\theta) & m_{14}(\theta)\\ m_{12}(\theta) & m_{22}(\theta) & m_{23}(\theta) & m_{24}(\theta)\\ -m_{13}(\theta) & -m_{23}(\theta) & m_{33}(\theta) & m_{34}(\theta)\\ m_{14}(\theta) & m_{24}(\theta) & -m_{34}(\theta) & m_{44}(\theta) \end{pmatrix}. \qquad (1.151)$$

If all particles have a plane of symmetry or, equivalently, particles and their mirror particles are presented in equal numbers, we obtain the block-diagonal structure

$$M(\theta) = \begin{pmatrix} m_{11}(\theta) & m_{12}(\theta) & 0 & 0 \\ m_{12}(\theta) & m_{22}(\theta) & 0 & 0 \\ 0 & 0 & m_{33}(\theta) & m_{34}(\theta) \\ 0 & 0 & -m_{34}(\theta) & m_{44}(\theta) \end{pmatrix}. \tag{1.152}$$

In the case of back-scattering, consequences for the linear and circular depolarization ratios have been reported by Mishchenko and Hovenier.[341]

1.9.2 Angular dependence of the scattering intensity of nondepolarized light

One of the main characteristics to be examined with light scattering is the angular dependence of the scattered intensity. The measurement is provided by illuminating an object with the light beam and recording the intensity of light scattered at different angles. Therefore, an optical nephelometer, the device measuring scattered light, is based on a source with small angular divergence and a light detector with a certain angle of view. Lasers appear to be the most suitable light sources in this case because of sufficient directness and high intensity of the laser beams.

To find particle sizes in a range of 0.02–0.2 μm, the method of the angular dependence asymmetry is used. It is based on recording of the scattering angular dependence deviation from that of Rayleigh form with greater particle size. The method of full angular dependence measurement is applied to quantify the particle sizes in a range of 0.1–10 μm, and that of small-angle light scattering is used to measure the particle sizes in a range of 1–300 μm.[342] Laser nephelometry is employed in immunology to quantitatively estimate the antigen–antibody reaction and to determine the concentration of components participating in the reaction. In particular, laser nephelometry was used to study the influence of various factors (temperature, pH of the medium, and others) on the rate of the reaction and of the formation of antigen–antibody complexes.[343]

A number of physically justified light scattering methods were developed to investigate the morphological parameters of erythrocytes (sizes, shape, concentration, and aggregation) under conditions approaching their native state.[344–346] They include the procedures of deriving the hematocrit ratio, aggregation function of erythrocytes, and concentration of hemoglobin derivatives via elastic light scattering. Particularly, a strong dependence of scattering angular dependences on the erythrocyte sizes that has been revealed for angles of 1–30 deg permits one to obtain their size-distribution function. At the same time, the surface roughness of pathological erythrocytes is

determined with a high accuracy by a higher scattered laser radiation intensity within angles exceeding 90 deg.

1.9.3 Measurements of the angular dependences of the scattering matrix elements

The simplest measuring technique for the LSM elements evaluation is based on the conventional nephelometer and additional optical elements placed ahead of and after the scattering medium under study. The linear polarizers and quarter-wave plates are employed as such elements.[12] The results of such measurement are the combinations of the LSM elements obtained by multiplying the matrices of optical elements placed ahead of the scattering object, the matrices of the scattering object itself, and those of optical elements placed after the scattering object (Fig. 1.23). In general, four measurements are necessary to obtain one LSM element. Despite the fact that this technique is reasonable even if quite cumbersome, its application may be followed by significant relative errors associated with small matrix elements obtained as differences of big signals. These errors can be avoided by modulating the polarization state in the incident and/or the scattered fields.

A laser polarization nephelometer has been described with the principle of operation relying on the modulation of the polarization state of incident and scattered light by mechanically rotating polarization elements.[339,347,348] The principle of operation is described by the following matrix equation:

$$\mathbf{S} = A_a \Phi_a M \Phi_p A_p \mathbf{S_0}, \tag{1.153}$$

where $\mathbf{S}$ and $\mathbf{S_0}$ are the Stokes vectors of recorded and source radiation, respectively; A and Φ are the Mueller matrices for the linear polarizer and the phase plate, respectively. As the phase plates are rotated, the intensity recorded by a photodetector, i.e., the first element of the Stokes vector $\mathbf{S}$, would depend on time. By multiplying the matrices in Eq. (1.153) and performing the appropriate trigonometric transformations, one can show that the output intensity would be represented as a Fourier series, namely,

$$I = a_0 + \sum_{k=1}^{K} (a_{2\,k} \cos 2\,k\varphi + b_{2\,k} \sin 2\,k\varphi), \tag{1.154}$$

where φ is the angle of orientation of the phase plate axis. The coefficients of this series are defined by the values of the matrix M elements of the object

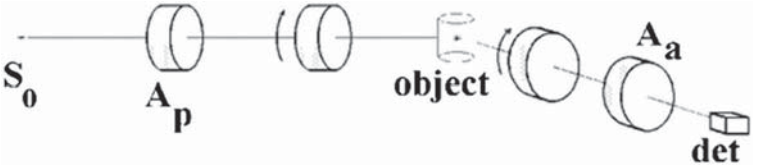

Figure 1.23 Schematics of a polarization nephelometer with the rotating phase plates.

under study, and their measurement ensures a system of linear equations to determine the matrix M. The number of equations and the degree of stipulation for this system of equations are dependent on choosing the ratio between the rotation rates of the phase plates. The proper choice of the rotation rates relation as 1:5 allows one to get an optimally stipulated system of linear equations to find the full matrix M of the object under study.

More sophisticated elecro-optical[349,350] and magnitoptical[351] modulation principles of polarization states are also used.

1.9.4 The LSM for some biological objects

A review of experimental studies of scattering polarization properties of biological tissues and cells the reader could find in the multiple literature.[9,76,207,283,294,302,306,310–321,328] The following regularities can be mentioned that allow for parameters of scattering particle structures or suspensions to be classified by analyzing their LSM. The distinction between elements M_{22} and M_{11} would serve as a measure for scattering particles to be nonspherical. These peculiarities were studied for different types of pollen[352] and marine organisms.[353,354] However, a similar distinction between elements M_{22} and M_{11} for a model of spherical particles may be caused by multiple scattering (see above).

As noted in Refs. 76, 352, and 355–358, element M_{34} is most specific for various bioparticles. This element is sensitive to small morphological alterations of scatterers. It has been shown that the element M_{34} is affected by a small surface roughness on a sphere.[356] It was also proven that M_{34} measurements may be the basis for determining the diameter of rod-shaped bacteria (*Esgherichia coli* cells) that is difficult to be measured using other techniques.[357]

In Refs. 352 and 355, the measuring results for the whole LSM of some biological particles are presented. A high specificity of element M_{34}/M_{11} was shown for every type of biological scatterer. Stable distinctions were revealed in the values of parameter M_{34}/M_{11} for spores of two mutant varieties of bacteria, which are distinguished by the variations of their specific structure and are invisible by means of traditional techniques. The distinctions of other matrix elements, however, were seen less clearly for these two types of similar scatterers. When scattering by biological particles is well described by the RG approximation, $M_{34} = 0$. Thus, M_{34} is a matrix element that suffers strongly from the deviation of the particle parameters from those that satisfy the RG approximation. Possibly, this is the reason for the M_{34}/M_{11} to be so sensitive to the characteristics of biological scatterers.[12]

The polarization characteristics for suspension of biological particles have been described in Ref. 207, where the sensitivity of different matrix elements to the variation of the scatterer shape and size is analyzed. It is noted that the

magnitudes of elements M_{33} and M_{44} measured in the backward scattering direction may serve as an indicator for the particle nonsphericity.

The polarization nephelometry is also used to examine blood corpuscles. The protocol for determination of the real part of the index of refraction of blood corpuscles based on the study of the angular structure of the LSM nonzero elements is described by Korolevich et al.[346] This protocol is useful for the normal or gamma distribution of polydisperse particles and does not require data on the particle concentration; it is only necessary to obey the condition of single scattering. The technique for determination of the real part of the relative index of refraction m is reduced to finding a scattering angle at which the LSM element is zero within a range of scattering angles from 80 to 120 deg. Further, the relative index of refraction m is derived accordingly to nomograms valid in the range from 1.02 to 1.07. If the element is not zero within the angular range of 80–120 deg, then $m > 1.07$, and it is needed to determine a scattering angle at which element M_{34} is also zero. The measuring of angular dependencies for the total LSM of blood erythrocytes enables one to distinguish between disc-like and spherulated cells[345] (Fig. 1.24). As it was noted in Ref. 76, the comparison between measured signals for all types of human white blood cells allows one to distinguish between two types of granulocytes.

The results of measuring the angular dependence of the LSM elements of the sliced samples of human skin dermis, bones, and muscular tissues were presented.[359] The LSM analysis of the tissue slices shows a high level of birefringence and a random nature of orientation of the bone tissue local structures. A determined orientation of optically active bundles of the muscular tissue is revealed in a quasi-harmonic behavior of the LSM element angular dependence. The random orientation of collagen bundles in the skin dermis results in an LSM transformation to its form inherent to a multiple-scattering diffuser.

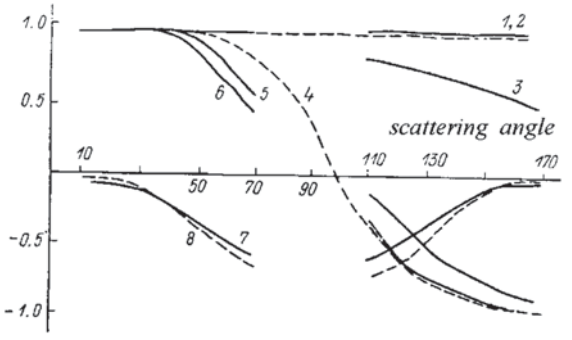

Figure 1.24 Angular distributions for the LSM elements: M_{22} (1, 2, 3) M_{33} (4, 5, 6), M_{12} (7), and M_{21} (8) for disc-like erythrocytes (3, 4, 7, 8) and spherocytes (2, 6). Dashed lines refer to theoretical analysis using the Mie formulae (from Ref. 345).

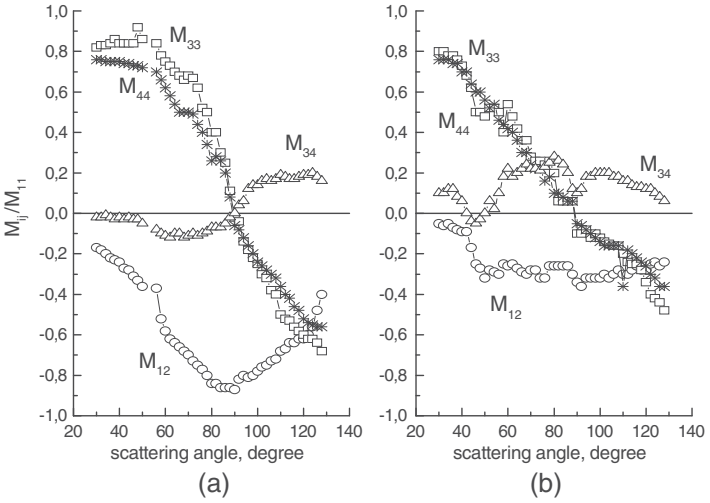

Figure 1.25 Experimental angular dependencies for the LSM elements of (a) normal (age of 56 y, 5 h after death), and (b) cataractous (age of 88 y, 5 h after death) human lenses. Measurements were performed at a wavelength of 633 nm.[360]

Study of transmission and scattering polarization properties of a tissue gives a basis that allows one to consider in what way the alteration of spatial protein organization would lead to turbidity. The measurements of the angular dependences of LSM elements for the human eye lens carried out using the laser polarization nephelometer[249] demonstrate substantial distinctions in these dependencies for normal and turbid (cataractous) lenses[360] (Fig. 1.25).

These distinctions are due to large nonspherical scattering particles appearing in the medium of a turbid lens (because of formation of high-molecular proteins). A transparent lens is featured by a monodisperse system of small-diameter scatterers. A turbid lens contains a reasonable fraction of larger scatterers. The high sensitivity of the LSM angular dependencies to the variations in the medium structure makes it possible to employ the LSM measurements for early diagnostics of the alterations in the tissue structure that are related to the cataract appearance.

The possibility of elastic light scattering utilization to quick identification of the bacteria suspensions is a highly attractive field of applications. However, the reproducibility of the light scattering measurements is often insignificant for various bacteria and other bioparticles obtained in different laboratories, unlike the scattering properties measured for suspensions of physical particles (i.e., suspension of identical polystyrene spheres serves as a standard). For example, the reproducibility and sensitivity of polarized light scattering were examined for cylinder samples of bacterial suspensions under different growing conditions.[361] The angular dependencies of certain LSM

elements (predominantly M_{34}/M_{11}) were studied. The M_{34}/M_{11} angular dependencies were found to be highly correlated with the bacterial cell sizes. From the viewpoint of significant variations revealed to different growing conditions, it was concluded that a better technique is necessary to distinguish scattering patterns associated with such alterations of bacterium properties.

1.9.5 Effects of circular light probing and optical activity

Many tissues and systems of bioparticles demonstrate the effects of optical activity that are manifested in circular dichroism and circular birefringence. The optical activity of biological objects may be conditioned by the optical activity of the substance they are formed from and by their structure peculiarities. Circular intensity differential scattering (CIDS) is a difference between scattered intensities for left and right circularly polarized (RCP) incident light. The CIDS effects can be investigated by measuring the LSM element M_{14}.[12] The so-called form-CIDS is an anisotropy caused by the helical structure of a particle.[76] The CIDS interrelation with the scatterer structure has been considered by Bustamante et al.[362–364] The measurements of CIDS are used to study secondary and ternary structures of macromolecules[365] and the polymerization of hemoglobin in sickling RBC.[366]

The experimental studies of the polarization properties of laser radiation scattered by optically active tissues[359] show that laser polarization nephelometry can be employed for developing noninvasive methods for diagnostics of the bone tissue structure.

Circularly and elliptically polarized laser light and a standard optical polarimeter were used to observe the alterations of polarization properties of light back-scattered from tissue samples at cancer development.[323,367] It was shown that by tracking the Stokes vector of the detected light on the Poincaré sphere, a differentiation between normal and cancerous tissue can be assessed.

If a tissue contains a substance exhibiting optical activity, then the polarization measurements provide a noninvasive procedure for determining the concentration of this substance. For example, an important diagnostic problem is the monitoring and precise control of blood sugar elevation for patients with diabetes.[368–371]

Polarimetric quantification of glucose is based on the phenomenon of optical rotatory dispersion whereby a chiral molecule in an aqueous solution will rotate the plane of linearly polarized light passing through the solution.[6,9,294,368–371] The angle of rotation depends linearly on the concentration of the chiral species, the pathlength through the sample, and a constant for the molecule called the specific rotation. The net rotation is expressed as $\varphi = \alpha_\lambda LC$, where α_λ is the specific rotation for the species in $dm^{-1}(g/L)^{-1}$ at the wavelength λ, L is the pathlength in dm, and C is the concentration in g/L. Glucose in the body is dextrorotatory (rotates light in

the right-handed direction) and has a specific rotation of $+52.6\ \mathrm{dm}^{-1}(\mathrm{g/L})^{-1}$ at the sodium D-line of 589 nm.

At physiological concentrations and pathlengths of about 1 cm, optical rotations due to glucose are on the order of 0.005 deg. A number of techniques for obtaining measurements with this high degree of accuracy exist and generally fall into two categories: those that utilize crossed polarizers to measure rotation via amplitude changes, and those that measure the relative phase shift of modulated polarized light passing through the sample.[9,294,368–371]

It is difficult to measure *in vivo* sugar concentration in blood because strong light scattering by the skin causes light depolarization. For this reason, a number of investigators have suggested the anterior chamber of the eye (aqueous humor) as a site that is well suited for polarimetric measurement since scatter in the eye is generally very small compared to other tissues.

The use of optical polarimetry for the noninvasive measurement of physiological glucose concentration in the anterior chamber of the eye of New Zealand white rabbits was reported.[371] Measurements were acquired using a custom-designed laser-based optical polarimetry system (Fig. 1.26). Aqueous humor-based polarimetric measurements were obtained by coupling light through the anterior chamber of the eye. Blood glucose levels were first stabilized and then altered with intravenous dextrose and insulin administration and measured every 3–5 min with a standard glucometer and intermittently with a glucose laser analyzer. Acquired polarimetric glucose signals were calibrated to measured blood glucose concentration. Errors in glucose concentration prediction were shown to be related to gross movement of the rabbit during the procedures, incurring time-varying corneal birefringence effects that directly affect the measured polarimetric signal. These effects can be compensated for with appropriate design modifications. The technique provides a basis for the development of a noninvasive polarimetric glucose monitor for home, personal, or hospital use.

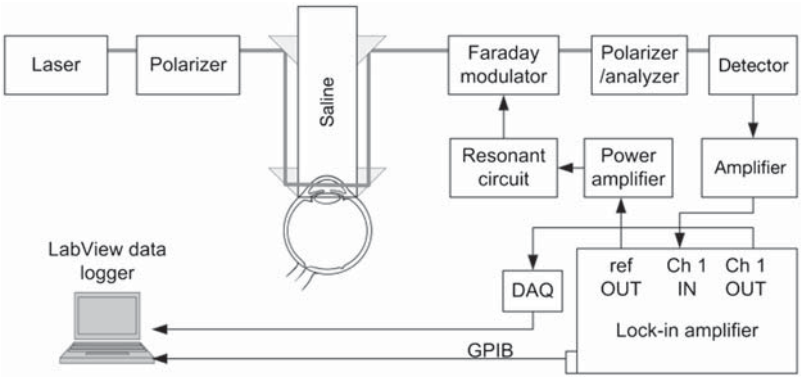

Figure 1.26 The polarimetric experimental setup employed for the sensing glucose concentration in the eye. DAQ, data acquisition; GPIB, general purpose interface bus.[371]

1.10 Controlling Optical Properties of Tissues

Reflection, absorption, and scattering in tissues and blood can be effectively controlled by different methods.[9,10,372–399] Tissue as a scattering medium shows all optical effects that are characteristic to turbid physical systems. It is well known that turbidity of a dispersive physical system can be effectively controlled using an immersion liquid by matching of refractive indices of the scatterers and the ground material. The living tissue allows one to control its optical (scattering) properties using various physical and chemical actions such as compression, stretching, dehydration, coagulation, UV irradiation, exposure to low temperature, and impregnation by chemical solutions, gels, and oils.[9,10,372–399]

Control of *in vivo* tissue optical properties is very important for many medical applications. A number of laser surgery, therapy, and diagnostic technologies include tissue compression and stretching for better transportation of the laser beam to underlying layers of tissue. The human eye compression technique allows one to perform transscleral laser coagulation of the ciliary body and retina/choroid.[375–377] The possibility of selective translucence of the upper tissue layers should be very useful for developing eye globe imaging techniques and for detecting local inhomogeneities hidden by a highly scattering medium in functional tomography. Results on control of human sclera optical properties by tissue impregnation with hyperosmotic chemicals, such as trazograph (x-ray contrast), glucose and polyethylene glycol (PEG), as well as hypaque-60 (x-ray contrast), were reported.[9,10,372–374,378,379,383–386]

In general, the reduced scattering coefficient μ_s' of tissue is dependent on refractive index mismatch between the extracellular fluid and the cellular membrane; between cytoplasm, cell nucleus, organelles, melanin, and cellular membrane; and for fibrous tissue (like sclera, dermis, and breast) between an interstitial medium and collagenous fibers. For hematous tissue like the liver, its impregnation by solutes with different osmolarity also leads to refractive index matching and reduction of the scattering coefficient, however, the effect is not so pronounced as for skin and sclera due to cells changing size as a result of osmotic stress.[372,373]

Soft tissue is composed of closely packed groups of cells entrapped in a network of fibers through which water percolates. At a microscopic scale, the tissue components have no pronounced boundaries. They appear to merge into a continuous structure with spatial variations in the refractive index. As it was discussed, to model such a complex structure, it is necessary to resort to a statistical approach.

It has already been shown that the tissue components that contribute most to the local refractive-index variations are the connective tissue fibers (bundles of elastin and collagen), cytoplasmic organelles (mitochondria, lysosomes, and peroxisomes), cell nuclei, and melanin granules.[9,204,248,378,400–403]

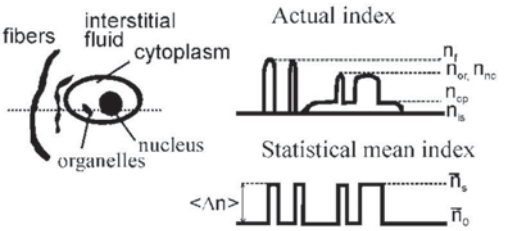

Figure 1.27 Spatial variations of the refractive index of a soft tissue.[204] A hypothetical index profile through several tissue components is shown along with the profile through a statistically equivalent volume of homogeneous particles.

Figure 1.27 shows a hypothetical index profile formed by measuring the refractive index along a line in an arbitrary direction through a volume of tissue. The widths of the peaks in the index profile are proportional to the diameters of the elements, and their heights depend on the refractive index of each element relative to that of its surroundings. In accordance with this model, the origin of the index variations will be presented by a statistically equivalent volume of discrete particles having the same index but different sizes.

The statistical mean index profile in Fig. 1.27 illustrates the nature of the approximation implied by this model. The average background index is defined as the weighted average of refractive indices of the cytoplasm and the interstitial fluid, n_{cp} and n_{is}, as[204]

$$\bar{n}_0 = f_{cp} n_{cp} + (1 - f_{cp}) n_{is}, \tag{1.155}$$

where f_{cp} is the volume fraction of the fluid in the tissue contained inside the cells, $n_{cp} = 1.367$, and $n_{is} = 1.355$.[402] Since approximately 60% of the total fluid in soft tissue is contained in the intracellular compartment, it follows from Eq. (1.155) that $\bar{n}_0 = 1.362$. The refractive index of a particle can be defined as the sum of the background index and the mean index variation

$$\bar{n}_s = \bar{n}_0 + \langle \Delta n \rangle, \tag{1.156}$$

which can be approximated by another volume–weight average

$$\langle \Delta n \rangle = f_f (n_f - n_{is}) + f_{nc} (n_{nc} - n_{cp}) + f_{or} (n_{or} - n_{cp}). \tag{1.157}$$

Here, subscripts *f*, *is*, *nc*, *cp*, and *or* refer to the fibers, interstitial fluid, nuclei, cytoplasm, and organelles, respectively, which are the major contributors to index variations. The terms in parentheses in this expression are the differences between the refractive indices of the three types of tissue components and their respective backgrounds; the multiplying factors are the volume fractions of the elements in the solid portion of the tissue. The refractive index of the connective-tissue fibers is about 1.47, which corresponds to about 55% hydration of collagen, its main component. The

nucleus and the cytoplasmic organelles in mammalian cells that contain similar concentrations of proteins and nucleic acids, such as mitochondria and the ribosomes, have refractive indices that lie within a relatively narrow range (1.38–1.41).[402] Accounting for this and supposing that $n_{nc} = n_{or} = 1.40$, the mean index variation can be expressed in terms of the fibrous-tissue fraction f_f only:

$$\langle \Delta n \rangle = f_f(n_f - n_{is}) + (1 - f_f)(n_{nc} - n_{cp}). \tag{1.158}$$

Collagen and elastin fibers comprise approximately 70% of the fat-free dry weight of the dermis, 45% of the heart, and 2 to 3% of the nonmuscular internal organs.[204] Therefore, depending on tissue type, $f_f = 0.02$–0.7, which corresponds to $<\Delta n> = 0.035$–0.09.

The mean refractive index $\bar{n}$ of a tissue is defined by the refractive indices of material of the scattering centers n_s and ground matter n_0 [see Eq. (1.155)]

$$\bar{n} = f_s n_s + (1 - f_s) n_0, \tag{1.159}$$

where f_s is the volume fraction of the scatterers.

The $n_s/n_0 \equiv m$ ratio determines the scattering coefficient. For example, in a simple monodisperse model of scattering dielectric spheres (Mie theory)[404]

$$\mu_s' = 3.28\pi a^2 \rho_s \left(\frac{2\pi a}{\lambda}\right)^{0.37} \times (m-1)^{2.09}, \tag{1.160}$$

where a is the radius of the particles and ρ_s is their volume density. Equation (1.160) is valid for noninteracting Mie scatterers $g > 0.9$; $5 < 2\pi a/\lambda < 50$; $1 < m < 1.1$.

It follows from Eq. (1.160) that even a 5% change in the refractive index of the ground matter ($n_0 = 1.35 \rightarrow 1.42$), when that of the scattering centers is $n_s = 1.47$, will cause a sevenfold decrease of μ_s'. In the limit of equal refractive indices for nonabsorbing particles, $m = 1$, and $\mu_s' \rightarrow 0$.

Light scattering and absorption of particles that compose tissue is calculated by Mie theory. The relevant parameters are the size (radius a) and shape of the particles, their wavelength-dependent complex refractive index

$$n_s(\lambda_0) = n_s'(\lambda_0) + i n_s''(\lambda_0), \tag{1.161}$$

the refractive index of the dielectric host (ground material) $n_0(\lambda_0)$, and the relative refractive index $m = n_s/n_0$. The imaginary part of the complex refractive index of scatterer material is responsible for light loss due to absorption. Mie theory yields the absorption and scattering efficiencies and the phase function from which the absorption and scattering coefficients $\mu_s = \rho\sigma_s$ and $\mu_a = \rho\sigma_a$ and the scattering anisotropy g are calculated; ρ is the scatterer (particle) density, σ_s and σ_a are the scattering and absorption cross sections, respectively [see Eqs. (1.15)–(1.17)].

The introduction of the specific scattering and absorption coefficients extrapolated to a volume fraction of 100% is useful for describing scattering and absorption properties of tissues with controlled structural properties.[405,406] In that case and when the particles are sufficiently diluted to prevent dependent scattering, the scattering, transport scattering and absorption coefficients are proportional to the dimensionless volume fraction of scatterers $c_s \equiv f_s$

$$\mu_s = c_s\bar{\sigma}_s, \mu_s' = c_s\bar{\sigma}_s[1 - g(\lambda_0,a)], \mu_a = c_s\bar{\sigma}_a, \tag{1.162}$$

where the specific scattering and absorption coefficients $\bar{\sigma}_s$ and $\bar{\sigma}_a$ are expressed in cm^{-1}. The optical parameters of broad-banded particle size distributions are averaged values over the distribution weighted by the volume fractions of particles with different diameters. The resulting specific optical coefficients are the averaged values and can be defined analogously to Eqs. (1.15)–(1.17).

Mie theory predicts that scattering introduced by spherical micrometer-sized particles is strongest if particle radius and wavelength are of the same order of magnitude. Mie theory is strictly applicable only to particles of particular regular shapes, but results are still useful if the shape is irregular. The oscillatory structure of the scattering coefficient and anisotropy factor as a function of particle size, which is observed with spherical particles (Fig. 1.28), is averaged out. The transport scattering coefficient increases

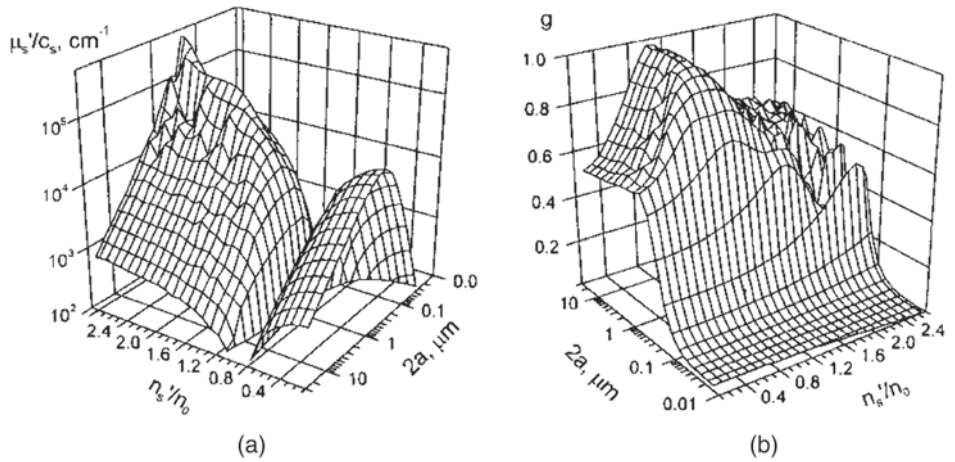

Figure 1.28 Scattering properties of nonabsorbing particles at the wavelength 633 nm calculated by Mie theory. (a) Transport scattering coefficient strongly depends on both the particle size and relative refractive index. This graph is approximately symmetric. The axis of symmetry is at $n_s'/n_0 = 1$. While the transparent scattering coefficient equals zero at that point, (b) the scattering anisotropy factor is maximal. In some parts of the range shown, the functions are not monotonous but rapidly oscillating.[406]

strongly with the ratio n_s'/n_0. In its turn, the scattering anisotropy factor is maximal when this ratio approaches 1 (Fig. 1.28).

For the matched refractive indices of scatterers and background material the scattering coefficient goes to zero, that means that only absorption is responsible now for the light beam extinction. However, as it follows from Mie theory, absorbing particles suspended in an index-matched medium cause strongly forward-directed resonance scattering. Light absorption by such particles is smaller than expected from their bulk absorption coefficient.[405,406] For 1-μm diameter particles with $n_s = 1.6$ and bulk absorption coefficient of their material equal to 10^4 cm^{-1} in an index-matched medium, the particle system absorption coefficient $\mu_a = c_s \times 4120$ cm^{-1}.

If particle size and ratio of refractive indices are fixed, the wavelength dependencies are caused by the spectral variation of the ratio of particle size and wavelength. For particles with a refractive index close to that of the host (see Fig. 1.28), the scattering coefficient of the particle system with a diameter of particles smaller than the wavelength decreases with wavelength, while that of a system with a diameter of particles larger than the wavelength is almost constant. The scattering anisotropy factor depends less on the wavelength. There are plateaus if the particles are much smaller (isotropic scattering) or larger (highly anisotropic scattering) than the wavelength with a steep increase between.[406]

It is possible to increase significantly the transmission through a soft tissue by its squeezing (compressing) or stretching. The optical clearing of living tissue is due to its optical homogeneity achieved through the removal of blood and interstitial fluid from the compressed site. This results in a higher refractive index of the ground matter, whose value becomes close to that of scatterers (cell membrane, muscle, or collagen fibers).[375,376] Indeed, the absence of blood in the compressed area also contributes to altered tissue absorption and refraction properties. Certain mechanisms underlying the effects of optical clearing in tissues were proposed in Refs. 375 and 376. It should be emphasized, however, that squeezing-induced effects in tissues containing little blood, such as sclera, are characterized by a marked inertia (a few minutes) because of the relatively slow water diffusion from the compressed region.[375,378] It was suggested that compression of sclera may displace water from interspace of collagen fibrils increasing the protein and mucopolysaccharide concentrations. Since these proteins and sugars have a refractive index closer to that of the collagen fibrils, a more index-matched environment can be created. On the other hand, compression reduces specimen thickness, which might increase the effective scatterer and chromophore concentration inside the tissue.[376] Therefore, compression may also give rise to the increase in tissue scattering and absorption coefficients. Sometimes the scatterer concentration increase is likely to be more dominant than the reduction in index mismatch.[376]

It is possible to achieve a marked impairment of scattering by matching the refractive indices of scattering centers and ground matter by means of intratissue administration of appropriate chemical agents. Conspicuous experimental optical clearing in the human sclera and skin in the visible and NIR wavelength range induced by administration of x-ray contrast (verografin, trazograph, hypaque, omnipaque, glucose, propylene glycol, polyethylene glycol, glycerol and other solutions) has been described in Refs. 9, 374, and 378–399. Coordination between refractive indices in multicomponent tissues showing polarization anisotropy (e.g., cornea) leads to its decrease.[9,248] Osmotic and diffusive processes that occur in sclera treated with an optical clearing agent (OCA) are also important.[378] Osmotic phenomena appear to be involved when optical properties of cells and tissues are modulated by sugar, alcohol, and electrolyte solutions. This may interfere with the evaluation of hemoglobin saturation with oxygen or identification of such absorbers as cytochrome oxidase in tissues by optical methods.[372,373]

A marked clearing effect through the human[385] and the rat[383] skin and the rabbit sclera[385,386] occurred for an *in vivo* tissue within a few minutes of topical application or intratissue injection of glycerol, glucose, verografin, or trazograph.

Albumin, a useful protein for index matching in phase contrast microscopy experiments, can be used as the immersion medium for tissue study and imaging.[402] Proteins smaller than albumin may offer a potential alternative to the relatively high scattering of albumin. Alternatively, medical diagnosis or contrasting of a lesion image can be provided by the enhancement of tissue scattering properties by applying, for instance, the acetic acid that was used successfully as a contrast agent in optical diagnostics of cervical tissue.[402] It has been suggested that the aceto-whitening effect seen in cervical tissue is due to coagulation of nuclear proteins. Therefore, an acetic acid probe may also prove extremely significant in quantitative optical diagnosis of precancerous conditions due to its ability to selectively enhance nuclear scatter.[402]

The loss of water by tissue seriously influences its optical properties. For instance, during *in vitro* study of the human aorta the absorption coefficient increased by 20% to 50%, especially in the visible range, when an average of 46.4% of the total tissue weight was lost as a result of dehydration.[406] The weight loss was accompanied with an average thickness shrinkage of 19.5%. The loss of water decreased the sample thickness. Primarily because of shrinkage the absorption coefficient was increased in the spectral range of 400 to 1300 nm. There was only a slight increase of 2–15% of the reduced scattering coefficient in the visible range.

Natural physiological changes in cells and tissues are also responsible for their altered optical properties, which may be used as a measure of these changes, e.g., for glucose concentration monitoring.[369,380–382]

A model of the human sclera in a local region can be represented as a slab with a thickness d that is filled by thin and long dielectric cylinders (collagen fibers) with average diameter ~ 100 nm and refractive index $n_c = 1.474$. The cylinders are located in planes that are parallel to the slab surface, but within each plane their orientations are random. The interstitial space is filled by a homogeneous base substance with the refractive index $n_0 = 1.345$. This refractive index is a controlled parameter and can be changed in the range from 1.345 to 1.474. For $n_c = n_0 = 1.474$, the medium becomes totally homogeneous and optically transparent if absorption of scatterers is small.[405,406]

The described model of tissue is applicable to any fibrous tissue including skin dermis and muscle. Indeed, refractive indices and fiber diameters should be changed. The transmission of collimated light by a tissue layer of thickness d is defined as Bouguer's law [Eq. (1.2)], where $\bar{\tau} \equiv \mu_t = \mu_a + \mu_s$ is the extinction coefficient, and μ_a and μ_s are the absorption and scattering coefficients, respectively. For the human sclera at the wavelength $\lambda = 650$ nm, the absorption coefficient $\mu_a \cong 0.08$ cm^{-1}, and the reduced scattering coefficient $\mu_s' = \mu_s(1 - g) \cong 25$ cm^{-1}, where g is the scattering anisotropy factor.[408] For $g = 0.9$, $\mu_s \cong 250$ cm^{-1}.

To describe the kinetics of the refractive index and corresponding decrease of the scattering coefficient when a chemical agent diffuses within the interstitial substance of a tissue, the model of free diffusion was used.[378,409] The approximate solution of diffusion equation for a plane slab with a thickness d, at the moment $t = 0$ and concentration c_0 (the initial concentration of this substance within the slab is equal to 0; i.e., $t = 0$, $0 \le x \le d$, $c = 0$) has the form

$$c \cong c_0[1 - \exp(-t/\tau)], \tag{1.163}$$

where

$$\tau = \frac{d^2}{\pi^2 D} \tag{1.164}$$

is the diffusion constant, D is the diffusion coefficient, and d is the thickness of the scleral sample. This relation is very close to the relation describing diffusion through a partially permeable membrane.[378,409] These equations are valid for diffusion through a homogeneous slab when OCA is applied to both surfaces of the slab. However, due to its fibrous structure, a tissue can be presented as a porous material that leads to modification of the agent diffusion coefficient

$$D = D_0/p. \tag{1.165}$$

Here, D_0 is the chemical agent diffusion coefficient within the interstitial fluid, and p is the porosity coefficient defined as

$$p = (V - V_c)/V, \tag{1.166}$$

where V is the volume of the scleral sample and V_c is the volume of collagen fibers.

When applying an OCA, a change in pH level of the environment is very important, because swelling or shrinkage of tissue is expected. The swelling or shrinkage of a fibrous tissue is caused not only by the increase (decrease) of collagen (elastin) fibril size but also by the increase (decrease) of the sample volume due to the rise (diminution) of the mean distance between fibrils. It is well known that the change of the environmental pH to the more acidic or more alkaline side from a colloid isoelectric point increases the degree of swelling. It is explained by the appearance of a positive or negative charge of colloid particles and, therefore, increase of hydration degree. In general, the initial pH condition of the tissue under study and the acid or alkaline nature of the impregnated solution may lead to different dependencies of tissue thickness or volume on chemical agent concentration (or time of impregnation) due to changes of pH. Such behavior of a tissue sample should be taken into account when optical measurements are used for estimation of tissue properties. For example, the swelling or shrinkage was observed for different initial conditions of scleral tissue sample preparation and solutions used.[9,378,384–386]

A fiber optic photodiode array spectrometer was used for *in vitro* and *in vivo* light transmittance or reflectance measurements of sclera in the spectral range 400–800 nm.[386] In *in vitro* study, the conjunctiva and ciliary body, as well as the retina with choroid were removed. The mean thickness of samples was about 0.5 mm. A sample under study was fixed on a plastic plate with a square aperture of 5×5 mm^2 (effective impregnation by a chemical agent via both surfaces of the sample was provided) and placed in a 5-ml cuvette filled with an OCA. Various solutions (glucose, trazograph, verografin, and propylene glycol) were used, which do not have strong absorbing bands within the used spectral range.

To understand the mechanisms of scleral tissue optical clearing, the collimated transmittance spectra and change of the scleral sample weight were measured concurrently with the administration of glucose solution.[386] Figure 1.29 illustrates the kinetics of transmittance spectra. It is easily seen that the untreated sclera is a poorly transparent media for visible light. Glucose administration makes this tissue highly transparent. As it follows from Fig. 1.30, the characteristic time response of human optical clearing is about 5 min.

Based on such measurements, the two-stage model of action of hyperosmotic liquid on a fibrous tissue was suggested.[386] At the first stage, which takes place approximately 5 min after a sample is placed in a glucose solution, besides substantial optical clearing, an increase of sample mass was observed. The latter is due to considerable swelling of collagen fibers in glucose solution with pH = 3.5 (40% glucose from a drugstore, prepared for

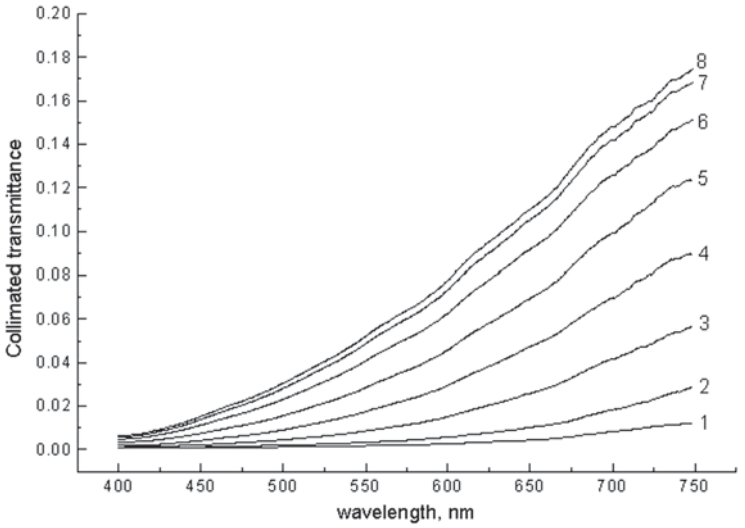

Figure 1.29 The time-dependent collimated transmittance of the human sclera sample impregnated by 40% glucose: (1) 10 sec, (2) 1 min, (3) 2 min, (4) 3 min, (5) 4 min, (6) 5 min, (7) 5 min, and (8) 8.5 min after the scleral sample was immersed in glucose.[386]

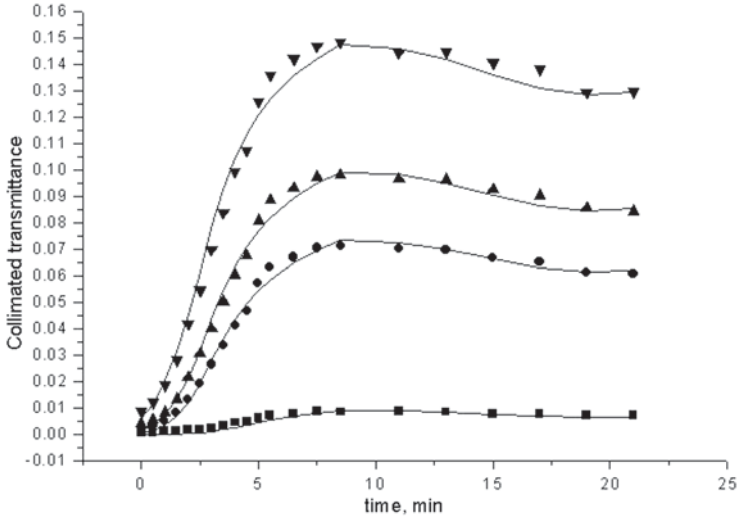

Figure 1.30 The time-dependent collimated transmittance of the human scleral sample measured at 420 nm (squares); 589 nm (circles); 630 nm (up triangles); and 700 nm (down triangles) concurrently with administration of 40% glucose. [386]

intravenous injection). In spite of tissue thickness (mass or volume) increase, the first stage is characterized by a highly increased tissue transmittance caused by a very effective refractive index matching.

During the following stage, which occurs after 5 min, the matter diffusion (and correspondingly refractive index matching) saturates, but tissue thickness

increases due to the glucose solution acting in the space between fibrils. At this stage, transmittance is also saturated and even goes slightly down.

To estimate the matter diffusion coefficient, the experimental data for collimated transmittance (Figs. 1.29 and 1.30) and the time-dependent measurements of tissue sample mass (thickness) changes under immersion solution action can be used. The model of glucose transport in fibrous tissue is described in Ref. 386. Equations (1.165) and (1.166) are the basis for this model, which can be used for reconstruction of the diffusion constant. The estimated average value of the diffusion coefficient of glucose transport in the scleral sample is equal to $(3.45 \pm 0.46) \times 10^{-6}$ cm^2/sec at a temperature of 20 °C.

In vivo measurements were done for a rabbit eye (see Fig. 1.31). The surface temperature of the rabbit eye was ~ 38 °C. As an OCA for the optical clearing of sclera, 40% glucose was administered to the eye by drops. A significant decrease of the reflectance during the first 5 min of glucose administration is seen. Dips appearing at 420, 530, and 570 nm are caused by blood perfusion. The lower reflectance at 420 nm is caused by the strong absorption of blood. Evidently, more fast decay reflects blood perfusion kinetics due to eye conjunctiva and sclera inflammation caused by light irradiation and the osmotic action of glucose. Because blood has less influence at 630 and 700 nm, measured kinetic responses can be used for *in vivo* estimation of diffusion coefficient for glucose in scleral tissue.

The kinetic response of optical properties (modulation depth and phase shift of intensity modulation of the back-scattered light) of the human eye sclera via interval of a chemical agent (solution, gel, or oil) administration was measured using a photon-density wave (frequency-domain) technique.

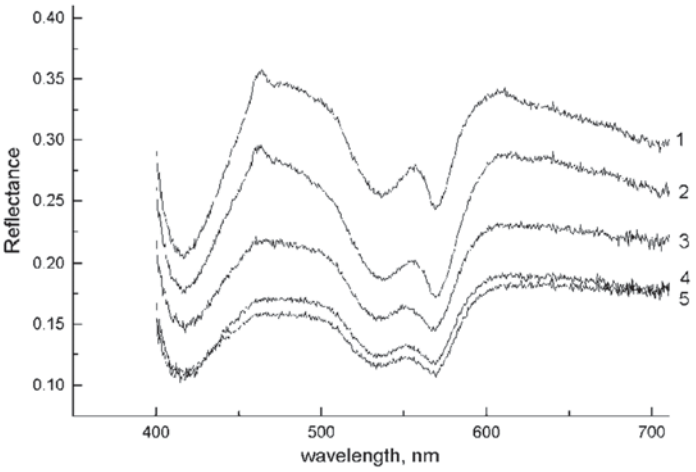

Figure 1.31 The *in vivo* time-dependent reflectance spectra of a rabbit eye sclera measured concurrently with administration of 40% glucose: (1) 1 min, (2) 4 min, (3) 21 min, (4) 25 min, and (5) 30 min after dropping the glucose solution into the rabbit eye.[386]

When intensity of the light source is modulated at a frequency ω, a photon density wave is induced in a scattering medium[9,372,380,408] (see Chapters 3 and 7)

$$A(r) = A_{dc} + A_{ac}\exp[-i(\omega t - \theta)], \tag{1.167}$$

where A_{dc}, A_{ac}, and $(\omega t - \theta)$ are the dc and ac components of the amplitude of the photon-density wave and its phase, respectively.

Photon-diffusion theory provides independent determination of the absorption and reduced scattering coefficients from measurements at a single modulation frequency. The expressions for the measured quantities as the phase delay θ and ac amplitude A_{ac} have been presented elsewhere[9] (see also Chapters 3 and 7). These expressions depend on the source–detector separation r, reduced scattering coefficient μ_s', and absorption coefficients μ_a.

The intensity and phase of photon-density waves generated by an NIR optical source were measured at several source–detector separations. The light source was a laser diode with a wavelength of 786 nm and 4-mW power at the end of a coupled multimode fiber (core diameter 62.5 μm).[374] The intensity modulation depth of approximately 80% at a frequency of 140 MHz was provided by modulation of the injection current of the laser diode. The experimental setup was designed at the University of Pennsylvania.

A multifiber detection system with small source–detector separations together with a Dicon multichannel fiber optic switcher has been used for immersion experiments on the human sclera *ex vivo*. The whole human eyeball was studied. Data shown in Fig. 1.32 are the temporal changes of ac amplitude during trazograph administration for three different source–detector separations and two different techniques of immersion solution administration—by injection and by drops. The clearing of scleral tissue was observed during the first 3 min of trazograph administration by injection. For small source–detector separations (about 1–2 mm) and a relatively large one (3.5 mm), the temporal

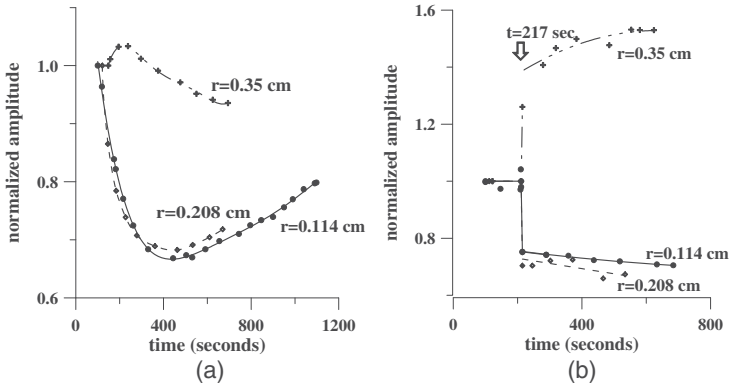

Figure 1.32 Frequency-domain measurements. The time-dependent changes in amplitude of optical signal from the human eye globe *ex vivo* after (a) trazograph injection and (b) trazograph drops in the vicinity of the detector fiber tip.[374]

dependencies are quite different. Keeping in mind that at the first 3 min after injection of the chemical agent the positive time scale corresponds to a decrease of scattering due to tissue immersion, the opposite tendencies of considered dependencies can be understood as the following. For small source–detector separation close to the back-reflectance geometry, intensity of reflected light decreases along with scattering; and for rather large separations, when lateral photon diffusion effects are important, intensity at first goes up with decreased scattering, but if scattering continues to decrease, intensity will lessen. That is why a local maximum on a curve for a separation of 3.5 mm was observed. At the third minute after chemical agent injection, due to its diffusion into neighboring tissue regions, amplitudes for all separations have a tendency to go to initial values. Another technique of chemical agent administration by drops shows the same tendencies for small and large separations as for injection, but essential changes of the amplitudes happen momentarily after chemical agent drops are applied, and then amplitudes slowly change in the opposite directions. Such behavior depends on the specific features of a chemical agent application, which are (1) superficial impregnation (underlines the importance of surface immersion effect and (2) continuous renovation of the chemical agent on the tissue surface (many drops during the measurement interval).

This study shows that the impregnation of the eye sclera by hyperosmotic chemical agents affects the reversible refractive index matching of the collagen fibrils and interstitial media that leads to dramatic reduction of the tissue scattering ability.

Inhomogeneities of the trazograph concentration in the tissue volume cause macroscopic spatial inhomogeneities of polarization structure of scattered light; such polarization structure of the sclera image can be easily observed using an optical scheme with a "white" light source and a tissue sample placed between two crossed polarizers. Figure 1.33 illustrates the evolution of such polarization images during scleral clearing.[9]

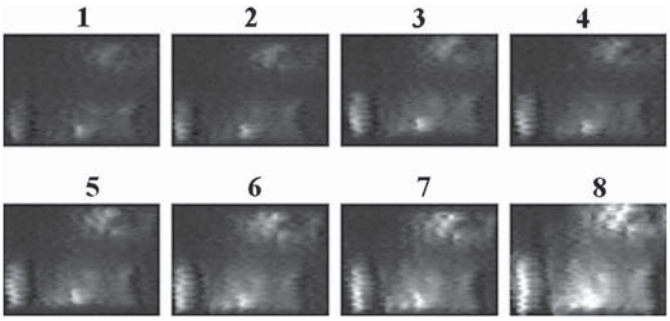

Figure 1.33 Polarization images of sclera sample (white light source, crossed polarizers) for different stages of sclera clearing. Time elapsed after trazograph administration: (1) 4 min, (2) 5 min, (3) 6 min, (4) 7 min, (5) 8 min, (6) 9 min, (7) 5 min, and (8) 10 min.[9] The tissue-supporting wires are seen for the translucent sample.

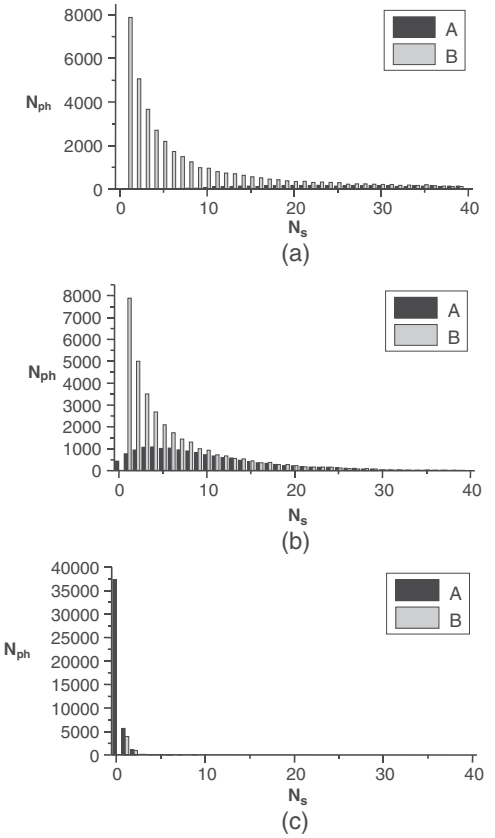

Figure 1.34 Model of the human eye sclera, refractive indices of scleral components: collagen, $n_c = 1.47$, and ground media, n_0. Calculated distributions of the number N_{ph} of (A) forward- and (B) back-scattered photons ($\lambda = 800$ nm) via number of collisions N_s (two integrating sphere geometry): (a) $n_0 = 1.35$ (normal tissue); (b) $n_0 = 1.39$ (slightly immersed tissue); and (c) $n_0 = 1.45$ (strongly immersed tissue).[9]

MC modeling of the initially collimated photons transport within the sclera tissue, represented as a fibrous structure combined of thin and long collagenous cylinders randomly distributed within the ground medium, allows one to understand the character of transition from multiple to single scattering due to refractive index matching.[9,229,378] Results of such modeling for a system of scattering cylinders with a mean diameter of 120 nm, a mean separation between fibrils centers of 285 nm, and a refractive index $n_c = 1.47$ surrounded by an interstitial medium with a changeable refractive index are shown in Fig. 1.34. Calculations were done in a geometry very close to the experimental one for 1-mm sample thickness.[9,229,378] The numbers of back- and forward-scattered photons collected by integrating spheres were calculated. It is easy to see that for partly matched refractive indices the unscattered and low-step scattered photons dominate in both

directions—forward and backward. In the NIR, the optical clearing of tissue and transformation of the scattering mode from multiple to low-step or even single begins much earlier than for visible light. The validity of such calculations were proved using spectral measurements of human scleral tissue at different stages of clearing.[9,378]

It has been shown that administration of osmolytes to fibrous tissue and cell structures allows one to control effectively their optical characteristics. The kinetics of tissue optical clearing are characterized by a time response of about 5–10 min, which is defined by the dynamics of refractive index matching, which in turn depends on the diffusivity of immersion OCA in tissue and tissue thickness. Tissue swelling plays an important role in tissue clearing; it leads to saturation or even a slight reduction of tissue optical transmittance for more prolonged action of some OCAs.

Temporal optical characteristics can be used to determine the diffusion coefficient of endogenous (metabolic) and exogenous (chemical agent) fluids in the human sclera, skin, and other tissues. Obtained magnitude for the diffusion coefficient of glucose in the human sclera corresponds well to values of the diffusion coefficient for small molecules diffusing in water with some hindering caused by fibrous structure of the tissue.[409]

Particularly for blood, the refractive index mismatch between erythrocyte cytoplasm and blood plasma is important. The refractive index of erythrocyte cytoplasm is mostly defined by hemoglobin concentration (blood hematocrit).[410] The scattering properties of blood are also dependent on erythrocyte volume and shape, which are defined by blood plasma osmolarity,[113,410] and aggregation or disaggregation ability.[411–414] The feasibility of index matching as a method to overcome the limited light penetration through blood for capturing tissue images has been demonstrated.[415–417] Glucose, low- and high-molecular dextrans, x-ray contrasting, glycerol, and other agents were used to increase the refractive index of blood plasma closer to that of erythrocyte cytoplasm to improve penetration depth so that images of objects behind the blood layer could be obtained.

The reduced scattering coefficient μ_s' of blood depends on a mismatch of averaged refractive indices of blood plasma and RBC cytoplasm. The ratio $n_{RBC}/n_{bp} \equiv m_{RBC}$ determines the scattering coefficient, n_{RBC} is the mean refractive index of RBC cytoplasm, and n_{bp} is the mean refractive index of the blood plasma. For modeling the RBC ensemble as a monodisperse system of noninteracting scattering dielectric spheres of radius a irradiated at an NIR wavelength λ, when $5 < 2\pi a/\lambda < 50$, anisotropy scattering factor $g > 0.9$, and $m_{RBC} \cong 1.05$, μ_s' is well described by Eq. (1.160).

The blood plasma contains up to 91% water, 6.5%–8% (about 70 g/L) various proteins, and about 2% low-molecular compounds. Because of the low concentration and relatively low refractive index of low-molecular chemical compounds, the mean blood plasma (background) index can be

estimated as the weighted average of the refractive indices of water (92%) n_w and proteins (8%) n_p

$$n_{bp} = f_w n_w + (1 - f_w) n_p, \tag{1.168}$$

where f_w is the volume fraction of water contained in plasma, $n_w = 1.329$ at 800 nm, and the index of proteins can be taken as $n_p = 1.470$.[9,218] Since approximately 92% of the total plasma is water, it follows from Eq. (1.168) that $n_{bp} = 1.340$.

The refractive index of RBC cytoplasm defined by the cell-bounded hemoglobin solution can be found from[410]

$$n_{RBC} = n_w + \beta c, \tag{1.169}$$

where c is the hemoglobin concentration in g/100 ml and $\beta = 0.001942$ at a wavelength of 589 nm. Since the scattering coefficient of blood is not significantly dependent on wavelength in the range from 580 to 800 nm, this value of β can be used for estimation of the refractive index of RBC in the NIR.[410]

As it follows from Eq. (1.160), about a tenfold reduction of the scattering coefficient μ_s' is expected when the refractive index of the blood plasma is changed from $n_{bp} = 1.340$ to 1.388 and the refractive index of RBC cytoplasm is kept constant, $n_{RBC} = 1.412$ (for hemoglobin concentration in cytoplasm of 400 g/L). [410]

A 1300-nm optical coherent tomography (OCT) system (see Chapter 7 in Volume 2) was used to take images of the reflector through circulating blood *in vitro*.[415] The total intensity of the signal off the reflector was used to represent penetration. As immersion substances, dextran (group refractive index of 1.52) and IV contrast (group refractive index of 1.46) were taken. Both dextran and IV contrast were demonstrated to increase penetration through blood: $69\% \pm 12\%$ for dextran and $45\% \pm 4\%$ for IV contrast. The studies of blood scattering reduction by the immersion technique using various solutions that are biocompatible with blood, such as saline, glucose, glycerol, propylene glycol, trazograph (x-ray contrasting substance for intravenous injection), and dextran, are described in Refs. 9, 416, and 417. For taking images of the reflector through a 1-mm layer of noncirculating fresh whole blood, 820- and 1310-nm OCT systems were applied. It was shown that for noncirculating blood sedimentation plays an important role in blood clearing using the immersion technique, and OCT allows for precise monitoring of blood sedimentation and aggregation. It was found that blood optical clearing is defined not only by the refractive index matching effect, but also by changes of RBC size and their aggregation ability when OCA are added. For example, when to whole blood twice diluted by a saline 6.5%-glycerol is added, the total attenuation coefficient is reduced from 42 to

20 cm^{-1}, and, correspondingly, the optical penetration at 820 nm increases to 117%. For other tested agents (glucose, dextrans, propylene glycol, and trazograph), the enhancement of penetration was from about 20% up to 150.5%.

Blood optical clearing has great perspectives for optical multimodal endoscopic imaging in clinics with using of OCT for atherosclerotic plaques and stent lesions monitoring.[418,419]

In a blood sedimentation study, the regular or irregular oscillations or jumps of the RBC/plasma boundary were observed. The 1-min time period of regular oscillations correlates well with the kinetics of the aggregation process, described by the two subsequent stages of formation of the linear and 3-D aggregates.[412,413,416,417]

Blood vessel's imaging through skin is another prospective optical clearing technology.[9,394,395,397,420–422] First demonstrated for rat skin by spectral reflectivity technique,[420] it is now widely used for different optical imaging modalities including speckle-correlation technologies.[397,422]

Blood vessels are also a pathway for OCA supply into living tissue. This was demonstrated for the first time for the animal model, when combined intravessel and intratissue injection were used for OCA delivery.[421]

1.11 Circularly Polarized Light

An alternative approach to the Mueller matrix and LSM has been developed.[367,423] The technique utilizes circularly polarized light. When circularly polarized light is multiply scattered within a turbid tissue-like scattering medium, the incident light is depolarized, and the depolarization rate depends strongly on the size and shape of scattering particles,[264,268] as well as on the number of scattering events.[424] A popular belief claims that linear polarization is better preserved in scattering tissue-like media compared to circularly polarized light. This, however, turns out to be true only when the size of scattering particles a is smaller than the wavelength of the incident light λ, $a < \lambda$. In media consisting larger scattering particle sizes ($a \geq \lambda$), the opposite situation happens. This phenomenon is known as the circular polarization *memory* of light,[425,426] and is of fundamental importance. Due to the intrinsic phase difference between its two basis linear components in the case of reflection at the medium surface, an incident state of circular polarization undergoes a flip in its helicity[426] and the same goes for the back-scattering of light. For the large particles with highly anisotropic scattering, the light becomes strongly forward scattered that preserves its initial helicity. Linear polarization possesses no such sense of the direction in which light travels.

Therefore, with a known stage of polarization of incident light, the helicity of detected optical radiation can be used to determine if it has been forward or back scattered. With the geometry of an experimental system that allows both portions of forward and back-scattered circularly polarized light to be

measured, changes in the medium under observation can be resolved by looking at the contribution of each part to the final signal. When combined with the knowledge of anisotropy of scattering particles within the medium, this effect provides a method for examining relevant properties of a scattering medium, including size, shape, number density, and refractive index of scattering particles.

The experimental realization of the technique utilizing circularly polarized light is presented in Fig. 1.35.

The back-scattered light is collected at distance d from the point of light incidence (see Fig. 1.35) and then passed through a polarimeter to measure its SOP. Incident circularly polarized light is propagated through the turbid medium and undergoes multiple-scattering events before being collected by the detector. The MC-based computational studies[428] indicated that when the source and detection areas are overlapped ($d = 0$), the detected signal is likely to be overwhelmed by the cross-polarized component due to single back-scattering events at or near the surface. Separation of the source and detector increases the pathlength of the light within the sample before reaching the detector, and thus increases the contribution of the co-polarized component to the detected signal. Too large a detecting distances result in complete depolarization of the incident light. The actual value of d causing complete depolarization is related to the optical properties of the medium, specifically the transport mean-free path l_{tr} ($l_{tr} = 1/\mu_s'$).

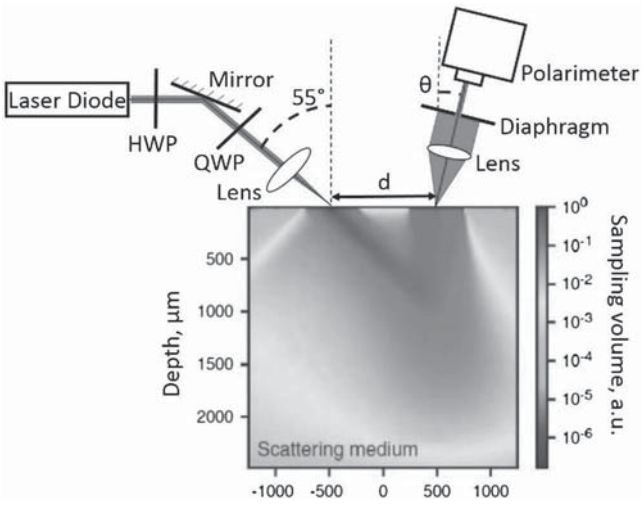

Figure 1.35 Schematic presentation of the experimental setup. Vertically polarized light from a laser diode (LQC639-30C, Newport, RI, 639 nm, 30 mW) is directed toward the sample at 55 deg from the normal. The light is then altered by a quarter wave plate into a state of RCP and/or right elliptically polarized (REP), and focused onto the surface of the tissue by a lens. The source detector separation d as well as the angle of detection θ can be varied to influence the sampling volume.[427,428] (See color plates.)

To visualize and quantify changes in light polarization associated with alterations that were built into models or changes in biological tissues, the use of the Poincaré sphere has been suggested.[367,423] The coordinates on the Poincaré sphere are defined by the Stokes parameters, defined as[1]

$$S_0 = I, \tag{1.170}$$

$$S_1 = Q = I \cdot \mathrm{DOP} \cdot \cos(2\psi)\cos(2\chi), \tag{1.171}$$

$$S_2 = U = I \cdot \mathrm{DOP} \cdot \sin(2\psi)\cos(2\chi), \tag{1.172}$$

$$S_3 = V = I \cdot \mathrm{DOP} \cdot \sin(2\chi), \tag{1.173}$$

where I is intensity, DOP is the degree of polarization and describes the portion of polarized light, χ is ellipticity angle, and ψ is azimuth angle. Using the Poincaré sphere makes it easier to visualize multiple polarization states at once for comparison purposes. The last three Stokes parameters are plotted in 3-D space, outlining a sphere with all possible polarization states (Fig. 1.36).

The Poincaré sphere has been used as a convenient graphical tool for the analysis of SOP of light scattered within biological tissue and tissue-like scattering meida.[367,423] Mapping the Stokes vector of the back-scattered light

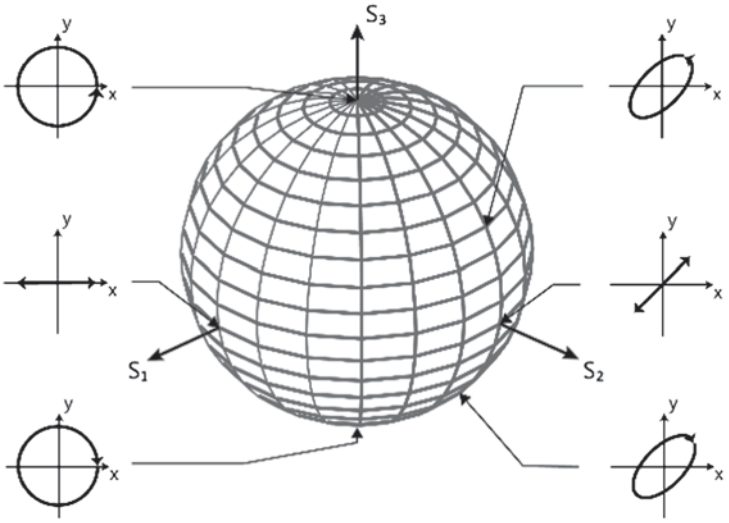

Figure 1.36 The Poincaré sphere describes all possible states of polarization. The distance from the center of the sphere indicates the degree of polarization; fully polarized states occupy a point on the surface of the sphere, whereas partially polarized states reside inside. Each point on the sphere represents one SOP so for instance a point at the northern pole $+S_3$ signifies right-handed circular polarization, and the south pole $-S_3$, left circular. States of linear polarization lie on the equator, and elliptical polarizations fill the remaining surface.

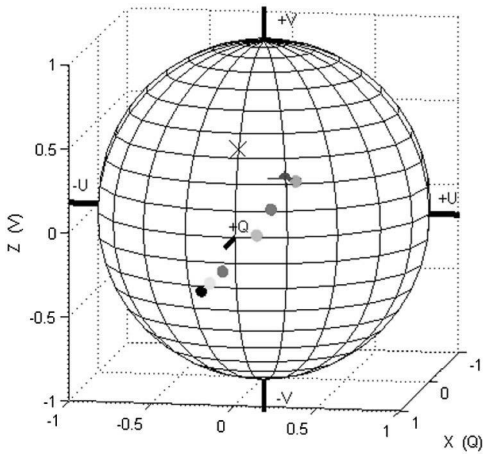

Figure 1.37 Position of the Stokes vector on the Poincaré sphere for right helically polarized light scattered in the water solutions of with dilution factor (from top): 1:1 (●– blue), 1:10 (●– green), 1:20 (●– red), 1:40 (●– cyan), 1:100 (●– magenta), 1:200 (●– yellow), and 1:500 (●– black). $d = 1$ mm and $\theta = 10$ deg. $\times$ indicates the Stokes vector of incident light.

on a Poincaré sphere demonstrated that the changes of polarization state correlates with the concentration of scattering particles and their sizes.

Figure 1.37 shows that SOP of light begins in a right handed elliptical polarization state and reverses its helicity to become left handed with the highly dilute Intralipid water solutions. The helicity of the polarization state remains right-handed with the water solutions of Intralipid up to dilution factor 1:40. After this point the polarization state changes more significantly, whereas the changes between the first and second measurement is minimal (see Fig. 1.37).

The results of measurements of the signature of the Stokes vector on the Poincaré sphere for the light scattered in the mono-disperse solutions of polystyrene microspheres (of known optical properties, see Table 1.1) are presented in Fig. 1.38.

Thus, the quantitative phantom studies utilizing polystyrene beads confirmed that the Stokes vector position on the Poincaré sphere depended on the size of the light-scattering particles, which in turn influenced the latitude of the Stokes vector mapped onto the Poincaré sphere. Based on the

Table 1.1 Optical properties of mono-disperse solutions of polystyrene microspheres used in the experiments.

	Diameter (μm)	Concentration (particles/ml)	g	I_s (cm^{-1})	μ_s' (cm^{-1})	Dilution factor
a	11 ± 0.25	3.55×10^7	0.912	68.6	6.0	1:1
b	5.9 ± 0.29	1.25×10^8	0.864	68.6	9.3	1:1.77
c	5.9 ± 0.29	8.09×10^7	0.864	44.3	6.0	1:2.74
d	5.9 ± 0.29	3.55×10^7	0.864	19.5	2.7	1:6.23

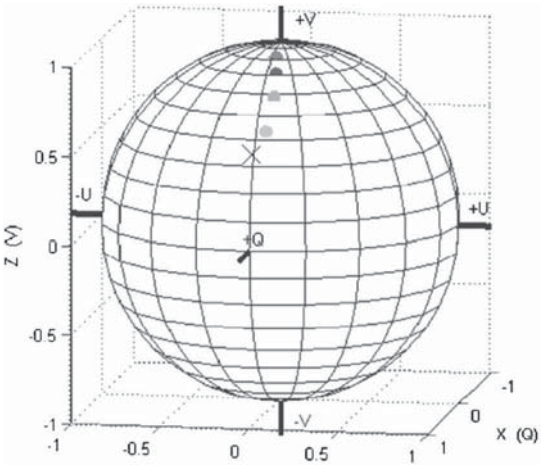

Figure 1.38 Position of Stokes vector on the Poincaré sphere for right-handed circularly/elliptically polarized light scattered in water solutions of microspheres, the scattering properties of which presented in Table 1.1: a (●– red), b (●– blue), c (●– green), and d (●– cyan), × indicates the Stokes vector of incident light. $d = 6$ mm and $\theta = 30$ deg.

Mie theory and the associated calculations of scattering pattern and polarization state, we can see that for small microspheres the scattering acts like a dipole. Figure 1.39(a) shows the S_3 component of Stokes vector (also known as V) of the light after a single-scattering event for a small (0.1 μm) microsphere as a function of the cosine of the scattering angle θ. Since the incident light is right circularly polarized the negative values for V indicate a helicity flip. We can see that back-scattering events (when cosine of scattering angle < 0) result in a helicity flip. The S-shaped curve can be explained by the attenuation of *p*- and *s*- components in terms of projections of the electric field vector. But for larger spheres this behaviour drastically changes. The S-shape is lost at a sphere size of 0.3 μm [Fig. 1.39(b)]. The angles resulting in helicity reversal become even more complicated at the sphere sizes used in the experiments described above [see Fig. 1.39(c) and (d)].

Figure 1.40 shows the results of a MC simulation[428] recording the spatial distribution of the V component of the Stokes vector on the surface of a scattering medium. The optical properties of media used in the modelling are presented in Table 1.1 (a–d), respectively. As one can see the bulk polarization state measured from the medium with the highest scattering anisotropy [see Fig. 1.40(a)] has the highest helicity preservation, or V component. The overall trend between ellipticity and changes of anisotropy of scattering is clearly seen between all the samples.

The results of phantom studies with water solutions of Intralpid and microspheres show clearly the response of backward scattered circular/elliptically polarized light. The results of MC modelling shows that phase shifts are involved in scattering by large spheres but that their helicity flips

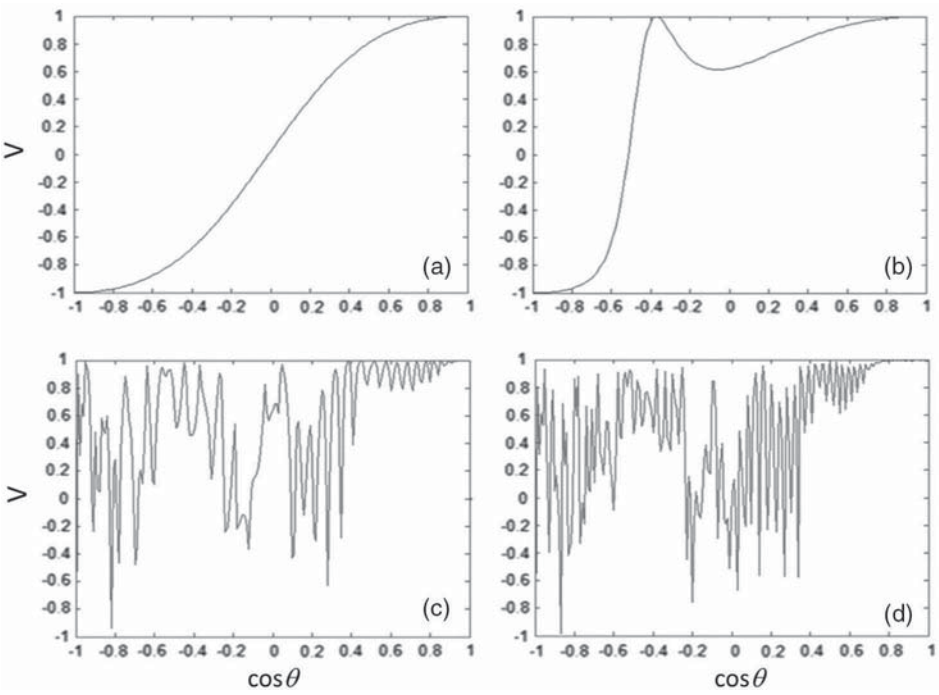

Figure 1.39 *V* component (S_3) of the outgoing Stokes vector vs. cosine of scattering angle calculated by using Mie theory[429] for the diameter of scattering particles: (a) 0.1 μm, (b) 0.3 μm, (c) 5.9 μm, and (d) 11 μm. The wavelength of light is 639 nm.

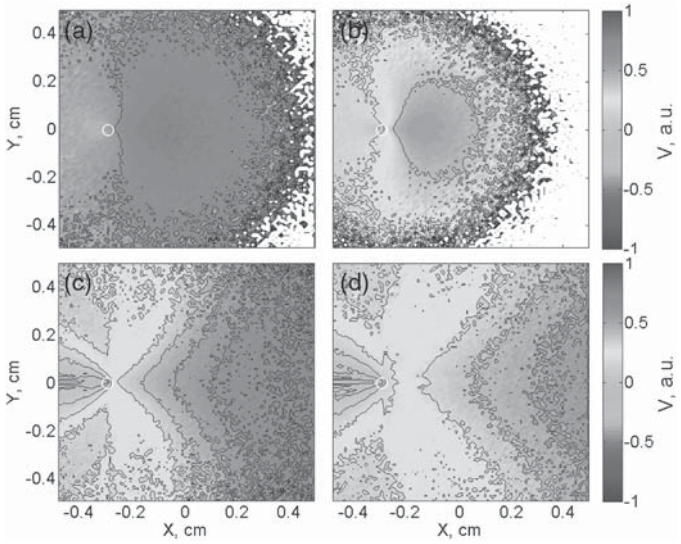

Figure 1.40 Spatial distribution of *V* component of the Stokes vector on the surface of scattering medium, obtained for circularly polarized light [1,0,0,1] of a wavelength of 639 nm incident to the surface of the medium at point (0,0) with the angle of 45 deg. The optical properties of scattering media are, respectively, presented in Table 1.1. (See color plates.)

occur at a complex range of scattering angles. The obtained results give a strong suggestion that changes in nuclear size in cells can be characterised by this technique. This provides a good foundation for further work implementing the noninvasive circularly/elliptically polarized light based diagnostic approach for early disease detection, as many forms of cancerous growths alter properties such as anisotropy and density of scattering sites.

Following the results discussed earlier, Fig. 1.41 illustrates the changes of SOP of light scattered during the tissue optical clearing by using water solutions of glycerol. As one can see in the first measurement, the initial right-handed elliptical polarization state gradually narrows and approaches linear polarization along the x axis. It is clearly seen that the incident right circularly polarized light retains its helicity over the measured time. Within the first 20 min, the SOP of the back-scattered light changed more rapidly than at later time intervals. Up to 30 min, the SOP decreases (see Fig. 1.41).

It has long been speculated that altered nuclear size and shape are representative of various underlying causes of altered nuclear morphology that occur during cancer onset. This altered nuclear morphology is thought to reflect primary changes in chromosome organization, which in turn can affect gene expression,[430] although the exact relationship between these parameters has still not been defined. It has also been proposed that the altered nuclear shape in cancer cells facilitates the formation of metastases because of reduced nuclear stiffness, which could increase the ability of transformed cells to penetrate tissue.[431] Consistent with these ideas is the notion that certain (as yet unidentified) factors in cells regulate or limit nuclear expansion.

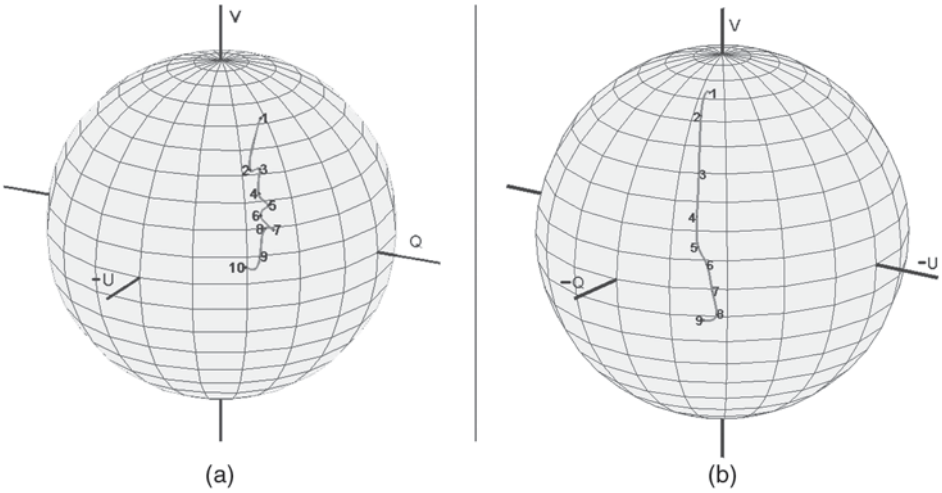

Figure 1.41 The position of the Stokes vector on the Poincaré sphere for right-handed circularly/elliptically polarized light scattered at *in vitro* tissue optical clearing by topical application of water solution of glycerol: (a) chicken skin sample and (b) bovine tendon sample. The SOP was recorded every 10 min during a time period of 100 and 90 min, respectively.

For example, several studies suggest that nuclear size is determined by cytoplasmic volume,[432] and it is well documented that the nuclear to cytoplasmic ratio decreases in cells as they move from being stem cells to being terminally differentiated.[431]

Abnormalities induced in tissues by cancerous changes include an increased nucleus-to-cytoplasm ratio and an overall increase in the volume density of cells.[433,434] These two effects, as shown with the phantom studies discussed above and confirmed by the results of theoretical studies,[435–437] impact greatly on the SOP of light propagated through the tissue. An increase in nuclear size leads to a higher forward scattering of light (Fig. 1.42).

Therefore, if the SOP of the scattered light is closer to the state of incident right circularly polarized light, i.e., to the north pole on the Poincaré sphere, then the tissue sample is either neoplastic potentially malignant or neoplastic malignant. If the state of polarization of the scattered light is close to the equator of the Poincaré sphere then the tissue sample is normal. The results of feasibility studies[439] show that the current approach can discriminate between cancerous and noncancerous tissue by mapping the Stokes vector of back-scattered light on a Poincaré sphere (see Fig. 1.43).

Multiple measurements were performed in a scanning approach on a human lung metastasis of thymic carcinoma embedded in paraffin wax.[367] The samples had a variety of tissue structures present, including both healthy and cancerous tissue. A pathologist reviewed the tissue prior to taking measurements, and the region of the cancer tissue was outlined on a 5-μm tissue section via histological haematoxylin and eosin staining and light microscopy.

Figure 1.44 is shown the averaged polarization states of detected light scattered from healthy and cancerous tissues complete with standard

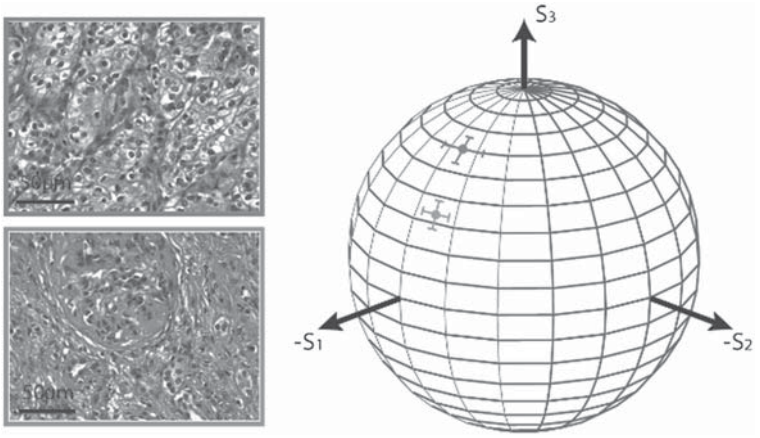

Figure 1.42 The SOP of the right-handed elliptically polarized light scattered from healthy (green) and cancerous (red) sites of kidney tissue.[438] (See color plates.)

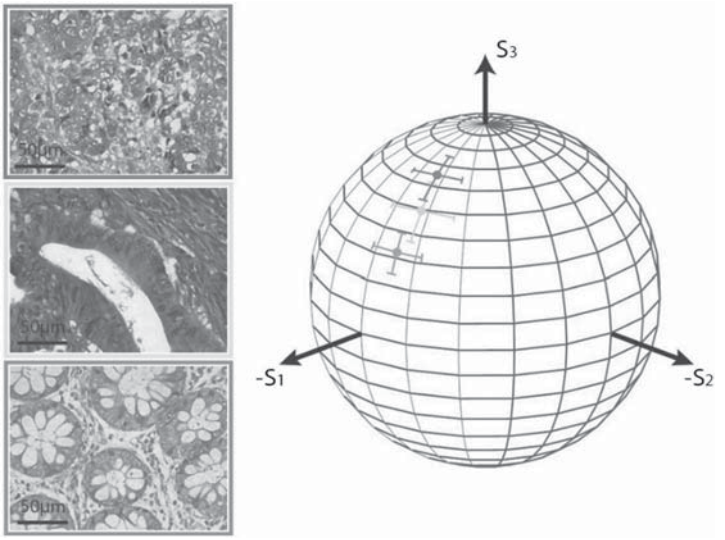

Figure 1.43 Position of the Stokes vector on the Poincaré sphere (right) correlates with the successive grades of colorectal cancer (normal colon, green; grade 2, yellow; grade 3, red) confirmed by microscopy (left three panels: normal colon, bottom; grade 2, middle; grade 3, top). (See color plates.)

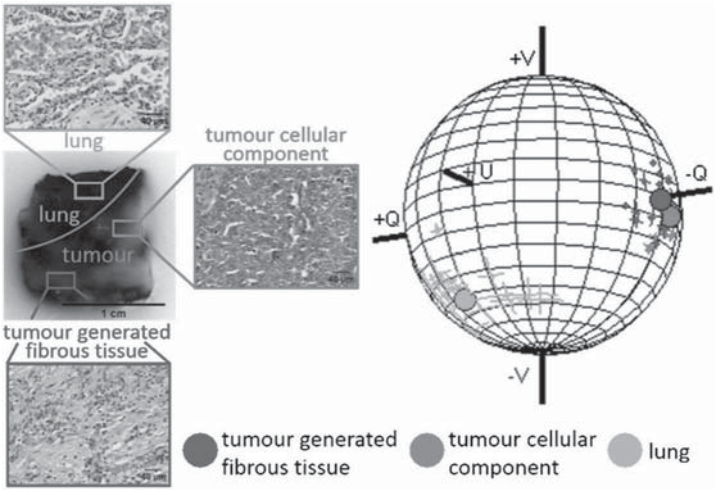

Figure 1.44 Lung tissue embedded in paraffin wax (left) shows the boundary between healthy lung and tumor tissue (red line) marked based on histological examination. Microscopy images of hematoxylin and eosin stained 5-μm tissue sections are shown in the colored squares, and their position on the block is marked by the corresponding squares. The Poincaré sphere (right) shows the mean Stokes vector of REP light back-scattered from the region of healthy lung tissue (green), tumor-generated fibrous tissue (blue) and the tumor cellular component (red); dots with error bars represent a single measurement, and the larger circles represent the mean SOP. $d = 1.5$ mm, and $\theta = 30$ deg. (See color plates.)

deviation. With right-handed elliptically polarized incident light, we can see on the figure that the ellipticity (latitude on the sphere) is much higher for the cancerous tissue. This is expected to be a result of the increased average size of lung cell nuclei (as can be seen in the corresponding microscope images). This leads to higher anisotropy and an increase in successive forward-scattering events contributing to the signal where co-polarized helicity has a stronger influence.

Thus, it has been shown that back-scattered circularly polarized light is highly sensitive to the presence of cells with enhanced plasticity. It has been found that the magnitude of the alterations defined by the Stokes vector on the Poincaré sphere is proportional to the grade of cancer. These results demonstrate a robust, sensitive, and unbiased method for identifying enhanced plasticity in tissues in real time before metastasis. In the bigger picture, this approach has the strong potential to revolutionize the current practice of cancer screening in living tissues to ensure the well-being of patients in the near future.

1.12 Summary

In this chapter, the basic theoretical approaches and methods that are widely used for calculations of angular distribution and total extinction of light scattered and absorbed by small particles or particle aggregates are discussed. At present there are a number of web sites with public domain computer codes that maintain up-to-date theoretical approaches that can be easily implemented for biomedical applications (see, e.g., Ref. 96). In the first part of the chapter, the direct and inverse spectroturbidimetric problems of disperse systems with random and ordered particle orientations have been considered in detail. We have shown how to estimate the average size, shape, and index of refraction of cells using the extinction (integral light scattering) spectra recorded at various orientations of a light beam with respect to an external orienting field.

In the second part of the chapter, it was shown that the model of discrete scatterers explains many experimental optical properties of various tissues, primarily the spectral dependences of light scattering and transmittance. It should be emphasized that a simple model of single light scattering by independent particles fails at theoretical simulation of optical properties of real tissues *in situ*, except in the case of specially prepared samples. For example, the high transparency of structurally nonhomogeneous tissues of the eye can be explained only by the concept of dependent light scattering from spatially ordered discrete scatterers. Accounting for the optical softness of structural elements of the majority of tissues, an adequate description of experimental data, including polarization and angular characteristics, can be achieved by using approximate variants of the multiple-wave scattering

theory. A prospective method for controlling of tissue optical properties is discussed. It was demonstrated in *in vitro* and *in vivo* studies that an effective reduction of tissue scattering could be achieved by a refractive index matching using tissue and blood immersion by OCA.

The experimental angular dependences of an LSM, i.e., a combination of angular and polarization light scattering characteristics, creates an informative basis for solving inverse problems that are important for noninvasive optical tissue diagnostics. The actual number of examples of successful application of optical polarization techniques in tissue optics is growing, because the capabilities of this approach are rather promising, especially at using the Poincaré sphere concept for fast recognition of pathology grade.

Acknowledgments

Many results presented in this chapter on modeling and measuring of tissue optical properties were generated by Irina L. Maximova, who was a very talented scientist and a great person. She passed away in 2013 during the work on the second edition of this handbook. We will remember her forever.

VVT is thankful for support from grant No. 14-15-00186 of the Russian Science Foundation and Russian Presidential Grant NSh-7898.2016.2. The work by NGK (Sections 1.1 to 1.5) was supported by grant No. 14-13-01167 from the Russian Science Foundation.

References

1. H. C. van de Hulst, *Light Scattering by Small Particles*, Wiley, New York (1957).
2. V. V. Sobolev, *Light Scattering in Planetary Atmospheres*, Pergamon, Oxford (1974).
3. A. Z. Dolginov, Yu. N. Gnedin, and N. A. Silant'ev, *Propagation and Polarization of Radiation in Cosmic Media*, Gordon and Breach, Basel (1995).
4. K. N. Liou, *Radiation and Cloud Processes in the Atmosphere: Theory, Observation, and Modeling*, Oxford Univ. Press, New York (1992).
5. M. S. Quinby-Hunt, P. G. Hull, and A. J. Hunt, "Polarized light scattering in the marine optics," Chapter 18 in *Light Scattering by Nonspherical Particles: Theory, Measurements, and Applications*, M. I. Mishchenko, J. W. Hovenier, and L. D. Travis, Eds., Academic Press, New York, pp. 525–554 (2000).
6. A. Ishimaru, *Wave Propagation and Scattering in Random Media*, Academic Press, San Diego (1978).
7. M. Kerker, *The Scattering of Light and Other Electromagnetic Radiation*, Academic Press, San Diego (1969).

8. V. I. Klenin, *Thermodynamics of Systems with Flexible Chain Polymers*, Elsevier, Amsterdam (1999).
9. V. V. Tuchin, *Tissue Optics: Light Scattering Methods and Instruments for Medical Diagnosis*, 3rd ed., **PM 254**, SPIE Press, Bellingham, WA, 2015.
10. V. V. Tuchin, "Light scattering study of tissues," *Phys.-Uspekhi* **40**, 495–515 (1997).
11. P. Chylek, G. Videen, D. J. W. Geldart, J. S. Dobbie, and H. C. W. Tso, "Effective medium approximations for heterogeneous particles," Chapter 9 in *Light Scattering by Nonspherical Particles: Theory, Measurements, and Applications*, M. I. Mishchenko, J. W. Hovenier, and L. D. Travis, Eds., Academic Press, San Diego, pp. 273–308 (2000).
12. C. F. Bohren and D. R. Huffman, *Absorption and Scattering of Light by Small Particles*, Wiley, New York (1983).
13. R. G. Newton, *Scattering Theory of Waves and Particles*, McGraw-Hill, New York (1966).
14. P. C. Waterman, "Symmetry, unitarity, and geometry in electromagnetic scattering," *Phys. Rev. D* **3**(4), 825–839 (1971).
15. M. I. Mishchenko, J. W. Hovenier, and L. D. Travis, Eds., *Light Scattering by Nonspherical Particles: Theory, Measurements, and Applications*, Academic Press, San Diego (2000).
16. M. I. Mishchenko, W. J. Wiscombe, and L. D. Travis, "Overview of scattering by nonspherical particles," Chapter 2 in *Light Scattering by Nonspherical Particles: Theory, Measurements, and Applications*, M. I. Mishchenko, J. W. Hovenier, and L. D. Travis, Eds., Academic Press, San Diego, pp. 29–60 (2000).
17. M. I. Mishchenko, L. Liu, and G. Videen, "Conditions of applicability of the single-scattering approximation," *Opt. Express* **15**, 7522–7527 (2007).
18. K. H. Ding and L. Tsang, "Effective propagation constants in media with densely distributed dielectric particles of multiple sizes and permittivities," in *Progress in Electromagnetic Research*, PIER 1, J. A. Kong, Ed., Elsevier, New York, pp. 241–295 (1989).
19. V. K. Varadan, V. N. Bringi, and V. V. Varadan, "Coherent electromagnetic wave propagation through randomly distributed dielectric scatterers," *Phys. Rev. D* **19**(8), 2480–2489 (1979).
20. S. M. Rytov, Y. A. Kravtsov, and V. I. Tatarskii, *Principles of Statistical Radiophysics*, Vol. 4, *Wave Propagation through Random Media*, Springer-Verlag, Berlin (1989).
21. L. Tsang, J. A. Kong, and R. T. Shin, *Theory of Microwave Remote Sensing*, Wiley, New York (1985).
22. H. C. van de Hulst, *Multiple Light Scattering: Tables, Formulas and Applications*, Academic Press, San Diego (1980).

23. P. Flatau, "SCATTERLIB: light scattering codes library," http://atol.ucsd.edu/~pflatau/scatlib/.
24. G. V. Rozenberg, "Electrodynamics of statistically inhomogeneous media and radiative transfer theory," in *Theoretical and Applied Light Scattering Problems*, B. I. Stepanov and A. P. Ivanov, Eds. (in Russian), Nauka i Tekhnika, Minsk, pp. 159–170 (1971).
25. M. I. Mishchenko, "Directional radiometry and radiative transfer: a new paradigm," *J. Quant. Spectrosc. Radiat. Transfer* **112**, 2079–2094 (2011).
26. V. K. Varadan, V. N. Bringi, V. V. Varadan, and A. Ishimaru, "Multiple scattering theory for waves in discrete random media and comparison with experiments," *Radio Sci.* **18**(3), 321–327 (1983).
27. M. Kaveh, "New phenomena in the propagation of optical waves through random media," *Waves Rand. Med.* **3**(1), 121–128 (1991).
28. V. I. Kuzmin and V. P. Romanov, "Coherent phenomena in light scattering from disordered systems," *Phys.-Uspekhi* **39**(3), 231–260 (1996).
29. C. A. Croxton, *Liquid State Physics: A Statistical Mechanical Introduction*, Cambridge Univ. Press (1974).
30. M. Born and E. Wolf, *Principles of Optics*, 4th ed., Pergamon, Oxford (1968).
31. V. A. Davis and L. Schwartz, "Electromagnetic propagation in close-packed disordered suspensions," *Phys. Rev. B* **31**(8), 5155–5165 (1985).
32. K. Furutsu, "Random-volume scattering: boundary effects, cross-sections, and enhanced backscattering," *Phys. Rev. A* **43**(6), 2741–2762 (1991).
33. Yu. N. Barabanenkov, Yu. A. Kravtsov, V. D. Ozrin, and A. I. Saichev, "Enhanced backscattering in optics," in *Progress in Optics*, Vol. **29**, E. Wolf, Ed., Elsevier, Amsterdam, pp. 65–197 (1991).
34. W. G. Tam and A. Zardecki, "Multiple scattering to the Beer–Lambert law: I. open detector," *Appl. Opt.* **21**(13) 2405–2412 (1982).
35. A. Zardecki and W. G. Tam, "Multiple scattering corrections to the Beer–Lambert law: II. detector with a variable field of view," *Appl. Opt.* **21**(13), 2413–2420 (1982).
36. N. G. Khlebtsov, "Role of multiple scattering in turbidimetric investigations of dispersed systems," *J. Appl. Spectrosc.* **40**(2), 243–247 (1984); translated from *Zh. Prikl. Spektr.* **40**(2), 320–325 (1984).
37. R. O. Gumprecht and C. M. Slipcevich, "Scattering of light by large spherical particles," *J. Chem. Phys.* **57**(1), 90–95 (1953).
38. P. Latimer, "Light scattering and absorption as methods of studying cell population parameters," *Ann. Rev. Biophys. Bioeng.* **11**(1), 129–150 (1982).
39. D. S. Saxon, "Tensor scattering matrix for the electromagnetic field," *Phys. Rev.* **100**(6), 1771–1775 (1955).

40. L. Lorenz, *Oeuvres Scientifiques*, Lehman and Stage, Copenhagen (1898).
41. A. E. H. Love, "The scattering of electric waves by a dielectric sphere," *Proc. London Math. Soc.* **30**(678), 308–321 (1899).
42. G. Mie, "Beiträge zur Optik trüber Medien, speziell kolloidaler Metallösungen," *Ann. Phys.* **25**(3), 377–445 (1908).
43. P. Debye, "Der Lichtdruck auf Kugeln von beliebigem Material," *Ann. Phys.* **30**, 57–136 (1909).
44. D. W. Rayleigh, "The incidence of light upon a transparent sphere of dimensions comparable with the wavelength," *Proc. R. Soc. London Ser. A* **84**, 25–46 (1910).
45. D. W. Rayleigh, "On the electromagnetic theory of light," *Philos. Mag.* **12**(73), 81–101 (1881).
46. D. W. Rayleigh, "On the dispersal of light by a dielectric cylinder," *Philos. Mag.* **36**, 365–376 (1918).
47. P. M. Morse and H. Feshbach, *Methods of Theoretical Physics*, McGraw-Hill, New York (1953).
48. F. Möglich, "Beugungserscheinungen an Korpen von ellipsoidischer Gestalt," *Ann. Phys.* **83**(13), 609–735 (1927).
49. Sh. Asano and G. Yamamoto, "Light scattering by a spheroidal particle," *Appl. Opt.* **14**(1), 29–49 (1975).
50. V. G. Farafonov, V. B. Il'in, and Th. Henning, "A new solution of the light scattering problem for axisymmetric particles," *JQSRT* **63**(2–6), 205–215 (1999).
51. I. R. Cirik and F. R. Cooray, "Separation of variables for electromagnetic scattering by spheroidal particles," Chapter 4 in *Light Scattering by Nonspherical Particles: Theory, Measurements, and Applications*, M. I. Mishchenko, J. W. Hovenier, and L. D. Travis, Eds., Academic Press, San Diego, pp. 89–130 (2000).
52. D. A. Varshalovich, A. N. Moskalev, and V. K. Khersonskii, *Quantum Theory of Angular Momentum*, World Scientific, Singapore (1988).
53. P. W. Barber and C. Yeh, "Scattering of electromagnetic waves by arbitrarily shaped dielectric bodies," *Appl. Opt.* **14**(12), 2864–2872 (1975).
54. M. I. Mishchenko, L. D. Travis, and A. Macke, "T–matrix method and its applications," Chapter 6 in *Light Scattering by Nonspherical Particles: Theory, Measurements, and Applications*, M. I. Mishchenko, J. W. Hovenier, and L. D. Travis, Eds., Academic Press, San Diego, pp. 147–172 (2000).
55. M. I. Mishchenko, L. D. Travis, and D. W. Mackowski, "T–matrix computations of light scattering by nonspherical particles: a review," *JQSRT* **55**(5), 535–575 (1996).
56. M. I. Mishchenko, L. D. Travis, and A. A. Lacis, *Scattering, Absorption, and Emission of Light by Small Particles*, Cambridge Univ. Press, Cambridge (2002).

57. M. I. Mishchenko, "Light scattering by randomly oriented axially symmetric particles," *J. Opt. Soc. Am. A* **8**(6), 871–882 (1991).
58. N. G. Khlebtsov, "Orientational averaging of light scattering observables in the T-matrix approach," *Appl. Opt.* **31**(25), 5359–5365 (1992).
59. K. S. Shifrin, Scattering of Light in a Turbid Medium, NASA Tech. Transl., NASA TT F-477 (1968).
60. A. J. Poggio and E. K. Miller, "Integral equation solutions of three-dimensional scattering problems," in *Computer Techniques for Electromagnetics*, R. Mittra, Ed., Pergamon, Oxford, pp. 159–264 (1973).
61. J. J. H. Wang, *Generalized Moment Methods in Electromagnetics: Formulation and Computer Solution of Integral Equations*, Wiley, New York (1991).
62. S. Ström, "On the integral equations for electromagnetic scattering," *Am. J. Phys.* **43**(12), 1060–1069 (1975).
63. N. G. Khlebtsov, "Integral equation for problems of light scattering by particles of the medium," *Opt. Spectrosc.* **57**(4), 399–401 (1984).
64. G. H. Goedecke and S. G. O'Brien, "Scattering by irregular inhomogeneous particles via the digitized Green's function algorithm," *Appl. Opt.* **27**(12), 2431–2438 (1988).
65. M. F. Iskander, H. Y. Chen, and J. E. Penner, "Optical scattering and absorption by branched chains of aerosols," *Appl. Opt.* **28**(15), 3083–3091 (1989).
66. A. Lakhtakia and G. W. Mulholland, "On two numerical techniques for light scattering by dielectric agglomerated structures," *J. Res. Natl. Inst. Stand. Technol.* **98**(6), 699–716 (1993).
67. K. Lumme and J. Rahola, "Comparison of light scattering by stochastically rough spheres, best-fit spheroids and spheres," *JQSRT* **60**, 439–450 (1998).
68. N. K. Uzunoglu, B. G. Evans, and A. R. Holt, "Evaluation of the scattering of an electromagnetic wave from precipitation particles by the use of Fredholm integral equations," *Electron. Lett.* **12**(12), 312–313 (1976).
69. A. R. Holt, N. K. Uzunoglu, and B. G. Evans, "An integral equation solution to the scattering of electromagnetic radiation by dielectric spheroids and ellipsoids," *IEEE Trans. Antennas Propag.* AP **26**(5), 706–712 (1978).
70. E. M. Purcell and C. R. Pennypacker, "Scattering and absorption of light by non-spherical dielectric grains," *Astrophys. J.* **186**(2), 705–714 (1973).
71. M. A. Yurkin and A. G. Hoekstra, "The discrete-dipole-approximation code ADDA: capabilities and known limitations," *J. Quant. Spectrosc. Radiat. Transfer* **112**, 2234–2247 (2011).
72. B. T. Draine, "The discrete-dipole approximation and its application to interstellar graphite grains," *Astrophys. J.* **333**(2, Pt.1), 848–872 (1988).

73. C. E. Dungey and C. F. Bohren, "Light scattering by nonspherical particles: a refinement to the coupled-dipole method," *J. Opt. Soc. Am. A* **8**(1), 81–87 (1991).
74. B. T. Draine and J. Goodman, "Beyond Clausius–Mossotti: wave propagation on a polarizable point lattice and the discrete dipole approximation," *Astrophys. J.* **405**(2), 685–697 (1993).
75. B. T. Draine, "The discrete dipole approximation for light scattering by irregular targets," Chapter 5 in *Light Scattering by Nonspherical Particles: Theory, Measurements, and Applications*, M. I. Mishchenko, J. W. Hovenier, and L. D. Travis, Eds., Academic Press, San Diego, pp. 131–145 (2000).
76. A. G. Hoekstra and P. M. A. Sloot, "Biophysical and biomedical applications of nonspherical scattering," Chapter 20 in *Light Scattering by Nonspherical Particles: Theory, Measurements, and Applications*, M. I. Mishchenko, J. W. Hovenier, and L. D. Travis, Eds., Academic Press, San Diego, pp. 585–602 (2000).
77. A. R. Jones, "Light scattering for particle characterization," *Progr. Energy. Combust. Sci.* **25**, 1–53 (1999).
78. A. Kokhanovsky, *Optics of Light Scattering Media: Problems and Solutions*, Wiley/Praxis, Chichester (1999).
79. A. G. Ramm, "Wave scattering by small bodies," *Rep. Math. Phys.* **21**(1), 69–77 (1985).
80. J. C. Ku and J. D. Felske, "The range of validity of the Rayleigh limit for computing Mie scattering and extinction efficiencies," *JQSRT* **31**(6), 569–574 (1984).
81. R. E. Kleinman and T. B. A. Senior, "Rayleigh scattering," in *Low and High Frequency Asymptotics*, V. K. Varadan and V. V. Varadan, Eds., Elsevier, Amsterdam, pp. 1–70 (1986).
82. A. F. Stevenson, "Solution of electromagnetic scattering problems as power series in the ratio (dimension of scattering)/wavelength," *J. Appl. Phys.* **24**(9), 1134–1142 (1953).
83. A. F. Stevenson, "Electromagnetic scattering by an ellipsoid in the third approximation," *J. Appl. Phys.* **24**(9), 1143–1151 (1953).
84. N. G. Khlebtsov, "Scattering matrix of anisotropic ellipsoids comparable in size to the wavelength of light," *Opt. Spectrosc.* **46**(2), 188–190 (1979).
85. D. W. Rayleigh, "On the diffraction of light by spheres of small refractive index," *Proc. R. Soc. London Ser. A.* **90**, 219–225 (1914).
86. P. Debye, "Zerstreuung von Röntgenstrahlen," *Ann. Phys.* **46**(4), 809–823 (1915).
87. P. Debye, "Molecular-weight determination by light scattering," *J. Phys. Colloid Chem.* **51**(1), 18–31 (1947).
88. M. Born, "Quantenmechanik der Stossvorgänge," *Z. Phys.* **38**(8), 803–827 (1926).

89. J.-C. Ravey, "Light scattering in the third-order and RGD approximation: the form anisotropy in electro-optics," *J. Colloid Interface Sci.* **56**(3), 540–556 (1976).
90. R. Pecora, Ed., *Dynamic Light Scattering. Applications of Photon Correlation Spectroscopy*, Plenum, New York (1985).
91. J. D. Klett and R. A. Sutherland, "Approximate methods for modeling the scattering properties of nonspherical particles: evaluation of the Wentzel–Kramers–Brillouin method," *Appl. Opt.* **31**(3), 373–386 (1992).
92. T. W. Chen, "High energy light scattering in the generalized eikonal approximation," *Appl. Opt.* **28**(19), 4096–4102 (1989).
93. G. H. Meeten, "Induced birefringence in colloidal dispersions," *J. Chem. Soc. Faraday Trans.* **75**(10, Pt. 2), 1406–1415 (1979).
94. J.-C. Ravey and P. J. Mazeron, "Light scattering by large spheroids in the physical optics approximation: numerical comparison with other approximate and exact results," *J. Opt.* (Paris) **14**(1), 29–41 (1983).
95. A. Macke, M. I. Mishchenko, K. Muinonen, and B. E. Carlson, "Scattering of light by large nonspherical particles: ray-tracing approximation versus T-matrix method," *Opt. Lett.* **20**(19), 1934–1936 (1995).
96. T. Wriedt, "List of electromagnetic scattering codes," http://imperator.cip–iw1.uni-bremen.de.
97. P. P. Silvester and R. L. Ferrary, *Finite Elements for Electrical Engineers*, Cambridge Univ. Press, New York (1996).
98. A. Talfove, Ed., *Advances in Computational Electrodynamics: The Finite-Difference-Time-Domain Method*, Artech House, Boston (1998).
99. V. A. Erma, "Exact solution for the scattering of electromagnetic waves from bodies of arbitrary shape: III. Obstacles with arbitrary electromagnetic properties," *Phys. Rev.* **179**(5), 1238–1246 (1969).
100. K. Muinonen, "Light scattering by stochastically shaped particles," Chapter 11 in *Light Scattering by Nonspherical Particles: Theory, Measurements, and Applications*, M. I. Mishchenko, J. W. Hovenier, and L. D. Travis, Eds., Academic Press, San Diego, pp. 323–352 (2000).
101. V. N. Kuzmin and V. A. Babenko, "Light scattering by a weakly anisotropic spherical particle," *Opt. Spectrosc.* **50**(3), 269–273 (1981).
102. D. Lacoste and B. A. Van Tiggelen, "Stokes parameters for light scattering from a Faraday-active sphere," *JQSRT* **63**(2–6), 305–319 (1999).
103. P. Latimer, "Light scattering by ellipsoids," *J. Colloid Interface Sci.* **53**(1), 102–109 (1975).
104. P. Latimer, "Predicted scattering by spheroids: comparison of approximate and exact methods," *Appl. Opt.* **19**(18), 3039–3041 (1980).
105. D. Deirmendjian, *Electromagnetic Scattering on Spherical Polydispersions*, Elsevier, New York (1969).

106. G. R. Fournier and B. T. N. Evans, "Approximation to extinction efficiency for randomly oriented spheroids," *Appl. Opt.* **30**(15), 2042–2048 (1991).
107. V. A. Bloomfield, "Biological applications," in *Dynamic Light Scattering. Application of Photon Correlation Spectroscopy*, R. Pecora, Ed., Plenum, New York, pp. 363–416 (1985).
108. G. Sittampalam, "Theory of light scattering measurements as applied to immunoprecipitation reactions," *Anal. Chem.* **56**(12), 2176–2180 (1984).
109. G. K. Von Schulthess, G. B Benedek, and R. W. de Blois, "Measurement of the cluster size distributions for high functionality antigenes cross-linked by antibody," *Macromolecules* **13**(4), 939–945 (1980).
110. J. H. W. Leuvering, P. J. H. M. Thal, M. van der Waart, and A. H. W. M. Schuurs, "A sol particle agglutination assay for human chorionic gonadotrophin," *J. Immunol. Methods* **45**, 183–194 (1981).
111. J. M. C. Martin, M. Paques, T. A. van der Velden-De Groot, and E. C. Beuvery, "Characterization of antibody labeled colloidal gold particles and their applicability in a sol particle immunoassay (SPIA)," *J. Immunoassay* **11**, 31–47 (1990).
112. P. Latimer, "Blood platelet aggregometer: predicted effects of aggregation, photometer geometry, and multiple scattering," *Appl. Opt.* **22**(8), 1136–1143 (1983).
113. S. Yu. Shchyogolev, "Inverse problems of spectroturbidimetry of biological disperse systems: an overview," *J. Biomed. Opt.* **4**(4), 490–503 (1999).
114. U. Comberg and T. Wriedt, "Comparison of scattering for aggregated particles based on different models," *JQSRT* **63**(2–6), 149–162 (1999).
115. K. A. Fuller and D. W. Mackowski, "Electromagnetic scattering by compounded spherical particles," Chapter 8 in *Light Scattering by Nonspherical Particles: Theory, Measurements, and Applications*, M. I. Mishchenko, J. W. Hovenier, and L. D. Travis, Eds., Academic Press, San Diego, pp. 225–272 (2000).
116. V. A. Markel and Th. F. George, Eds., *Optics of Nanostructured Materials*, Wiley, New York (2000).
117. A. E. Moskalensky, D. I. Strokotov, A. V. Chernyshev, V. P. Maltsev, and M. A. Yurkin, "Additivity of light-scattering patterns of aggregated biological particles," *J. Biomed. Opt.* **19**, 085004 (2014).
118. P. Latimer and F. Wamble, "Light scattering by aggregates of large colloidal particles," *Appl. Opt.* **21**(12), 2447–2455 (1982).
119. V. A. Markel, V. M. Shalaev, E. B. Stechel, W. Kim, and R. L. Armstrong, "Small-particle composites: I. Linear optical properties," *Phys. Rev. B* **53**(5), 2425–2436 (1996).
120. Yu-lin Xu, "Electromagnetic scattering by an aggregate of spheres," *Appl. Opt.* **34**(21), 4573–4588 (1995).

121. Yu-lin Xu, "Electromagnetic scattering by an aggregate of spheres: far field," *Appl. Opt.* **36**(36), 9496–9508 (1997).
122. D. W. Mackowski and M. I. Mishchenko, "Calculation of the T-matrix and the scattering matrix for ensembles of spheres," *J. Opt. Soc. Am. A* **13**(11), 2266–2278 (1996).
123. P. Meakin, "Models for colloidal aggregation," *Ann. Rev. Phys. Chem.* **39**, 237–267 (1988).
124. M. Y. Lin, H. M. Lindsay, D. A. Weitz, R. C. Ball, R. Klein, and P. Meakin, "Universality of fractal aggregates as probed by light scattering," *Proc. R. Soc. London Ser. A* **423**(1864), 71–87 (1989).
125. N. G. Khlebtsov and A. G. Melnikov, "Structure factor and exponent of scattering by polydisperse fractal colloidal aggregates," *J. Colloid Interface Sci.* **163**(1), 145–151 (1994).
126. R. Botet, P. Rannou, and M. Cabane, "Sensitivity of some optical properties of fractals to the cut-off functions," *J. Phys. A: Math. Gen.* **28**, 297–316 (1995).
127. N. G. Khlebtsov, "Spectroturbidimetry of fractal clusters: test of density correlation cutoff," *Appl. Opt.* **35**(21), 4261–4270 (1996).
128. J. Cai, N. Lu, and C. M. Sorensen, "Analysis of fractal cluster morphology parameters: structural coefficient and density correlation function cutoff," *J. Colloid Interface Sci.* **171**(2), 470–473 (1995).
129. C. M. Sorensen, J. Cai, and N. Lu, "Test of static structure factors for describing light scattering from fractal soot aggregates," *Langmuir* **8**(8), 2064–2069 (1992).
130. M. Novak and T. G. Deway, Eds., *Fractal Frontiers*, World Scientific, Singapore (1999).
131. V. M. Shalaev, *Nonlinear Optics of Random Media: Fractal Composites and Metal Dielectric Films*, Springer-Verlag, Berlin (2000).
132. M. V. Berry and I. C. Percival, "Optics of fractal clusters such as smoke," *Opt. Acta.* **33**(5), 577–591 (1986).
133. N. G. Khlebtsov, "Optics of fractal clusters in the anomalous diffraction approximation," *J. Mod. Opt.* **40**(11), 2221–2235 (1993).
134. R. Jullien, "The application of fractals to investigations of colloidal aggregation and random deposition," *New. J. Chem.* **14**(3), 239–253 (1990).
135. M. C. Daniel and D. Astruc, "Gold nanoparticles: assembly, supramolecular chemistry, quantum-size-related properties, and applications toward biology, catalysis, and nanotechnology," *Chem. Rev.* **104**, 293–346 (2004).
136. T. P. Sau and D. Goia, "Biomedical application of gold nanoparticles," in *Fine Particles in Medicine and Pharmacy*, E. Matijević, Ed., Springer, New York, pp. 101–145 (2012).

137. L. A. Dykman and N. G. Khlebtsov, "Gold nanoparticles in biomedical applications: recent advances and perspectives," *Chem. Soc. Rev.* **41**, 2256–2282 (2012).
138. E. C. Dreaden, A. M. Alkilany, X. Huang, C. J. Murphy, and M. A. El-Sayed "The golden age: gold nanoparticles for biomedicine," *Chem. Soc. Rev.* **41**, 2740–2779 (2012).
139. K. E. Sapsford, W. R. Algar, L. Berti, K. B. Gemmill, B. J. Casey, E. Oh, M. H. Stewart, and I. L. Medintz, "Functionalizing nanoparticles with biological molecules: developing chemistries that facilitate nanotechnology," *Chem. Rev.* **113**, 1904–2074 (2013).
140. M. Quinten, *Optical Properties of Nanoparticle Systems*, Wiley-VCH Verlag, Weinheim (2011).
141. M. I. Stockman, "Nanoplasmonics: past, present, and glimpse into future," *Opt. Express* **19**, 22029–22106 (2011).
142. K. M. Mayer and J. H. Hafner, "Localized surface plasmon resonance sensors," *Chem. Rev.* **111**, 3828–3857 (2011).
143. D. A. Giljohann, D. S. Seferos, W. L. Daniel, M. D. Massich, P. C. Patel, and C. A. Mirkin, "Gold nanoparticles for biology and medicine," *Angew. Chem. Int. Ed.* **49**, 3280–3294 (2010).
144. P. Baptista, E. Pereira, P. Eaton, G. Doria, A. Miranda, I. Gomes, P. Quaresma, and R. Franco, "Gold nanoparticles for the development of clinical diagnosis methods," *Anal. Bioanal. Chem.* **391**, 943–950 (2008).
145. Sh. Gupta, S. Huda, P. K. Kilpatrick, and O. D. Velev, "Characterization and optimization of gold nanoparticle–based silver-enhanced immunoassays," *Anal. Chem.* **79**, 3810–3820 (2007).
146. L. A. Dykman, S. A. Staroverov, V. A. Bogatyrev, and S. Y. Shchyogolev, *Gold Nanoparticles as an Antigen Carrier and an Adjuvant*, Nova Science, New York (2010).
147. P. G. Luo and F. J. Stutzenberger, "Nanotechnology in the detection and control of microorganisms," *Adv. Appl. Microbiol.* **63**, 145–181 (2008).
148. M. K. Yu, J. Park, and S. Jon, "Targeting strategies for multifunctional nanoparticles in cancer imaging and therapy, *Theranostics* **2**, 3–34 (2012).
149. C. Loo, L. Hirsch, M. Lee, E. Chang, J. West, N. Halas, and R. Drezek, "Gold nanoshell bioconjugates for molecular imaging in living cells," *Opt. Lett.* **30**, 1012–1014 (2005).
150. J. Park, A. Estrada, K. Sharp, K. Sang, J. A. Schwartz, D. K. Smith, Ch. Coleman, J. D. Payne, B. A. Korgel, A. K. Dunn, and J. W. Tunnell, "Two-photon-induced photoluminescence imaging of tumors using near-infrared excited gold nanoshells," *Opt. Express* **16**, 1590–1599 (2008).
151. L. V. Wang, Ed., *Photoacoustic Imaging and Spectroscopy*, CRS Press, Boca Raton, FL (2009).

152. L. C. Kennedy, L. R. Bickford, N. A. Lewinski, A. J. Coughlin, Y. Hu, E. S. Day, J. L. West, and R. A. Drezek, "A new era for cancer treatment: gold-nanoparticle-mediated thermal therapies," *Small* **7**, 169–183 (2011).
153. D. Pissuwan, T. Niidome, and M. B. Cortie, "The forthcoming applications of gold nanoparticles in drug and gene delivery systems," *J. Control. Release* **149**, 65–71 (2011).
154. L. A. Dykman and N. G. Khlebtsov, "Uptake of engineered gold nanoparticles into mammalian cells, *Chem. Rev.* **114**, 1258–1288 (2014).
155. G. F. Paciotti, L. Myer, D. Weinreich, D. Goia, N. Pavel, R. E. McLaughlin, and L. Tamarkin, "Colloidal gold: a novel nanoparticle vector for tumor directed drug delivery," *Drug Deliv.* **11**, 169–183 (2004).
156. C. R. Patra, R. Bhattacharya, E. Wang, A. Katarya, J. S. Lau, S. Dutta, M. Muders, S. Wang, S. A. Buhrow, S. L. Safgren, M. J. Yaszemski, J. M. Reid, M. M. Ames, P. Mukherjee, and D. Mukhopadhyay, "Targeted delivery of gemcitabine to pancreatic adenocarcinoma using cetuximab as a targeting agent," *Cancer Res.* **68**, 1970–1978 (2008).
157. Jose L. Arias, Ed., *Nanotechnology and Drug Delivery*, CRS Press, Boca Raton, FL (2015).
158. N. G. Khlebtsov and L. A. Dykman, "Biodistribution and toxicity of engineered gold nanoparticles: a review of in vitro and in vivo studies," *Chem. Soc. Rev.* **40**, 1647–1671 (2011).
159. K. L. Kelly, E. Coronado, L. L. Zhao, and G. C. Schatz, "The optical properties of metal nanoparticles: the influence of size, shape, and dielectric environment," *J. Phys. Chem. B* **107**, 668–677 (2003).
160. M. A. Yurkin, "Computational approaches for plasmonics," in *Handbook of Molecular Plasmonics*, D. F. Sala and S. D'Agostino, Eds., Pan Stanford Publishing, Singapore, pp. 83–135 (2013).
161. N. G. Khlebtsov, "T-matrix method in plasmonics: an overview," *J. Quant. Spectrosc. Radiat. Transfer* **123**, 184–217 (2013).
162. N. G. Khlebtsov, "Optics and biophotonics of nanoparticles with a plasmon resonance," *Quant. Electron.* **38**, 504–529 (2008).
163. A. Lakhtakia, "Strong and weak forms of the method of moments and the coupled dipole method for scattering of time-harmonic electromagnetic fields," *Int. J. Mod. Phys.* **3**, 583–603 (1992)
164. M. Meier and A. Wokaun, "Enhanced fields on large metal particles: dynamic depolarization," *Opt. Lett.* **8**, 581–583 (1983).
165. A. Moroz, "Depolarization field of spheroidal particles," *J. Opt. Soc. Am. B* **26**, 517–527 (2009).
166. E. A. Coronado and G. C. Schatz, "Surface plasmon broadening for arbitrary shape nanoparticles: a geometrical probability approach," *J. Chem. Phys.* **119**, 3926–3934 (2003).

167. A. Moroz, "Electron mean-free path in a spherical shell geometry," *J. Phys. Chem. C* **112**(29), 10641–10652 (2008).
168. C. J. Noguez, "Surface plasmons on metal nanoparticles: the influence of shape and physical environment," *J. Phys. Chem. C* **111**, 3806–3819 (2007).
169. B. N. Khlebtsov, A. G. Melnikov, V. P. Zharov, and N. G. Khlebtsov, "Absorption and scattering of light by a dimer of metal nanospheres: comparison of dipole and multipole approaches," *Nanotechnology* **17**, 1437–1445 (2006).
170. Y.-Y. Yu, S.-S. Chang, C.-L. Lee, and C. R. Ch. Wang, "Gold nanorods: electrochemical synthesis and optical properties," *J. Phys. Chem. B.* **101**(34), 6661–6664 (1997).
171. S. Link, M. B. Mohamed, and M. A. El-Sayed, "Simulation of the optical absorption spectra of gold nanorods as a function of their aspect ratio and the effect of the medium dielectric constant," *J. Phys. Chem. B* **103**, 3073–3077 (1999).
172. B. N. Khlebtsov, V. P. Zharov, A. G. Melnikov, V. V. Tuchin, and N. G. Khlebtsov, "Optical amplification of photothermal therapy with gold nanoparticles and nanoclusters," *Nanotechnology* **17**(20), 5167–5179 (2006).
173. N. G. Khlebtsov, L. A. Trachuk, and A. G. Melnikov, "The effect of the size, shape, and structure of metal nanoparticles on the dependence of their optical properties on the refractive index of a disperse medium," *Opt. Spectrosc.* **98**, 83–90 (2005).
174. J. Pérez-Juste, I. Pastoriza-Santos, L. M. Liz-Marzán, and P. Mulvaney, "Gold nanorods: synthesis, characterization and applications," *Coordination Chem. Rev.* **249**, 1870–1901 (2005).
175. M. Pelton, M. Liu, H. Y. Kim, G. Smith, P. Guyot-Sionnest, and N. F. Scherer, "Optical trapping and alignment of single gold nanorods by using plasmon resonances," *Opt. Lett.* **31**, 2075–2077 (2006).
176. C. Sönnichsen and A. P. Alivisatos, "Gold nanorods as novel nonbleaching plasmon-based orientation sensors for polarized single-particle microscopy," *Nano Lett.* **5**, 301–304 (2005).
177. B. N. Khlebtsov, V. A. Khanadeev, and N. G. Khlebtsov, "Observation of extra-high depolarized light scattering spectra from gold nanorods," *J. Phys. Chem. C.* **112**(33), 12760–12768 (2008).
178. R. Atkinson, W. R. Hendren, G. A. Wurtz, W. Dickson, A. V. Zayats, P. Evans, and R. J. Pollard, "Anisotropic optical properties of arrays of gold nanorods embedded in alumina," *Phys. Rev. B* **73**, 235402–235408 (2006).
179. M. B. Cortie, X. Xu, and M. J. Ford, "Effect of composition and packing configuration on the dichroic optical properties of coinage metal nanorods," *Phys. Chem. Chem. Phys.* **8**, 3520–3527 (2006).

180. J. Grand, P.-M. Adam, A.-S. Grimault, A. Vial, M. Lamy de la Chapelle, J.-L. Bijeon, S. Kostcheev, and P. Royer, "Optical extinction spectroscopy of oblate, prolate and ellipsoid shaped goldnanoparticles: experiments and theory," *Plasmonics* **1**, 135–140 (2006).
181. Ch. J. Orendorff and C. J. Murphy, "Quantitation of metal content in the silver-assisted growth of gold nanorods," *J. Phys. Chem. B* **110**, 3990–3994 (2006).
182. H. Liao and J. H. Hafner, "Gold nanorod bioconjugates," *Chem. Mater.* **17**, 4636–4641 (2005).
183. L. R. Hirsch, A. M. Gobin, A. R. Lowery, F. Tam, R. A. Drezek, N. J. Halas, and J. L. West, "Metal nanoshells," *Ann. Biomed. Eng.* **34**(1), 15–22 (2006).
184. B. N. Khlebtsov and N. G. Khlebtsov, "Enhanced solid-phase immunoassay using gold nanoshells: effect of nanoparticle optical properties," *Nanotechnology* **19**, 435703 (2008).
185. G. Akchurin, B. Khlebtsov, G. Akchurin, V. Tuchin, V. Zharov, and N. Khlebtsov, "Gold nanoshell photomodification under single nanosecond laser pulse accompanied by color-shifting and bubble formation phenomena," *Nanotechnology* **19**, 015701 (2008).
186. B. N. Khlebtsov and N. G. Khlebtsov, "Biosensing potential of silica/gold nanoshells: sensitivity of plasmon resonance to the local dielectric environment," *J. Quant. Spectrosc. Radiat. Transfer* **106**, 154–169 (2007).
187. L. A. Trachuk, S. A. Vrublevsky, B. N. Khlebtsov, A. G. Melnikov, and N. G. Khlebtsov, "Optical properties of gold spheroidal particles and nanoshells: effect of the external dielectric medium," *Proc. SPIE* **5772**, 1–10 (2005).
188. H. Wang, D. W. Brandl, F. Le, P. Nordlander, and N. J. Halas, "Nanorice: a hybrid plasmonic nanostructure," *Nano Lett.* **6**, 827–832 (2006).
189. L. A. Trachuk, A. G. Melnikov, B. N. Khlebtsov, and N. G. Khlebtsov, "Dependence of the optical properties of metal nanoparticles on the external dielectric medium: effects of the particle size, shape, and structure," *Proc. SPIE* **5829**, 127–137 (2005).
190. K. Kolwas, S. Demianiuk, and M. Kolwas, "Optical excitation of radius–dependent plasmon resonances in large metal clusters," *J. Phys. B* **29**, 4761–4770 (1996).
191. N. G. Khlebtsov, A. G. Melnikov, V. A. Bogatyrev, and L. A. Dykman, "Optical properties and biomedical applications of nanostructures based on gold and silver bioconjugates," in *Photopolarimetry in Remote Sensing*, G. Videen, Ya. S. Yatskiv, and M. I. Mishchenko, Eds., NATO Science Series, II. Mathematics, Physics, and Chemistry, **Vol. 161**, Kluwer Academic, Dordrecht, pp. 265–308 (2004).
192. V. A. Markel, "Divergence of dipole sums and the nature of non-Lorentzian exponentially narrow resonances in one-dimensional periodic

arrays of nanospheres," *J. Phys. B: At. Mol. Opt. Phys.* **38**, L115–L121 (2005).
193. B. Lamprecht, G. Schider, R. T. Lechner, H. Ditlbacher, J. R. Krenn, A. Leitner, and F. R. Aussenegg, "Metal nanoparticle gratings: influence of dipolar particle interaction on the plasmon resonance," *Phys. Rev. Lett.* **84**, 4721–4724 (2000).
194. S. Malynych and G. Chumanov, "Light-induced coherent interactions between silver nanoparticles in two-dimensional arrays," *J. Am. Chem. Soc.* **125**, 2896–2898 (2003).
195. B. N. Khlebtsov, V. A. Khanadeyev, J. Ye, D. W. Mackowski, G. Borghs, and N. G. Khlebtsov, "Coupled plasmon resonances in monolayers of metal nanoparticles and nanoshells," *Phys. Rev. B* **77**(3), 035440 (2008).
196. K.-H. Su, Q.-H. Wei, X. Zhang, J. J. Mock, D. R. Smith, and S. Schultz, "Interparticle coupling effects on plasmon resonances of nanogold particles," *Nano Lett.* **3**, 1087–1090 (2003).
197. B. Lamprecht, A. Leitner, and F. R. Aussenegg, "SHG studies of plasmon dephasing in nanoparticles," *Appl. Phys. B* **68**, 419–423 (1999)
198. D. Mackowski, "Electrostatics analysis of radiative absorption by sphere clusters in the Rayleigh limit: application to soot particles," *Appl. Opt.* **34**, 3535–3545 (1995).
199. M. A. Hayat, *Principles and Techniques of Electron Microscopy, Biological Applications 1*, Van Nostrand Reinhold, New York (1970).
200. G. Kumar and J. M. Schmitt, "Micro-optical properties of tissue," *Proc. SPIE* **2679**, 106–116 (1996).
201. R. L. Fante, "Electromagnetic propagation in turbulent media," *Proc. IEEE* **63**, 1669–1692 (1975).
202. J. A. Ogilvy, *Theory of Wave Scattering from Random Rough Surfaces*, Hilger, Bristol (1991).
203. D. A. Zimnyakov, V. V. Tuchin, and A. A. Mishin, "Spatial speckle correlometry in applications to tissue structure monitoring," *Appl. Opt.* **36**, 5594–5607 (1997).
204. J. M. Schmitt and G. Kumar, "Optical scattering properties of soft tissue: a discrete particle model," *Appl. Opt.* **37**(13), 2788–2797 (1998).
205. O. V. Volkova, V. A. Shakhmatova, and A. A. Mironova, Eds., *Atlas of Scanning Electron Microscopy Images of Cells, Tissues, and Organs* (in Russian), Medicine, Moscow (1987).
206. J. W. Goodman, *Statistical Optics*, Wiley-Interscience, New York (1985).
207. S. Ya. Sid'ko, V. N. Lopatin, and L. E. Paramonov, *Polarization Characteristics of Suspensions of Biological Particles* (in Russian), Nauka, Novosibirsk (1990).
208. R. D. Dyson, *Cell Biology: A Molecular Approach*, Allyn and Bacon, Boston (1974).

209. A. P. Ivanov, A. Ya. Khairullina, and T. N. Kharkova, "Experimental detection of cooperative effects in a dispersing volume," *Opt. Spectrosc.* **28**(2), 380–387 (1970).
210. M. J. Hogan, J. A. Alvardo, and J. Weddel, *Histology of the Human Eye*, 638–677, W. B. Sanders, Philadelphia (1971).
211. Q. Zhou and R. W. Klinghton, "Light scattering and form birefringence of parallel cylindrical arrays that represent cellular organelles of the retinal nerve fiber layer," *Appl. Opt.* **36**(10), 2273–2285 (1997).
212. G. Videen and D. Ngo, "Light scattering multipole solution for a cell," *J. Biomed. Opt.* **3**(2), 212–220 (1998).
213. G. B. Benedek, "Theory of transparency of the eye," *Appl. Opt.* **10**(3), 459–473 (1971).
214. A. Brunsting and P. Mullaney, "Differential light scattering from spherical mammalian cells," *Biophys. J.* **14**, 439–453 (1974).
215. J. M. Schmitt and G. Kumar, "Turbulent nature of refractive-index variations in biological tissue," *Opt. Lett.* **21**, 1310–1312 (1996).
216. J. Beutham, O. Minet, J. Helfmann, M. Herrig, and G. Muller, "The spatial variation of the refractive index in biological cells," *Phys. Med. Biol.* **41**(3), 369–382 (1996).
217. P. S. Tuminello, E. T. Arakawa, B. N. Khare, J. M. Wrobel, M. R. Querry, and M. E. Milham, "Optical properties of Bacillus subtilis spores from 0.2 to 2.5 mm," *Appl. Opt.* **36**, 2818–2824 (1997).
218. F. A. Duck, *Physical Properties of Tissue: A Comprehensive Reference Book*, Academic Press, San Diego (1990).
219. K. W. Keohane and W. K. Metcalf, "The cytoplasmic refractive index of lymphocytes, its significance and its changes during active immunisation," *Quart. J. Exp. Physiol. Cognate Med. Sci.* **44**, 343–346 (1959).
220. F. P. Bolin, L. E. Preuss, R. C. Taylor, and R. J. Ference, "Refractive index of some mammalian tissues using a fiber optic cladding method," *Appl. Opt.* **28**, 2297–2303 (1989).
221. O. V. Angelski, A. G. Ushenko, A. D. Arkhelyuk, S. B. Ermolenko, and D. N. Burkovets, "Scattering of laser radiation by multifractal biological structures," *Opt. Spectrosc.* **88**(3), 444–447 (2000).
222. V. F. Izotova, I. L. Maksimova, I. S. Nefedov, and S. V. Romanov, "Investigation of Mueller matrices of anisotropic nonhomogeneous layers in application to optical model of cornea," *Appl. Opt.* **36**(1), 164–169 (1997).
223. J. D. Bancroft and A. Stevens, Eds., *Theory and Practice of Histological Techniques*, Churchill Livingstone, Edinburgh and New York (1990).
224. D. M. Maurice, *The Cornea and Sclera: The Eye*, H. Davson, Ed., Academic Press, Orlando, pp. 1–158 (1984).

225. M. S. Borcherding, L. J. Blasik, R. A. Sittig, J. W. Bizzel, M. Breen, and H. G. Weinstein, "Proteoglycans and collagen fiber organization in human corneoscleral tissue," *Exp. Eye Res.* **21**, 59–70 (1975).
226. S. Vaezy and J. I. Clark, "Quantitative analysis of the microstructure of the human cornea and sclera using 2-D Fourier methods," *J. Microsc.* **175**(Pt. 2), 93–99 (1994).
227. O. V. Angelsky and P. P. Maksimyak, "Optical correlation diagnostics of random fields and objects," *Opt. Eng.* **34**(4), 937–981 (1995).
228. R. W. Hart and R. A. Farrell, "Light scattering in the cornea," *J. Opt. Soc. Am.* **59**(6), 766–774 (1969).
229. I. L. Maksimova, D. A. Zimnyakov, and V. V. Tuchin, "Control of optical properties of biotissues: I. Spectral properties of the eye sclera," *Opt. Spectrosc.* **89**(1), 78–86 (2000).
230. Y. Kamai and T. Ushiki, "The three-dimensional organization of collagen fibrils in the human cornea and sclera," *Invest. Ophtalmol. Vis. Sci.* **32**, 2244–2258 (1991).
231. S. Vaezy and J. I. Clark, "A quantitative analysis of transparency in the human sclera and cornea using Fourier methods," *J. Microsc.* **163**, 85–94 (1991).
232. F. A. Bettelheim, "Physical basis of lens transparency," in *The Ocular Lens: Structure, Function and Pathology*, H. Maisel, Ed., Marcel Dekker, New York, pp. 265–300 (1985).
233. A. Tardieuand and M. Delaye, "Eye lens proteins and transparency from light transmission theory to solution x-ray structural analysis," *Ann. Rev. Biophys. Chem.* **17**, 47–70 (1988).
234. A. V. Krivandin, "On the supramolecular structure of eye lens crystallins: the study by small-angle x-ray scattering," *Biofizika* **46**(6), 1274–1278 (1997).
235. S. Vaezy and J. I. Clark, "Characterization of the cellular microstructures of ocular lens using 2-D power law analysis," *Ann. Biomed. Eng.* **23**, 482–490 (1995).
236. J. Feder, *Fractals*, Plenum, New York and London (1988).
237. Y. Sakurada, J. Uozumi, and T. Asakura, "Scaling properties of the Fresnel diffraction field produced by one dimensional regular fractals," *Pure Appl. Opt.* **3**(3), 374–380 (1994).
238. R. W. James, *The Optical Principles of Diffraction of X-rays: The Crystalline State II*, L. Bragg, Ed., London (1950).
239. J. M. Ziman, *Models of Disorder: The Theoretical Physics of Homogeneously Disordered Systems*, Cambridge Univ. Press, London, New York, and Melbourne (1979).
240. M. S. Wertheim, "Exact solution of the Percus–Yevick integral equation for hard spheres," *Phys. Rev. Lett.* **10**(8), 321–323 (1963).

241. J. L. Lebovitz, "Exact solution of generalized Percus–Yevick equation for a mixture of hard spheres," *Phys. Rev.* **133**(4A), 895–899 (1964).
242. R. J. Baxter, "Ornstein–Zernike relation and Percus–Yevick approximation for fluid mixtures," *J. Chem. Phys.* **52**(9), 4559–4562 (1970).
243. A. P. Ivanov, V. A. Loiko, and V. P. Dik, *Light Propagation in Densely Packed Disperse Media*, Nauka i Technika, Minsk (1988).
244. I. L. Maksimova and L. P. Shubochkin, "Light-scattering matrices for a close-packed binary system of hard spheres," *Opt. Spectrosc.* **70**(6), 745–748 (1991).
245. R. L. McCally and R. A. Farrell, "Light scattering from cornea and corneal transparency," in *Noninvasive Diagnostic Techniques in Ophtalmology*, B. R. Master, Ed., Springer-Verlag, New York (1990).
246. L. Reynolds, *Optical Diffuse Reflectance and Transmittance from an Anisotropically Scattering Finite Blood Medium*, Ph.D. thesis, Univ. of Washington, Seattle (1975).
247. V. G. Vereshchagin and A. N. Ponyavina, "Statistical characteristic and transparency of thin closely packed disperse layer," *Zh. Prikl. Spektr. (J. Appl. Spectrosc.)* **22**(3), 518–524 (1975).
248. I. L. Maksimova, V. V. Tuchin, and L. P. Shubochkin, "Polarization features of eye's cornea," *Opt. Spectrosc.* **60**(4), 801–807 (1986).
249. I. L. Maksimova, V. V. Tuchin, and L. P. Shubochkin, "Light scattering matrices of the crystalline lens," *Opt. Spectrosc.* **65**(3), 365–368 (1988).
250. G. Marguez, L. V. Wang, S.-P. Lin, J. A. Swartz, and S. L. Thomsen, "Anisotropy in the absorption and scattering spectra of the chicken breast tissue," *Appl. Opt.* **37**(4), 798–804 (1998).
251. S. Zigman, G. Sutliff, and M. Rounds, "Relationships between human cataracts and environmental radiant energy: cataract formation, light scattering and fluorescence," *Lens Eye Toxicity Res.* **8**, 259–280 (1991).
252. V. V. Tuchin and D. M. Zhestkov, "Tissue structure and eye lens transmission and scattering spectra," *Proc. SPIE* **3053**, 123–128 (1997).
253. Yu. P. Sinichkin, S. R. Utz, and H. A. Pilipenko, "Spectroscopy of human skin in vivo: I. reflection spectra," *Opt. Spectrosc.* **80**(2), 228–234 (1996).
254. N. G. Khlebtsov, V. V. Nikiforov, A. G. Melnikov, T. K. Merkulova, and L. N. Serdobintsev, "Elastic scattering spectroscopy of Yersinia pestis capsular protein solutions," *Biopolym. Cell* **6**(2), 81–87 (1990).
255. V. Twersky "Interface effects in multiple scattering by large, low refracting, absorbing particles," *J. Opt. Soc. Am.* **60**(7), 908–914 (1970).
256. M. Lax, "Multiple scattering of waves: II. The effective field in dense system," *Phys. Rev.* **85**(4), 621–629 (1952).

257. K. M. Hong, "Multiple scattering of electromagnetic waves by a crowded monolayer of spheres: application to migration imaging films," *J. Opt. Soc. Am.* **70**(7), 821–826 (1980).
258. A. Ishimary and Y. Kuga, "Attenuation constant of a coherent field in a dense distribution of particles," *J. Opt. Soc. Am.* **72**(10), 1317–1320 (1982).
259. A. N. Ponyavina, "Selection of optical radiation in scattering by partially ordered disperse media," *Zh. Prikl. Spektr. (J. Appl. Spectrosc.)* **65**(5), 721–733 (1998).
260. T. R. Smith, "Multiple scattering in the cornea," *J. Mod. Opt.* **35**(1), 93–101 (1988).
261. P. A. Zhu, A. K. Fung, and K. W. Wong, "Effective propagation constants in dense random media under effective medium approximation," *Radio Sci.* **22**, 234–250 (1987).
262. V. Twersky, "Absorption and multiple scattering by biological suspensions," *J. Opt. Soc. Am.* **60**, 1084–1093 (1970).
263. J. M. Steinke and A. P. Shepherd, "Diffusion model of the optical absorbance of whole blood," *J. Opt. Soc. Am. A* **5**, 813–822 (1988).
264. D. W. Rayleigh, "On the influence of obstacles arranged in rectangular order on the properties of a medium," *Philos. Mag.* **34**, 481–502 (1892).
265. R. P. Hemenger, "Birefringence of a medium of tenuous parallel cylinders," *Appl. Opt.* **28**(18), 4030–4034 (1989).
266. J. Lenoble, Ed., *Radiative Transfer in Scattering and Absorbing Atmospheres: Standard Computational Procedures*, A. Deepak Publishing, Hampton, VA (1985).
267. M. M. R. Williams, *Mathematical Methods in Particle Transport Theory*, Wiley, New York (1971).
268. A. H. Hielsher, J. R. Mourant, and I. J. Bigio, "Influence of particle size and concentration on the diffuse backscattering of polarized light from tissue phantoms and biological cell suspensions," *Appl. Opt.* **36**, 125–135 (1997).
269. V. V. Tuchin, S. R. Utz, and I. V. Yaroslavsky, "Tissue optics, light distribution, and spectroscopy," *Opt. Eng.* **33**(10), 3178–3188 (1994).
270. G. Yoon, A. J. Welch, M. Motamedi, and M. C. J. Van Gemert, "Development and application of three-dimensional light distribution model for laser irradiated tissue," *IEEE J. Quantum Electron.* **23**(10), 1721–1733 (1987).
271. G. Müller, B. Chance, and R. Alfano et al., Eds., *Medical Optical Tomography: Functional Imaging and Monitoring* IS11, SPIE Press, Bellingham, WA (1993).
272. G. Müller and A. Roggan, Eds., *Laser-Induced Interstitial Thermotherapy* **PM25**, SPIE Press, Bellingham, WA (1995).

273. V. V. Tuchin, Ed., *Selected Papers on Tissue Optics: Applications in Medical Diagnostics and Therapy* **MS102**, SPIE Press, Bellingham, WA (1994).
274. B. B. Das, F. Liu, and R. R. Alfano, "Time-resolved fluorescence and photon migration studies in biomedical and random media," *Rep. Prog. Phys.* **60**, 227–292 (1997).
275. Tuan Vo-Dinh, Ed., *Biomedical Photonics Handbook*, CRC Press, Boca Raton, FL (2003; 2nd ed., 2014).
276. J. M. Schmitt, A. H. Gandjbakhche, and R. F. Bonnar, "Use of polarized light to discriminate short-photons in a multiply scattering medium," *Appl. Opt.* **31**, 6535–6546 (1992).
277. P. Bruscaglioni, G. Zaccanti, and Q. Wei, "Transmission of a pulsed polarized light beam through thick turbid media: numerical results," *Appl. Opt.* **32**, 6142–6150 (1993).
278. M. I. Mishchenko, L. D. Travis, and A. A. Lacis, *Multiple Scattering of Light by Particles: Radiative Transfer and Coherent Backscattering*, Cambridge Univ. Press, Cambridge (2006).
279. D. Bicout, C. Brosseau, A. S. Martinez, and J. M. Schmitt, "Depolarization of multiply scattering waves by spherical diffusers: influence of the size parameter," *Phys. Rev. E* **49**, 1767–1770 (1994).
280. M. Dogariu and T. Asakura, "Photon pathlength distribution from polarized backscattering in random media," *Opt. Eng.* **35**, 2234–2239 (1996).
281. A. Ambirajan and D. C. Look, "A backward Monte Carlo study of the multiple scattering of a polarized laser beam," *J. Quant. Spectrosc. Radiat. Transfer* **58**, 171–192 (1997).
282. D. A. Zimnyakov, Yu. P. Sinichkin, P. V. Zakharov, and D. N. Agafonov, "Residual polarization of non-coherently backscattered linearly polarized light: the influence of the anisotropy parameter of the scattering medium," *Waves Random Media* **11**, 395–412 (2001).
283. I. A. Vitkin and R. C. N. Studinski, "Polarization preservation in diffusive scattering from in vivo turbid biological media: effects of tissue optical absorption in the exact backscattering direction," *Opt. Commun.* **190**, 37–43 (2001).
284. A. A. Kokhanovsky, "Reflection and polarization of light by semi-infinite turbid media: simple approximations," *J. Colloid Interface Sci.* **251**, 429–433 (2002).
285. L. Dagdug, G. H. Weiss, and A. H. Gandjbakhche, "Effects of anisotropic optical properties on photon migration in structured tissues," *Phys. Med. Biol.* **48**, 1361–1370 (2003).
286. H. H. Tynes, G. W. Kattawar, E. P. Zege, I. L. Katsev, A. S. Prikhach, and L. I. Chaikovskaya, "Monte Carlo and multicomponent approximation methods for vector radiative transfer by use of effective mueller matrix calculations," *Appl. Opt.* **40**(3), 400–412 (2001).

287. I. M. Stockford, S. P. Morgan, P. C. Y. Chang, and J. G. Walker, "Analysis of the spatial distribution of polarized light backscattering," *J. Biomed. Opt.* **7**(3), 313–320 (2002).
288. S. Bartel and A. H. Hielscher, "Monte Carlo simulations of the diffuse backscattering mueller matrix for highly scattering media," *Appl. Opt.* **39**, 1580–1588 (2000).
289. K. Y. Yong, S. P. Morgan, I. M. Stockford, and M. C. Pitter, "Characterization of layered scattering media using polarized light measurements and neural networks," *J. Biomed. Opt.* **8**(3), 504–511 (2003).
290. S. V. Gangnus, S. J. Matcher, and I. V. Meglinski, "Monte Carlo modeling of polarized light propagation in biological tissues," *Laser Phys.* **14**, 886–891 (2004).
291. B. C. Wilson and G. A. Adam, "Monte Carlo model for the absorption and flux distributions of light in tissue," *Med. Phys.* **10**, 824–830 (1983).
292. L.-H. Wang, S. L. Jacques, and L.-Q. Zheng, "MCML: Monte Carlo modeling of photon transport in multi-layered tissues," *Comput. Methods Prog. Biomed.* **47**, 131–146 (1995).
293. L.-H. Wang, S. L. Jacques, and L.-Q. Zheng, "CONV: convolution for responses to a finite diameter photon beam incident on multi-layered tissues," *Comput. Methods Prog. Biomed.* **54**, 141–150 (1997).
294. V. V. Tuchin, L. V. Wang, and D. A. Zimnyakov, *Optical Polarization in Biomedical Applications*, Springer-Verlag, New York (2006).
295. C. J. Hourdakis and A. Perris, "A Monte Carlo estimation of tissue optical properties for the use in laser dosimetry," *Phys. Med. Biol.* **40**, 351–364 (1995).
296. L. T. Perelman, J. Wu, I. Itzkan, and M. S. Feld, "Photon migration in turbid media using path integrals," *Phys. Rev. Lett.* **72**, 1341–1344 (1994).
297. G. Bal and M. Moscoso, "Theoretical and numerical analysis of polarization for time-dependent radiative transfer equations," *J. Quant. Spectrosc. Radiat. Transfer* **70**, 75–98 (2001).
298. X. Wang and L. V. Wang, "Propagation of polarized light in birefringent turbid media: time-resolved simulations," *Opt. Express* **9**(5), 254–259 (2001).
299. X. Wang and L. V. Wang, "Propagation of polarized light in birefringent turbid media: a Monte Carlo study," *J. Biomed. Opt.* **7**(3), 279–290 (2002).
300. I. L. Maksimova, S. V. Romanov, and V. F. Izotova, "The effect of multiple scattering in disperse media on polarization characteristics of scattered light," *Opt. Spectrosc.* **92**(6), 915–923 (2002).
301. L. V. Wang and H.-I. Wu, *Biomedical Optics: Principles and Imaging*, Wiley-Interscience, Hoboken, NJ (2007).

302. V. Shankaran, J. T. Walsh Jr, and D. J. Maitland, "Comparative study of polarized light propagation in biological tissues," *J. Biomed. Opt.* **7**(3), 300–306 (2002).
303. M. J. Rakovic and G. W. Kattawar, "Theoretical analysis of polarization patterns from incoherent backscattering of light," *Appl. Opt.* **37**(15), 3333–3338 (1998).
304. I. L. Maksimova, S. N. Tatarintsev, and L. P. Shubochkin, "Multiple scattering effects in laser diagnostics of bioobjects," *Opt. Spectrosc.* **72**, 1171–1177 (1992).
305. K. C. Hadley and I. A. Vitkin, "Optical rotation and linear and circular depolarization rates in diffusively scattered light from chiral, racemic, and achiral turbid media," *J. Biomed. Opt.* **7**(3), 291–299 (2002).
306. L. O. Svaasand and Ch. J. Gomer, "Optics of tissue," in *Dosimetry of Laser Radiation in Medicine and Biology* IS5, SPIE Press, Bellingham, WA, pp. 114–132 (1989).
307. A. N. Yaroslavsky, I. V. Yaroslavsky, T. Goldbach, and H. -J. Schwarzmaier, "Influence of the scattering phase function approximation on the optical properties of blood determined from the integrating sphere measurements," *J. Biomed. Opt.* **4**(1), 47–53 (1999).
308. H. Horinaka, K. Hashimoto, K. Wada, and Y. Cho, "Extraction of quasi-straightforward-propagating photons from diffused light transmitting through a scattering medium by polarization modulation," *Opt. Lett.* **20**, 1501–1503 (1995).
309. S. P. Morgan, M. P. Khong, and M. G. Somekh, "Effects of polarization state and scatterer concentration optical imaging through scattering media," *Appl. Opt.* **36**, 1560–1565 (1997).
310. M. R. Ostermeyer, D. V. Stephens, L. Wang, and S. L. Jacques, "Nearfield polarization effects on light propagation in random media," OSA TOPS 3, Optical Society of America, Washington, DC, pp. 20–25 (1996).
311. L. V. Wang, G. L. Coté, and S. L. Jacques, Eds., "Special section on tissue polarimetry," *J. Biomed. Opt*. **7**(3), 278–397 (2002).
312. R. R. Anderson, "Polarized light examination and photography of the skin," *Arch. Dermatol.* **127**, 1000–1005 (1991).
313. A. W. Dreher and K. Reiter, "Polarization technique measures retinal nerve fibers," *Clin. Vis. Sci.* **7**, 481–485 (1992).
314. N. Kollias, "Polarized light photography of human skin," in *Bioengineering of the Skin: Skin Surface Imaging and Analysis*, K.-P. Wilhelm, P. Elsner, E. Berardesca, and H. I. Maibach, Eds., CRC Press, Boca Raton, FL, pp. 95–106 (1997).
315. S. L. Jacques, R. J. Roman, and K. Lee, "Imaging superficial tissues with polarized light," *Lasers Surg. Med.* **26**, 119–129 (2000).
316. S. L. Jacques, J. C. Ramella-Roman, and K. Lee, "Imaging skin pathology with polarized light," *J. Biomed. Opt.* **7**(3), 329–340 (2002).

317. N. Ghosh, M. F. G. Wood, and I. A. Vitkin, "Polarized light assessment of complex turbid media such as biological tissues via Mueller matrix decomposition," in *Handbook of Photonics for Biomedical Science*, V. V. Tuchin, Ed., CRC Press, Taylor & Francis Group, London, pp. 253–282 (2010).
318. N. Ghosh and I. A. Vitkin, "Concepts, challenges and applications of polarized light in biomedicine: a tutorial review," *J. Biomed. Opt.* **16**(11), 110801-1–29 (2010).
319. S. Alali, M. Ahmad, A. J. Kim, N. Vurgun, M. F. G. Wood, and I. A. Vitkin, "Quantitative correlation between light depolarization and transport albedo of various porcine tissues," *J. Biomed. Opt.* **17**(4), 045004 (2012).
320. D. Layden, N. Ghosh, and A. Vitkin, "Quantitative polarimetry for tissue characterization and diagnosis," in *Advanced Biophotonics: Tissue Optical Sectioning*, R. K. Wang and V. V. Tuchin, Eds., CRC Press, Taylor & Francis Group, Boca Raton, FL, London, and New York, pp. 73–108 (2013).
321. A. Pierangelo, S. Manhas, A. Benali, C. Fallet, J.-L. Totobenazara, M.-R. Antonelli, T. Novikova, B. Gayet, A. De Martino, and P. Validire, "Multispectral Mueller polarimetric imaging detecting residual cancer and cancer regression after neoadjuvant treatment for colorectal carcinomas," *J. Biomed. Opt.* **18**(4), 046014-1–9 (2013).
322. E. E. Gorodnichev, S. V. Ivliev, A. I. Kuzovlev, and D. B. Rogozkin, "Transillumination of highly scattering media by polarized light," in *Light Scattering Reviews 8. Radiative Transfer and Light Scattering*, A. A. Kokhanovsky, Ed., Springer Praxis, Berlin and Heidelberg, pp. 317–361 (2013).
323. C. Macdonald, A. Doronin, A. F. Peña, M. Eccles, and I. Meglinski, "Diffusing-wave polarimetry for tissue diagnostics," *Proc. SPIE* **8940**, 894007 (2014).
324. E. Du, H. He, N. Zeng, M. Sun, Y. Guo, J. Wu, S. Liu, and H. Ma, "Mueller matrix polarimetry for differentiating characteristic features of cancerous tissues," *J. Biomed. Opt.* **19**(7), 076013 (2014).
325. E. E. Gorodnichev and D. B. Rogozkin, "Small angle multiple scattering in random inhomogeneous media," *JETP* **107**, 209–235 (1995).
326. J. Ramella-Roman, S. Prahl, and S. Jacques, "Three Monte Carlo programs of polarized light transport into scattering media: part I," *Opt. Express* **13**(12), 4420–4438 (2005); part II, *Opt. Express* **13**(25), 10392–10405 (2005).
327. M. J. Rakovic, G. W. Kattawar, M. Mehrubeoglu, B. D. Cameron, L.-H. V. Wang, S. Rastegar, and G. L. Coté, "Light backscattering polarization patterns from turbid media: theory and experiment," *Appl. Opt.* **38**, 3399–3408 (1999).

328. S. L. Jacques, M. Ostemeyer, L.-H. Wang, and D. Stephens, "Polarized light transmission through skin using video reflectometry: toward optical tomography of superficial tissue layers," in *Lasers in Surgery: Advanced Characterization, Therapeutics, and Systems VI*, R. R. Anderson, Ed., *Proc. SPIE* **2671**, 199–220 (1996).
329. G. Yao and L.-H. V. Wang, "Two-dimensional depth-resolved Mueller matrix characterization of biological tissue by optical coherence tomography," *Opt. Lett.* **24**, 537–539 (1999).
330. S. Jiao, G. Yao, and L.-H. V. Wang, "Depth-resolved two-dimensional Stokes vectors of backscattered light and Mueller matrices of biological tissue measured by optical coherence tomography," *Appl. Opt.* **39**, 6318–6324 (2000).
331. V. F. Izotova, I. L. Maksimova, and S. V. Romanov, "Color of biotissues and artificial disperse systems under diffuse scattering of light," *Proc. SPIE* **4001**, 279–285 (2000).
332. G. V. Bally, *Optics in Biomedical Sciences*, Springer-Verlag, Berlin (1982).
333. J. W. Hovenier, H. C. van de Hulst, and C. V. M. van der Mee, "Conditions for the elements of the scattering matrix," *Astron. Astrophys.* **157**, 301–310 (1986).
334. J. W. Hovenier, "Structure of a general pure Mueller matrix," *Appl. Opt.* **33**, 8318–8324 (1994).
335. E. S. Fry and G. W. Kattawar, "Relationships between elements of the Stokes matrix," *Appl. Opt.* **20**, 2811–2814 (1981).
336. R. W. Shaefer, "Inequalities between the elements of the Mueller scattering matrix," *Appl. Opt.* **20**, 2875–2881 (1981).
337. G. W. Kattawar and E. S. Fry, "Inequalities between the elements of the Mueller scattering matrix: comments," *Appl. Opt.* **21**, 18 (1982).
338. J. J. Gil and E. Bernabeu, "A depolarization criterion in Mueller matrix," *Opt. Acta* **32**, 259–261 (1985).
339. V. F. Izotova, I. L. Maksimova, and S. V. Romanov, "Utilization of relation between elements of the Mueller matrices for estimating properties of objects and the reliability of experiments," *Opt. Spectrosc.* **80**(5), 753–759 (1996).
340. J. W. Hovenier and C. V. M. van der Mee, "Relationships for matrices describing scattering by small particles," Chapter 3 in *Light Scattering by Nonspherical Particles: Theory, Measurements, and Applications*, M. I. Mishchenko, J. W. Hovenier, and L. D. Travis, Eds., Academic Press, New York, pp. 62–85 (2000).
341. J. W. Mishchenko and L. D. Hovenier, "Depolarization of light backscattered by randomly oriented nonspherical particles," *Opt. Lett.* **20**, 1356–1358 (1995).

342. A. V Priezzhev, V. V. Tuchin, and L. P. Shubochkin, *Laser Diagnostics in Biology and Medicine* (in Russian), Nauka, Moscow (1989).
343. G. J. Buffone, J. Savory, and J. Hermans, "Evaluation of kinetic light scattering as an approach to the measurement of specific proteins with the centrifugal analyzer: II. theoretical considerations," *Clin. Chem.* **21**(12), 1735–1746 (1975).
344. A. Ya. Khairullina, T. V. Oleinik, and I. L. Katsev, "Possibility of optic diagnostics of mono- and multi-layer structures simulating human organs," *Opt. Spectrosc.* **75**(1), 130–137 (1993).
345. A. N. Korolevich, A. Ya. Khairullina, and L. P. Shubochkin, "Scattering matrix for 'soft' particles," *Opt. Spectrosc.* **68**(2), 403–409 (1990).
346. A. N. Korolevich, A. Ya. Khairullina, and L. P. Shubochkin, "Effects of aggregation of large biological particles on the scattering matrix elements," *Opt. Spectrosc.* **77**(2), 278–282 (1994).
347. V. F. Izotova, I. L. Maksimova, and S. V. Romanov, "Simulation of polarization characteristics of the crystalline lens during protein aggregation with regard to multiple scattering," *Opt. Spectrosc.* **86**(6), 902–908 (1999).
348. V. F. Izotova, I. L. Maksimova, and S. V. Romanov, "Analysis of errors of a laser polarization nephelometer," *Opt. Spectrosc.* **80**(6), 905–1001 (1996).
349. A. J. Hunt and D. R. Huffman, "A new polarization-modulated light scattering instrument," *Rev. Sci. Instrum.* **44**(12), 1753–1762 (1973).
350. R. C. Thompson, J. R. Bottiger, and E. S. Fry, "Measurement of polarized light interactions via the Mueller matrix," *Appl. Opt.* **19**(8), 1323–1332 (1980).
351. R. M. A. Azzam, Polarimeter, US Patent No. 4.306.809 (1981).
352. W. S. Bickel, J. F. Davidson, D. R. Huffman, and R. Kilkson, "Application of polarization effects in light scattering: a new biophysical tool," *Proc. Natl. Acad. Sci. USA* **73**, 486–490 (1976).
353. K. J. Voss and E. S. Fry, "Measurement of the Mueller matrix for ocean water," *Appl. Opt.* **23**, 4427–4439 (1984).
354. K. D. Lofftus, M. S. Quinby-Hunt, A. J. Hunt, F. Livolant, and M. Maestre, "Light scattering by Prorocentrum micans: a new method and results," *Appl. Opt.* **31**, 2924–2931 (1992).
355. W. S. Bickel and M. E. Stafford, "Biological particles as irregularly shaped particles," in *Light Scattering by Irregularly Shaped Particles*, D. Schuerman, Ed., Plenum, New York, pp. 299–305 (1980).
356. A. G. Hoekstra and P. M. A. Sloot, "Dipolar unit size in coupled-dipole calculations of the scattering matrix elements," *Appl. Opt.* **18**, 1211–1213 (1993).

357. B. V. Bronk, S. D. Druger, J. Czege, and W. P. van de Merwe, "Measuring diameters of rod-shaped bacteria in vivo with polarized light scattering," *Biophys. J.* **69**, 1170–1177 (1995).
358. W. P. van de Merwe, Z.-Z. Li, B. V. Bronk, and J. Czege, "Polarized light scattering for rapid observation of bacterial size changes," *Biophys. J.* **73**, 500–506 (1997).
359. O. V. Angelsky, A. G. Ushenko, A. Yu. Ushenko, V. P. Pishak, and A. P. Peresunko, "Statistical, correlation, and topological approaches in diagnostics of the structure and physiological state of birefringent biological tissues," in *Handbook of Photonics for Biomedical Science*, V. V. Tuchin, Ed., CRC Press, Taylor & Francis Group, London, pp. 283–322 (2010).
360. V. V. Tuchin, I. L. Maksimova, A. N. Yaroslavskaya, T. N. Semenova, S. N. Tatarintsev, V. I. Kochubey, and V. F. Izotova, "Human eye lens spectroscopy and modeling of its transmittance," *Proc. SPIE* **2126**, 393–406 (1994).
361. W. P. van de Merwe, D. R. Huffman, and B. V. Bronk, "Reproducibility and sensitivity of polarized light scattering for identifying bacterial suspension," *Appl. Opt.* **28**(23), 5052–5057 (1989).
362. C. Bustamante, I. Tinoco, Jr., and M. F. Maestre, "Circuar intensity differential scattering of light by helical structures: III. A general polarizability tensor and anomalous scattering," *J. Chem. Phys.* **74**, 4839–4850 (1981).
363. C. Bustamante, I. Tinoco, Jr., and M. F. Maestre, "Circular intensity differential scattering of light by helical structures. IV. Randomly oriented species," *J. Chem. Phys.* **76**, 3440–3446 (1982).
364. C. Bustamante, M. F. Maestre, D. Keller, and I. Tinoco, Jr., "Differential scattering (CIDS) of circularly polarized light by dense particles," *J. Chem. Phys.* **80**, 4817–4823 (1984).
365. S. Zietz, A. Belmont, and C. Nicolini, "Differential scattering of circularly polarized light as a unique probe of polynucleosome superstructure," *Cell Biophys.* **5**, 163–187 (1983).
366. C. T. Gross, H. Salamon, A. J. Hunt, R. I. Macey, F. Orme, and A. T. Quintanilha, "Hemoglobin polymerization in sickle cells studied by circular polarized light scattering," *Biochim. Biophys. Acta* **1079**(2), 152–160 (1991).
367. B. Kunnen, C. Macdonald, A. Doronin, S. Jacques, M. Eccles, and I. Meglinski, "Application of circularly polarized light for non-invasive diagnosis of cancerous tissues and turbid tissue-like scattering media," *J. Biophotonics* **8**(4), 317–323 (2015).
368. R. J. McNichols and G. L. Cote, "Optical glucose sensing in biological fluids: an overview," *J. Biomed. Opt.* **5**(1), 5–16 (2000).
369. V. V. Tuchin, Ed., *Handbook of Optical Sensing of Glucose in Biological Fluids and Tissues*, CRC Press, Taylor & Francis Group, London (2009).

370. M. F. G. Wood, N. Ghosh, X. Guo, and I. A. Vitkin, "Towards noninvasive glucose sensing using polarization analysis of multiply scattered light," in *Handbook of Optical Sensing of Glucose in Biological Fluids and Tissues*, V. V. Tuchin, Ed., CRC Press, Taylor & Francis Group, London, pp. 469–450 (2009).
371. G. Purvinis, B. D. Cameron, and D. M. Altrogge, "Noninvasive polarimetric-based glucose monitoring: an in vivo study," *J. Diabetes Sci. Technol.* **5**(2), 380–387 (2011).
372. B. Chance, H. Liu, T. Kitai, and Y. Zhang, "Effects of solutes on optical properties of biological materials: models, cells, and tissues," *Anal. Biochem.* **227**, 351–362 (1995).
373. H. Liu, B. Beauvoit, M. Kimura, and B. Chance, "Dependence of tissue optical properties on solute-induced changes in refractive index and osmolarity," *J. Biomed. Opt.* **1**, 200–211 (1996).
374. V. V. Tuchin, J. Culver, C. Cheng, S. A. Tatarkova, M. DellaVecchia, D. A. Zimnyakov, A. Chaussky, A. G. Yodh, and B. Chance, "Refractive index matching of tissue components as a new technology for correlation and diffusing–photon spectroscopy and imaging," *Proc. SPIE* **3598**, 111–120 (1999).
375. P. O. Rol, *Optics for Transscleral Laser Applications*, Dissertation for the degree of Doctor of Natural Sciences, Zurich (1992).
376. E. K. Chan, B. Sorg, D. Protsenko, M. O'Neil, M. Motamedi, and A. J. Welch, "Effects of compression on soft tissue optical properties," *IEEE J. Sel. Topics Quantam Electron.* **2**(4), 943–950 (1996).
377. B. Nemati, H. G. Rylander, III, and A. J. Welch, "Optical properties of conjunctiva, sclera, and the ciliary body and their consequences for transscleral cyclophotocoagulation," *Appl. Opt.* **35**(19), 3321–3327 (1996).
378. V. V. Tuchin, I. L. Maksimova, D. A. Zimnyakov, I. L. Kon, A. H. Mavlutov, and A. A. Mishin, "Light propagation in tissues with controlled optical properties," *J. Biomed. Opt.* **2**(4), 401–417 (1997).
379. Z. S. Sacks, R. M. Kurtz, T. Juhasz, and G. A. Mourau, "High precision subsurface photodisruption in human sclera," *J. Biomed. Opt.* **7**(3), 442–450 (2002).
380. J. S. Maier, S. A. Walker, S. Fantini, M. A. Franceschini, and E. Gratton, "Possible correlation between blood glucose concentration and the reduced scattering coefficient of tissues in the near infrared," *Opt. Lett.* **19**, 2062–2064 (1994).
381. M. M. Cope, M. Essenpreis, and D. Bocker, "Influence of glucose concentration on light scattering in tissue-simulating phantoms," *Opt. Lett.* **19**, 2170–2172 (1994).
382. J. T. Bruulsema, J. E. Hayward, and T. J. Farrell et al., "Correlation between blood glucose concentration in diabetics and noninvasively

measured tissue optical scattering coefficient," *Opt. Lett.* **22**, 190–192 (1997).
383. G. Vargas, E. K. Chan, J. K. Barton, H. G. Rylander III, and A. J. Welch, "Use of an agent to reduce scattering in skin," *Laser. Surg. Med.* **24**, 138–141 (1999).
384. V. V. Tuchin, "Coherent optical techniques for the analysis of tissue structure and dynamics," *J. Biomed. Opt.* **4**(1), 106–124 (1999).
385. V. V. Tuchin, "Controlling of tissue optical properties," *Proc. SPIE* **4001**, 30–53 (2000).
386. A. N. Bashkatov, V. V. Tuchin, E. A. Genina, Yu. P. Sinichkin, N. A. Lakodina, and V. I. Kochubey, "The human sclera dynamic spectra: in vitro and in vivo measurements," *Proc. SPIE* **3591**, 311–319 (1999).
387. V. V. Tuchin, "Optical immersion as a new tool to control optical properties of tissues and blood," *Laser Phys.* **15**(8), 1109–1136 (2005).
388. V. V. Tuchin, "Optical clearing of tissue and blood using immersion method," *J. Phys. D: Appl. Phys.* **38**, 2497–2518 (2005).
389. V. V. Tuchin, *Optical Clearing of Tissues and Blood*, **PM 154**, SPIE Press, Bellingham, WA (2006).
390. V. V. Tuchin, "A clear vision for laser diagnostics," *IEEE J. Sel. Topics Quantam Electron.* **13**(6), 1621–1628 (2007).
391. E. A. Genina, A. N. Bashkatov, and V. V. Tuchin, "Tissue optical immersion clearing," *Expert Rev. Med. Devices* **7**(6), 825–842 (2010).
392. E. A. Genina, A. N. Bashkatov, K. V. Larin, and V. V. Tuchin, "Light–tissue interaction at optical clearing" in *Laser Imaging and Manipulation in Cell Biology*, F. S. Pavone, Ed., Wiley-VCH Verlag GmbH & Co. KGaA, Weinheim, pp. 115–164 (2010).
393. K. V. Larin, M. G. Ghosn, A. N. Bashkatov, E. A. Genina, N. A. Trunina, and V. V. Tuchin, "Optical clearing for OCT image enhancement and in-depth monitoring of molecular diffusion," *IEEE J. Sel. Topics Quantam Electron.* **18**(3) 1244–1259 (2012).
394. D. Zhu, K. V. Larin, Q. Luo, and V. V. Tuchin, "Recent progress in tissue optical clearing," *Laser Photonics Rev*. **7**(5), 732–757 (2013).
395. D. Zhu, Q. Luo, and V. V. Tuchin, "Tissue optical clearing," in *Advanced Biophotonics: Tissue Optical Sectioning*, R. K. Wang and V. V. Tuchin, Eds., CRC Press, Taylor & Francis Group, Boca Raton, FL, London, and New York, pp. 621–672 (2013).
396. R. K. Wang and V. V. Tuchin, "Optical coherence tomography: light scattering and imaging enhancement," in *Coherent-Domain Optical Methods: Biomedical Diagnostics, Environmental Monitoring and Material Science*, 2nd ed., V. V. Tuchin, Ed., Springer-Verlag, Berlin, Heidelberg, and New York, pp. 665–742 (2013).

397. J. Wang, Y. Zhang, P. Li, Q. Luo, and D. Zhu, "Review: tissue optical clearing window for blood flow monitoring (invited paper)," *IEEE J. Sel. Topics Quantam Electron.* **20**(2), 6801112-1–12 (2014).
398. O. Nadiarnykh and P. J. Campagnola, "SHG and optical clearing," in *Second Harmonic Generation Imaging*, F. S. Pavone and P. J. Campagnola, Eds., CRC Press, Taylor & Francis Group, Boca Raton, FL; London; and New York, pp. 169–189 (2014).
399. E. A. Genina, A. N. Bashkatov, Yu. P. Sinichkin, I. Yu. Yanina, and V. V. Tuchin, "Optical clearing of biological tissues: prospects of application in medical diagnostics and phototherapy [review]," *J. Biomed. Photonics Eng.* **1**(1), 22–58 (2015).
400. D. E. Freund, R. L. McCally, and R. A. Farrell, "Effects of fibril orientations on light scattering in the cornea," *JOSA A* **3**, 1970–1982 (1986).
401. R. A. Farrell, D. E. Freund, and R. L. McCally, "Research on corneal structure," *Johns Hopkins Appl. Phys. Lab. Tech. Dig.* **11**(1–2), 191–199 (1990).
402. R. Drezek, A. Dunn, and R. Richards-Kortum, "Light scattering from cells: finite-difference time-domain simulations and goniometric measurements," *Appl. Opt.* **38**(16), 3651–3661 (1999).
403. B. Beauvoit, T. Kitai, and B. Chance, "Contribution of the mitochondrial compartment to the optical properties of the rat liver: a theoretical and practical approach," *Biophys. J.* **67**, 2501–2510 (1994).
404. R. Graaff, J. G. Aarnoudse, J. R. Zijp, P. M. A. Sloot, F. F. M. de Mul, J. Greve, and M. H. Koelink, "Reduced light scattering properties for mixtures of spherical particles: a simple approximation derived from Mie calculations," *Appl. Opt.* **31**, 1370–1376 (1992).
405. G. C. Beck, N. Akgun, A. Ruck, and R. Steiner, "Design and characterization of a tissue phantom system for optical diagnostics," *Lasers Med. Sci.* **13**, 160–171 (1998).
406. G. C. Beck, N. Akgun, A. Ruck, and R. Steiner, "Developing optimized tissue phantom systems for optical biopsies," *Proc. SPIE* **3197**, 76–85 (1997).
407. W.-C. Lin, M. Motamedi, and A. J. Welch, "Dynamics of tissue optics during laser heating of turbid media," *Appl. Opt.* **35**(19), 3413–3420 (1996).
408. L. O. Svaasand, B. J. Tromberg, R. C. Haskell, T.-T. Tsay, and M. W. Berns, "Tissue characterization and imaging using photon density waves," *Opt. Eng.* **32**, 258–266 (1993).
409. A. Kotyk and K. Janacek, *Membrane Transport: An Interdisciplinary Approach*, Plenum, New York (1977).
410. A. Roggan, M. Friebel, K. Dorschel, A. Hahn, and G. Mueller, "Optical properties of circulating human blood in the wavelength range 400–2500 nm," *J. Biomed. Opt.* **4**, 36–46 (1999).
411. A. H. Gandjbakhche, P. Mills, and P. Snabre, "Light-scattering technique for the study of orientation and deformation of red

blood cells in a concentrated suspension," *Appl. Opt.* **33**, 1070–1078 (1994).
412. V. L. Voeikov, C. N. Novikov, and N. D. Vilenskaya, "Low-level chemiluminescent analysis of nondiluted human blood reveals its dynamic system properties," *J. Biomed. Opt.* **4**, 54–60 (1999).
413. A. V. Priezzhev, O. M. Ryaboshapka, N. N. Firsov, and I. V. Sirko, "Aggregation and disaggregation of erythrocytes in whole blood: study by backscattering technique," *J. Biomed. Opt.* **4**, 76–84 (1999).
414. L. D. Shvartsman and I. Fine, "Optical transmission of blood: effect of erythrocyte aggregation," *IEEE Trans. Biomed. Eng.* **50**, 1026–1033 (2003).
415. M. Brezinski, K. Saunders, C. Jesser, X. Li, and J. Fujimoto, "Index matching to improve OCT imaging through blood," *Circulation* **103**, 1999–2003 (2001).
416. X. Xu, R. K. Wang, J. B. Elder, and V. V. Tuchin, "Effect of dextran-induced changes in refractive index and aggregation on optical properties of whole blood," *Phys. Med. Biol.* **48**, 1205–1221 (2003).
417. V. V. Tuchin, X. Xu, and R. K. Wang, "Dynamic optical coherence tomography in optical clearing, sedimentation and aggregation study of immersed blood," *Appl. Opt.OT* **41**(1), 258–271 (2002).
418. Y. Ozaki, H. Kitabata, and H. Tsujioka et al., "Comparison of contrast media and low-molecular-weight dextran for frequency-domain optical coherence tomography," *Circ. J.* **76**(4), 922–927 (2012).
419. J. Li, H. Minami, E. Steward, T. Ma, D. Mohar, C. Robertson, K. Shung, Q. Zhou, P. Patel, and Z. Chen, "Optimal flushing agents for integrated optical and acoustic imaging systems," *J. Biomed. Opt.* **20**(5), 056005 (2015)
420. E. I. Galanzha, V. V. Tuchin, A. V. Solovieva, T. V. Stepanova, Q. Luo, and H. Cheng, "Skin backreflectance and microvascular system functioning at the action of osmotic agents," *J. Phys. D: Appl. Phys.* **36**, 1739–1746 (2003).
421. O. Zhernovaya, V. V. Tuchin, and M. J. Leahy, "Blood optical clearing studied by optical coherence tomography," *J. Biomed. Opt.* **18**(2), 026014-1–8 (2013).
422. R. Shi, M. Chen, V. V. Tuchin, and D. Zhu, "Accessing to arteriovenous blood flow dynamics response using combined laser speckle contrast imaging and skin optical clearing," *Biomed. Opt. Express* **6**(6), 1977–1989 (2015).
423. C. Macdonald and I. Meglinski, "Backscattering of circular polarized light from a disperse random medium influenced by optical clearing," *Laser Phys. Lett.* **8**(4), 324–328 (2011).
424. L. F. Rojas-Ochoa, D. Lacoste, R. Lenke, P. Schurtenberger, and F. Scheffold, "Depolarization of backscattered linearly polarized light," *J. Opt. Soc. Am. A* **21**, 1799–1804 (2004).

425. M. Xu and R. R. Alfano, "Circular polarization memory of light," *Phys. Rev. E* **72**, 065601(R) (2005).
426. Y. L. Kim, P. Pradhan, M. H. Kim, and V. Backman, "Circular polarization memory effect in low-coherence enhanced backscattering of light," *Opt. Lett.* **31**, 2744–2746 (2006).
427. A. Doronin and I. Meglinski, "Online object oriented Monte Carlo computational tool for the needs of biomedical optics," *Biomed. Opt. Express* **2**(9), 2461–2469 (2011).
428. A. Doronin, C. Macdonald, and I. Meglinski, "Propagation of coherent polarized light in highly scattering turbid media," *J. Biomed. Opt.* **19**(2), 025005 (2014).
429. S. Prahl, "Maetzler's MATLAB Code for Mie Theory," Oregon Medical Laser Centre: http://omlc.ogi.edu/software/mie/.
430. S. He, K. L. Dunn, P. S. Espino, B. Drobic, L. Li, J. Yu, J-M. Sun, H. Y. Chen, S. Pritchard, and J. R. Davie, "Chromatin organization and nuclear microenvironments in cancer cells," *J. Cell. Biochem.* **104**, 2004–2015 (2008).
431. K. N. Dahl, A. J. Ribeiro, and J. Lammerding, "Nuclear shape, mechanics, and mechanotransduction," *Circ. Res.* **102**(11), 1307–1318 (2008).
432. F. R. Neumann and P. Nurse, "Nuclear size control in fission yeast," *J. Cell Biol.* **179**(4), 593–600 (2007).
433. M. Webster, K. L. Witkin, and O. Cohen-Fix, "Sizing up the nucleus: nuclear shape, size and nuclear–envelope assembly," *J. Cell Sci.* **122**(10), 1477–1486 (2009).
434. Y. Masui, "Towards understanding the control of the division cycle in animal cells," *Biochem. Cell. Biol.* **70**(10–11), 920–945 (1992).
435. V. L. Kuzmin and I. V. Meglinski, "Backscattering of linearly and circularly polarized light in randomly inhomogeneous media," *Opt. Spectrosc.* **106**(2), 257–267 (2009).
436. V. L. Kuzmin and I. V. Meglinski, "Anomalous polarization phenomena of light scattered in random media," *J. Exp. Theor. Phys.* **137**(5), 742–753 (2010).
437. I. Meglinski and V. L. Kuzmin, "Coherent backscattering of circularly polarized optical radiation from a disperse random medium," *Prog. Electromagn. Res. M* **16**, 47–61 (2011).
438. I. Meglinski, C. Macdonald, A. Karl, H. Yoon, and M. Eccles, "The mapping of tissues scattering properties on the Poincaré sphere," in *Biomedical Optics, OSA Technical Digest* (Optical Society of America), paper BW3B.6 (2012).
439. I. Meglinski, C. Macdonald, A. Doronin, and M. Eccles, "Screening cancer aggressiveness by using circularly polarized light," in *Optics in the Life Sciences*, OSA Technical Digest (online) (Optical Society of America), paper BM2A.4 (2013).

Nikolai G. Khlebtsov is the head of the Nanobiotechnology Laboratory at the Russian Academy of Sciences' Institute of Biochemistry and Physiology of Plants and Microorganisms. He has published over 400 scientific works, including two monographs and seven book chapters. His current research interests are biophotonics and nanobiotechnology of plasmon-resonant and hybrid multifunctional nanoparticles, nanostructures for SERS, and biomedical applications of plasmonic and hybrid composite nanoparticles.

Irina L. Maksimova (1959–2013) was a professor and chair of Optics and Biophotonics at Saratov State University. Her research interests included light scattering, polarized light analysis, tissue optics, laser medicine, and nanobiophotonics. She authored more than 100 peer-reviewed papers. Prof. Maksimova was one of the pioneers of modeling the polarization properties of eye tissues and designing precise algorithms for their measurements. In 2013, she was named the best supervisor of Ph.D. students at SSU.

Igor Meglinski is the head of the Opto-Electronics and Measurement Techniques Laboratory at the University of Oulu, Finland. For the last 20 years, his research interests have been concerned with the interface between physics, optical and biomedical engineering, sensor technologies, and life sciences, focusing on the development of new non-invasive imaging/diagnostic techniques and their application in medicine and biology, material sciences, pharmacy, food, environmental monitoring, and health care industries. He pioneered the application of diffusing wave spectroscopy (DWS) to non-invasively monitor blood flow and blood microcirculation, the application of circularly polarized light for practical cancer diagnosis, the generalization of the Monte Carlo model to simulate the coherent effects of multiple scattering of light, and the development of online computational tools for the biophotonics and biomedical optics community. Prof. Meglinski has authored or co-authored over 200 research papers in peer-reviewed scientific journals, proceedings of international conferences, book chapters, patents, and professional magazines. He has delivered over 450 presentations at major international conferences, including over 200 invited lectures and plenary talks. He is the Node Leader for the Biophotonics4Life Worldwide Consortium (BP4L), Fellow of the Institute of Physics (London, UK), and Fellow of SPIE.

Lihong V. Wang holds the Gene K. Beare Distinguished Professorship of Biomedical Engineering at Washington University in St. Louis. His book entitled *Biomedical Optics: Principles and Imaging*, one of the first textbooks in the field, won the 2010 Joseph W. Goodman Book Writing Award. He edited the first book on photoacoustic tomography. Professor Wang has published 435 peer-reviewed journal articles and delivered 430 keynote, plenary, or invited talks. His Google Scholar *h*-index and citations have reached 100 and 40,000, respectively. His laboratory was the first to report functional photoacoustic tomography, 3D photoacoustic microscopy, photoacoustic endoscopy, photoacoustic reporter gene imaging, the photoacoustic Doppler effect, and the universal photoacoustic reconstruction algorithm. He is the Editor-in-Chief of the *Journal of Biomedical Optics*. He chairs the annual conference on Photons plus Ultrasound. He received NIH's FIRST, NSF's CAREER, NIH Director's Pioneer, and NIH Director's Transformative Research awards. He also received the OSA C. E. K. Mees Medal, IEEE Technical Achievement Award, IEEE Biomedical Engineering Award, SPIE Britton Chance Biomedical Optics Award, and Senior Prize of the International Photoacoustic and Photothermal Association for "seminal contributions to photoacoustic tomography and Monte Carlo modeling of photon transport in biological tissues." An honorary doctorate was conferred on him by Lund University, Sweden. His lab is transitioning to Caltech.

Valery V. Tuchin is a professor and chairman of Optics and Biophotonics at Saratov National Research State University. He is also the head of laboratory at the Institute of Precision Mechanics and Control, RAS, and the supervisor of Interdisciplinary Laboratory of Biophotonics at Tomsk National Research State University. His research interests include biophotonics, tissue optics, laser medicine, tissue optical clearing, and nanobiophotonics. He is a member of SPIE, OSA, and IEEE, guest professor of HUST (Wuhan) and Tianjin Universities of China, and adjunct professor of the Limerick University (Ireland) and National University of Ireland (Galway). He is a fellow of SPIE and OSA, and has been awarded Honored Science Worker of the Russia, SPIE Educator Award, FiDiPro (Finland), Chime Bell Prize of Hubei Province (China), and Joseph W. Goodman Book Writing Award (OSA/SPIE).

Index

HANDBOOK OF OPTICAL BIOMEDICAL DIAGNOSTICS

SECOND EDITION

Volume 2: Methods

Valery V. Tuchin

EDITOR

Since the publication of the first edition of the *Handbook* in 2002, optical methods for biomedical diagnostics have developed in many well-established directions, and new trends have also appeared. The text has been updated and expanded into two volumes.

Volume 1: Light–Tissue Interaction features eleven chapters, five of which focus on the fundamental physics of light propagation in turbid media such as biological tissues. The six following chapters introduce near-infrared techniques for the optical study of tissues and provide a snapshot of current applications and developments in this dynamic and exciting field. Topics include the scattering of light in disperse systems, the optics of blood, tissue phantoms, a comparison between time-resolved and continuous-wave methods, and optoacoustics.

Volume 2: Methods begins by describing the basic principles and diagnostic applications of optical techniques based on detecting and processing the scattering, fluorescence, FT IR, and Raman spectroscopic signals from various tissues, with an emphasis on blood, epithelial tissues, and human skin. The second half of the volume discusses specific imaging technologies, such as Doppler, laser speckle, optical coherence tomography (OCT), and fluorescence and photoacoustic imaging.

ISBN 9781628419139

SPIE.

P.O. Box 10
Bellingham, WA 98227-0010

ISBN: 9781628419139
SPIE Vol. No.: PM263